Controlled Growth of Organo-Metal Halide Perovskite Quantum Dots and Two dimensional Nanosheets for Blue Light Emission and Photodetection

A Thesis Submitted to
Indian Institute of Technology Guwahati
For the Degree of

Doctor of Philosophy

By

Sumaya Parveen

Department of Physics
Indian Institute of Technology Guwahati
Guwahati-781039, India

February 2021

Dedicated to

…..My beloved parents, brother and husband

for their endless love, support and encouragement

Department of Physics
Indian Institute of Technology Guwahati
Guwahati-781039, India

STATEMENT

The work contained in the thesis entitled "**Controlled Growth of Organo-Metal Halide Perovskite Quantum Dots and Two dimensional Nanosheets for Blue Light Emission and Photodetection**" has been carried out by me at Indian Institute of Technology Guwahati under the supervision of **Prof. P. K. Giri**, Professor, Department of Physics, Indian Institute of Technology Guwahati. This work has not been submitted elsewhere for the award of any degree.

Sumaiya Parveen

Roll No. - **156121029**

Senior Research Fellow
Department of Physics
Indian Institute of Technology Guwahati
Guwahati-781039, India

Prof. P. K. Giri
Professor
Department of Physics
Indian Institute of Technology Guwahati
Guwahati-781039, India
Phone: ***+91 361 2582703****, Fax:* ***+91 361 2690762***
Email: ***giri@iitg.ac.in***

CERTIFICATE

This is to certify that the work contained in the thesis entitled "***Controlled Growth of Organo-Metal Halide Perovskite Quantum Dots and Two dimensional Nanosheets for Blue Light Emission and Photodetection***" has been carried out by **Ms. Sumaiya Parveen** at Indian Institute of Technology Guwahati under my supervision. This work has not been submitted elsewhere for the award of any degree.

Prof. P. K. Giri
Thesis supervisor

ACKNOWLEDGEMENT

It gives me immense pleasure to acknowledge everyone who have contributed in the journey towards successful completion of my PhD Thesis. I am overwhelmed in all humbleness and gratefulness to acknowledge my depth to all those who have helped me in my PhD journey.

The first and foremost I would like to express my sincere gratitude to my supervisor Prof. P. K. Giri for his insightful guidance and constant support throughout my thesis. I owe my sincerest gratitude to him for giving me the opportunity to work under his guidance. I have been fortunate to have an advisor who not only the guided me to conduct research through critical thinking, but also introduced me to the importance of leadership and communication in science. I am indebted to him for suggesting me this interesting topic, helping me understand it and guiding me in writing my manuscripts. I am thankful to him for giving me the complete freedom in my work and providing the essential arrangements, laboratory facilities and moral support throughout my PhD work to achieve the goal. I cannot imagine a better PhD advisor and this work would not have been possible without his vision, knowledge and expertise.

I express my sincere gratitude to my Doctoral Committee members, Dr. Gagan Kumar (Chairman), Dr. Subhash Thota, and Dr. A. S. Achalkumar for their regular review of my work, critical inputs, insightful comments and valuable suggestions.

I would like to express my heartfelt gratitude towards our Head of the Department of Physics and other faculty members of Physics department for their constant help and support towards the completion of my Ph.D. research work and providing me a research friendly environment. This research work would not have been possible without the support of the members from the Central Instruments Facilities and Centre for Nanotechnology as they provide latest research facilities to conduct my work. I am immensely grateful to Indian Institute of Technology Guwahati for providing the fellowship, good accommodation in this beautiful campus, safe and enjoyable working environment. A special thanks to the scientific/technical officers, Dr. Sidananda Sarma, Indrajit Talukdar, Kaustubh Acharya, Chandan Borgohain, Dr. Kula K. Senapati, and Madhurjya Borah for their help and co-operation to complete my work. I also like to extend my thankfulness to junior technical superintendents Ashim Malakar, Sujit Deb, and Milan Mahadani who helped in the characterization of my samples. I am also thankful to Central Workshop, Department of Mechanical Engineering for the fabrication of essential components used in my experimental setup.

I am also grateful to get the opportunity to work with the groups outside IIT Guwahati: Prof. Minoru Fuji and Dr. Sugimoto from Kobe University, Japan, Dr. Wolfgang Theis and A. J. Pattison from University of Birmingham, UK whom I like to thank for providing the opportunity to use some of their laboratory facilities. I would also like to thank Ponnappa Kechanda Prasanna and Dr. Sudip Chakraborty from IIT Indore for helping me with theoretical calculations and sharing their expertise with me.

I am grateful to get a fun filled research environment in our group. I would like to express my gratitude to my seniors Dr. Sk. Md. Obaidullah, Dr. Ramesh Ghosh, Dr. Jitendra Kumar, Dr. Rajender Gone, and Dr. Kamal Kumar Paul for their constant help and support in my PhD journey. Thanks to my lab mates Dr. Sumana Paul, Somorjit, Dr. Larionette, Dr. Joydip, Dr. Ruma, Abhilasha, Tarik, Koushik, Ravinder, Abdul, and Tadasha for their help and support. It was a lot of fun to discuss with all the lab mates about both science and life and I have learned a lot from all of them. I would like to thank my close friends Neda and Ankita who made my PhD journey colorful. I feel very grateful to have such friends who always try their best to help me in everything and have always been by my side in this journey. I would like to thank them for their kindness to me, and also for their close concerns to my life as friends.

Finally, I would like to express deepest gratitude towards my father Sk Sahabuddin and my mother Lutfa Begum without whom this journey would not have been possible. They always have been the driving force that encouraged me to follow my dreams and pursue my passion for physics. It is rightly said, ‘Behind every successful daughter there are parents who believe in her unconditionally’. I truly like to thank them for always believe and having faith in me even in my failure days, though thank you is not enough for them for whatever they have done for me. I will always be indebted to them for their selfless love, support, care, affection, encouragement and prayers. The characteristics that they inculcated in me in my childhood have always helped me in all aspects of my life. I would also like to thank my brother Sk Zahin Mujahid who has always been a bundle of joy and brightens up my life. His presence made my life cheerful as he always tries to motivate me and makes me laugh when I feel low. Without a doubt my husband Mir Alimuddin has been the biggest strength and support over the past three years. It was his patience, care and affection, that made me overcome my failures and encouraged me to strive for excellence. Hence, I would like to thank my husband for his unwavering tolerance, support and understanding. I would also like to thank my in-laws for their constant support, prayer during my PhD. It is my honor to be able to include salutation to my idol Prophet Muhammad (peace be upon him) whose life is a guidance for me to the right

path. Last but not the least I would like to express my sincere gratitude towards The Almighty without whose blessing I can't achieve anything in life. My success is only by The Almighty Allah.

Sumaiya Parveen

IIT Guwahati

CONTENTS

SYNOPSIS

Organo-metal halide perovskite is currently one of the most far reaching and promising materials owing to its exceptional performance in various optoelectronic devices. In particular, $CH_3NH_3PbBr_3$ ($MAPbBr_3$, MA = CH_3NH_3) thin film and nanomaterial systems have been used in various next-generation devices, such as light-emitting diodes (LED), phototransistor, photodetectors, solar cells and lasers due to its remarkable characteristics, such as low cost, long-range charge transport, tunable optical bandgap, high absorption coefficient and high photoluminescence (PL) quantum yield (QY).

To improve the optical and structural quality of perovskite thin film, various deposition techniques and numerous morphology control procedures have been adopted. The film morphology has great impact on its transport and optical properties, such as injection, separation, and recombination of charge carriers and these are known to be strongly correlated to grain size, grain boundaries, molecular packing, and surface roughness of the film. Though intensive work is being done on perovskite materials, the detailed analysis of growth model and correlation between of microstructural with optical properties of hybrid perovskite $CH_3NH_3PbBr_3$ are not studied properly. We have studied growth kinetics and scaling behavior of $CH_3NH_3PbBr_3$ thin films on various substrates using a vacuum co-evaporation method. Among various deposition techniques, vacuum deposition techniques are believed to yield smooth, low roughness and uniform film. However, controlling the growth and surface morphology of perovskite film using the vacuum co-evaporation method possess several fundamental challenges due to its hybrid nature. We evaluate the evolution of the structural and optical properties of the $CH_3NH_3PbBr_3$ thin films grown by vacuum co-evaporation method at various substrate temperatures (25–100 °C) and various thicknesses (4–120 nm).

Although co-evaporation technique provides smooth and uniform perovskite thin film, the emission efficiency of bulk perovskite film is very low for the application of optoelectronic device and due to its bulk nature, the film is very unstable for practical application. To improve the emission intensity and stability, we have synthesized template grown perovskite quantum dots (QDs), since QDs are expected to provide high PL emission yield due to quantum confinement effect (QCE). The reported PL QY of template grown perovskite nanocrystals (NCs) is typically quite low and needs further improvement for device applications.

Currently, the research in perovskite nanomaterials is extended to two-dimensional (2D) layered perovskite structure by virtue of their appealing features, such as good environmental stability, large lateral size, narrow band absorption and emission spectra, long diffusion length, long carrier lifetime, and excellent charge transport properties. Layered perovskites are generally nanomaterials with micron size lateral dimension and strong QCE in vertical dimension, which is responsible for very interesting photophysical properties. For the first time, we report a highly reproducible and facile solvothermal route to synthesize perovskite nanosheets (NSs) and tailor its thickness and optical band gap by changing the solvothermal temperature. Increase in solvothermal temperature enables precise tuning of the thickness from 14 layers down to 2 layers, giving rise to a systematic shift in the PL peak position towards the blue region.

Though green luminescent perovskites achieved near unity QY long back, achieving a stable deep blue emission with near unity quantum yield from halide perovskite has remained a great challenge. Incorporating dopants is currently considered as an effective means to broaden the practical application of perovskite nanomaterials and to overcome some inherent shortcomings such as toxicity, low external quantum efficiency and poor stability. Our newly introduced solvothermal route is proved to be an effective route to develop perovskite nanomaterials. However, the emission efficiency decreases with decreasing thickness of the NS, To improve the emission efficiency, the rare-earth dopants (Ce^{3+}, Tb^{3+}) are introduced inside $CH_3NH_3PbBr_3$ NS. With Ce doping at high concentration, we achieved a deep blue emitting NSs with 100 % QY, narrow linewidth (~24 nm), and a color coordinate of (0.145, 0.054) closely matching with the standard color Rec. 2020 (0.131, 0.046) specification, making it one of the most efficient perovskite blue light emitters reported to date.

Highly sensitive photodetector is another extremely desirable device in recent times for the applications in various fields, such as environmental monitoring, remote sensing, fiber-optics communication etc. Reportedly, 2D perovskites are supposed to give better photodetection properties compared to 3D/0D structure due to large lateral size and high diffusion length. We have done a comparative study on the photodetection properties between solvothermally synthesized undoped $CH_3NH_3PbBr_3$ NS and $EuCl_3$ doped $CH_3NH_3PbBr_3$ NS. Eu doped 2D $CH_3NH_3PbBr_3$ photodetector exhibits self-biased behavior with photocurrent to dark current ratio of ~10^3 and enhances the responsivity significantly compared undoped perovskite.

This thesis encompasses a controlled growth of 3D perovskite thin film, 0D QDs and 2D perovskite NS systems for tunable optoelectronic properties and its applications in white/blue LEDs and photodetectors. We have developed novel synthetic routes to synthesize high quality, stable perovskite nanomaterials with impressive optical properties. We have proposed the synthesis of deep blue emitting 2D NSs with 100 % PL QY for the first time by improving the material properties. Further, we have achieved high performance, self-biased photodetection using 2D Eu^{3+} doped perovskite NS. We believe that our studies are significant to address the current challenges in perovskite research community, such as low stability, toxicity, low emission efficiency etc. The thesis work is organized in seven chapters, which is briefly discussed below:

Chapter 1 presents a brief introduction to perovskite crystal structure and properties, perovskite thin film deposition methods, challenges with 3D perovskite structure, synthesis procedures of perovskite nanomaterials and their applications in optoelectronics. In addition, fundamental issues related to growth/synthesis mechanism and optoelectronic properties of perovskite is discussed. A brief discussion on the experimental techniques used in this thesis is presented and finally the motivation of the present thesis work is addressed in the end.

Chapter 2 elucidates the controlled growth of vacuum deposited 3D $CH_3NH_3PbBr_3$ thin film and its structural evolution on SiO_2 and ITO substrates at various substrate temperatures (25–100 °C) and various thicknesses (4–120 nm). The growth dynamic of perovskite thin film is studied with the help of scaling parameters using atomic force microscopy (AFM), height-height correlation function (HHCF), X-ray diffraction, UV-vis absorption and PL analyses. For the first time, we have investigated the substrate temperature dependent growth front scaling parameters for perovskite thin film in the temperature range 50-100 °C and activation energies are calculated to be 0.10 eV and 0.15 eV for the film on ITO and SiO_2 substrates, respectively, which implies an easier diffusion of molecules in case of ITO substrate. The scaling parameter dependent optical properties of the perovskite thin film are also addressed in this chapter.

Chapter 3 presents a novel synthetic route for the template assisted growth of size tunable perovskite ($CH_3NH_3PbBr_3$ and $CH_3NH_3PbI_3$) QDs. Fluorine doped mesoporous TiO_2 (F-TiO_2) template acts as a template and the nucleation site for the growth of perovskite QDs. We have demonstrated the growth of $CH_3NH_3PbI_3$ and $CH_3NH_3PbBr_3$ QDs with the size tuned from 1.7 nm to 5.1 nm inside mesoporous F-TiO_2 template by a simple solution processed method. The optical tunability of the QDs is quantitatively discussed with the help of Brus equation, which

confirms the strong confinement affect. As a result, the enhancement of PL QY from 5 % to 57 % in $CH_3NH_3PbBr_3$ QDs and 1 % to 25 % in $CH_3NH_3PbI_3$ QDs is observed. Low temperature PL analysis is also discussed in detail to investigate the excitonic properties of the QDs. High optical stability (10 h) of the QDs is inferred to the partial coverage of the QDs by TiO_2 nanocrystals restricting its complete exposure to the external environment.

In **Chapter 4,** we have discussed about the structural evolution of 2D perovskite nanomaterials synthesized using a novel, highly reproducible, and facile solvothermal route. Precise tuning of the NS thickness (18.5–1.2 nm) is discussed using AFM and TEM analyses. We have qualitatively discussed the growth mechanism of the NS based on the classical theory using XRD analysis. Systematic tuning of the bandgap from green luminescent nanorods to cyan luminescent 2D QDs is observed simply by varying the solvothermal temperature with a maximum PL QY of ~84 %. Further, practical applications of the synthesized NS are explored as white light converter and photodetector. The 2D perovskite photodetector exhibits a stable and very fast rise/fall time (24 μs/103 μs) along with high responsivity and detectivity of ~1.93 A/W and 1.04×10^{12} Jones, respectively. The efficacy of the current solvothermal method for fast, convenient, and controllable synthesis of the large-area, stable 2D perovskite layers and their uses in various optoelectronic devices are demonstrated in this chapter.

In **Chapter 5,** we have addressed the doping of rare earth elements in the 2D perovskite NS for high performance optoelectronics. Two-dimensional layered structure of the perovskite NS allows easy and effortless substitution of the rare-earth dopant ions Ce^{3+} and Tb^{3+}. Size (thickness) tunability of the NS in the range 8.4–1.6 nm with increasing doping concentration is discussed based on TEM and AFM analyses. Characteristic diffraction peaks corresponding to 2D perovskite phases at low angles ($2\theta<14.81^{o}$) are observed in the rare-earth ion doped NS confirming the formation of pure layered structure. The excitonic absorption peak of the NS is tuned by 42 nm and 86 nm to the deep blue region with Ce^{3+} and Tb^{3+} doping, respectively, mainly due to strong quantum confinement effect. We also achieved 100 % emission efficiency from the blue 2D nanoplatelet with narrow line width (~24 nm) and a color coordinate of (0.145, 0.054) closely matching with the standard color Rec. 2020 (0.131, 0.046) specification, making it one of the most efficient perovskite blue light emitters reported till date. Multiple PL peaks appear at low temperature due to the coexistence of ordered and disordered orthorhombic phases. We have investigated the role of dopants in the achieving the high QY and deep blue emission in 2D perovskite using density functional theory (DFT) based calculation of its electronic structure. The experimental results are fully supported by the DFT calculation

results. Due to decrease in formation energy in the doped 2D NS, the stability of the perovskite NS increases post Ce and Tb doping.

In **Chapter 6** we have presented the performance of Eu^{3+} doped 2D perovskite NS based photodetectors. Evolution of perovskite NS from 10 layer thickness to monolayer QDs with increasing Eu^{3+} doping concentration is addressed with the help of TEM and AFM analyses. Due to smaller size of Eu^{3+} dopants than the host Pb^{2+}, the doped system has less strain compared to undoped system with desirable morphology and properties. We have studied the performance of europium doped perovskite photodetector in detail and compared it with the undoped one. Eu^{3+} doped 2D perovskite photodetector exhibits self-biased photocurrent, high switching ratio (~10^3), fast response time (17.5 μs/ 38.5 μs), high responsivity (5.29 A/W) under 405 nm laser excitation. The rise and fall times are ~3 times and ~4.4 times faster in the doped device compared to that of the undoped one due to efficient charge separation and passivation of trap states with the introduction of lanthanide ion in the perovskite crystal. The Eu^{3+} doped perovskite photodetector shows excellent operational and storage stability, suitable for practical applications.

Chapter 7 presents the summary and highlights of the contributions of the present thesis. Future scope of work on the perovskite nanomaterials for the optoelectronics application are also presented in the end.

LIST OF PUBLICATIONS:

A. *In Peer-Reviewed Journals:*

1. Sumaiya Parveen, Kamal K. Paul. Ruma Das, P. K. Giri, 'Large Exciton Binding Energy, High Photoluminescence Quantum Yield and Improved Photostability of Organo-Metal Halide Hybrid Perovskite Quantum Dots Grown on a Mesoporous TiO_2 Template'. ***J. Colloids & Inter. Sci.*** *539, 619 (2019).*

2. Sumaiya Parveen, Kamal Kumar Paul, and P. K. Giri, 'Precise Tuning of the Thickness and Optical Properties of Highly Stable 2D Organometal Halide Perovskite Nanosheets Through a Solvothermal Process and its Applications as a White LED and a Fast Photodetector'. ***ACS Appl. Mater. Interfaces,*** *12, 5, 6283-6297 (2020).*

3. Sumaiya Parveen, Sk Md. Obaidulla, P. K. Giri, 'Growth kinetics of hybrid perovskite thin films on different substrates at elevated temperature and its direct correlation with the microstructure and optical properties'. ***Applied Surface Science*** *530 (2020) 147224).*

4. Sumaiya Parveen, Ponnappa Kechanda Prasanna, Sudip Chakraborty, P. K. Giri, 'Stable Deep Blue Emission with Unity Quantum Yield in Organic-Inorganic Halide Perovskite 2D Nanosheets Doped with Cerium and Terbium at High Concentrations'. ***J. Mater. Chem. C,*** *2021,9, 2437-2454.*

5. Sumaiya Parveen, P. K. Giri, 'Europium Doped Organo-Metal Halide 2D Perovskite Nanosheet Based UV Photodetector with Improved Responsivity and Fast Response'. *(Submitted).*

6. Ruma Das, Sumaiya Parveen, Abhilasha Bora, and P. K. Giri, 'Origin of High Photoluminescence Yield and High SERS Sensitivity of Nitrogen-Doped Graphene Quantum Dots'. ***Carbon*** 160, 273–286 (2020).

B. *Conference Papers Presented:*

1. Sk Obaidulla, Sumaiya Parveen and P. K. Giri, '*Study of growth dynamics of VOPc organic thin films on ITO coated glass substrate*', International Conference on Functional Materials **(ICFM 2016)**, *IIT Kharagpur, 12-14 December*, 2016.

2. Sumaiya Parveen and P. K. Giri, '*Understanding the Growth Dynamics of Organometal Halide Perovskite ($CH_3NH_3PbBr_3$) Thin Films on SiO_2 and ITO Coated Glass Substrate*', (A discussion meeting on hybrid perovskite) **(HyPe-2017)**, *S. N. Bose National Centre for Basic Sciences, 14-15 December, 2017.*

3. Sumaiya Parveen, Kamal Kumar Paul and P. K. Giri, '*High Photoluminescence Yield from Organometal Halide Perovskite Quantum Dots Confined in a Mesoporous TiO_2 Template*

Grown by Rapid Thermal Annealing', International Conference on Optoelectronic and Nano Materials for Advanced Technology **(icONMAT-2019)**, *Cochin University of Science and Technology, Kerala, India, January 3– 5, 2019.*

4. Sumaiya Parveen, Kamal Kumar Paul and P. K. Giri, '*High Photoluminescence Yield from Organometal Halide Perovskite Quantum Dots Confined in a Mesoporous TiO_2 Template Grown by Rapid Thermal Annealing*'. ***AIP Conference Proceedings*** *2082, 050011 (2019).*

5. Sumaiya Parveen and P. K. Giri, '*Precise tuning of the thickness and optical properties of highly stable 2D organometal halide perovskite nanosheets through a solvothermal process and its applications as a white LED and a fast photodetector*', International Conference on Advanced Nanomaterials and Nanotechnology **(ICANN-2019)**, *IIT Guwahati, Assam, India, December 18–21, 2019.*

6. Sumaiya Parveen and P. K. Giri, 'Large Exciton Binding Energy, High Photoluminescence Quantum Yield and Improved Photostability of Organo-Metal Halide Hybrid Perovskite Quantum Dots Grown on a Mesoporous TiO_2 Template', International Conference on Nano Science and Technology **(ICONSAT-2020)**, *S. N. Bose Center, Kolkata, March 5–7, 2020.*

C. *Workshops Attended:*

1. *'3rd National Workshop on MEMS/NEMS and Theranostic devices (NWNTD)', IIT Guwahati 21–23 March, 2017.*
2. *'5th National Workshop on MEMS/NEMS and Theranostic devices (NWNTD)', IIT Guwahati 21-23rd February, 2019.*

LIST OF ABBREVIATIONS

Abbreviation	***Description***
FESEM	Field emission scanning electron microscopy
EDX	Energy-dispersive x-ray
TEM	Transmission electron microscopy
FETEM	Field emission transmission electron microscopy
STEM	Scanning transmission electron microscopy
HRTEM	High-resolution transmission electron microscopy
XRD	X-ray diffraction
XPS	X-ray photoelectron spectroscopy
UV-vis	Ultraviolet-visible
NIR	Near infrared
PL	Photoluminescence
PLE	Photoluminescence excitation
TRPL	Time-resolved photoluminescence
FWHM	Full width at half maximum
CIE	Commission international d'Eclairage
0D	Zero-dimensional
1D	One-dimensional
2D	Two-dimensional
QD	Quantum dot
NS	Nanosheet

Chapter 1

Introduction

Over the past decade, metal halide perovskite materials are at the cutting edge of the optoelectronics field due to their exciting and favorable characteristics that surpass the previously achieved device efficiency at an unprecedented rate. Perovskite has emerged as a new class of revolutionary materials within a short period of time courtesy to its superior optical and electrical properties and easy manufacturing. In just five years, the power conversion efficiency of perovskite solar cells have reached from 3.4 % to 22.1 % whereas, other solar cells took decades to reach that efficiency. Interestingly, in conjunction with excellent performance in photovoltaic devices, perovskite materials have been found to be a good candidate for light-emitting devices by virtue of their good balance of various properties. Particularly, low-dimensional perovskite materials have sparked massive attention due to their superior optical properties and render them as highly appealing for a plethora of optoelectronic applications. Inspired by the rapid progress in graphene and MoS_2 as prototype two-dimensional (2D) materials, recently, 2D perovskite has emerged as a new member in the family of 2D materials. It is of fundamental interest to have a detailed understanding of the various growth techniques of perovskite nanostructures, doping strategy, and its effect on shape, size, bandgap and other properties of the material. A through, understanding of its physical properties is necessary for the development of photovoltaic and optoelectronic devices. In this chapter, we briefly review important features of perovskite thin film and nanostructures, various techniques used for the growth of shape-controlled perovskite nanostructures and the fundamental issues related to the controlled growth of halide perovskite nanostructures. We also highlight the doping mechanism and its effect on the stability, photophysical properties, and optoelectronics application of perovskite materials. The existing challenges, along with the focus of the present thesis and the outline of the thesis are described at the end of the chapter.

1.1. Crystal Structure of Metal Halide Perovskite

The name perovskite is used for wide range of earth abundant materials having stoichiometry of ABX_3, where A is any organic or inorganic cations (typically, $CH_3NH_3^+$, Cs^+, Rb^+ etc.), B can be

any divalent metal ion (Pb^{2+}, Sn^{2+} etc.) and X is halide anions (Cl^-, Br^- and I^-). The name perovskite was chosen in honor of eminent Russian mineralogist, Count Lev Alexevich von Perovski. Perovskite crystal structure was first discovered inside a meteorite containing $CaTiO_3$ (calcium titanate) in the Ural Mountains by geologist Gustav Rose in 1839. Oxide perovskite (ABO_3) was the first family of perovskite and has been widely studied in the 20th centuries on account of their interesting magnetic and dielectric properties. However, since last decade, there has been an explosion of research activity on the metal halide perovskites due to their fascinating optical properties, low-cost synthesis, and remarkable device performance. In its stable form, metal perovskite has a cubic structure with corner-sharing BX_6 octahedral and A cation positioned in the cuboctahedra voids. However, metal halide perovskites undergo one or two phase transitions with the variation of temperature.

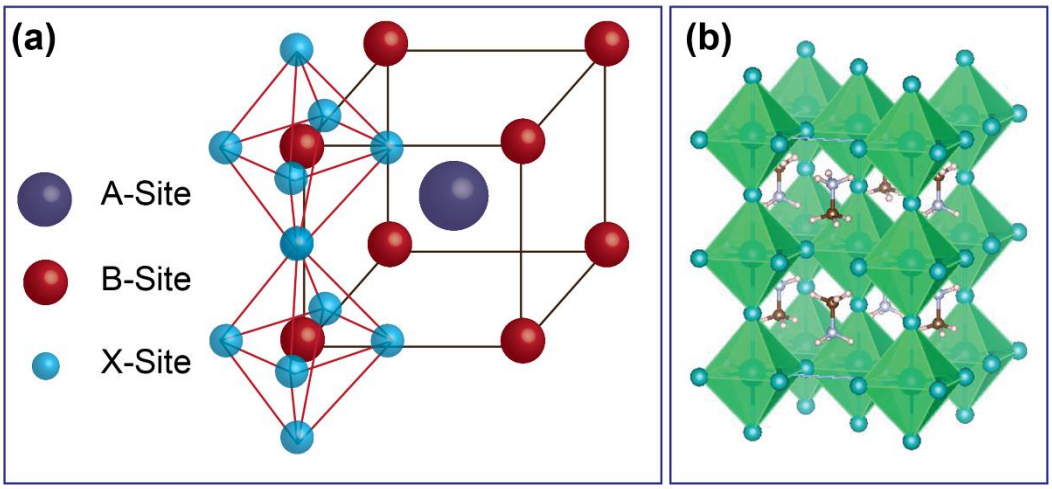

Fig. 1.1. Crystal structure of cubic phase of (a) ABX_3 perovskite and (b) $CH_3NH_3PbBr_3$ perovskite.

The probability of forming (or not) a perovskite structure is generally estimated using the Goldschmidt tolerance factor (t) and the octahedral factor (μ)[1]. t and μ are defined as, $t = (r_A + r_X)/\sqrt{2}\,(r_B + r_X)$ and $\mu = r_B/r_X$, where r_A, r_B and r_X are the ionic radii of A, B and X constituents. For stable perovskite structure, the tolerance factor, t should be nearly equal to 1, however, empirical condition for cubic perovskite structure is found to be $0.80 < t < 0.90$ and $0.40 < \mu < 0.90$[1]. The main perovskite structure used in this thesis is of the form $CH_3NH_3PbBr_3$ (CH_3NH_3=MA, $MAPbBr_3$), where A site is occupied by organic cation MA and crystal structure is presented in **Fig. 1.1**. t and μ factors for $MAPbBr_3$ are 0.84 and 0.61 (r_{MA} = 1.8 Å, r_{Pb} = 1.19 Å and r_{Br} = 1.96 Å), respectively, indicating a stable cubic structure at room temperature. Note that

these factors do not consider ionic or covalent-bonding interactions, vibrational motion, or hydrogen bonding which may distort the symmetric cubic structure[2]. The crystal structure of $MAPbBr_3$ perovskite changes with temperature. Orthorhombic phase is the low-temperature ground state of $MAPbBr_3$, which is stable up to 145 K[3]. It maintains tetragonal phase in the temperature range 145 K to 237 K and with increasing temperature, it stabilizes to a more symmetric cubic phase (> 237 K)[3].

In contrast to 3D ABX_3 perovskite structure, layered perovskite structure has the general formula of $(RNH_3)_2A_{n-1}B_nX_{3n+1}$ where n is any definite integer[1]. n=1 and infinity correspond to pure 2D layered and 3D perovskite structure, respectively. Conceptually, low dimensional perovskite is derived by cutting the inorganic 3D network of three-dimensional ABX_3 perovskite structure into smaller pieces. In the 2D structure, due to large A cation size the cubic symmetry is broken and the 3D structure is separated along <001> or <110> directions (**Fig. 1.2**)[4]. For lead halide perovskite, layered perovskite structure is formed typically when A cation size exceeds 2.6 Å[1].

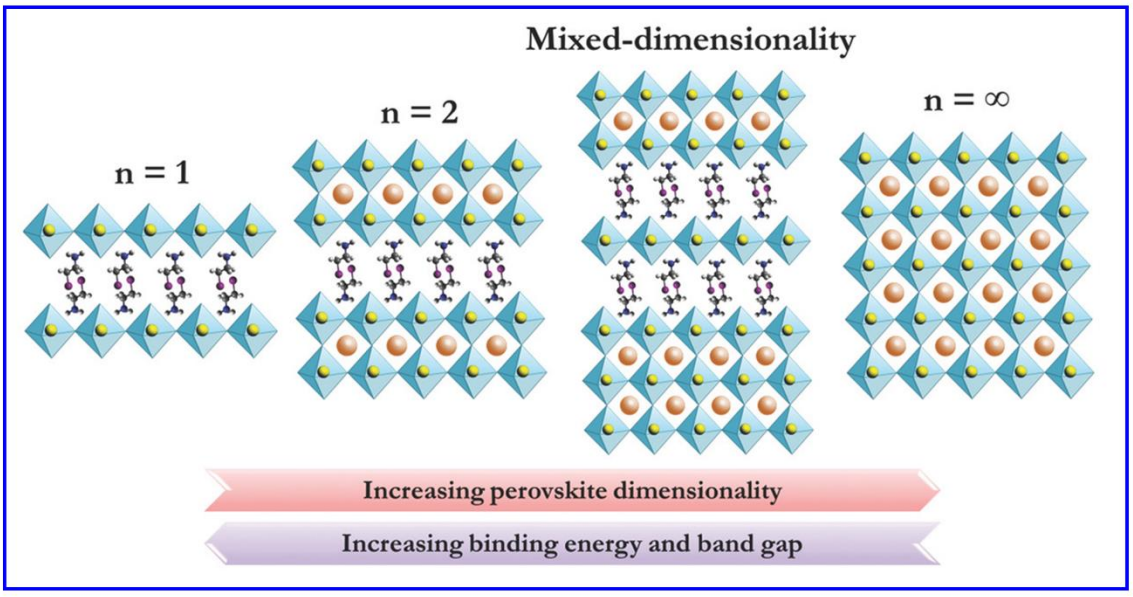

Fig. 1.2. Illustrated image of layered 2D perovskite crystal structure. Adopted from Ref. [4]

1.2. Band Structure of Metal Halide Perovskite

Metal halide perovskite has a direct bandgap nature due to its crystal symmetry. Theoretically, bandgap of a material is determined by the difference between the highest and the lowest occupied molecular orbital energy levels, called as valence band maxima (VBM) and conduction band

minima (CBM), respectively, in semiconductor physics. VBM of metal halide perovskite is reported to be anti-bonding hybrid state of the metal s and halide p orbitals from the first principles electronic structure calculations[5]. Hence, all the electronic and optical transitions are occurred mostly within the inorganic ($PbBr_6$) octahedron[2]. Organic cation does not have much influence in the band structure of the perovskite but it can modulate the band by controlling the lead-halide bond distance. The conduction band minimum (CBM) is affected by the hybrid of metal p and halide p orbitals and bonding between s and d states of Pb[6]. Therefore, VBM is mostly anti-

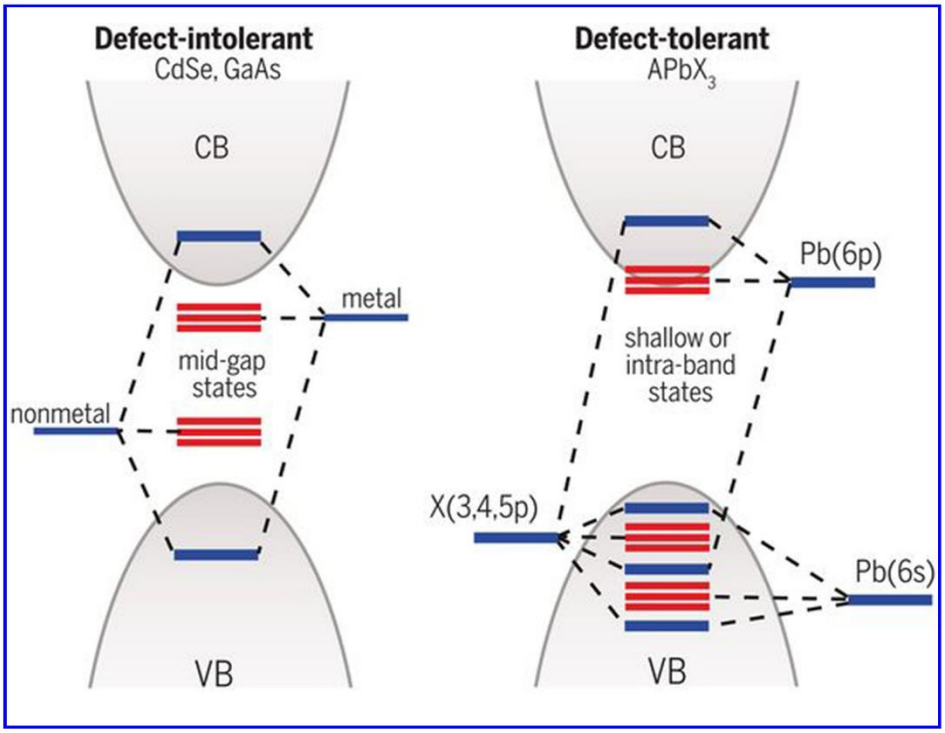

Fig. 1.3. Schematic diagram of the band structure of defect intolerant conventional semiconductors and defect tolerant perovskite materials. Adopted from Ref. [7]

bonding type and CBM exhibits non-bonding type bond. The conduction band is less affected by the structural distortions or other factors due to poor orbital overlap. Any change in the perovskite lattice or say Pb-X (X=Cl, Br and I) bond destabilizes the VBM. But, the defect electronic states mostly stay near the valence band edge or within it because of anti-bonding VBM. This makes the perovskite structure more defect tolerant and thus external factors do not put negative impact on the optoelectronic properties unlike other inorganic semiconductors, as shown in **Fig. 1.3**[7]. A change in the halide composition of the perovskite from Cl to Br to I results in the change of the

valence orbital from 3p to 4p to 5p, respectively, causing a systematic reduction in the bandgap from ~ 3.0 eV to 1.55 eV[8]. Changing the ratio of I-Br or Br-Cl can tune the optical bandgap of the perovskite due to comparable ionic size, but replacing I by Cl does not tune the bandgap significantly due to large size difference. This is one of the significant advantages of perovskite structure, which allows bandgap tuning from UV to visible to infrared region just by replacing the halide ions.

1.3. 3D $MAPbX_3$ Perovskite Thin Film

Perovskite materials have emerged as a new research paradigm since 2009 for the photovoltaic and optoelectronic applications. Easy tunability of bandgap of the perovskite enforces the research community to tune the morphology of the organic-inorganic halide perovskite by decreasing the dimension. Crystal structure of perovskite is highly dependent on chemical composition, temperature and synthesis procedures. Over the years, various deposition techniques have been developed for $MAPbX_3$ thin films to overcome the shortcomings. To increase the device efficiency, surface morphology, thickness and grain size of perovskite thin film have been modified through controlled deposition methods[9]. Here we will briefly discuss about some of the main scalable $MAPbX_3$ perovskite thin film deposition methods.

1.3.1. Spin Coating Method

Spin coating is the most widely used and one of the simplest deposition methods for the perovskite thin film. In one-step spin coating method, the precursor materials MAX and PbX_2 are mixed in a single polar solvent, typically N-dimethylformamide (DMF), dimethyl sulfoxide (DMSO) or gamma-butyrolactone (GBL). The solution is stirred for few hours at room temperature or low temperature (~60 ºC) to mix the precursors properly and spin coated on the substrates at high speed (see **Fig. 1.4(a)**)[10]. Then the substrate is annealed to form the perovskite later. The one-step spin coating method was first developed by Kojima et al. in 2009 for the fabrication of $MAPbI_3$ sensitized solar cell[11]. In the two-step spin coating method, first reported by Im et al., the preparation of single solution is not needed[12]. However, MAX and PbX_2 solutions are separately prepared in the proper solvents. First MAX solution is spin coated on the substrate followed by waiting for ~10-30 second followed by spin coating of PbX_2 solution (see **Fig. 1.4(a)**)[10]. Subsequently, the substrate is placed on the hot plate for annealing. The rotational speed, time and

viscosity of the solution determine the thickness of the thin film. The spin coating method was first used to deposit hybrid $(C_6H_5C_2H_4NH_3)_2PbI_4$ layered perovskite in the year 1994[13]. To improve the film quality, modified spin coating method has been developed, such as hot casting process, anti-solvent washing/solvent engineering, gas quenching, anti-solvent/solvent extraction etc. In the hot casting approach, the substrate is heated prior to spin coating and the precursor solution

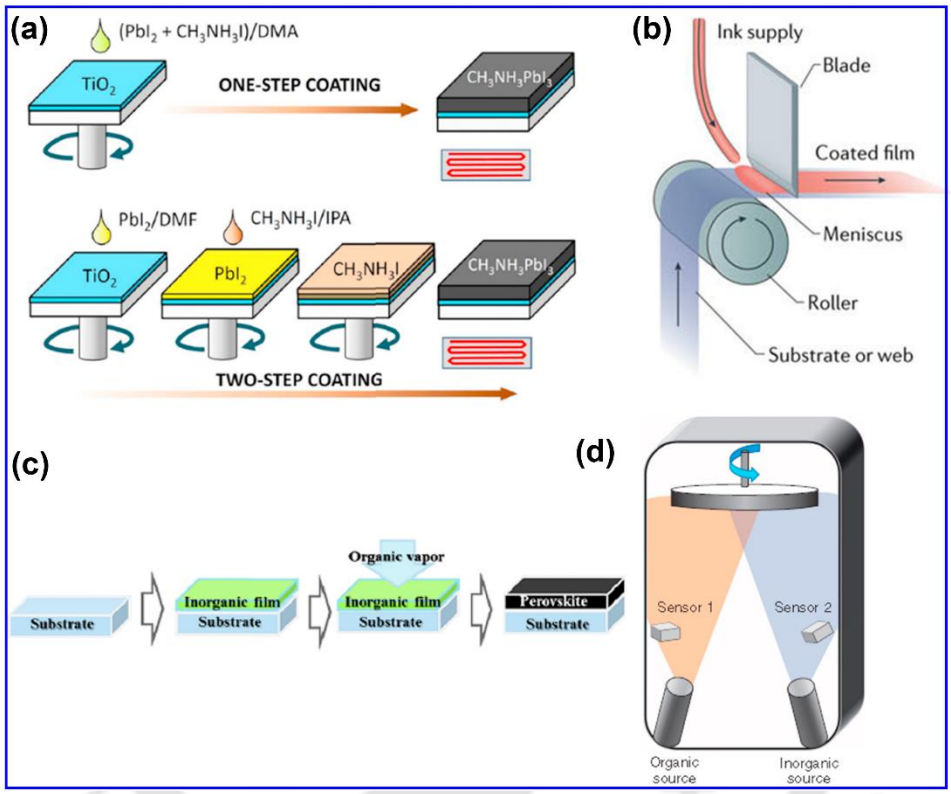

Fig. 1.4. Various deposition methods of perovskite thin film: (a) Spin coating method, (b) Blade coating method, (c) Vapor assisted solution process and (c) co-evaporation method. Adopted from Ref[10, 14]

was also maintained at 70 ºC which enforces rapid crystalline growth during deposition[15]. The solvent engineering approach is a slight modification to the spin coating method, where any non-polar anti-solvent (toluene, chlorobenzene, or diethyl ether) is dripped on to the substrate while spinning. Addition of anti-solvent accelerates the super-saturation of the precursor solution which in turn increases the nucleation process giving rise to uniform film[16]. Though spin coating method is useful for lab scale studies for small area devices, however, it has some bottlenecks when it comes to large-scale production or commercialization. Due to different miscibility of the precursor materials, the crystallization rate is different for various components in a single film and

inadequate control over the crystal growth also leads to poor coverage, pinholes and cracks in the film.

1.3.2. Blade Coating

In this method, a blade is moved across the surface to spread the precursor ink on the substrate to form wet thin films, as shown in **Fig. 1.4(b)**[14, 17, 18]. The thickness of the film depends on the concentration of precursor ink, blade-moving frequency, and the gap between blade and substrate. It is a scalable technique and used for roll-to-roll production of perovskite solar cells. Previously, this method was used for polymer solar cells and first perovskite solar cell fabrication using blade coating was reported by Kim et al. with power conversion efficiency (PCE) of 10.44%[19]. A maximum of ~ 20 % power conversion efficiency is achieved in perovskite solar cell using blade coating method[20, 21]. Generally, blade coated perovskite thin films are homogeneous, pinhole free, polycrystalline in nature. However, the ink space in blade coating method is not fully enclosed which opens the possibility of change in ink chemistry over time. Blade coating is not only used for the deposition of uniform film but the crystal orientation direction could also be controlled in the direction of blade. Hence this method can be used to prepare single crystalline structure[17, 22]. This method still has some limitations for the deposition of uniform thin film due to complex fluid dynamics and formation intermediate phases that coexist during the crystallization process[23].

1.3.3. Vapor Assisted Solution Process

It is hybrid sequential method with a combination of vacuum deposition and solution process. PbX_2 film is first deposited using spin coating method and then the film is kept in MAX vapor environment by sprinkling MAX powder around the film in a capped petri dish to induce gas-solid crystallization process (see **Fig.1.4(c)**)[10]. However, a dissolution process may occur during the second step since the formed $MAPbBr_3$ may be ionized under Br rich environment and further, recrystallizes with increased duration. Hence, MABr deposition duration, temperature and quality of the inorganic film are very crucial for the high-quality perovskite film. A maximum external quantum efficiency (EQE) of ~ 4.36 % is achieved using this method for $MAPbBr_3$ LED[24]. Alternatively, PbX_2 film can also be prepared using any physical vapor deposition (PVD) or chemical vapor deposition methods. In the second step, MABr can be introduced to the film in the

form of powder, solution or vapor to convert the inorganic layer to hybrid halide perovskite[25-29]. However, proper diffusion of the organic component while reacting with the compact inorganic film is still challenging in two-step methods[23].

1.3.4. Vacuum Deposition Technique

Various vacuum deposition techniques such as co-evaporation, sequential deposition, CVD, PVD, flash evaporation have been adopted to prepared uniform perovskite bulk film. Vacuum deposition method has many advantages in comparison to the solution process, such as uniform, pinhole free, low roughness film without using any toxic solvent. During co-evaporation method, two solid precursors MAX and PbX_2 are kept in separate crucibles and heated under vacuum till the required sublimation temperature is reached(see **Fig. 1.4(d)**)[10]. Under high vacuum, the precursor materials slowly evaporate, diffuse and then assemble at substrates to form perovskite crystal[9]. This method allows controllable fine-tuning of the film thickness. Liu et al. first reported co-evaporation of MAI and $PbCl_2$ to fabricate perovskite solar cells with PCE ~ 15.4 %[30]. $MAPbBr_3$ perovskite LED fabricated using co-evaporation method achieved an EQE of ~ 0.06 %[31]. In the sequential deposition method, MABr is deposited on pre-deposited PbX_2 film. In flash evaporation method, a tantalum heater foil is pre-coated with perovskite and then it is placed in a vacuum chamber to feed it by a strong current. In the process, perovskite film is deposited within few second due to high current without any decomposition[32]. The film thickness is controlled by the amount of the precursor material and the distance between heater to substrate. This method can deposit organic-inorganic halide, all inorganic, layered 2D perovskites with different A cations[33]. CVD is used in industrial process to fabricate large area devices. High-quality perovskite film can be formed using CVD in a low-pressure environment and EQE of 0.02 % is achieved from metal halide perovskite LED[34]. Even though vacuum deposited perovskite thin films show low roughness, highly-uniform morphology, the luminescence efficiency is inferior compared to solution-processed film. During evaporation, some unreacted precursors may stay in the perovskite film, which induce non-stoichiometry and limit the luminescence efficiency.

1.3.5. Challenges in the Growth of Perovskite Thin Film

Despite the availability of various deposition methods, there are still several challenges for the controlled growth of thin film to fully explore their optoelectronics application. To reach the

record-setting device efficiency, careful attention is required at each step of the growth processing. Electroluminescence (EL) efficiencies of 3D perovskite LEDs are still very low compared for commercialization. Low photoluminescence (PL) quantum yield (QY) of bulk perovskite film is attributed to easy dissociation of excitons due to low exciton binding energy, large grain size. Even the small grains of metal halide perovskite film contains many grain boundaries, pinholes, and defects which severely increase the leakage current and non-radiative recombination resulting in the reduction of the luminescence efficiency of the perovskite LEDs. 3D bulk films are very unstable in ambient conditions and easily decompose, which needs to be addressed. In comparison, nanostructured perovskites exhibit better ambient stability and are thus a subject of intense research.

1.4. Organometal Halide Perovskite Nanomaterials

Reducing the size of the semiconductor materials is one of the popular and effective approaches to manipulate photophysical properties. Ever since the discovery of $MAPbBr_3$ quantum dots (QDs) in 2014, perovskite nanomaterials have aroused great attention in a very short period. Perovskite nanomaterials have become one of the important divisions of nanomaterial-based optoelectronics devices due to their excellent device performance. Here, we have briefly discussed various organic

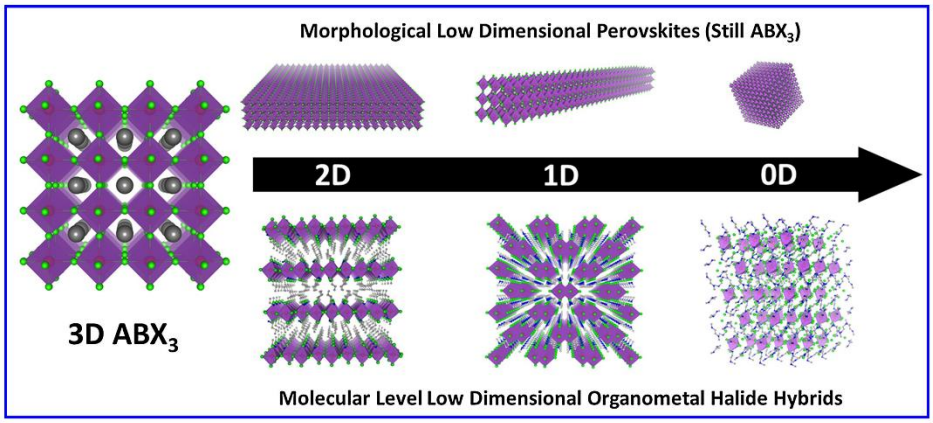

Fig. 1.5. $MAPbX_3$ metal halide perovskites with different dimensionalities. Adopted from Ref. [35]

-inorganic halide perovskite ($MAPbX_3$) nanomaterials, their synthesis procedures and applications. **Fig. 1.5** shows the morphological and molecular level illustration images of $MAPbX_3$ perovskite with decreasing dimensionality from 3D bulk film to 2D nanoplatelets, 1D nanorods,

0D quantum dots to obtain quantum confinement effect, which strongly influences its photophysical properties.

1.4.1. 2D Layered $MAPbX_3$ Perovskite

In the layered perovskite, 3D cubic symmetry is broken by separating the inorganic octahedral layer in the <100> or <110> direction with the introduction of large A cations or long-chain ligands[1]. 2D layered structure can also be prepared with $MAPbX_3$ composition by reducing the thickness to form 2D nanoplatelets, nanosheet (NS), and nanodisk[36-38]. The number of sheets of inorganic layers decides the layer number of the 2D perovskite, which are attached with weak Van der Waal force, but are fundamentally different from other 2D semiconductors[1]. The restriction only along one dimension of 2D perovskite results in advantages of quantum confinement effect of 1D with higher exciton binding energy and low defect density[39]. Along with this, it retains high carrier mobility along horizontal direction due to its large lateral size[40]. The structure of the layered perovskite nanostructure can be considered as quantum-well like with

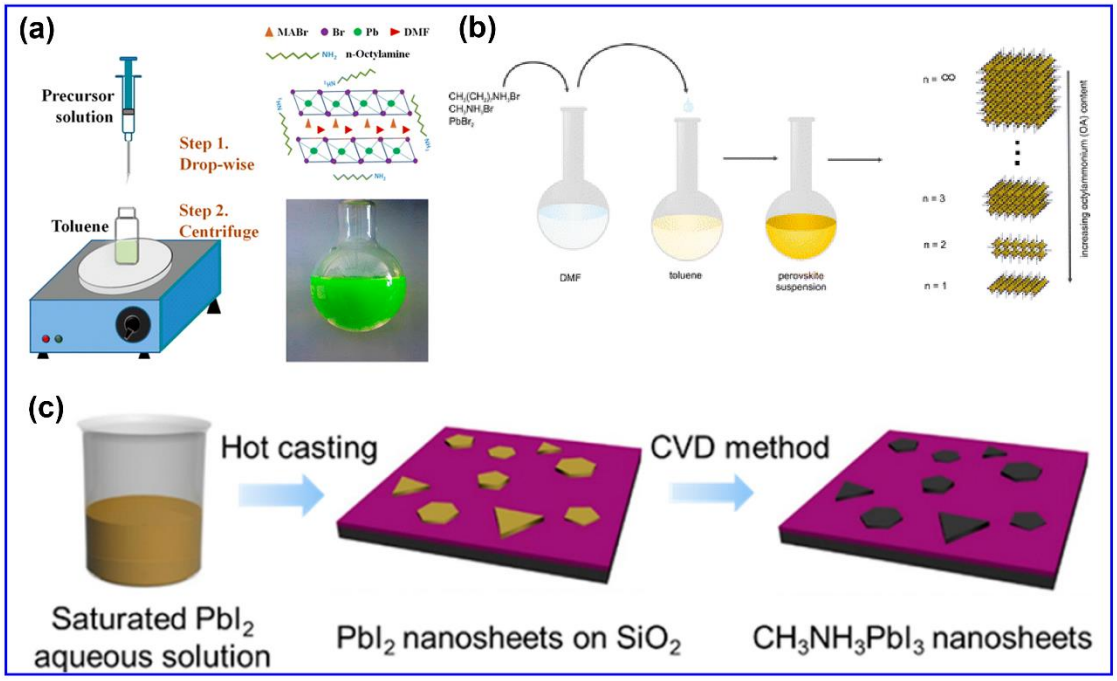

Fig. 1.6. Synthesis of 2D $MAPbX_3$ perovskite NSs: (a,b) LARP method, (c) vapor-phase conversion method. Adopted from Ref. [41-43]

inorganic sheets and organic molecules act as wells and barriers, respectively. Different dielectric environments of the wells and barriers increase the electron-hole interaction giving rise to

enhanced binding energy and reduced forbidden electron transition contributing to high luminescence efficiency[1]. Synthesis of 2D layered perovskite has been carried out by both solution process and vapor deposition methods, some of them are discussed here.

1.4.1.1. Solution Process

This is one of the most commonly used techniques to grow nanostructured perovskites. Initially, colloidal perovskite nanoplatelets were observed during optimization of QDs synthesis parameters. A higher amount of capping ligand in the precursor solution during synthesis results into the formation of nanoplatelets with high PL QY[44, 45]. Ligand assisted reprecipitation (LARP) method is also hugely used for the synthesis of perovskite nanomaterials through the careful selection of capping ligands and solvents (see **Fig. 1.6(a)**). Cho et al. modulated the layer thickness of the $MAPbBr_3$ perovskite nanoplatelet by changing the chain length and concentration of the added alkylammonium cations using the modified LARP method[46]. Ling et al. fabricated LED based on $MAPbBr_3$ perovskite nanoplatelets using modified LARP method with brightness up to 10,590 cd/m^2[44]. Using the room temperature colloidal method, Manna and coworkers finely tuned the thickness of the perovskite nanoplatelets from 3 to 5 layers at low reaction temperature[47]. Similar to LARP method, Feldmann et al. synthesized $MAPbBr_3$ nanoplatelets by adding dilute solution of $PbBr_2$, MABr and n-Octylammonium bromide (OABr) in DMF into vigorously stirred toluene (see **Fig. 1.6(b)**)[43]. Long chains of octylammonium suppress the crystal growth in one direction and changes the thickness, and PL of the perovskite nanoplatelets is tuned by tuning the ratio of MABr to OABr[43]. Ogale et al. synthesized 2D $MAPbX_3$ NSs using electrospray technique in conjunction with anti-solvent extraction by intercalation via host-guest chemistry[48]. Regardless of the inhomogeneous distribution of solution-processed perovskite NSs, interesting optical properties make it feasible for optoelectronics applications. The main advantage of LARP method is that it is a low-temperature synthesis process and can be performed in ambient condition[49]. However, its main drawback is that polar solvent which is used during the synthesis process may dissolve in the perovskite nanomaterials during purification[49].

1.4.1.2. Vapor Deposition Method

Compared to the solution process, in-situ growth of layered perovskite on different substrates makes it available for direct use in devices. Xiang and coworkers were the first ones to report the fabrication perovskite NS based solar cells and lasers using two-step CVD method[50]. Bao et al. combined solution process and vapor-phase conversion method to synthesize monolayer 2D $MAPbI_3$ nanoplatelet for the fabrication of photodetector (see **Fig. 1.6(c)**)[42]. Shi and coworkers prepared single-crystalline ultrathin large-scale $MAPbCl_3$ NS using CVD method and identified the favorable role of weak Van der Waals film−substrate interaction on the nucleation and growth of the two-dimensional morphology out of non-layered materials compared to conventional epitaxy[51]. The deposition of hybrid perovskites is still challenging in vacuum deposition method.

1.4.2. 0D $MAPbX_3$ Perovskite Nanoparticles

Perovskite NPs show superior optoelectronic properties compared to their bulk counterparts due to a large surface to volume ratio, strong quantum confinement effect, high exciton binding energy. Exceptional light generation ability of perovskite nanoparticles (NPs) has attracted sustained interest for the development of commercial display devices due to their unique optical properties such as narrow emission bandwidth, unity PL QY, high ambient stability, etc. Since the discovery of the first $CsPbX_3$ perovskite nanocrystal, it has become a hall of fame and wide variety of perovskite NPs have been synthesized via various solution processes. Due to the temperature instability of organic cation, the synthesis of $MAPbX_3$ NPs is conducted at low temperatures. One of the remarkable properties of perovskite material, as opposed to conventional semiconductors, is its low formation energy enabling the preparation of perovskite NPs merely at room temperature just by mixing or grinding the precursor materials. Here, we will briefly discuss various synthesis procedures of $MAPbX_3$ NPs and their properties.

1.4.2.1. Template Assisted Growth

Considering the strategy for the synthesis of other QDs, $MAPbBr_3$ NPs were first synthesized using mesoporous Al_2O_3 film by Miyasaka and coworkers in 2012[52]. DMF solution comprising of bulk perovskite was spin coated on porous Al_2O_3 film and perovskite nanoparticles are formed due to rapid self-organization inside the pores during annealing process. In 2015, Bolink et al. modified this method slightly to achieve high PL QY by first mixing precursors MABr, $PbBr_2$ and

Al_2O_3 nanocrystal and then spin coated the solution on glass or quartz substrate[53]. $MAPbBr_3$ NPs size can be tuned by varying the template pore size. Additionally, mesoporous silica and TiO_2 have also been used for the growth of perovskite NPs[54]. Even without the use of any ligands, template assisted grown $MAPbBr_3$ NPs show >50 % PL QY due to the intrinsic tolerance of electronic structure to the defects of the template grown materials[55].

1.4.2.2. Hot Injection Method

Perez-Prieto and coworkers who did pioneering work by preparing colloidal $MAPbBr_3$ NPs employed a non-template synthesis method[45]. They used widespread hot injection method for the synthesis of 6 nm sized $MAPbBr_3$ NPs. Typically, $PbBr_2$ and MABr precursors were first added into a non-coordinated solvent system, octadecylene (ODE) combined with oleic acid and octylamine (OA) in sequence[39]. After a short period, light yellow nanoparticles were precipitated out with the addition of acetone. Here, the long-chain ammonium and acids acted as capping ligands which endow stability in QDs solution and restricts the crystal growth. Though high luminescence properties of perovskite NPs is achieved using this method, poor crystallinity, presence of impure phase, instability in polar solvent and temperature make it unattractive for the synthesis of organometal halide perovskite NPs. However, pure inorganic perovskite NPs prepared via hot injection method exhibit very impressive photophysical properties.

1.4.2.3. Ligand Assisted Reprecipitation Method

To overcome poor solubility of $MAPbBr_3$ perovskite precursors in octadecylene, Dong et al. synthesized colloidal $MAPbBr_3$ NPs by incorporating n-octylamine and oleic acid as ligands into the reprecipitation process with absolute PL QY up to 70 %[41]. This room temperature synthesis method is widely used for the synthesis of organometal halide perovskite due to low cost and easy processing. Slight increment in precipitation temperature increased the PL QY up to 93 % due to increased crystallinity of NPs and the efficient surface passivation of long-chain ligands[56]. Zhong and coworkers further studied the role of the key parameters (sequence of solvent mixing, solvent ratio, amount of ligands, etc.) which determine the degree of super-saturation to refine the size and shape of the colloidal perovskite NPs following the reverse LARP approach by changing the sequence of mixing the solvents[57]. Toluene was slowly added in the DMF precursor solution to prepare single-crystalline $MAPbBr_3$ nanocubes and nanowires[57]. LARP is simple room

temperature synthesis method for the production of NPs with high PL QY. However, the as-prepared NPs are very difficult to separate from the reaction solution due to the instability in polar solvents hindering their applications in high performance devices[58].

1.4.3. 1D Organometal Halide Perovskite Nanowires

Along with 2D layered perovskite and 0D nanoparticles, 1D perovskite nanowire or nanorod is another important nanostructure as it is an excellent candidate for the optically pumped laser application due to its great optical properties and strong isotropy. Zhu et al. developed a surface-initiated solution growth strategy of $MAPbI_3$ nanowire using lead acetate ($PbAc_2$) solid thin film deposited on glass substrate in contact with a high concentration MAX solution in isopropanol at room temperature with lasing QY approaching 100 %[59]. $MAPbI_3$ nanowires were developed by low-temperature solution-processed crystallization using a simple slip-coating method[60]. Yang et al. accomplished direct growth of vertical $MAPbBr_3$ nanorod array by coating a saturated methanolic solution of lead acetate onto PEDOT:PSS coated ITO/glass substrate and fabricated the first hybrid perovskite nanorod array LEDs[61].

1.5. Doping in Organometal Halide Perovskite

Doping, surface engineering, interface engineering or other strategies have been adopted extensively to overcome the drawbacks which are present in pristine perovskite, such as the high non-radiative recombination from surface defects, charge-carrier injection barrier caused by trapping defects, low-efficient blue LEDs, toxicity and so on. Doping of impurity ions provides an effective way to solve these issues by stabilizing the crystal structure and improving the optoelectronic properties. Ionic nature of ABX_3 type perovskite endows easy incorporation of dopants in the host crystal. Most of the dopants do not introduce deep trap levels as they do in other conventional semiconductors due to defect tolerant nature of perovskite[7, 62-66]. Though intensive doping study is going on inorganic $CsPbX_3$ perovskite, but volatile nature of hybrid perovskite in an exposed environment makes the doping process quite challenging in $MAPbX_3$ type perovskite. However, the low bandgap phase of inorganic perovskite ($CsPbI_3$) is not ideal for luminescent perovskite phase, since it easily transforms from the perovskite phase to wider gap yellow phase[67-69]. Dopants in the $MAPbX_3$ perovskite may replace organic cation, Pb site ion, or halide anion depending on the size of the dopants. MA can be replaced by monovalent cations

and Pb ions should be replaced by other bivalent or heterovalent metal ions. Commonly used A site cations are MA^+ (2.70 Å), formamidinium (FA^+) (2.79 Å) and inorganic cesium (Cs^+) (1.88 Å)[67]. Among these, the size of MA cation is perfect for perfect cubic structure, but it suffers from unsatisfactory thermal stability[70, 71], whereas, inorganic Cs cation is much more stable at high temperature allowing high-temperature synthesis procedure. The sizes of other organic cations such as rubidium (Rb^+) and potassium (K^+) are very small to form stable perovskite structures[67]. However, Rb doped mesoporous perovskite solar cell ($FA_{0.8}MA_{0.15}Rb_{0.05}PbI_{2.55}Br_{0.45}$) was fabricated by Zhang et al. via gas quenching method and achieved a remarkable PCE of 19.6 % [72].

Mixed halide perovskite is an effective way to tune the bandgap of perovskite over UV to infrared region. Kumawat et al. first reported the mixed halide-based blue $MAPb(Br_xCl_{1-x})_3$ ($0 < x < 1$) perovskite LED in 2015 with tunable emission from sky blue to blue region by changing the halide from Br to Cl ratio[73]. Though the device performance was poor, but they achieved electroluminescence (EL) at 482 nm by employing $MAPbBr_{1.08}Cl_{1.92}$ as the active layer. By increasing Cl content, Shi et al. demonstrated deep blue emission at 450 nm but EL was observed only at low temperature[74]. Though adding Cl in $MAPbI_3$ based perovskite does not change the bandgap, but it has a strong impact on carrier mobility and carrier's thermalization time[75]. Huang and coworkers observed improvement in carrier mobility (560 $cm^2V^{-1}s^{-1}$) with Cl doping in $MAPbBr_3$ single crystal and presented high-resolution gamma-ray energy spectrum detection at room temperature under small electric field[76]. Wang et al. fabricated blue LED by adding ethyl ammonium bromide in $MAPbBr_3$ and achieved a maximum EQE of 2.6 % at 485 nm[77].

Substitution of Pb site ion by other ions should fulfill both the criteria of tolerance and octahedral factors to form perovskite structure. Tremendous efforts have been devoted to incorporate transition metals (Mn^{2+}, Cu^{2+}, Fe^{2+}, Zn^{2+}), metalloids (Sn^{2+}, Bi^{3+}) and lanthanide materials (Ce^{3+}, Eu^{3+}, Yb^{3+}, etc.), etc. in the halide perovskite crystal[78-83]. Sn^{2+} was the first candidate to be considered as a replacement of Pb^{2+} in $MAPbX_3$ to reduce the lead toxicity[81, 82]. But Sn doped perovskite crystal was found to be very unstable in nature since Sn^{2+} quickly oxidizes to Sn^{4+} upon exposure to atmosphere[78]. Kanatzidis et al. extended the light absorption to near-infrared region (~1050 nm) with anomalous bandgap behavior of Sn doped $CH_3NH_3Sn_{1-x}Pb_xI_3$ alloys[81]. To overcome the facile oxidation of Sn^{2+}, Yan and coworkers developed a new strategy by combining

$FASnI_3$ with $MAPbI_3$ and the best-performing cell achieved a PCE of 15.08 % with negligible hysteresis[84]. Bakr et al. incorporated other trivalent ions, such as Bi^{3+}, Au^{3+}, or In^{3+} into $MAPbX_3$, and observed doping-induced band gap tuning and considerable enhancement of electrical conductivity by 104-fold for Bi-doped bulk crystals[85]. The bandgap of the pristine perovskite crystal was found to be narrowed down with the increase in Bi^{3+} dopants amount. However, Snaith et al. subsequently claimed that the incorporation of Bi^{3+} could not lead to bandgap narrowing in $MAPbBr_3$ crystals and the previously observed bandgap change is just a misinterpretation from light transmission measurements resulting from the significant increase in the sub-bandgap density of states[80]. Wang et al. fabricated Nd^{3+} doped $MAPbI_3$ perovskite solar cell with PCE of 21.15 % due to the reduction in trap states, prolong charge carrier lifetimes, and high charge carrier mobility[86]. The doping of Eu^{2+} ions into the $MAPbI_3$ perovskites enhances both the stability and PCE of solar cells[87]. Doping study in organometal halide perovskite is less explored compared to inorganic perovskite due to the instability of organic cation. However, there still remain a large number of elements that can be explored as dopants to improve the device performance of organometal halide perovskite.

1.6. Applications

Low-dimensional perovskite material is widely used in the optoelectronics field and has generated extensive interest as a material of choice for a variety of applications (see **Fig. 1.7**). Due to excellent emissive properties, $MAPbBr_3$ nanomaterials are mostly studied in the LED, photodetector and laser fields with limited studies in solar cells.

1.6.1. Dye-Sensitized Solar Cells

There are countless research articles on perovskite thin film based solar cells, but only a few report target perovskite nanomaterial-based solar cell. Zhang et al. reported that lowering the dimension of perovskite from 3D to 2D till 1D potentially improves charge transport behavior due to a slower recombination rate[88]. 1D perovskite nanowires are also found to be a good light absorption layer in perovskite solar cells and show better performance compared to perovskite NPs. Grätzel's group reported the first perovskite nanowires-based solar cell and the device showed a photocurrent density of 19.12 mA/cm^2 at the voltage of 1.052 V, and a fill factor of 0.721, leading to a PCE of 14.71 %[89]. Perovskite QD sensitized solar cell was first demonstrated by Park's group in 2011

with a PCE of 6.54 %, a record value at that time. Kojima et al. fabricated $MAPbX_3$ (X = Br, I) NP based solar cell having the device structure of $MAPbX_3/TiO_2$ using lithium halide and halogen as redox couple and achieved 3.13 % and 3.81 % efficiency in $MAPbBr_3$ and $MAPbI_3$ solar cells, respectively[11]. Mali et al. fabricated solar cells using different sizes of $MAPbBr_3$ NPs using PTAA (poly triarylamine, a high hole mobility polymer) and Spiro-MeOTAD polymers as hole transporters and achieved a high efficiency of 11.46 %[90].

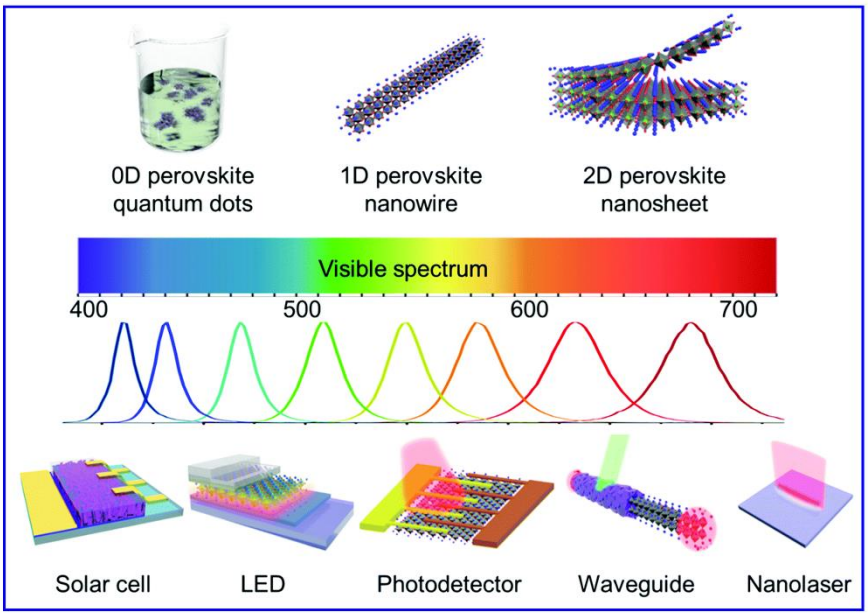

Fig. 1.7. Application of perovskite nanomaterials. Adopted from Ref. [88]

1.6.2. Photodetector

Hybrid perovskite materials are promising for the fabrication of sensitive and fast photodetector due to high carrier lifetime, high quantum yield, effective absorption and high charge carrier mobility. $MAPbI_3$, $MAPbBr_3$, $MAPbCl_3$, $MAPbI_{3-x}Cl_x$, $MAPbBr_{3-x}Cl_x$, and $MAPbBr_{3-x}I_x$ have been extensively studied in the field of photodetectors and shown exceptional photodetection performance[91-98]. The first study on perovskite-based photodetectors consisted of continuous films with tiny perovskite particles, leading to devices with ultrafast speed and good overall performances[49, 99, 100]. However, compared to other morphology, 2D and 1D perovskite nanomaterials exhibit better photodetection performance due to high exciton binding energy and quantum confinement effect[49, 101]. High photo responsivity of 950 A/W, on/off ratio ~10^6 and photoconductive gain of around 2200 were achieved by sandwiching 2D $MAPbI_3$ perovskite NPs

between highly conductive graphene layers[49, 102]. Horvath et al. fabricated 1D $MAPbI_3$ based photodetectors with ~10^4 times faster photoresponse speed than that of the photodetectors based on monolayer MoS_2 and graphene[60]. Photo responsivity of $MAPbI_3$ nanowire photodetectors was increased to 1.3 A/W by aligning the nanowires, which is almost 260 times larger than that in a nonaligned one[60, 103]. Jang et al. combined $MAPbBr_3$ thin film and $MAPbBrI_2$ NPs to fabricate photodetector by spin coating the solution on SiO_x substrate with Au contacts[104]. Nakamura et al. reported lateral $MAPbI_{3-x}Cl_x$ thin film photodetector protected by a spin-coated water-resistant fluorescent polymer (CYTOP)[94]. The device exhibited high responsivity of 14.4 A/W, high environmental stability and waterproof properties for the spin-coated CYTOP layer[94]. Yan et al. reported a low voltage (0.5 V) broadband phototransistors on $MAPbI_{3-x}Cl_x$/poly-(3,4-ethylenedioxythiophene):poly-(styrenesulfonate) (PEDOT:PSS) heterojunction with an ultra-high responsivity of 10^9 A/W and specific detectivity of ~10^{14} Jones in a broad spectral response range from 350 to 1100 nm due to the pronounced photo gaining effect[105]. However, the effect of doping on the photodetection performance is not explored.

1.6.3. LED

High color purity, easy solution processing, low bandwidth and high exciton binding energy make perovskite nanomaterials perfect candidate for the next generation lighting and display applications. The figure of merit, EL efficiency of LEDs is correlated to charge carrier dynamics[88] and effective charge carrier injection at the interface between active layer and charge selective layers is paramount to obtain high EL efficiency[49]. The first breakthrough in perovskite-based LED was reported in 2014 with $MAPbBr_3$ based green LED, which exhibited a bright EL with luminance of 364 cd/m^2 and EQE of 0.1 % at room temperature[91]. Within a year after first report, the $MAPbBr_3$-based LEDs demonstrated a 20-fold increase in luminous efficiency and remarkable improvement in luminance and EQE (20000 cd/m^2, 3.5 %), benefitting from elaborate interfacial engineering techniques[58, 106]. The maximum EQE for a $MAPbBr_3$ thin-film LED has reached the stirring value of 8.5 % within very short span of time[58, 107]. A higher degree of charge transfer process between active layer and n-type layers was observed in $MAPbBr_3$ NPs compared to the bulk film[108]. Kumar et al. fabricated 2D $MAPbBr_3$ NPs based perovskite LEDs with EQE of 0.29 % and with the help of organic host material 4,4′-bis(N-carbazolyl)-1,1′-biphenyl (CBP), 2.07 % efficiency was further improved to 2.31 %[109]. Kim et

al. constructed efficient $MAPbBr_3$ NP-LEDs with CE of 15.5 cd/A and EQE of 5.1 % without using any complex post-treatments and multi-layers[110]. $MAPbX_3$ (X = Br, I) nanowire-based LED was demonstrated by Yang and coworkers exhibiting green EL at 533 nm with a small linewidth of 26 nm[61]. Organic capping ligands were used for the synthesis of colloidal nanocrystal. However it suppresses the charge injection resulting in to low brightness and high turn-on voltage[35]. To overcome this, Park's group reported *in-situ* formed $MAPbBr_3$ nanocrystalline films with excess MABr for highly efficient LEDs with a maximum EQE of 8.21 % and current efficiency of 34.46 cd/A[111]. In situ formed $MAPbI_3$ and $MAPbBr_3$ QD film-based LEDs showed a peak EQE of 7.9 % and 7 %, respectively[112]. Di et al. proposed a methodology of growing metal halide NPs in a polymer matrix without using additional capping agents[114]. Wang's group successfully fabricated a red perovskite LED with a very high EQE of 11.7 %, by employing multi-quantum wells[49, 113].

1.6.4. White LED

Recently, phosphor-converted white light-emitting diodes have become one of the most popular and useful light-emitting source due to easy production, energy saving, high efficiency, improved stability, and long lifetime. High color rendering index and tunable correlated color temperature are preferable for comfortable indoor white light. Zhang et al. fabricated a prototype wide-color gamut phosphor-converted white light-emitting diode using a mixture of green emitting $MAPbBr_3$ NPs, a red emitting inorganic $K_2SiF_6:Mn^{4+}$ phosphor and blue emitting GaN chips producing white-lighting luminescence with color coordinates of (0.33, 0.27) and CCT of 5772 K[41]. Following a similar architecture, Zhou et al. fabricated white LED with $MAPbBr_3$ NPs/PVDF nanocomposite as an emissive layer and blue emitting InGaN chips and $K_2SiF_6:Mn^{4+}$ phosphor exhibiting luminous efficiency of 109 lm/W at 20 mA current and wide colour gamut (121 % of NTC standard)[114]. The stability of white light converter was improved by using the composites of $MAPbBr_3/NaNO_3$ with the same device configuration[115]. Teunis et al. achieved white light emission from ultra-small size $MAPbBr_3$ NPs (~1.5 nm) using high-temperature method and surprisingly these smaller NPs showed a white light emission even after ligand exchange[116].

1.6.4. Laser

Long carrier lifetime, large diffusion length, high fluorescence yield and wavelength tunability also make lead halide perovskites ideal choice for lasing as these properties contribute to decrease in pumping threshold and obtain high optical gain. The first demonstrations of perovskite material in laser applications were reported in 2014, when Xing et al. reported the gain properties of bulk $MAPbI_3$ thin films and noted that amplified spontaneous emission could also be seen in the functional photovoltaic device[49, 117]. Room temperature, continuous-wave operation was achieved by Li et al. in 2018 with a distributed feedback laser utilizing thermally nanoimprinted $MAPbI_3$ film[49, 118]. The imprinting process significantly improved the crystalline quality which in turn reduced the scattering at the grain boundaries. Xiong et al. fabricated $MAPbI_3$ nanowire-based laser exhibiting 777 nm near-infrared light with low threshold of 11 $\mu J/cm^2$ and a quality factor of 405[119]. Zhu et al. showed room-temperature and wavelength-tunable lasing from single-crystal $MAPbI_3$ nanowires with very low lasing thresholds (220 nJ/cm^2) and exceptionally high-quality factors (Q ~3,600)[59].

1.7. Challenges in Fabrication and Applications of Organometal Halide Perovskite

Though reasonable development has been made regarding the room temperature and high temperature synthesis of organometal halide perovskite nanomaterials, a proper good strategy for the controlled synthesis to obtain various morphologies is still lacking. Most of the synthesis processes produce large size perovskite NPs which show weak quantum confinement effect. Newer approaches for controlled synthesis is needed to prepare ultra-small (<2 nm) NPs to use the advantage of the strong quantum confinement effect in the devices. Upscale production of perovskite nanomaterials like other semiconductors can also be beneficial for industrial use. Compared to inorganic perovskite, the progress of $MAPbX_3$ type perovskite is lagging behind in terms of various aspects. Organometal halide perovskite family with interesting optical properties can be expanded by introducing suitable dopants. Alternatively, potential lead-free hybrid perovskites and their applications in device should be analyzed. Among different lower dimensional perovskite, 2D perovskite exhibit many interesting optoelectronic properties, which needs to be studied in greater extent. Long-term stability is a critical issue that need to be addressed seriously for the practical application and commercialization of perovskite-based devices. Specifically, 3D $MAPbI_3$ is extremely sensitive to moisture, UV irradiation, oxygen, heat and

electric field due to its intrinsic chemical instability which deteriorates the device performance. Ion migration was also found in mixed halide perovskite under illumination resulting into phase segregation[120]. Though at room temperature $MAPbBr_3$ shows cubic structure, $MAPbI_3$ transforms from tetragonal at room temperature to cubic phase at around 57 °C, resulting in significant changes in photophysical properties[121]. In contrast, low dimensional perovskite is shown to exhibit better stability compared to its 3D counterpart. However, it is still not stable enough to compete with conventional inorganic semiconductors and more detailed investigation is needed regarding the degradation mechanism. The discovery of new family of perovskite mainly relies on trial and error methods, and proper guidelines need to be developed for the precise control of dimensionality and crystal structure and resulting photophysical properties.

1.8. Focus of the Present Thesis

Despite the significant advancement, there are still several challenges to the fabrication of high-quality perovskite thin film and nanostructure for their applications in the diverse area of nanotechnology. In the present thesis, we have attempted the growth of 3D, 2D and 0D perovskite nanosheet (NS) and investigated their optoelectronic properties. The main objectives of the present thesis are as follows:

- Study the anomalous scaling behavior of the vacuum-deposited $CH_3NH_3PbBr_3$ hybrid perovskite thin film on different substrates and its correlation with its microstructural and optical properties.
- Study the template assisted growth of size-tunable hybrid perovskite ($CH_3NH_3PbI_3$ and $CH_3NH_3PbBr_3$) QDs and investigation on the optical properties and photostability.
- A fast solvothermal synthesis of 2D perovskite NS with precise control of thickness only by solvothermal temperature control is discussed for the first time.
- Application of perovskite NS in white light emission and fast, UV-visible photodetector.
- Development of a novel strategy to achieve stable and deep blue emission with absolute unity PL QY through Ce^{3+} and Tb^{3+} doping at high concentration in 2D $CH_3NH_3PbBr_3$ NS using a solvothermal method and its application in solid state lighting.
- Theoretical analysis of Ce/Tb dopants in the electronic structure of the 2D $MAPbBr_3$ perovskite.

- Growth of Eu^{3+} doped $CH_3NH_3PbBr_3$ NS using simple solvothermal route and fabrication of a high performance self-biased $Eu@CH_3NH_3PbBr_3$ based photodetector.

1.9. Organization of the Thesis

The complete thesis work is presented in seven chapters. This chapter, i.e., **Chapter 1** presented a summary of the various dimensional halide perovskite materials including latest developments, key properties, doping strategies and their promising applications. **Chapter 2** presents the growth kinetics and scaling behavior of vacuum deposited $CH_3NH_3PbBr_3$ thin film on various substrates and correlation of scaling exponents with its microstructural and optical properties. **Chapter 3** presents novel synthetic route for the template-assisted growth of size tunable perovskite QDs and its optical tunability through quantitative analysis. **Chapter 4** discusses a novel, highly reproducible and facile solvothermal route to synthesize and tailor the thickness and optical band gap of organic −inorganic halide perovskite NSs and its application as light converter and photodetector. In **Chapter 5**, we demonstrate a novel strategy to achieve stable and deep blue emission with absolute unity PL QY through Ce^{3+} and Tb^{3+} doping at high concentration in 2D $CH_3NH_3PbBr_3$ NS using a solvothermal method. The effect of Ce/Tb dopants in the electronic structure of the 2D perovskite is investigated using density functional theory based calculations to reveal the origin of large blue shift and high PL QY in the doped NSs. **Chapter 6** presents europium doped 2D layered mixed halide perovskite NS self-biased, stable photodetector. **Chapter 7** summarizes the major findings and important conclusions of the present thesis and future directions of work.

References

[1] S.A. Veldhuis, P.P. Boix, N. Yantara, M. Li, T.C. Sum, N. Mathews, S.G. Mhaisalkar, Perovskite Materials for Light-Emitting Diodes and Lasers, Adv. Mater., 28 (2016) 6804-6834.
[2] S. Brittman, G.W.P. Adhyaksa, E.C. Garnett, The Expanding World of Hybrid Perovskites: Materials Properties and Emerging Applications, MRS Commun., 5 (2015) 7-26.
[3] P. Sadhukhan, A. Pradhan, S. Mukherjee, P. Sengupta, A. Roy, S. Bhunia, S. Das, Low temperature excitonic spectroscopy study of mechano-synthesized hybrid perovskite, Appl. Phys. Lett., 114 (2019) 131102.

[4] T.M. Koh, V. Shanmugam, J. Schlipf, L. Oesinghaus, P. Müller-Buschbaum, N. Ramakrishnan, V. Swamy, N. Mathews, P.P. Boix, S.G. Mhaisalkar, Nanostructuring Mixed-Dimensional Perovskites: A Route Toward Tunable, Efficient Photovoltaics, Adv. Mater., 28 (2016) 3653-3661.
[5] R. Prasanna, A. Gold-Parker, T. Leijtens, B. Conings, A. Babayigit, H.-G. Boyen, M.F. Toney, M.D. McGehee, Band Gap Tuning via Lattice Contraction and Octahedral Tilting in Perovskite Materials for Photovoltaics, J. Am. Chem. Soc., 139 (2017) 11117-11124.
[6] Z. Xiao, Y. Zhou, H. Hosono, T. Kamiya, N.P. Padture, Bandgap Optimization of Perovskite Semiconductors for Photovoltaic Applications, Chem. Eur. J., 24 (2018) 2305-2316.
[7] M.V. Kovalenko, L. Protesescu, M.I. Bodnarchuk, Properties and Potential Optoelectronic Applications of Lead Halide Perovskite Nanocrystals, Science, 358 (2017) 745.
[8] S. Parveen, K.K. Paul, P.K. Giri, Precise Tuning of the Thickness and Optical Properties of Highly Stable 2D Organometal Halide Perovskite Nanosheets through a Solvothermal Process and Their Applications as a White LED and a Fast Photodetector, ACS Appl. Mater. Interfaces, 12 (2020) 6283-6297.
[9] Y.-H. Kim, S. Kim, S.H. Jo, T.-W. Lee, Metal Halide Perovskites: From Crystal Formations to Light-Emitting-Diode Applications, Small Methods, 2 (2018) 1800093.
[10] Q. Chen, N. De Marco, Y. Yang, T.-B. Song, C.-C. Chen, H. Zhao, Z. Hong, H. Zhou, Y. Yang, Under the Spotlight: The Organic–Inorganic Hybrid Halide Perovskite for Optoelectronic Applications, Nano Today, 10 (2015) 355-396.
[11] A. Kojima, K. Teshima, Y. Shirai, T. Miyasaka, Organometal halide perovskites as visible-light sensitizers for photovoltaic cells, J. Am. Chem. Soc., 131 (2009) 6050-6051.
[12] J.-H. Im, H.-S. Kim, N.-G. Park, Morphology-Photovoltaic Property Correlation in Perovskite Solar Cells: One-Step Versus Two-Step Deposition of CH3NH3PbI3, APL Mater., 2 (2014) 081510.
[13] M. Era, S. Morimoto, T. Tsutsui, S. Saito, Organic-Inorganic Heterostructure Electroluminescent Device Using a Layered Perovskite Semiconductor (C6h5c2h4nh3)2pbi4, Appl. Phys. Lett., 65 (1994) 676-678.
[14] Z. Li, T.R. Klein, D.H. Kim, M. Yang, J.J. Berry, M.F.A.M. van Hest, K. Zhu, Scalable Fabrication of Perovskite Solar Cells, Nat. Rev. Mater., 3 (2018) 18017.
[15] W. Nie, H. Tsai, R. Asadpour, J.-C. Blancon, A.J. Neukirch, G. Gupta, J.J. Crochet, M. Chhowalla, S. Tretiak, M.A. Alam, H.-L. Wang, A.D. Mohite, High-Efficiency Solution-Processed Perovskite Solar Cells With Millimeter-Scale Grains, Science, 347 (2015) 522.
[16] N.J. Jeon, J.H. Noh, Y.C. Kim, W.S. Yang, S. Ryu, S.I. Seok, Solvent Engineering For High-Performance Inorganic–Organic Hybrid Perovskite Solar Cells, Nat. Mater., 13 (2014) 897-903.
[17] Y. Shao, Y. Fang, T. Li, Q. Wang, Q. Dong, Y. Deng, Y. Yuan, H. Wei, M. Wang, A. Gruverman, J. Shield, J. Huang, Grain Boundary Dominated Ion Migration in Polycrystalline Organic–Inorganic Halide Perovskite Films, Energy Environ. Sci., 9 (2016) 1752-1759.
[18] S. Tang, Y. Deng, X. Zheng, Y. Bai, Y. Fang, Q. Dong, H. Wei, J. Huang, Composition Engineering in Doctor-Blading of Perovskite Solar Cells, Adv. Energy Mater., 7 (2017) 1700302.
[19] Z. Yang, C.-C. Chueh, F. Zuo, J.H. Kim, P.-W. Liang, A.K.Y. Jen, High-Performance Fully Printable Perovskite Solar Cells via Blade-Coating Technique under the Ambient Condition, Adv. Energy Mater., 5 (2015) 1500328.
[20] Y. Deng, X. Zheng, Y. Bai, Q. Wang, J. Zhao, J. Huang, Surfactant-Controlled Ink Drying Enables High-Speed Deposition of Perovskite Films for Efficient Photovoltaic Modules, Nat Energy, 3 (2018) 560-566.
[21] W.-Q. Wu, Q. Wang, Y. Fang, Y. Shao, S. Tang, Y. Deng, H. Lu, Y. Liu, T. Li, Z. Yang, A. Gruverman, J. Huang, Molecular Doping Enabled Scalable Blading of Efficient Hole-Transport-Layer-Free Perovskite Solar Cells, Nat Commun, 9 (2018) 1625.
[22] L. Lee, J. Baek, K.S. Park, Y.-E. Lee, N.K. Shrestha, M.M. Sung, Wafer-Scale Single-Crystal Perovskite Patterned Thin Films Based on Geometrically-Confined Lateral Crystal Growth, Nat Commun, 8 (2017) 15882.

[23] T. Soto-Montero, W. Soltanpoor, M. Morales-Masis, Pressing Challenges of Halide Perovskite Thin Film Growth, APL Mater., 8 (2020) 110903.
[24] H. Ji, Z. Shi, X. Sun, Y. Li, S. Li, L. Lei, D. Wu, T. Xu, X. Li, G. Du, Vapor-Assisted Solution Approach for High-Quality Perovskite CH3NH3PbBr3 Thin Films for High-Performance Green Light-Emitting Diode Applications, ACS Appl. Mater. Interfaces, 9 (2017) 42893-42904.
[25] Y. Liang, Y. Yao, X. Zhang, W.-L. Hsu, Y. Gong, J. Shin, E.D. Wachsman, M. Dagenais, I. Takeuchi, Fabrication Of Organic-Inorganic Perovskite Thin Films For Planar Solar Cells Via Pulsed Laser Deposition, AIP Adv., 6 (2016) 015001.
[26] A. Ioakeimidis, C. Christodoulou, M. Lux-Steiner, K. Fostiropoulos, Effect of PbI2 Deposition Rate on Two-Step PVD/CVD All-Vacuum Prepared Perovskite, J. Solid State Chem., 244 (2016) 20-24.
[27] W. Soltanpoor, C. Dreessen, M.C. Sahiner, I. Susic, A.Z. Afshord, V.S. Chirvony, P.P. Boix, G. Gunbas, S. Yerci, H.J. Bolink, Hybrid Vapor-Solution Sequentially Deposited Mixed-Halide Perovskite Solar Cells, ACS Appl. Energy Mater., 3 (2020) 8257-8265.
[28] J.M.C.d. Silva Filho, V.A. Ermakov, F.C. Marques, Perovskite Thin Film Synthesised from Sputtered Lead Sulphide, Sci. Rep., 8 (2018) 1563.
[29] M.R. Leyden, L.K. Ono, S.R. Raga, Y. Kato, S. Wang, Y. Qi, High Performance Perovskite Solar Cells by Hybrid Chemical Vapor Deposition, J. Mater. Chem. A, 2 (2014) 18742-18745.
[30] M. Liu, M.B. Johnston, H.J. Snaith, Efficient Planar Heterojunction Perovskite Solar Cells by Vapour Deposition, Nature, 501 (2013) 395-398.
[31] L. Gil-Escrig, A. Miquel-Sempere, M. Sessolo, H.J. Bolink, Mixed Iodide–Bromide Methylammonium Lead Perovskite-based Diodes for Light Emission and Photovoltaics, J. Phys. Chem. Lett., 6 (2015) 3743-3748.
[32] J. Ávila, C. Momblona, P.P. Boix, M. Sessolo, H.J. Bolink, Vapor-Deposited Perovskites: The Route to High-Performance Solar Cell Production?, Joule, 1 (2017) 431-442.
[33] D.B. Mitzi, M.T. Prikas, K. Chondroudis, Thin Film Deposition of Organic−Inorganic Hybrid Materials Using a Single Source Thermal Ablation Technique, Chem. Mater., 11 (1999) 542-544.
[34] M.R. Leyden, L. Meng, Y. Jiang, L.K. Ono, L. Qiu, E.J. Juarez-Perez, C. Qin, C. Adachi, Y. Qi, Methylammonium Lead Bromide Perovskite Light-Emitting Diodes by Chemical Vapor Deposition, J. Phys. Chem. Lett., 8 (2017) 3193-3198.
[35] C. Zhou, H. Lin, Q. He, L. Xu, M. Worku, M. Chaaban, S. Lee, X. Shi, M.-H. Du, B. Ma, Low dimensional metal halide perovskites and hybrids, Mater. Sci. Eng. R, 137 (2019) 38-65.
[36] Y. Bekenstein, B.A. Koscher, S.W. Eaton, P. Yang, A.P. Alivisatos, Highly Luminescent Colloidal Nanoplates of Perovskite Cesium Lead Halide and Their Oriented Assemblies, J. Am. Chem. Soc., 137 (2015) 16008-16011.
[37] J. Shamsi, Z. Dang, P. Bianchini, C. Canale, F. Di Stasio, R. Brescia, M. Prato, L. Manna, Colloidal Synthesis of Quantum Confined Single Crystal CsPbBr3 Nanosheets with Lateral Size Control up to the Micrometer Range, J. Am. Chem. Soc., 138 (2016) 7240-7243.
[38] Z. Yuan, Y. Shu, Y. Tian, Y. Xin, B. Ma, A Facile One-Pot Synthesis of Deep Blue Luminescent Lead Bromide Perovskite Microdisks, Chem. Commun., 51 (2015) 16385-16388.
[39] P. Fu, Q. Shan, Y. Shang, J. Song, H. Zeng, Z. Ning, J. Gong, Perovskite Nanocrystals: Synthesis, Properties and Applications, Sci. Bull., 62 (2017) 369-380.
[40] W. Tian, C. Zhao, J. Leng, R. Cui, S. Jin, Visualizing Carrier Diffusion in Individual Single-Crystal Organolead Halide Perovskite Nanowires and Nanoplates, J. Am. Chem. Soc., 137 (2015) 12458-12461.
[41] F. Zhang, H. Zhong, C. Chen, X.-g. Wu, X. Hu, H. Huang, J. Han, B. Zou, Y. Dong, Brightly Luminescent and Color-Tunable Colloidal CH3NH3PbX3 (X= Br, I, Cl) Quantum Dots: Potential Alternatives for Display Technology, ACS nano, 9 (2015) 4533-4542.

[42] J. Liu, Y. Xue, Z. Wang, Z.-Q. Xu, C. Zheng, B. Weber, J. Song, Y. Wang, Y. Lu, Y. Zhang, Q. Bao, Two-Dimensional CH3NH3PbI3 Perovskite: Synthesis and Optoelectronic Application, ACS Nano, 10 (2016) 3536-3542.
[43] J.A. Sichert, Y. Tong, N. Mutz, M. Vollmer, S. Fischer, K.Z. Milowska, R. García Cortadella, B. Nickel, C. Cardenas-Daw, J.K. Stolarczyk, Quantum Size Effect in Organometal Halide Perovskite Nanoplatelets, Nano Lett., 15 (2015) 6521-6527.
[44] Y. Ling, Z. Yuan, Y. Tian, X. Wang, J.C. Wang, Y. Xin, K. Hanson, B. Ma, H. Gao, Bright Light-Emitting Diodes Based on Organometal Halide Perovskite Nanoplatelets, Adv. Mater., 28 (2016) 305-311.
[45] S. Gonzalez-Carrero, R.E. Galian, J. Pérez-Prieto, Maximizing the Emissive Properties of CH3NH3PbBr3 Perovskite Nanoparticles, J. Mater. Chem. A, 3 (2015) 9187-9193.
[46] J. Cho, Y.-H. Choi, T.E. O'Loughlin, L. De Jesus, S. Banerjee, Ligand-Mediated Modulation of Layer Thicknesses of Perovskite Methylammonium Lead Bromide Nanoplatelets, Chem. Mater., 28 (2016) 6909-6916.
[47] Q.A. Akkerman, S.G. Motti, A.R. Srimath Kandada, E. Mosconi, V. D'Innocenzo, G. Bertoni, S. Marras, B.A. Kamino, L. Miranda, F. De Angelis, A. Petrozza, M. Prato, L. Manna, Solution Synthesis Approach to Colloidal Cesium Lead Halide Perovskite Nanoplatelets with Monolayer-Level Thickness Control, J. Am. Chem. Soc., 138 (2016) 1010-1016.
[48] R. Naphade, S. Nagane, G.S. Shanker, R. Fernandes, D. Kothari, Y. Zhou, N.P. Padture, S. Ogale, Hybrid Perovskite Quantum Nanostructures Synthesized by Electrospray Antisolvent–Solvent Extraction and Intercalation, ACS Appl. Mater. Interfaces, 8 (2016) 854-861.
[49] M. Liu, H. Zhang, D. Gedamu, P. Fourmont, H. Rekola, A. Hiltunen, S.G. Cloutier, R. Nechache, A. Priimagi, P. Vivo, Halide Perovskite Nanocrystals for Next-Generation Optoelectronics, Small, 15 (2019) 1900801.
[50] Q. Zhang, S.T. Ha, X. Liu, T.C. Sum, Q. Xiong, Room-Temperature Near-Infrared High-Q Perovskite Whispering-Gallery Planar Nanolasers, Nano Lett., 14 (2014) 5995-6001.
[51] Y. Wang, Y. Shi, G. Xin, J. Lian, J. Shi, Two-Dimensional van der Waals Epitaxy Kinetics in a Three-Dimensional Perovskite Halide, Cryst. Growth Des., 15 (2015) 4741-4749.
[52] A. Kojima, M. Ikegami, K. Teshima, T. Miyasaka, Highly Luminescent Lead Bromide Perovskite Nanoparticles Synthesized with Porous Alumina Media, Chem. Lett., 41 (2012) 397-399.
[53] G. Longo, A. Pertegás, L. Martínez-Sarti, M. Sessolo, H.J. Bolink, Highly Luminescent Perovskite–Aluminum Oxide Composites, J. Mater. Chem. C, 3 (2015) 11286-11289.
[54] D.N. Dirin, L. Protesescu, D. Trummer, I.V. Kochetygov, S. Yakunin, F. Krumeich, N.P. Stadie, M.V. Kovalenko, Harnessing Defect-Tolerance at the Nanoscale: Highly Luminescent Lead Halide Perovskite Nanocrystals in Mesoporous Silica Matrixes, Nano Lett., 16 (2016) 5866-5874.
[55] V. Malgras, S. Tominaka, J.W. Ryan, J. Henzie, T. Takei, K. Ohara, Y. Yamauchi, Observation of Quantum Confinement in Monodisperse Methylammonium Lead Halide Perovskite Nanocrystals Embedded in Mesoporous Silica, J. Am. Chem. Soc., 138 (2016) 13874-13881.
[56] H. Huang, A.S. Susha, S.V. Kershaw, T.F. Hung, A.L. Rogach, Control of Emission Color of High Quantum Yield CH3NH3PbBr3 Perovskite Quantum Dots by Precipitation Temperature, Adv. Sci., 2 (2015) 1500194.
[57] F. Zhang, C. Chen, S.V. Kershaw, C. Xiao, J. Han, B. Zou, X. Wu, S. Chang, Y. Dong, A.L. Rogach, H. Zhong, Ligand-Controlled Formation and Photoluminescence Properties of CH3NH3PbBr3 Nanocubes and Nanowires, ChemNanoMat, 3 (2017) 303-310.
[58] D. Chen, X. Chen, Luminescent Perovskite Quantum Dots: Synthesis, Microstructures, Optical Properties and Applications, J. Mater. Chem. C,, 7 (2019) 1413-1446.
[59] H. Zhu, Y. Fu, F. Meng, X. Wu, Z. Gong, Q. Ding, M.V. Gustafsson, M.T. Trinh, S. Jin, X.Y. Zhu, Lead Halide Perovskite Nanowire Lasers with Low Lasing Thresholds and High Quality Factors, Nat. Mater, 14 (2015) 636-642.

[60] E. Horváth, M. Spina, Z. Szekrényes, K. Kamarás, R. Gaal, D. Gachet, L. Forró, Nanowires of Methylammonium Lead Iodide (CH3NH3PbI3) Prepared by Low Temperature Solution-Mediated Crystallization, Nano Lett., 14 (2014) 6761-6766.
[61] A.B. Wong, M. Lai, S.W. Eaton, Y. Yu, E. Lin, L. Dou, A. Fu, P. Yang, Growth and Anion Exchange Conversion of CH3NH3PbX3 Nanorod Arrays for Light-Emitting Diodes, Nano Letters, 15 (2015) 5519-5524.
[62] X. Zhang, L. Li, Z. Sun, J. Luo, Rational Chemical Doping of Metal Halide Perovskites, Chem. Soc. Rev., 48 (2019) 517-539.
[63] N. Pradhan, S. Das Adhikari, A. Nag, D.D. Sarma, Luminescence, Plasmonic, and Magnetic Properties of Doped Semiconductor Nanocrystals, Angew. Chem. Int. Ed. , 56 (2017) 7038-7054.
[64] H.D. Nelson, S.O.M. Hinterding, R. Fainblat, S.E. Creutz, X. Li, D.R. Gamelin, Mid-Gap States and Normal vs Inverted Bonding in Luminescent Cu+- and Ag+-Doped CdSe Nanocrystals, J. Am. Chem. Soc., 139 (2017) 6411-6421.
[65] J. Kim, S.-H. Lee, J.H. Lee, K.-H. Hong, The Role of Intrinsic Defects in Methylammonium Lead Iodide Perovskite, J. Phys. Chem. Lett., 5 (2014) 1312-1317.
[66] A.J. Houtepen, Z. Hens, J.S. Owen, I. Infante, On the Origin of Surface Traps in Colloidal II–VI Semiconductor Nanocrystals, Chem. Mater., 29 (2017) 752-761.
[67] L. Xu, S. Yuan, H. Zeng, J. Song, A Comprehensive Review of Doping in Perovskite Nanocrystals/Quantum Dots: Evolution of Structure, Electronics, Optics, and Light-Emitting Diodes, Materials Today Nano, 6 (2019) 100036.
[68] L. Protesescu, S. Yakunin, S. Kumar, J. Bär, F. Bertolotti, N. Masciocchi, A. Guagliardi, M. Grotevent, I. Shorubalko, M.I. Bodnarchuk, C.-J. Shih, M.V. Kovalenko, Dismantling the “Red Wall” of Colloidal Perovskites: Highly Luminescent Formamidinium and Formamidinium–Cesium Lead Iodide Nanocrystals, ACS Nano, 11 (2017) 3119-3134.
[69] R.E. Beal, D.J. Slotcavage, T. Leijtens, A.R. Bowring, R.A. Belisle, W.H. Nguyen, G.F. Burkhard, E.T. Hoke, M.D. McGehee, Cesium Lead Halide Perovskites with Improved Stability for Tandem Solar Cells, J. Phys. Chem. Lett., 7 (2016) 746-751.
[70] S. Singh, D. Kabra, Influence of Solvent Additive on the Chemical and Electronic Environment of Wide Bandgap Perovskite Thin Films, J. Mater. Chem. C, 6 (2018) 12052-12061.
[71] N. Yantara, S. Bhaumik, F. Yan, D. Sabba, H.A. Dewi, N. Mathews, P.P. Boix, H.V. Demir, S. Mhaisalkar, Inorganic Halide Perovskites for Efficient Light-Emitting Diodes, J. Phys. Chem. Lett., 6 (2015) 4360-4364.
[72] M. Zhang, J.S. Yun, Q. Ma, J. Zheng, C.F.J. Lau, X. Deng, J. Kim, D. Kim, J. Seidel, M.A. Green, S. Huang, A.W.Y. Ho-Baillie, High-Efficiency Rubidium-Incorporated Perovskite Solar Cells by Gas Quenching, ACS Energy Lett., 2 (2017) 438-444.
[73] N.K. Kumawat, A. Dey, A. Kumar, S.P. Gopinathan, K.L. Narasimhan, D. Kabra, Band Gap Tuning of CH3NH3Pb(Br1–xClx)3 Hybrid Perovskite for Blue Electroluminescence, ACS Appl. Mater. Interfaces, 7 (2015) 13119-13124.
[74] X.-B. Shi, Y. Liu, Z. Yuan, X.-K. Liu, Y. Miao, J. Wang, S. Lenk, S. Reineke, F. Gao, Optical Energy Losses in Organic–Inorganic Hybrid Perovskite Light-Emitting Diodes, Adv. Opt. Mater, 6 (2018) 1800667.
[75] M.E.-A. Madjet, A.V. Akimov, F. El-Mellouhi, G.R. Berdiyorov, S. Ashhab, N. Tabet, S. Kais, Enhancing the Carrier Thermalization Time in Organometallic Perovskites by Halide Mixing, Phys. Chem. Chem. Phys., 18 (2016) 5219-5231.
[76] H. Wei, D. DeSantis, W. Wei, Y. Deng, D. Guo, T.J. Savenije, L. Cao, J. Huang, Dopant Compensation in Alloyed CH3NH3PbBr3−xClx Perovskite Single Crystals for Gamma-Ray Spectroscopy, Nat. Mater, 16 (2017) 826-833.
[77] Q. Wang, J. Ren, X.-F. Peng, X.-X. Ji, X.-H. Yang, Efficient Sky-Blue Perovskite Light-Emitting Devices Based on Ethylammonium Bromide Induced Layered Perovskites, ACS Appl. Mater. Interfaces, 9 (2017) 29901-29906.

[78] H.-C. Wang, W. Wang, A.-C. Tang, H.-Y. Tsai, Z. Bao, T. Ihara, N. Yarita, H. Tahara, Y. Kanemitsu, S. Chen, R.-S. Liu, High-Performance CsPb1−xSnxBr3 Perovskite Quantum Dots for Light-Emitting Diodes, Angew. Chem. Int. Ed., 56 (2017) 13650-13654.
[79] W. Liu, Q. Lin, H. Li, K. Wu, I. Robel, J.M. Pietryga, V.I. Klimov, Mn2+-Doped Lead Halide Perovskite Nanocrystals with Dual-Color Emission Controlled by Halide Content, J. Am. Chem. Soc., 138 (2016) 14954-14961.
[80] P.K. Nayak, M. Sendner, B. Wenger, Z. Wang, K. Sharma, A.J. Ramadan, R. Lovrinčić, A. Pucci, P.K. Madhu, H.J. Snaith, Impact of Bi3+ Heterovalent Doping in Organic–Inorganic Metal Halide Perovskite Crystals, J. Am. Chem. Soc., 140 (2018) 574-577.
[81] F. Hao, C.C. Stoumpos, R.P.H. Chang, M.G. Kanatzidis, Anomalous Band Gap Behavior in Mixed Sn and Pb Perovskites Enables Broadening of Absorption Spectrum in Solar Cells, J. Am. Chem. Soc., 136 (2014) 8094-8099.
[82] H.-J. Feng, T.R. Paudel, E.Y. Tsymbal, X.C. Zeng, Tunable Optical Properties and Charge Separation in CH3NH3SnxPb1–xI3/TiO2-Based Planar Perovskites Cells, J. Am. Chem. Soc., 137 (2015) 8227-8236.
[83] S. Thapa, G.C. Adhikari, H. Zhu, A. Grigoriev, P. Zhu, Zn-Alloyed All-Inorganic Halide Perovskite-Based White Light-Emitting Diodes with Superior Color Quality, Sci Rep, 9 (2019) 18636.
[84] W. Liao, D. Zhao, Y. Yu, N. Shrestha, K. Ghimire, C.R. Grice, C. Wang, Y. Xiao, A.J. Cimaroli, R.J. Ellingson, N.J. Podraza, K. Zhu, R.-G. Xiong, Y. Yan, Fabrication of Efficient Low-Bandgap Perovskite Solar Cells by Combining Formamidinium Tin Iodide with Methylammonium Lead Iodide, J. Am. Chem. Soc., 138 (2016) 12360-12363.
[85] L. Dou, A.B. Wong, Y. Yu, M. Lai, N. Kornienko, S.W. Eaton, A. Fu, C.G. Bischak, J. Ma, T. Ding, N.S. Ginsberg, L.-W. Wang, A.P. Alivisatos, P. Yang, Atomically Thin Two-Dimensional Organic-Inorganic Hybrid Perovskites, Science, 349 (2015) 1518.
[86] K. Wang, L. Zheng, T. Zhu, X. Yao, C. Yi, X. Zhang, Y. Cao, L. Liu, W. Hu, X. Gong, Efficient Perovskite Solar Cells by Hybrid Perovskites Incorporated with Heterovalent Neodymium Cations, Nano Energy, 61 (2019) 352-360.
[87] X. Wu, H. Li, K. Wang, X. Sun, L. Wang, CH3NH3Pb1−xEuxI3 mixed halide perovskite for hybrid solar cells: the impact of divalent europium doping on efficiency and stability, RSC Advances, 8 (2018) 11095-11101.
[88] Y. Zhang, J. Liu, Z. Wang, Y. Xue, Q. Ou, L. Polavarapu, J. Zheng, X. Qi, Q. Bao, Synthesis, Properties, and Optical Applications of Low-Dimensional Perovskites, Chem. Commun., 52 (2016) 13637-13655.
[89] J.-H. Im, J. Luo, M. Franckevičius, N. Pellet, P. Gao, T. Moehl, S.M. Zakeeruddin, M.K. Nazeeruddin, M. Grätzel, N.-G. Park, Nanowire Perovskite Solar Cell, Nano Lett., 15 (2015) 2120-2126.
[90] S.S. Mali, C.S. Shim, C.K. Hong, Highly Stable and Efficient Solid-State Solar Cells Based on Methylammonium Lead Bromide (CH3NH3PbBr3) Perovskite Quantum Dots, NPG Asia Mater., 7 (2015) e208-e208.
[91] Z.-K. Tan, R.S. Moghaddam, M.L. Lai, P. Docampo, R. Higler, F. Deschler, M. Price, A. Sadhanala, L.M. Pazos, D. Credgington, F. Hanusch, T. Bein, H.J. Snaith, R.H. Friend, Bright Light-Emitting Diodes Based on Organometal Halide Perovskite, Nat Nanotechnol., 9 (2014) 687.
[92] L. Wang, G.D. Yuan, R.F. Duan, F. Huang, T.B. Wei, Z.Q. Liu, J.X. Wang, J.M. Li, Tunable Bandgap in Hybrid Perovskite CH3NH3Pb(Br3−yXy) Single Crystals And Photodetector Applications, AIP Adv., 6 (2016) 045115.
[93] Y. Fang, Q. Dong, Y. Shao, Y. Yuan, J. Huang, Highly Narrowband Perovskite Single-Crystal Photodetectors Enabled by Surface-Charge Recombination, Nat. Photon., 9 (2015) 679-686.
[94] Y. Guo, C. Liu, H. Tanaka, E. Nakamura, Air-Stable and Solution-Processable Perovskite Photodetectors for Solar-Blind UV and Visible Light, J. Phys. Chem. Lett., 6 (2015) 535-539.

[95] H.-W. Chen, N. Sakai, A.K. Jena, Y. Sanehira, M. Ikegami, K.-C. Ho, T. Miyasaka, A Switchable High-Sensitivity Photodetecting and Photovoltaic Device with Perovskite Absorber, J. Phys. Chem. Lett., 6 (2015) 1773-1779.
[96] H. Deng, X. Yang, D. Dong, B. Li, D. Yang, S. Yuan, K. Qiao, Y.-B. Cheng, J. Tang, H. Song, Flexible and Semitransparent Organolead Triiodide Perovskite Network Photodetector Arrays with High Stability, Nano Lett., 15 (2015) 7963-7969.
[97] F. Li, C. Ma, H. Wang, W. Hu, W. Yu, A.D. Sheikh, T. Wu, Ambipolar Solution-Processed Hybrid Perovskite Phototransistors, Nat. Commun., 6 (2015) 8238.
[98] X. Hu, X. Zhang, L. Liang, J. Bao, S. Li, W. Yang, Y. Xie, High-Performance Flexible Broadband Photodetector Based on Organolead Halide Perovskite, Adv. Funct. Mater., 24 (2014) 7373-7380.
[99] L. Dou, Y. Yang, J. You, Z. Hong, W.-H. Chang, G. Li, Y. Yang, Solution-Processed Hybrid Perovskite Photodetectors with High Detectivity, Nat. Commun., 5 (2014) 5404.
[100] J. Ding, Y. Liu, H. Fang, Y. Wang, Q. Li, J.-L. Sun, Q. Yan, Nanosecond-Response Speed Sensor Based on Perovskite Single Crystal Photodetector Array, ACS Photonics, 5 (2018) 3172-3178.
[101] T. Qiu, Y. Hu, F. Xu, Z. Yan, F. Bai, G. Jia, S. Zhang, Recent Advances in One-Dimensional Halide Perovskites for Optoelectronic Applications, Nanoscale, 10 (2018) 20963-20989.
[102] H.-C. Cheng, G. Wang, D. Li, Q. He, A. Yin, Y. Liu, H. Wu, M. Ding, Y. Huang, X. Duan, van der Waals Heterojunction Devices Based on Organohalide Perovskites and Two-Dimensional Materials, Nano Lett., 16 (2016) 367-373.
[103] H. Deng, D. Dong, K. Qiao, L. Bu, B. Li, D. Yang, H.-E. Wang, Y. Cheng, Z. Zhao, J. Tang, H. Song, Growth, Patterning and Alignment of Organolead Iodide Perovskite Nanowires for Optoelectronic Devices, Nanoscale, 7 (2015) 4163-4170.
[104] D.M. Jang, K. Park, D.H. Kim, J. Park, F. Shojaei, H.S. Kang, J.-P. Ahn, J.W. Lee, J.K. Song, Reversible Halide Exchange Reaction of Organometal Trihalide Perovskite Colloidal Nanocrystals for Full-Range Band Gap Tuning, Nano Lett., 15 (2015) 5191-5199.
[105] C. Xie, P. You, Z. Liu, L. Li, F. Yan, Ultrasensitive Broadband Phototransistors Based on Perovskite/Organic-Semiconductor Vertical Heterojunctions, Light: Sci. Appl, 6 (2017) e17023-e17023.
[106] J. Wang, N. Wang, Y. Jin, J. Si, Z.-K. Tan, H. Du, L. Cheng, X. Dai, S. Bai, H. He, Z. Ye, M.L. Lai, R.H. Friend, W. Huang, Interfacial Control Toward Efficient and Low-Voltage Perovskite Light-Emitting Diodes, Adv. Mater., 27 (2015) 2311-2316.
[107] H. Cho, S.-H. Jeong, M.-H. Park, Y.-H. Kim, C. Wolf, C.-L. Lee, J.H. Heo, A. Sadhanala, N. Myoung, S. Yoo, S.H. Im, R.H. Friend, T.-W. Lee, Overcoming the Electroluminescence Efficiency Limitations of Perovskite Light-Emitting Diodes, Science, 350 (2015) 1222.
[108] P. Kumar, C. Muthu, V.C. Nair, K.S. Narayan, Quantum Confinement Effects in Organic Lead Tribromide Perovskite Nanoparticles, J. Phys. Chem. C, 120 (2016) 18333-18339.
[109] S. Kumar, J. Jagielski, S. Yakunin, P. Rice, Y.-C. Chiu, M. Wang, G. Nedelcu, Y. Kim, S. Lin, E.J.G. Santos, M.V. Kovalenko, C.-J. Shih, Efficient Blue Electroluminescence Using Quantum-Confined Two-Dimensional Perovskites, ACS Nano, 10 (2016) 9720-9729.
[110] Y.-H. Kim, C. Wolf, Y.-T. Kim, H. Cho, W. Kwon, S. Do, A. Sadhanala, C.G. Park, S.-W. Rhee, S.H. Im, R.H. Friend, T.-W. Lee, Highly Efficient Light-Emitting Diodes of Colloidal Metal–Halide Perovskite Nanocrystals beyond Quantum Size, ACS Nano, 11 (2017) 6586-6593.
[111] J.-W. Lee, Y.J. Choi, J.-M. Yang, S. Ham, S.K. Jeon, J.Y. Lee, Y.-H. Song, E.K. Ji, D.-H. Yoon, S. Seo, H. Shin, G.S. Han, H.S. Jung, D. Kim, N.-G. Park, In-Situ Formed Type I Nanocrystalline Perovskite Film for Highly Efficient Light-Emitting Diode, ACS Nano, 11 (2017) 3311-3319.
[112] L. Zhao, Y.-W. Yeh, N.L. Tran, F. Wu, Z. Xiao, R.A. Kerner, Y.L. Lin, G.D. Scholes, N. Yao, B.P. Rand, In Situ Preparation of Metal Halide Perovskite Nanocrystal Thin Films for Improved Light-Emitting Devices, ACS Nano, 11 (2017) 3957-3964.

[113] N. Wang, L. Cheng, R. Ge, S. Zhang, Y. Miao, W. Zou, C. Yi, Y. Sun, Y. Cao, R. Yang, Y. Wei, Q. Guo, Y. Ke, M. Yu, Y. Jin, Y. Liu, Q. Ding, D. Di, L. Yang, G. Xing, H. Tian, C. Jin, F. Gao, R.H. Friend, J. Wang, W. Huang, Perovskite Light-Emitting Diodes Based on Solution-Processed Self-Organized Multiple Quantum Wells, Nat. Photon., 10 (2016) 699-704.
[114] Q. Zhou, Z. Bai, W.-g. Lu, Y. Wang, B. Zou, H. Zhong, In Situ Fabrication of Halide Perovskite Nanocrystal-Embedded Polymer Composite Films with Enhanced Photoluminescence for Display Backlights, Adv. Mater., 28 (2016) 9163-9168.
[115] G. Yang, Q. Fan, B. Chen, Q. Zhou, H. Zhong, Reprecipitation Synthesis of Luminescent CH3NH3PbBr3/NaNO3 Nanocomposites with Enhanced Stability, J. Mater. Chem. C, 4 (2016) 11387-11391.
[116] M.B. Teunis, K.N. Lawrence, P. Dutta, A.P. Siegel, R. Sardar, Pure White-Light Emitting Ultrasmall Organic–Inorganic Hybrid Perovskite Nanoclusters, Nanoscale, 8 (2016) 17433-17439.
[117] G. Xing, N. Mathews, S.S. Lim, N. Yantara, X. Liu, D. Sabba, M. Grätzel, S. Mhaisalkar, T.C. Sum, Low-Temperature Solution-Processed Wavelength-Tunable Perovskites for Lasing, Nat. Mater., 13 (2014) 476-480.
[118] Z. Li, J. Moon, A. Gharajeh, R. Haroldson, R. Hawkins, W. Hu, A. Zakhidov, Q. Gu, Room-Temperature Continuous-Wave Operation of Organometal Halide Perovskite Lasers, ACS Nano, 12 (2018) 10968-10976.
[119] J. Xing, X.F. Liu, Q. Zhang, S.T. Ha, Y.W. Yuan, C. Shen, T.C. Sum, Q. Xiong, Vapor Phase Synthesis of Organometal Halide Perovskite Nanowires for Tunable Room-Temperature Nanolasers, Nano Lett., 15 (2015) 4571-4577.
[120] E.T. Hoke, D.J. Slotcavage, E.R. Dohner, A.R. Bowring, H.I. Karunadasa, M.D. McGehee, Reversible Photo-Induced Trap Formation in Mixed-Halide Hybrid Perovskites for Photovoltaics, Chem. Sci., 6 (2015) 613-617.
[121] T. Baikie, Y. Fang, J.M. Kadro, M. Schreyer, F. Wei, S.G. Mhaisalkar, M. Graetzel, T.J. White, Synthesis and Crystal Chemistry of the Hybrid Perovskite (CH3NH3)PbI3 for Solid-State Sensitised Solar Cell Applications, J. Mater. Chem. A, 1 (2013) 5628-5641.

Chapter 2

Growth Kinetics of Hybrid Perovskite Thin Films on Different Substrates at Elevated Temperature and Its Direct Correlation with the Microstructure and Optical Properties

In this chapter, the growth kinetics and scaling behavior of vacuum deposited $CH_3NH_3PbBr_3$ thin film on various substrates are presented and the same is correlated with its microstructural and optical properties. AFM analysis reveals an abrupt change in the grain features for thickness, $d \geq 40$ nm. Based on the evaluation of the scaling parameters, the perovskite films exhibit an anomalous scaling behavior for $d < 40$ nm, and stable growth for $d \geq 40$ nm. Interestingly, the growth exponent (β) is found to be distinctly different, ~0.22 and ~0.90, for the films on ITO and SiO_2 substrates, respectively. The study of the temperature-dependent growth kinetics yields higher activation energy (E_a) for SiO_2 (~0.15 eV) than that of ITO (~0.10 eV) substrates indicating mound-like growth on SiO_2 substrate. Structural and photoluminescence (PL) studies reveal better crystallinity of the film on ITO, which is consistent with its low E_a value. Optical absorbance and PL analyses reveal a blue shift in the bandgap with decreasing thickness attributed to the lattice expansion. These findings provide new insights on the growth kinetics and optimum conditions for the vacuum deposition of hybrid perovskite thin films on various substrates.

2.1. Introduction

Organo-metal halide perovskite is currently one of the most far-reaching and promising materials due to its exceptional performance in various optoelectronic devices. In particular, $CH_3NH_3PbBr_3$ ($MAPbBr_3$, MA= CH_3NH_3) thin film and nano system have been used in various next-generation devices, such as light-emitting diodes (LED)[1-4], phototransistor[5], photodetectors[6-11], solar cells [12-16] and laser[17-20] etc.. Recently, the power conversion efficiency of perovskite-based solar cells achieved a record high value of 23 %, higher than any other thin-film based photovoltaic devices [21]. The external quantum efficiency of the perovskite-based LED is reported to achieve a value of 21.6 %, which is close to the value reported for organic LEDs [22-24]. However, the poor stability of perovskite-based devices is a major concern. Based on the application, it is important to achieve high quality and stable thin film with desirable morphology to improve the

performance and stability of the perovskite-based optoelectronic devices. For the improvement of the structural and optical quality of the film, various deposition techniques, such as solution processing, vapor phase method, and numerous morphology control procedures have been adopted. In particular, transport phenomena, such as injection, separation, and recombination of charge carriers are known to be strongly correlated to grain size, grain boundaries, molecular packing, and surface roughness of the film[25, 26]. Hence, an in-depth knowledge of the surface roughness and grain size is crucial for the enhancement of device fabrication and optimization of optoelectronic properties. For example, the mobility of the charge carriers is directly related to the grain size and correlation length of the molecules in thin-film transistor [27]. Various methods have been reported to improve the surface morphology of the perovskite film in the solution process. However, precise control of grain boundaries and surface roughness are better achieved using the vacuum deposition method. Further, vacuum deposited processed better suited for large area devices with reproducible performance.

In the literature, the growth kinetics and scaling properties of several pure organic and some inorganic thin films have been studied [25, 28-31]. However, the detailed analysis of surface roughness, grain size, and growth model of hybrid perovskite $MAPbBr_3$ is not reported yet. Controlling the growth and surface morphology of perovskite film, using the vacuum co-evaporation method possesses several fundamental challenges due to its hybrid nature, the inorganic part ($PbBr_2$) of $MAPbBr_3$ being dominated by strong binding energies. In contrast, the organic part (MABr) is bounded by relatively weak van der Waals forces, and it has higher degrees of freedom than the inorganic counterpart. Owing to the different orientations of organic and inorganic parts of the perovskite, the deposition process does not follow the conventional growth models. The growth kinetics of $MAPbI_3$ film is recently reported by Liu et al [32], however an in-depth analysis of the scaling exponents and its correlation with the structural and optical properties of the film are not explored yet. Further, it is important to understand the effect of molecular-level interaction of perovskite $MAPbBr_3$ molecules with different substrates for its practical applications. Interestingly, the vacuum deposition is an established method and well suited for large-scale fabrication of optoelectronic devices. However, very few studies have addressed the growth kinetics and scaling behavior of vacuum-deposited perovskite thin films and its correlation, if any, to the observed optoelectronic properties of the films. Due to immense technological implications and emerging applications of perovskite thin films, it is imperative to develop a

thorough understanding of the growth kinetics of vacuum-deposited perovskite thin film to optimize the quality of the film and the related device performance.

Here, the growth kinetics of vacuum deposited $MAPbBr_3$ thin film on ITO, and SiO_2 substrates are studied along with the effect of various growth parameters on the structural and optical properties of the film. $MAPbBr_3$ thin film was deposited using a vacuum co-evaporation method at various substrate temperatures (25-100 °C) and various thicknesses (4-120 nm). The variation in surface morphology and statistical behavior of the films as a function of its thickness and growth temperature with film thickness is studied with the help of FESEM and AFM images. The scaling parameters were extracted from the height-height correlation function (HHCF) to develop an insight into the growth pattern on different substrates. Optical absorption, photoluminescence (PL) and time resolved PL (TRPL) analyses were carried out to understand the effect of growth parameters on the optical properties of the films. Low-temperature PL analysis was carried out to evaluate the radiative recombination and non-radiative defects, exciton phonon coupling, and the exciton binding energy of the vacuum deposited $MAPbBr_3$ film. Finally, we have attempted to correlate the growth/scaling parameters with that of the structural and optical characteristics of the films on two different substrates.

2.2. Experimental Procedure

2.2.1. Materials

The starting materials for the present work are methylamine solution (CH_3NH_3, 33 wt% in absolute ethanol, Sigma-Aldrich), lead (II) bromide ($PbBr_2$, 99.999 %, Sigma-Aldrich), hydrobromic acid (HBr, 48 wt% in water, Sigma-Aldrich), N,N-dimethylformamide (DMF, >99 %, Sigma-Aldrich), and diethyl ether (>99 %, Merck).

2.2.2. Synthesis Procedures

2.2.2.1. Synthesis of CH_3NH_3Br

To prepare the CH_3NH_3Br powder, 8 mL of diluted methylamine solution in ethanol was stirred in 250 mL round-bottom flask, and then 3 mL of hydrobromic acid was slowly added in an ice bath with vigorous stirring at 800 rpm for 2 h. Subsequently, the solution was heated at 70 °C for

7 h with continuous stirring to evaporate the solvent. The obtained white CH_3NH_3Br powder was washed several times with ethanol and dried at 60 °C.

2.2.2.2. Deposition of $MAPbBr_3$ Thin Film

$MAPbBr_3$ thin film was thermally evaporated in a high vacuum evaporation chamber (HHV, Bangalore) with a base pressure ~10^{-6} mbar. Before the deposition, the substrates were cleaned sequentially by deionized water, acetone, and 2-propanol with sonication for 15 min each to remove the organic contamination from the substrate. Afterward, the substrates were again rinsed with deionized water followed by heating at ~200 °C and allowed to cool down slowly to room temperature. The substrates were then transferred to the evaporation chamber and placed on a substrate holder. The sublimation temperatures of CH_3NH_3Br and $PbBr_2$ were maintained at 120 ºC and 280 ºC, respectively, and then simultaneously deposited onto the substrates. The substrate holder was placed above the crucible and heated at different temperatures. The substrate holder was rotated at a slow speed (~40 rpm) to enable uniformity of the deposited film. The deposition rate (~0.6 Å/s) was maintained at a very low value to allow enough time for the molecules to interact with the substrate and deposit uniformly, and the film thickness was monitored in-situ using a quartz thickness monitor. $MAPbBr_3$ thin films of various thicknesses (4-120 nm) were deposited for different durations (1, 3.5, 7, 14, 28 and 36 min) and at various substrate temperatures (T_s = 50, 60, 70, 80 and 100 °C).

2.3. Characterization Techniques

The molecular stability of the precursor organic molecule MABr was examined using thermogravimetric analysis (TGA) (NETZSCH) in Ar gas. The surface morphology of the $MAPbBr_3$ thin film was characterized using FESEM (Sigma, Zeiss) and AFM (Cypher, Oxford Instruments) measurements. For the structural characterization, high power X-ray diffractometer (Rigaku RINT 2500 TRAX-III, Cu-Kα radiation) was utilized in powder mode. UV-Vis absorption spectra were recorded using a commercial spectrophotometer (PerkinElmer, Lamda 950). The room temperature steady-state PL spectra of $MAPbBr_3$ film were recorded using a 405 nm diode laser excitation with the help of a commercial fluorometer (Fluoromax-4, Horiba Scientific). Low temperature (80–300 K) PL measurements were carried out using a liquid nitrogen-cooled optical cryostat (Optistat DNV, Oxford Instruments) attached to the above fluorometer and excited with

a 405 nm laser. Time-resolved PL measurements were performed using a 405 nm pulsed laser excitation, with an instrument response time of < 50 ps (LifeSpecII, Edinburgh Instruments).

2.4. Results and Discussions

2.4.1. Molecular Stability and Morphology Studies

Since the structure of the organic component of the perovskite molecule is susceptible to temperature, the molecular stability of MABr and $PbBr_2$ were first characterized by TGA measurement (see **Fig. 2.1**). TGA data show that the MABr and $PbBr_2$ are stable up to ~220 ºC and 500 ºC, respectively. Our optimized sublimation temperatures for MABr and $PbBr_2$ are ~120 ºC and 280 ºC, respectively, which ensures that the molecules are not fragmented or decomposed during the vacuum deposition process.

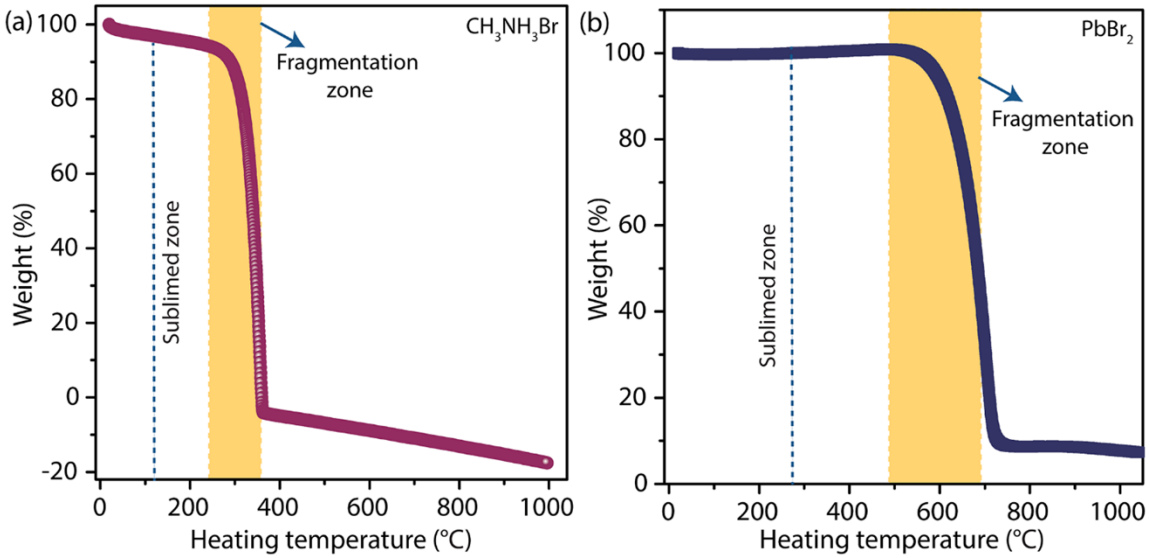

Fig. 2.1. Thermogravimetric analysis plot for (a) CH_3NH_3Br and (b) $PbBr_2$ molecules.

The surface morphology of vacuum deposited $MAPbBr_3$ thin film was first investigated using FESEM imaging. FESEM image of the 20 nm (thickness) perovskite thin film (see **Fig. 2.2(a)**) reveals large grain size and partial/incomplete surface coverage, while the 40 nm thin film shows complete surface coverage, with compact and uniform morphology, without any pinholes (see **Fig. 2.2(b)**). FESEM image of the 120 nm film (**Fig. 2.2(c)**) reveals the presence of larger crystal grains with a complete surface coverage. Note that the substrate temperature was maintained at 50 ºC for these samples.

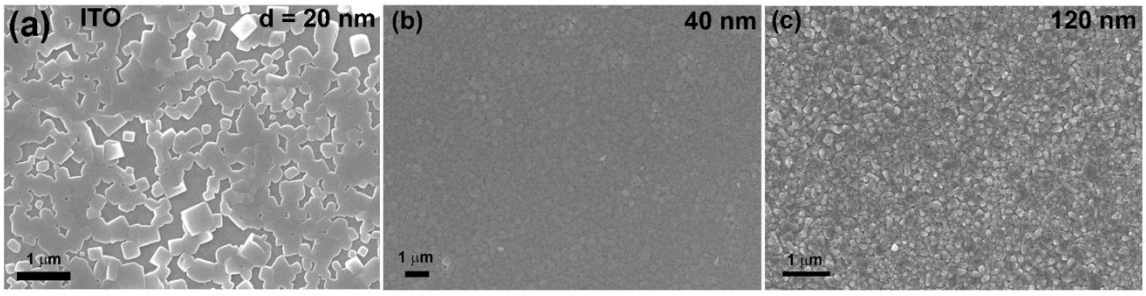

Fig. 2.2. FESEM images of $MAPbBr_3$ films of various thicknesses: (a) 20 nm, (b) 40 nm, and (c) 120 nm on the ITO-glass substrate at 50 ºC.

The surface morphology of the vacuum-deposited film and statistical parameters of the growth kinetics were analyzed by AFM imaging in the tapping mode (size: 512×512 pixel) to avoid any damage to the film. To optimize the growth parameters, we attempted different sublimation temperatures of the precursors, and various substrate temperatures (T_s). The optimized conditions, which provided uniform and compact surface morphology, are adopted for further experiments. AFM topography images of 40 nm $MAPbBr_3$ thin film deposited at room temperature (T_s = 25 ºC) show very abrupt grain features on both the ITO and SiO_2 substrates (**See Fig. 2.3**).

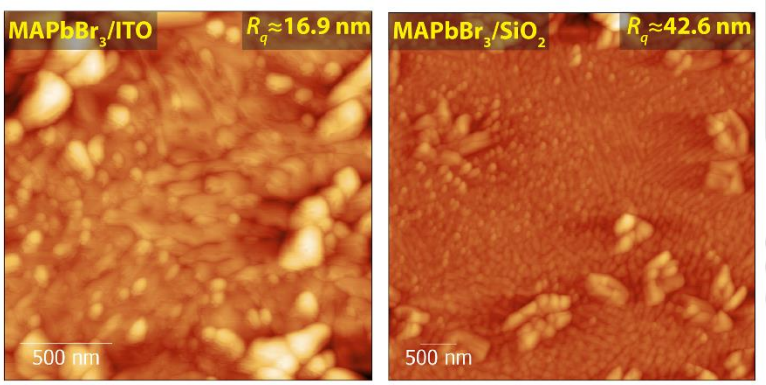

Fig. 2.3. AFM topography images of the perovskite film of 40 nm thickness grown on ITO and SiO_2 without any substrate heating (T_s = 25 ºC).

Therefore, for the stable growth of the film, the substrate temperature was chosen as 50 ºC, which is much less than the molecule desorption temperature. Multiple AFM images/scans were taken at different locations of the film to check the surface morphology, and the typical images are shown in **Fig. 2.4**. AFM topography images (area 2 μm × 2 μm) of the $MAPbBr_3$ thin films of various thicknesses on ITO and SiO_2 substrates deposited at 50 ºC are presented in the upper and lower panels of **Fig. 2.4**. AFM images of the bare ITO and SiO_2 substrates are shown in the first column

of **Fig. 2.4**, indicating an extremely smooth surface for the SiO_2 substrate. When the perovskite film of thickness 4 nm is deposited, large-sized, isolated spherical crystals are observed, which are divergently distributed, resulting in higher surface roughness than the corresponding substrate. As shown by the arrows in **Fig. 2.4**, at the initial stage of the growth (d ~ 4 nm), large number of grains are formed along with small grains before covering the substrate. Here, the molecules follow a hit and stick model at the surface height level since the molecule remains at the position where it was deposited. As the film thickness increases to 10 nm, the isolated grains/crystals grew in number and formed bigger clusters, which are uniformly distributed, and eventually the surface roughness decreases for the film on both the substrates (**Fig. 2.4**). As the film thickness increases

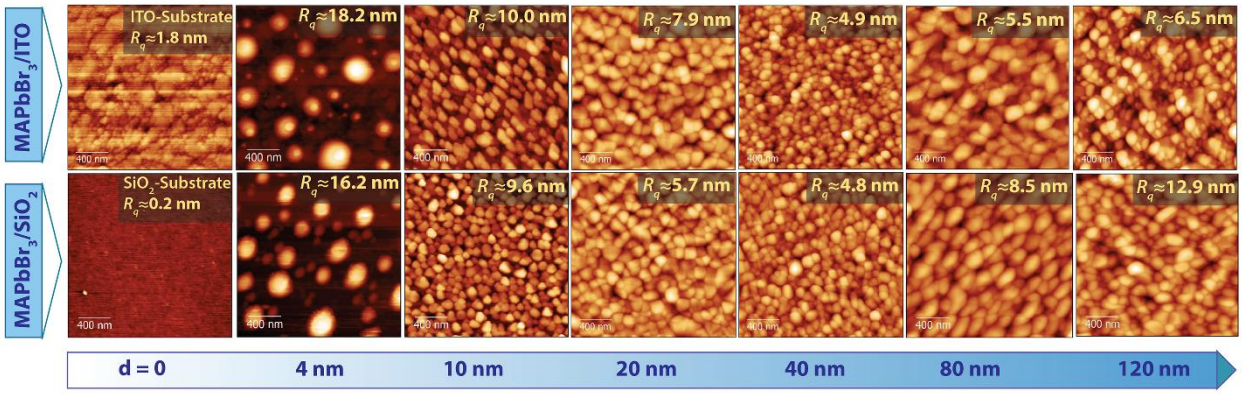

Fig. 2.4. AFM topography images (scan size: 2×2 µm) of bare substrates and perovskite thin film of various thicknesses (d ~ 4 –120) nm on ITO coated glass and SiO_2 substrate, respectively; RMS roughness (R_q) for each film is mentioned in the inset of the corresponding image.

to 20 nm, crystal size is enlarged due to coalescence of the small crystals, which results in higher coverage of the surface with perovskite film consisting of very few open channels. For the 40 nm film, secondary nucleation takes place, resulting in the full coverage of the substrate and reduction in the surface roughness and grain size. With further increase in the film thickness (> 40 nm), the crystallites are no longer spherical, revealing the presence of anisotropy as the clusters agglomerate. In addition, there is an increase in grain size as well as surface height (see **Fig. 2.4**) due to vertical nucleation of the grains. The variation in grain size and RMS roughness of $MAPbBr_3$ film grown on ITO and SiO_2 substrates are shown in **Fig. 2.5(a,b)** revealing quite similar behavior for both the substrates. However, at higher thickness the RMS roughness is much higher for the film grown on SiO_2 substrate as compared to that of ITO substrate, indicating a different growth mechanism for the SiO_2 substrate. More uniform growth of the film on ITO substrates is

observed perhaps due to better accommodation of perovskite molecules on the ITO substrates. Interestingly, we observed the minimum surface roughness and minimum grain size for the film thickness of 40 nm on both the substrates. Therefore, the film thickness of 40 nm is considered optimum here for the growth of smooth and compact film at a substrate temperature of 50 ºC. The effect of substrate temperatures on the growth of perovskite film is studied next for further optimization of the film (40 nm) quality.

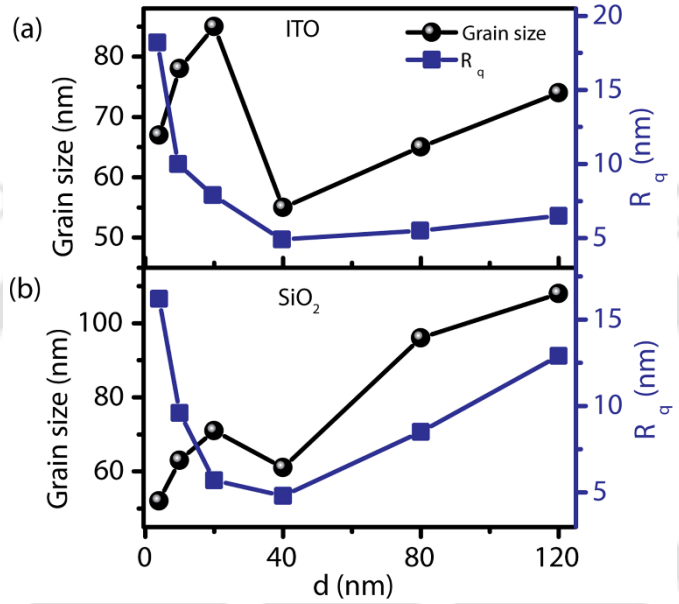

Fig. 2.5. Comparison of grain size and RMS surface roughness of $MAPbBr_3$ films as a function of film thicknesses (d) grown on (a) ITO and (b) SiO_2 substrates.

Topographical AFM images of the optimized perovskite thin film (40 nm) grown on ITO and SiO_2 substrates at various substrate temperatures, T_s = 50 -100 ºC, are shown in **Fig. 2.6**. As the substrate temperature is increased, the crystallite size and RMS surface roughness (R_q) of the films are increased systematically (see **Fig. 2.6**). At T_s = 60 ºC, coalescence of two crystal grains is clearly discernable for the film on ITO substrates, while larger surface roughness (R_q ~9.4 nm) is observed for the film on SiO_2 substrate and it reveals a mound-like growth behavior. In the ITO case, as the substrate temperature is increased from 70 ºC to 80 ºC, the nearly spherical crystallites change its shape to anisotropic and irregular shape, and the grain size is dramatically increased from ~43 nm to ~123 nm. This is probably due to the coalescence of smaller grains to the larger elongated grains through the diffusion process. At T_s = 100 ºC, the presence of small crystallites on large grain feature is noticeable because of the fact that the substrate temperature was close to the MABr

sublimation temperature; so, the thermodynamic driving forces may be dominantly responsible for the overall evolution of the surface morphology (see **Fig. 2.6**). At high substrate temperatures, the crystallite shape changes from spherical to highly anisotropic and surface roughness is largely increased along with large grain size for the film deposited on SiO_2 substrates, indicating the

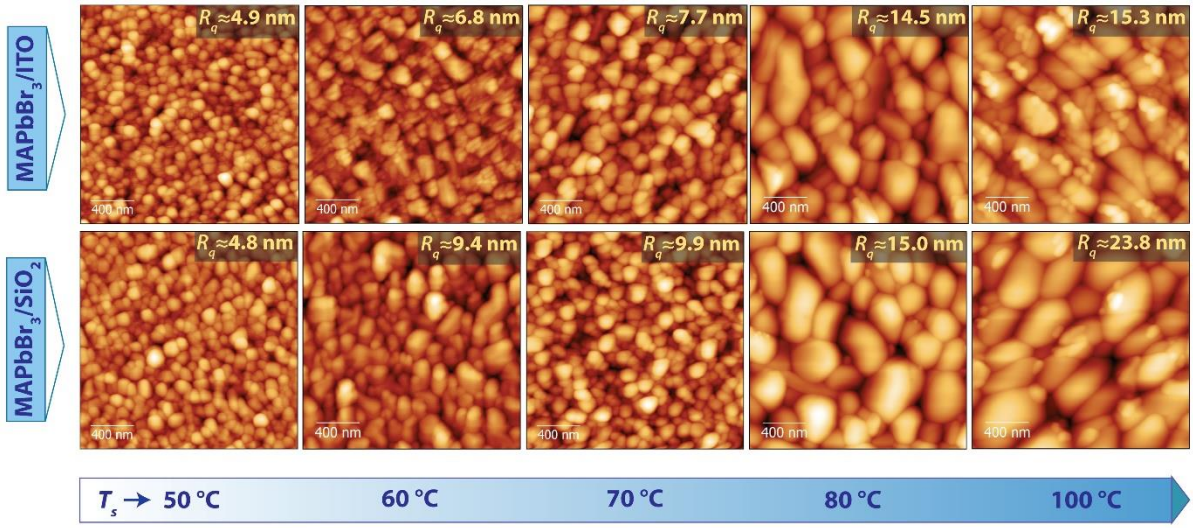

Fig. 2.6. AFM topography images (scan size: 2×2 µm) of optimized perovskite film (40 nm) deposited at various substrate temperatures T_s = 50-100 ºC on ITO coated glass substrate and SiO_2/Si substrate; the corresponding RMS roughness (R_q) is mentioned on the respective images.

predominance of island-like growth. It is clear that with increasing substrate temperature, the grain size and RMS surface roughness increase systematically, as shown in **Fig. 2.7(a,b)**. These results indicate the significant role played by the substrate temperature on the morphological and structural evolution of perovskite film, which are studied here for the first time.

To elucidate the details of the growth kinetics, it is necessary to identify various scaling exponents: roughness (α), growth (β), and dynamic ($1/z$) exponents. The scaling concept considerably simplifies the description of the thin film surface and introduces various aspects of a rough surface. The scaling exponents are calculated from height-height correlation function (HHCF), $g(r)$, which is defined as the statistical average of the mean square of height difference between two surface positions separated by a lateral distance r, is given by, $g(r) = \langle [h(r + r') - h(r')]^2 \rangle$, where, $h(r')$ and $h(r + r')$ are the surface heights at r' and $(r + r')$, respectively. HHCF is extracted from the AFM images taken at different regions by spatial averaging for a distance much larger than r to avoid the edge effects using Gwyddion software [29]. Sinha et al. proposed the functional form of HHCF for the isotropic self-affine surface [33], $g(r) = 2w^2[1 - exp\{-(r/\xi)^{2\alpha}\}]$. Hence, $g(r)$

behaves differently in two different regions depending on the relative magnitude of r and correlation length, ξ: (i) $g(r) \propto r^{2\alpha}$ for, $r \ll \xi$, where α is the roughness exponent $(0 \leq \alpha \leq 1)$ and (ii) $g(r) = 2w^2$ for, $r \gg \xi$, where w is the mean square surface roughness defined by $w = \langle (h - \langle h \rangle)^2 \rangle^{1/2}$. w and ξ depend on the film thickness (d) and vary according to the power-law: $w \propto d^{\beta}$ and $\xi \propto d^{1/z}$, where β and $1/z$ are the growth and dynamic scaling exponents, respectively [29]. **Fig. 2.8(a,b)** show a comparison of the HHCF in the log-log scale for $MAPbBr_3$ film of various thicknesses (d = 4-120 nm) grown on the ITO and SiO_2 substrates, respectively. It is

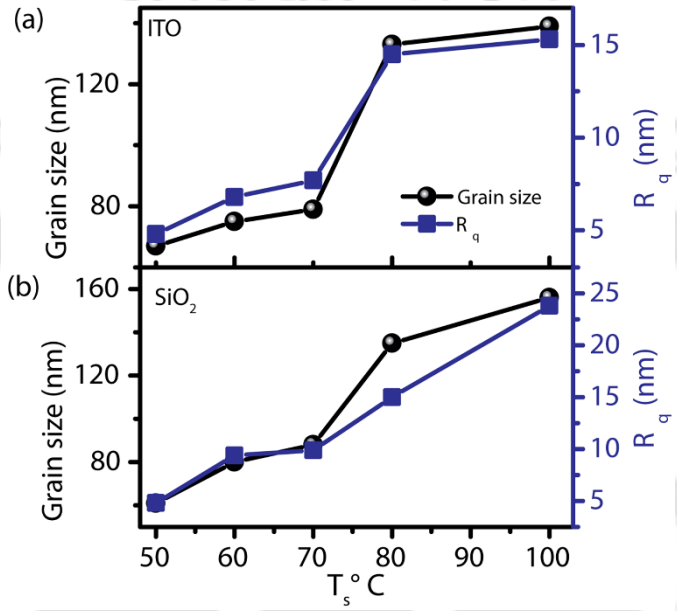

Fig. 2.7. Comparison of grain size and RMS surface roughness of optimized perovskite films grown on (a) ITO and (b) SiO_2 substrates as a function of substrate temperature (T_s).

evident that the HHCF, *g(r)*, is significantly increased after the deposition of the film on both the substrates. At low thickness, before the formation of continuous film, *g(r)* value is high, and with increasing film thickness *g(r)* values systematically goes down until d = 40 nm, and afterward, it again shifts upward with increasing thickness, as revealed from **Fig. 2.8(a,b)**. Thus, at the initial stages of the growth, *g(r)* displays an anomalous behavior for both the substrates, since in general, the HHCF shifts upward with increasing thickness for other organic materials [29]. **Fig. 2.8(c,d)** show the variation in HHCF as a function of the substrate temperature (T_s = 50-100 ºC) for the optimized film (d=40 nm) on ITO and SiO_2 substrates, respectively. On both the substrates, the *g(r)* value of the film (40 nm) shifts upward with the increase in substrate temperature. As discussed above, the HHCF increases linearly for small r and saturates at larger r following the

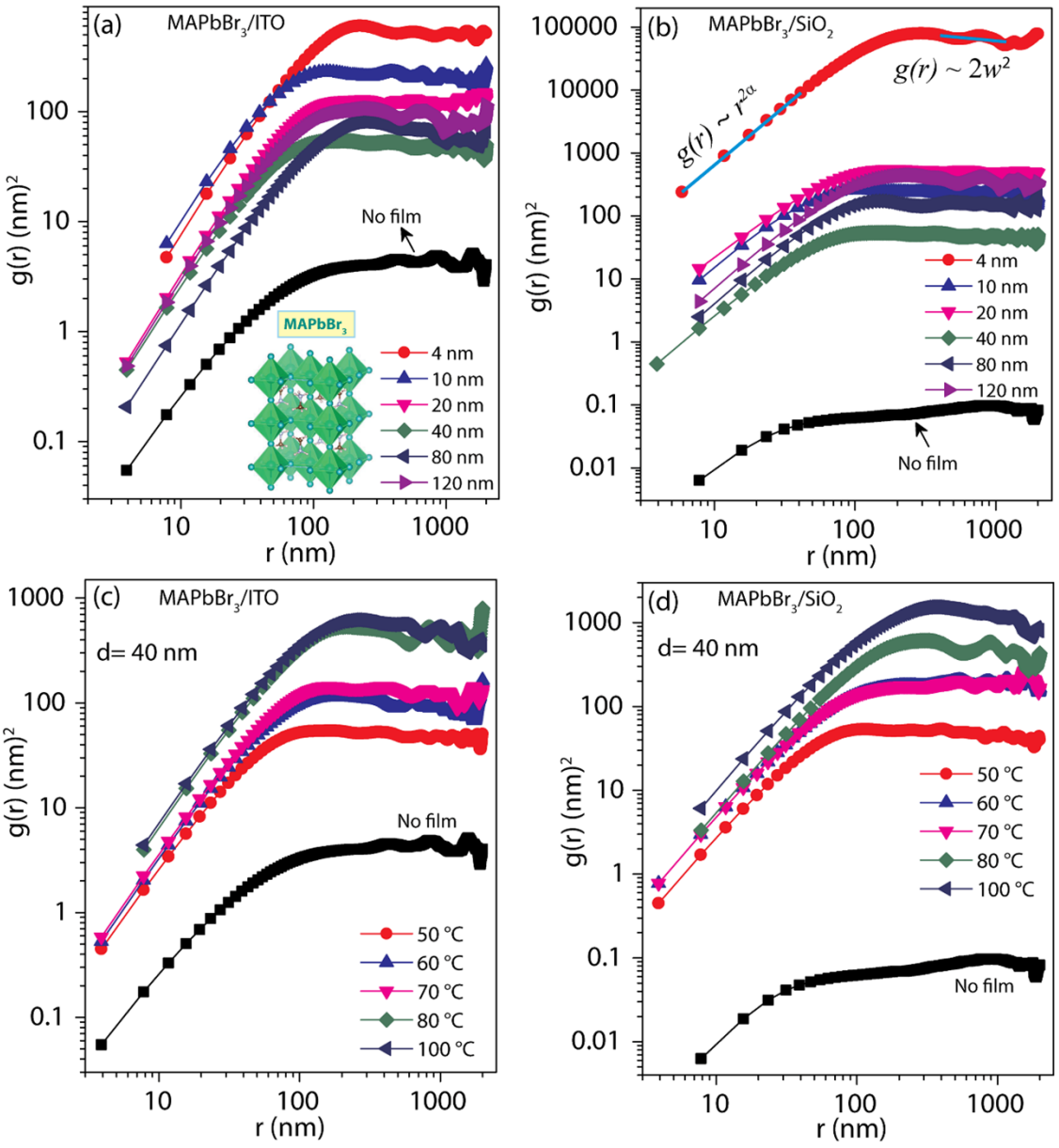

Fig. 2.8. HHCF *g(r)* as a function of distance *r* for $MAPbBr_3$ thin films on (a) ITO and (b) SiO_2 substrate with various film thicknesses. HHCF *g(r)* as a function of distance *r* for optimized $MAPbBr_3$ thin film (40 nm) at various substrate temperatures on (c) ITO and (d) SiO_2 substrate.

asymptotic behavior. Roughness exponent, α, is calculated from the linear fitting of the *g(r)* vs. *r* plot in the linear region, and RMS roughness, *w*, is calculated from the intercept at the higher *r* region. The behavior of HHCF as a function of film thickness suggests two different growth modes for the films: (a) an anomalous growth mode before full coverage of the substrate (i.e. at $d < 40$ nm), and (b) a stable growth mode after the formation of the compact film (at $d \geq 40$ nm). **Fig. 2.9(a)** shows the variation of roughness exponent, α, with the film thickness on ITO and SiO_2

substrates. The value of α varies largely in the anomalous growth region, and it is nearly constant in the stable growth region. The average value of α in the stable growth region is 0.90 and 0.91 for the film grown on ITO and SiO_2 substrates, respectively (see **Fig. 2.9(a)**). At higher substrate temperature, the average roughness exponent, α, is found to be 0.93 for the film grown on ITO and SiO_2 substrates (see **Fig. 2.9(b)**). **Fig. 2.9(c)** shows the schematic representation of the local

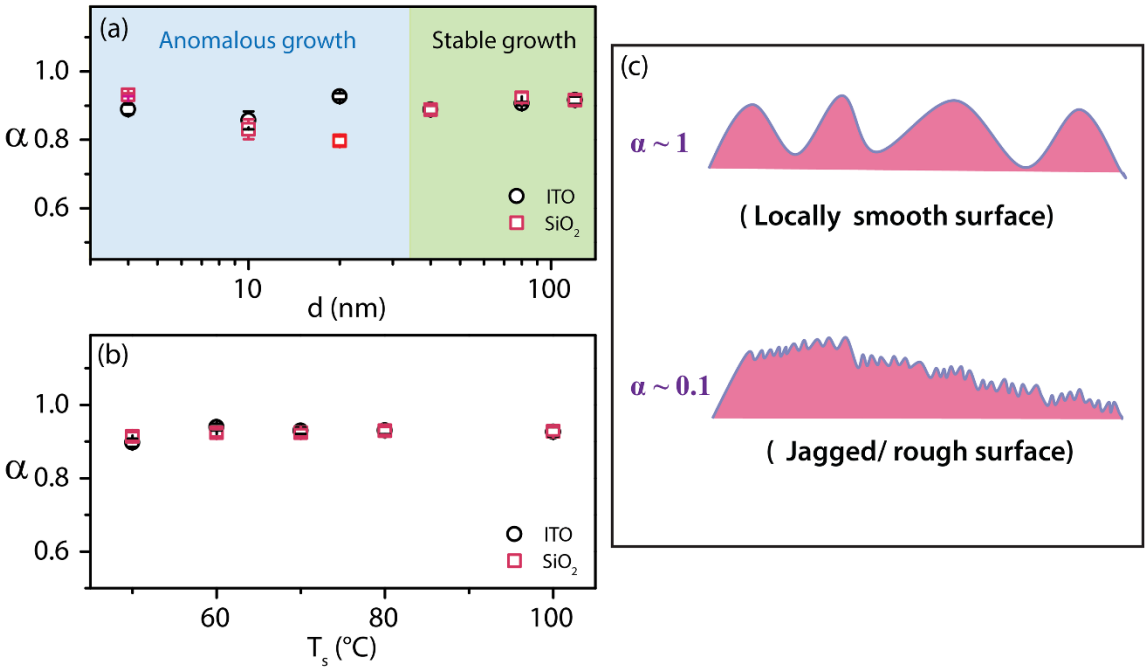

Fig. 2.9. Roughness exponent, α, as a function of $MAPbBr_3$ film (a) thickness, d and (b) substrate temperature, T_s. (c) Schematic of film surface morphology for different values of roughness exponent (α).

surface of the film for the low and high values of α. Note that α represents the short-range roughness/surface-irregularity of self-affine surface; a near-unity roughness exponent corresponds to a locally smooth film. In the present case, the value of α is found to be close to unity signifying a locally smooth surface. **Fig. 2.10(a)** shows the variation of RMS roughness, w, as a function of the thickness of the film grown on ITO and SiO_2 substrates. At the initial stage of the growth, an anomalous behavior is observed with scaling exponent, $\beta<0$ followed by crossover to $\beta>0$, and this kind of behavior is reported for rubrene molecule[30]. Since the scaling behavior is unstable in lower thickness region, the linear fit for w vs. d plot applies to the higher thickness region ($d \geq 40$ nm), and the growth exponent, β is calculated from the slope showing the distinct values of β as 0.21 ± 0.01 and 0.90 ± 0.05 for the film grown on ITO and SiO_2 substrates, respectively. Interestingly, larger value of β for the film on SiO_2 substrate as compared to that on ITO substrate

signifies large step-edge barrier or Ehrlich-Schwöbel barrier (E_{ES}), which restricts the molecules to diffuse over the nearest step and favors the growth on the same step resulting into the island-like growth, as revealed from the AFM images [29, 34]. High β (> 1/2) value is often associated with rapid roughening behavior [34], as seen in the AFM images for the film on SiO_2 substrates. In the random deposition (RD) limit, $w_{RD} \sim D\sqrt{d/D}$, is expected to give an upper limit on w [35], where D is the molecular size, here ~11.913203 Å (lattice constant of $MAPBr_3$ along c-direction, as most of the molecules are adsorbed vertically on the SiO_2 substrate), and d is the film thickness. We found β>1/2 (here, β ~ 0.71 for d = 40 nm; $w \sim d^{\beta}$), which is consistent with the earlier calculated value (β>1/2 from HHCF analysis). This limit is attained if every particle stayed on the surface height where it was deposited [36]. In our case, the rapid roughening occurs probably due to the transportation of matter to the higher layers which is acquired from thermodynamic driving force (as, e.g., substrate temperature T_S = 50 °C and slow deposition process), and this kind of rapid roughening is reported for other organic molecules [36].

The growth exponent (β) and roughness exponent (α) generally reveal the vertical features of the surface, but it does not provide any information about the lateral correlation between two surface heights separated by r. To gain an insight into the lateral features, the lateral correlation length (ξ) is calculated from the autocorrelation function ($R(r)$) which is extracted from the AFM images using Gwyddion software. ξ measures the correlation of surface heights separated laterally by r and is defined as the value of r, at which autocorrelation function decreases to $1/e$ th of its original value, i.e., $R(\xi) \equiv 1/e$. ξ denotes a representative lateral dimension of a rough surface and the two points are considered to be correlated if the distance between two surface points is within ξ. Hence, the auto-correlation function $R(r)$ is an important characteristic function to describe the surface morphology of thin film, as different rough surfaces may have different autocorrelation functions. Correlation length is calculated from autocorrelation function and it is plotted as a function of the film thickness in **Fig. 2.10(b)**. The ξ vs d plot is fitted with a straight line in the stable growth region to obtain the dynamic exponent ($1/z$). Dynamic exponent, $1/z$, is found to be 0.32 ± 0.03 and 0.44 ± 0.01 for the films deposited on ITO and SiO_2 substrates, respectively. Note that the scaling exponents are not fully independent; these are generally connected by the given relation: $\beta/\alpha \cong 1/z$ [37-40]. In the present case, β/α (ITO) = $1/z$ - 0.09 and β/α (SiO_2) = $1/z$ + 0.55, indicating a pronounced deviation from the scaling law for the SiO_2 case.

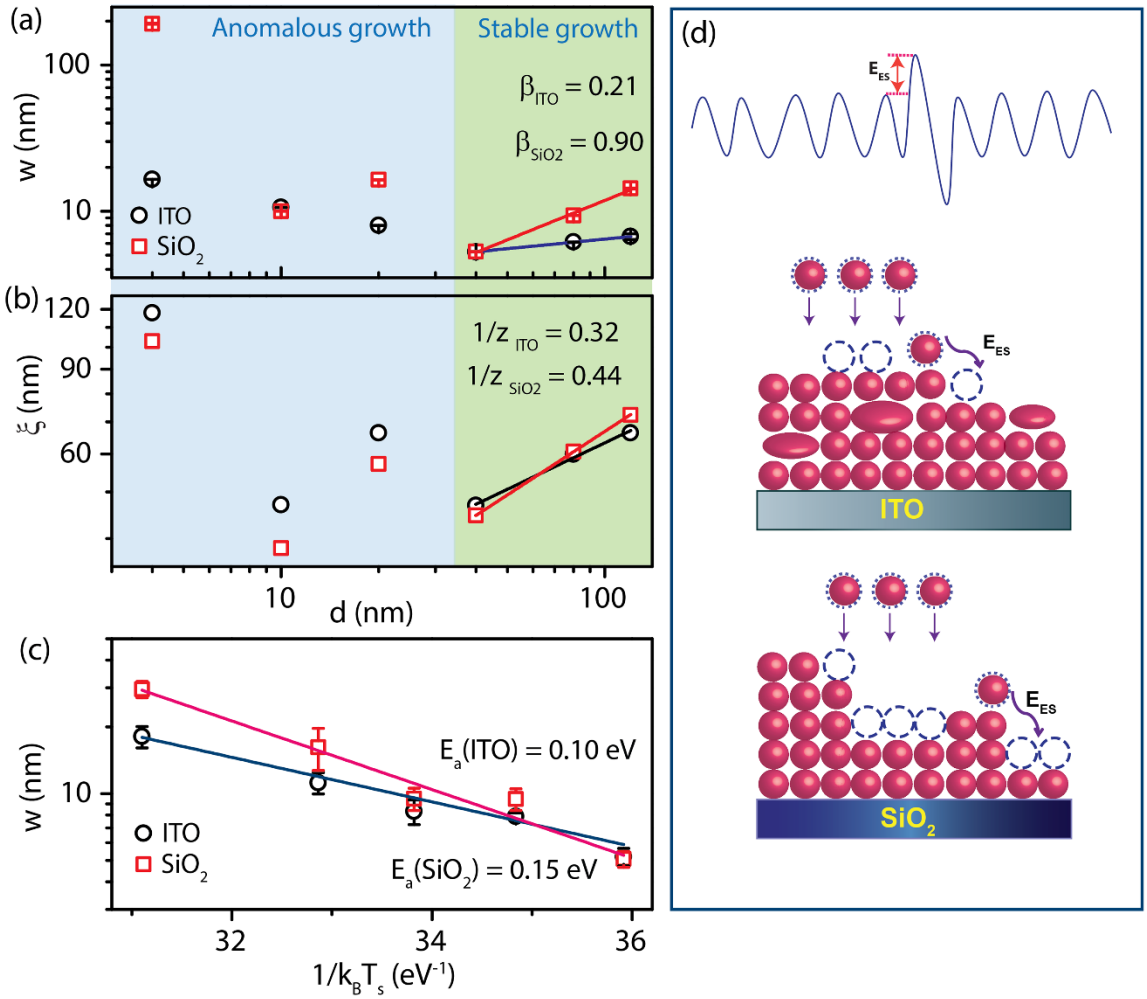

Fig. 2.10. (a) RMS roughness, *w*, and (b) correlation length, ξ, as a function of perovskite film thickness on various substrates. (c) RMS roughness, *w*, as a function of substrate temperatures for the optimized film thickness (40 nm) grown on ITO and SiO_2 substrates. The symbols in each figure correspond to the experimental data, and the solid line signifies the fitted data. (d) Schematic of the growth models for the perovskite thin films on ITO and SiO_2 substrates. E_{ES} represents the Ehrlich-Schwöbel barrier energy.

It has been reported that in the case of vertical growth of molecules [34], deviation from the scaling law is prominent. To understand the origin of the roughening during the growth, we have deposited the perovskite thin film at different substrate temperatures, which enables the calculation of molecular activation energy. As shown in **Fig. 2.10(c)**, with the increase in substrate temperature T_s, the RMS roughness (w) amplitude increases, and it closely follows an Arrhenius behavior given by $w \propto exp(-E_a/k_BT_s)$, where E_a and k_B are the activation energy and Boltzmann constant, respectively. The activation energy of the molecule is often associated with rotational and translational barriers of the molecular diffusion. Hence, it is essential to gain the knowledge about the activation energy to engineer the performance of various optoelectronic devices. The activation

energies calculated from the fitted parameters for the *ln(w)* vs $1/k_BT_s$ plot for the films grown on ITO and SiO_2 substrates are found to be 0.10 ± 0.01 eV and 0.15±0.01 eV, respectively, as shown in **Fig. 2.10(c)**. The values of various scaling exponents are tabulated in **Table 2.1**. A comparison of various scaling exponents calculated in the present case with the earlier reported values of different organic and inorganic films is presented in **Table 2.2**. Interestingly, the activation energy of the perovskite film on the ITO substrate (0.10 eV) is lower than that of the SiO_2 substrate (0.15

Table 2.1. *Details of the scaling exponents of the $CH_3NH_3PbBr_3$ thin film on different substrates. d and T_s correspond to the thickness and substrate temperature.*

Film	Substrate	Roughness exponent, <α>		Growth exponent, β	Dynamic scaling exponent, 1/z	Activation energy, E_a (eV)
		d variation	T_s variation			
$MAPbBr_3$	ITO	0.90	0.93	0.22	0.32	0.10
	SiO_2	0.91	0.93	0.90	0.44	0.15

Table 2.2. *A summary of experimentally determined scaling exponents and activation energy (E_a) for the perovskite thin films and several organic and inorganic thin films reported in the literature.*

Thin film/ Substrate	β	1/z	E_a (eV)	Ref
$MAPbBr_3$/ITO	0.22	0.32	0.10	This work
$MAPbBr_3/SiO_2$	0.90	0.44	0.15	This work
Oligomer/Si	0.28	0.31	0.37	[25, 31]
ZnO/glass	0.53	-	-	[28]
$SnCl_2Pc$/Si	0.21	0.12	-	[29]
$SnCl_2Pc$/glass	0.48	0.26	-	
$MAPbI_3$/Si	0.79	0.78	-	[32]
PTCDA/glass	0.54	0.25	-	[34]

eV), which implies an easier diffusion of molecules in case of ITO substrate. Higher activation energy or a large step-edge barrier for the film on SiO_2 substrate indicates that the perovskite molecules cannot diffuse easily to the adjacent layer/ island, i.e., lateral diffusion is less probable

giving rise to 3D island-like growth on SiO_2 substrate (See **Fig. 2.10(d)**). In contrast, the film on the ITO substrate prefers to diffuse to lower layer and grow side by side resulting in the smoother film at higher thickness. Therefore, the higher values of β and E_a in case of SiO_2 suggest a large step-edge barrier preventing new molecules from diffusing to a lower layer, which leads to the upward growth of the film on the SiO_2 substrate and, as a consequence, the surface roughness of $MAPbBr_3$ is very high [34]. However, the barrier height is relatively lower in case of ITO substrate, which allows the new molecules to diffuse to the next lower level after looking for more energetically favorable positions resulting in very uniform and homogeneous growth of the film (see **Fig. 2.10(d)**).

Note that we have observed a dramatic change in the surface morphology of $MAPBr_3$ film above d> 20 nm. It is highly inhomogeneous at d ~ 4 nm with large grains (bright spots in **Fig. 2.1**) in between small grains and high surface height (~ 500 nm), while at d ~ 40 nm, uniform grains with low surface height (~ 25 nm) are observed. Note that at higher thickness (e.g., d=120 nm), the RMS roughness is considerably higher in case of SiO_2 substrate than that of ITO substrate. One plausible explanation for the transition in morphology at higher thickness/deposition time is as follows. At low thicknesses (d < 40 nm), $MAPBr_3$ molecules remain on the surface height level where it was initially deposited. Here shadowing effect is negligible, since the substrate holder was rotated during the deposition. On the other hand, at higher thickness ($d \geq 40$ nm), reemission of molecules as well as diffusion of molecules might occur from large surface height, and at the same time, smaller grains may effectively increase their surface height due to the incoming flux of large number of molecules. Next, coalescence may occur between two adjacent grains and thus the roughness is low at higher thickness. However, in case of SiO_2, due to large activation barrier, diffusion of molecules is not pronounced and hence RMS roughness is not as low as that of ITO substrate. Another possible mechanism that may contribute to the surface roughness is the dissociation of the molecules at higher substrate temperature. The large grains (lateral size ≈ 312 nm), which was observed at d ~ 4 nm, might dissociate into smaller grains (lateral size ≈ 200 nm) at higher thickness/ deposition time ($d \geq 40$ nm) due to high thermal mass (high temperatures of the molecules due to the thermal energy gained during the sublimation process) and the substrate at elevated temperature. After dissociation, grains may become thermodynamically more stable and relaxed; consequently, the overall morphology is uniform at higher thickness. Further, due to the difference in temperature between the sublimed molecules and the substrate (at relatively lower

temperature), lattice strain is introduced in the films (as indicated from the XRD analysis). Also, the evolution of surface roughness with thickness may be partly related to the change in conformational degrees of freedom of the molecules[30]. At the higher thickness, the molecules orient their direction to strongly interacting planar molecules which triggered the smoothness of the film[30].

2.4.2. Structural Analysis

With the above understanding of growth kinetics of the film on two different substrates, it would be interesting to correlate the growth behavior with its crystal structure. The structural quality of the vacuum deposited $MAPbBr_3$ film at different stages of growth is evaluated from the XRD analysis. **Fig. 2.11(a)** shows a comparison of the XRD pattern for different thicknesses of the films grown on ITO substrate. Even at low thickness (~ 4 nm), the XRD pattern reveals a highly crystalline film on the ITO substrate as compared to that of the SiO_2 case. Note that the intense XRD peak at 35.30º is related to ITO substrate and its intensity decreases with the increase in deposition time/film thickness due to the complete coverage of the substrates with perovskite film. The intensity of perovskite (100) diffraction peak at 14.97° is the highest for the film thickness of 40 nm on ITO. A closer look at the XRD peak for (100) plane reveals a systematic shift towards higher 2θ angle with increasing thickness of the film (see **Fig. 2.11(a)**). As film thickness increased from 4 nm to 120 nm, the 2θ value increases by ~ 0.11º, implying a decrease in interplanar spacing with increasing thickness. It is evident that as the film thickness increases, the crystal lattice spacing decreases, which may affect the bandgap of the film (discussed later). The XRD patterns of perovskite film as a function of thickness on the SiO_2 substrates are shown in **Fig. 2.11(b)**. Only (100) diffraction peak is observed at 14.97º for the 4 nm film on SiO_2 substrates indicating growth of the molecules primarily along the (100) direction. At higher thickness, along with highly intense (100) diffraction peak, (200) and (210) diffraction peaks are also observed at 30.20º and 33.90º, respectively. Note that the XRD pattern of the films grown on SiO_2 substrate reveals the presence of (100), (200) and a slight trace of (210) diffraction peaks, while the film grown on ITO substrates is relatively smoother as compared to SiO_2, and it shows multiple diffraction peaks, which is consistent with the lower β value, and lower activation energy for the ITO substrate. As discussed earlier, higher β value for SiO_2 case implies a higher step-edge barrier leading to the island like growth and steepness of the perovskite crystallites. The presence of (200)

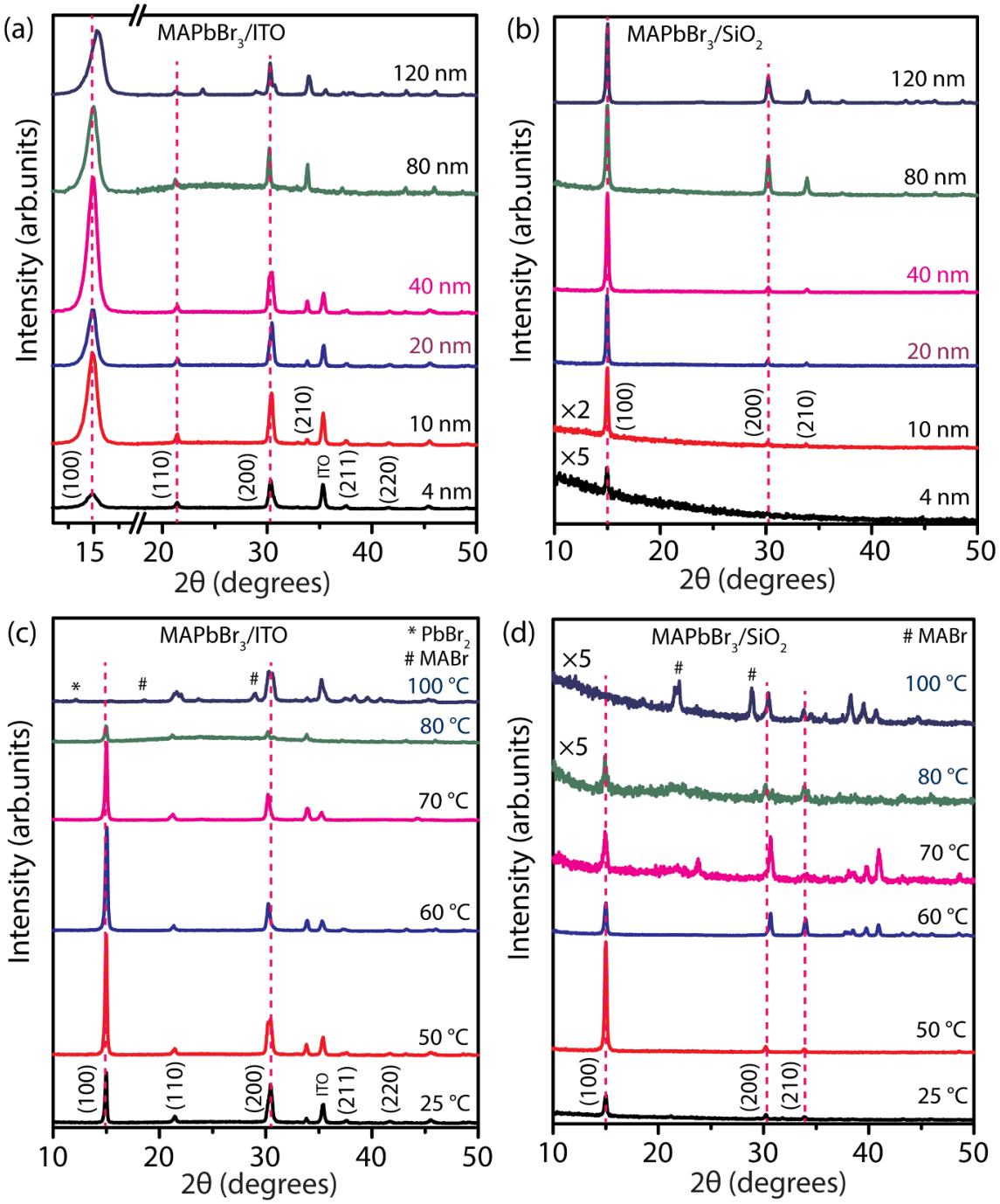

Fig. 2.11. (a, b) Comparison of the XRD pattern of perovskite film of various thicknesses on ITO and SiO_2 substrates, respectively. (c,d) Comparison of the XRD pattern of $MAPbBr_3$ film of an optimized thickness (40 nm) grown at various substrate temperatures on ITO and SiO_2 substrates, respectively.

and (210) peaks for the higher thickness of the film on SiO_2 indicates mound plus layer type growth. At higher thickness, the intermolecular interaction increases due to the presence of excess molecules and some molecules could overcome the step-edge/potential barrier to reach the lower

steps. At lower thicknesses, perovskite film prefers to grow along the upward direction instead of the lateral direction on the SiO_2 substrate. However, the molecular plane of $MAPbBr_3$ is oriented parallel to the ITO substrates, which maximizes the intermolecular interactions in a direction normal to the surface [34]. This configuration allows the freshly deposited molecules to overcome the step-edge barrier, and molecules could diffuse to the energetically favorable adjacent lower layer resulting in a layered configuration and a relatively smooth morphology. Our results for the perovskite film on ITO substrates show better crystallinity due to more stable molecular configuration. **Fig. 2.11(c)** shows the effect of substrate temperature (T_s) on the XRD pattern of the 40 nm (optimized) perovskite film on the ITO substrate. As the T_s increases, the intensity of the principal peak (100) decreases systematically, and at T_s = 100 ºC, the peak disappears completely, while the peaks related to perovskite precursors and ITO substrate appear in the XRD pattern. This is likely to be caused by the partial degradation/desorption of the perovskite molecule at high substrate temperature. Substrate temperature (T_s) dependence of the film crystallinity on the SiO_2 substrate is shown in **Fig. 2.11(d)** showing nearly identical behavior as that of the ITO case, except the relatively lower intensity of the XRD peaks in SiO_2 case. Our results show that high crystallinity and smooth surface of the perovskite film is obtained for the ITO substrate at T_s = 50 ºC and d = 40 nm, which are considered as optimum for the device quality film.

2.4.3. Optical Analysis

The effect of film thickness on the optical properties of the $MAPbBr_3$ film was studied through optical absorption and emission spectra. UV-Vis absorption spectra of perovskite films of various thicknesses are shown in **Fig. 2.12(a)** revealing a systematic blue shift in the absorption edge with the increase in thickness. The excitonic absorption peak at the absorption edge is observed for the films at room temperature, which is the characteristics of a strong excitonic transition. The bandgap of the vacuum-deposited film was obtained from the corresponding Tauc plot. **Fig. 2.12(b)** shows the comparison of the Tauc plot of $MAPbBr_3$ film of thicknesses 10, 40, and 120 nm calculated from corresponding absorption spectra. As the film thickness decreases, we observed a systematic blue shift of the absorption edge, perhaps related to the lattice distortion. The Tauc plot reveals the bandgap of 2.29, 2.25 and 2.24 eV for the films of thickness 10, 40, and 120 nm, respectively. The slopes of the Tauc Plot corresponding to thickness 10 nm, 40 nm and 120 nm are 10.14, 5.43 and 10.45. Weaker slope or weaker Urbach tail in 40 nm thick film implies

the presence of less disordered state. 40 nm film shows uniform and pin-hole free film which supports the weaker slope in Tauc plot. Lower and higher thickness film exhibit anisotropy and irregularity. The PL emission spectra of the films were recorded with the 405 nm laser excitation.

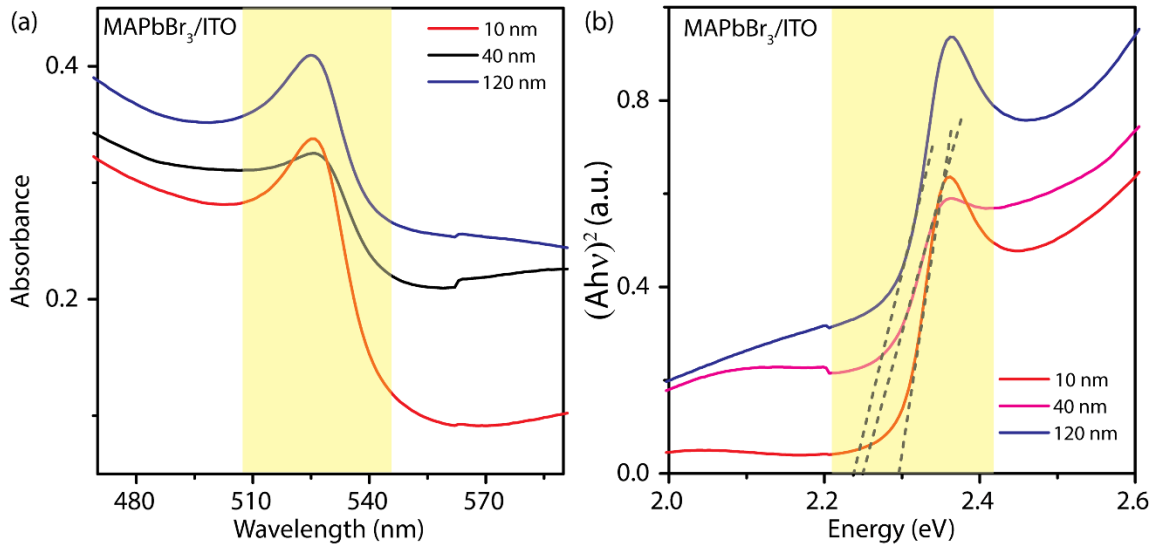

Fig. 2.12. (a) Absorption spectra and the corresponding (b) tauc plot of perovskite films grown on ITO with various thicknesses.

A comparison of the normalized PL spectra (normalized to 1) of $MAPbBr_3$ films is shown in **Fig. 2.13(a)** revealing a systematic blue shift (15 nm) in peak position with decreasing film thickness. The observed emission peaks are at 525, 530, 530, 532, 533, and 540 nm for the film thicknesses 4, 10, 20, 40, 80, and 120 nm, respectively. Inset of **Fig. 2.13(a)** shows the change in PL peak intensity with film thickness (calculated at the corresponding PL peak value and normalized with the film thickness) revealing the highest PL intensity for 10 nm film, and the PL intensity reduces at higher thickness possibly due to the presence of nonradiative recombination centers. Note that the large blue shift in the PL peak with the change in thickness from 120 nm to 80 nm cannot be explained through the quantum size effect. The blue shift can be explained from the change in the lattice constant of the perovskite crystallites in the film. Interestingly, we find a clear correlation among the film thickness, interplanar spacing, and the PL peak shift, as shown in **Fig. 2.13(b)**. It is evident that as the film thickness increases, the crystal lattice spacing decreases (inset of **Fig. 2.13(b)**), and correspondingly the bandgap decreases. For conventional semiconductors, the bandgap is inversely proportional to the interplanar spacing [41]. In general, decrease in interplanar spacing leads to the stronger binding force between valence electrons with the core atoms, and as

a result, the valence electrons move to the lower levels which in turn, increases the energy gap between the conduction and valence band. However, in the case of perovskite semiconductor, the bandgap increases as the interplanar spacing increases. The bandgap of perovskite is primarily determined by the bonding between the metal (Pb cation), and the halide (Br anion), which form the [$PbBr_6$] octahedral structure [42-44]. The valence band maximum (VBM) is determined by

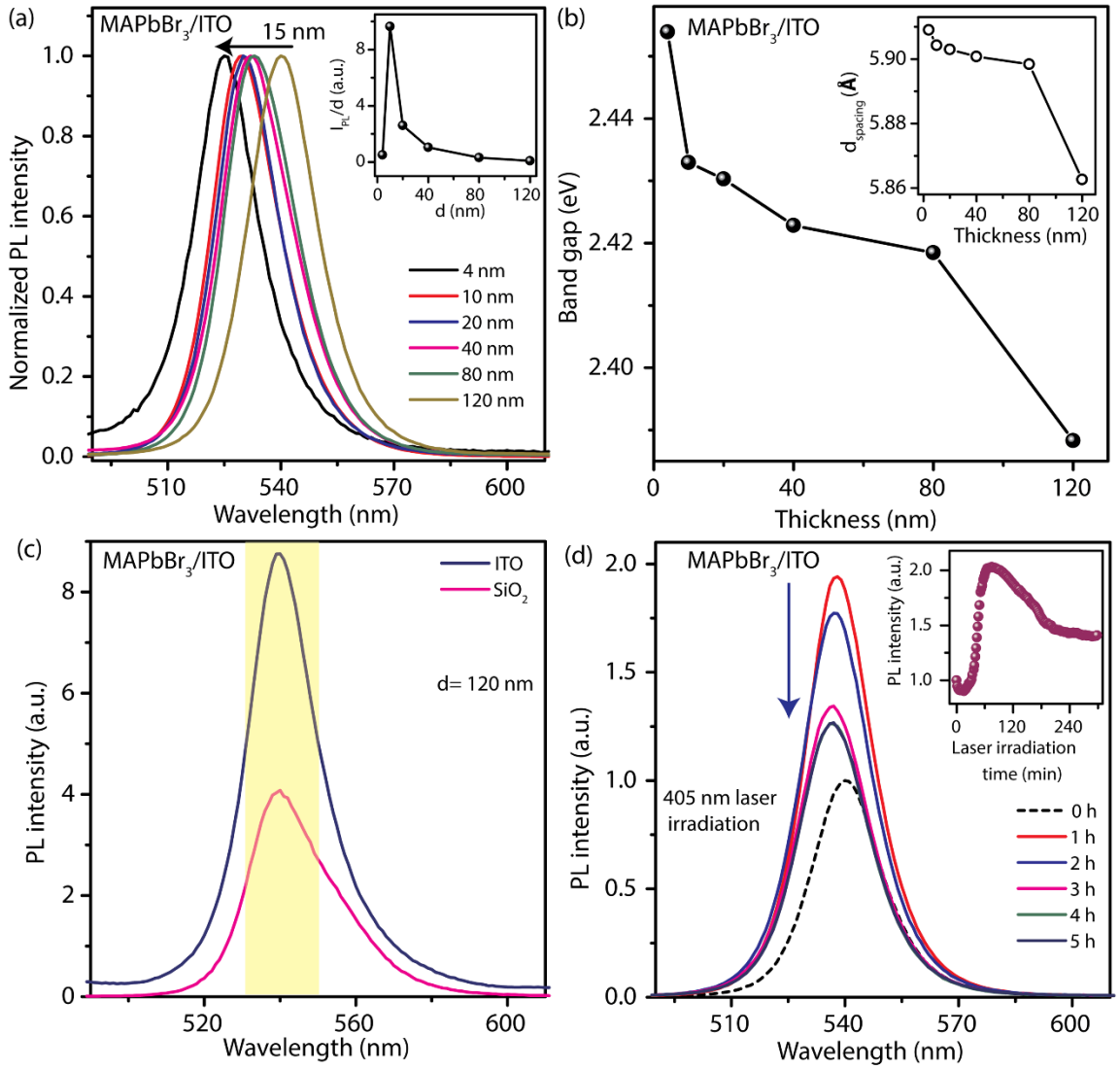

Fig. 2.13. (a) Normalized PL spectra of perovskite film with different thicknesses on the ITO substrate; the inset shows the variation of PL intensity with film thickness where PL intensity (I_{PL}) is normalized by the thickness (d) of the film. (b) Change in bandgap with the thickness of perovskite film; the inset shows change in (100) interplanar spacing ($d_{spacing}$) with thickness. (c) Comparison of PL spectra of the perovskite film (120 nm) grown on ITO and SiO_2 substrates. (d) Temporal change in PL spectra of $MAPbBr_3$ film (120 nm) on ITO substrate recorded at specific intervals under continuous laser illumination (405 nm, 15 mW); the inset shows the change in PL intensity as a function of time under continuous laser illumination.

antibonding hybrid states of the halide *p* and metal *s* orbitals, while the conduction band minimum (CBM) is affected by a hybrid of metal *p* and halide *p* orbitals and bonding between *s* and *d* states of Pb [42, 43]. The conduction band is mostly comprised of a nonbonding hybrid of Pb and Br atoms, which makes it less affected by any structural distortion [43]. However, VBM is extremely sensitive to lattice distortion; any change in the lattice structure of the perovskite increases the Pb-Br overlap, which destabilizes the VBM and increases the bandgap [43]. It is reported that the bandgap isotopically increases as the interplanar spacing increases due to the shift in VBM to the higher energy levels [43, 45]. Taking advantage of this behavior, the bandgap of perovskite can be easily tuned from 1.5 to 3 eV by changing the halide compositions from I to Cl via Br [46]. Thus, the blue shift in the PL peak at lower thickness is ascribed to the decrease in the lattice constant of the perovskite crystals.

Next, we discuss the substrate-dependent intensity of the PL spectra, as shown in **Fig. 2.13(c)**. For the film thickness of 120 nm, PL intensity is ~2.2 times stronger for ITO substrate than that of SiO_2 substrate. As revealed from the growth kinetics analysis, the film on ITO favors uniform and compact growth due to lower step-edge barrier (0.1 eV), and the molecular orientation favors the growth of the film with high structural and optical quality than that of SiO_2. Since the molecules could easily move towards lower levels on the ITO substrate, it leads to the formation of more compact film comprising fewer pinholes and low trap states, resulting in higher PL intensity. The optical stability of the perovskite film (120 nm) on the ITO substrate is examined under continuous irradiation of 405 nm laser, and the PL spectra were recorded at regular intervals, and results are shown in **Fig. 2.13(d)**. During the first 1 hr, the PL peak intensity (measured at 540 nm) increases by ~100 % due to laser exposure and afterward the intensity decreases and finally it reaches a plateau with intensity higher than the initial value (see the inset of **Fig. 2.13(d)**). The initial increase in PL intensity is believed to be caused by laser-induced heating and defect healing. Improved optical performance under prolonged laser exposure has been reported [47, 48]. Prolonged laser exposure is stated to cause local heating, which in turn reduces the defect concentration resulting in higher PL emission [47, 49]. Thus, the vacuum-deposited perovskite thin films are highly stable under UV laser exposure, which is significant for their practical application.

Low-temperature PL measurement was conducted in the temperature range 80-300 K at an interval of 10 K, to assess the contribution of radiative and nonradiative processes, and the results are shown in **Fig. 2.14(a)**. The inset of **Fig. 2.14(a)** shows the PL intensity count as a function of temperature for the sample with film thickness 120 nm. Note that higher thickness samples showed lower intensity of PL due to the contribution of nonradiative channels. As the temperature decreases from 300 to 80 K, integrated PL intensity systematically increases by a factor of ~682, due to the reduced thermal quenching and the suppression of the nonradiative processes at low

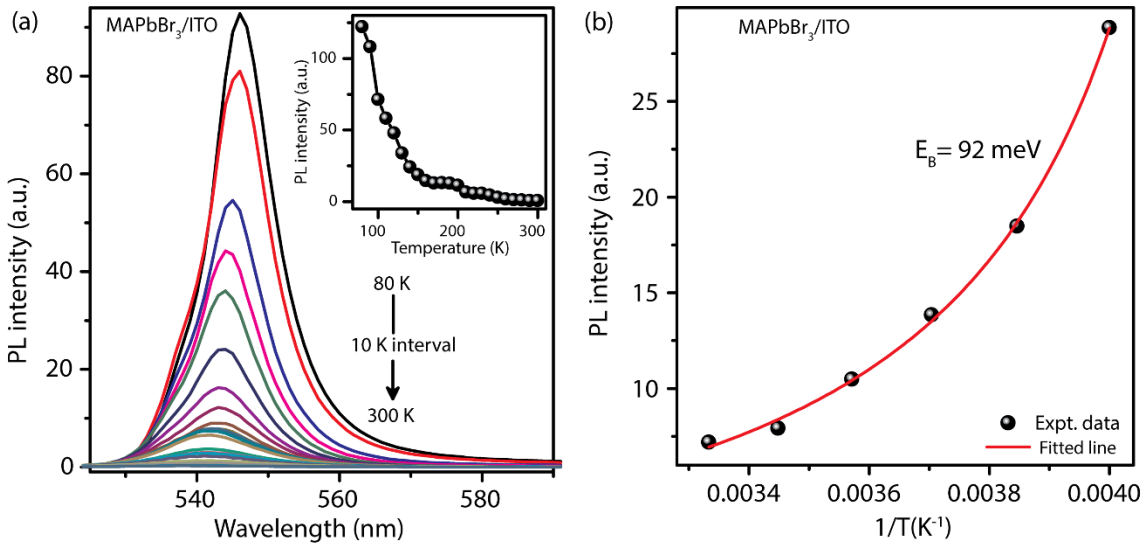

Fig. 2.14. (a) Temperature-dependent PL spectra of perovskite film (120 nm) in the temperature range 80 - 300 K; the inset shows the temperature dependence of PL intensity. (b) Integrated PL intensity vs. inverse of the temperature for 120 nm perovskite film. The experimental data are fitted with the modified Arrhenius equation.

temperatures. Since the PL emission is quite stable and intense near room temperature, the exciton binding energy can be calculated from the temperature-dependent intensity of the spectra. **Fig. 2.14(b)** shows the variation in PL intensity with inverse of temperature in the high-temperature region (250-300 K) and the experimental data are fitted with a modified Arrhenius equation [46], given by,

$$I(T) = I_0/(1 + Aexp(-E_B/k_BT)) \qquad (2.1)$$

where, $I(T)$ and I_0 are integrated PL intensities at T K and 0 K, respectively, A, E_B, k_B are the constant, exciton binding energy, and Boltzmann constant. Exciton binding energy extracted from the fitted data is found to be ~92 meV for the $MAPbBr_3$ film, which is relatively higher than the reported values. Exciton binding energy of the bulk perovskite film prepared using the solution

method is reported to be in the range 30-70 meV [50-52]. In the present case, the exciton binding energy (> k_BT) is relatively large compared to the earlier reported values [50-52]. Higher exciton binding energy of the film than the room temperature thermal energy (k_BT) is responsible for the stable PL emission at room temperature, mainly caused by excitonic recombination. This is consistent with the absorption spectrum, where the excitonic peak is observed even at room temperature, making the film appropriate for optoelectronic device applications.

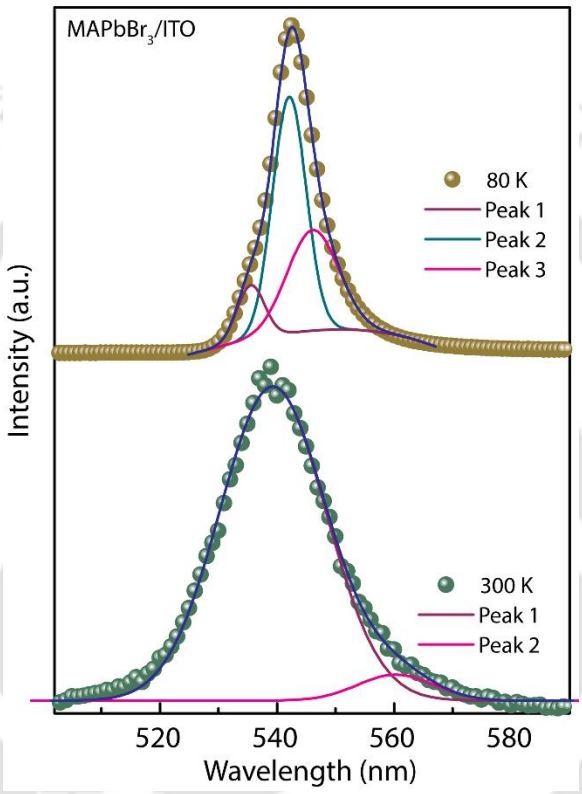

Fig. 2.15. Deconvulated PL spectra of $MAPbBr_3$ film measured at 80 K and 300 K. The symbols represent the experimental data and the solid lines represent the fitted Gaussian peaks.

A closer look at the shape of the PL spectra, particularly at low temperatures, reveals its asymmetric line shape. The deconvulated PL spectra of the perovskite film at 80 and 300 K are presented in **Fig. 2.15**. The PL spectrum at 300 K is deconvulated with two peaks, where peak 1 and peak 2 correspond to free exciton and bound exciton recombination, respectively. At room temperature, PL emission is mostly due to the free exciton recombination (peak 1). However, at lower temperatures, the contribution from the bound excitonic recombination becomes significant (peak 2), as shown in **Fig. 2.15**.

Note that the FWHM of the PL spectra increases with increasing temperature (see **Fig. 2.16(a)**), due to exciton-phonon coupling, longitudinal optical (LO) contribution and enhanced drift motion of the carriers at a higher temperature which causes the redistribution of the carriers and in turn results into the broadening of the PL spectra [50, 53]. Inset of **Fig. 2.16(a)** shows the comparison of the PL spectra (normalized to 1) of the film taken at 80 and 300 K, revealing the FWHM of ~45 and ~92 meV, respectively. Narrow linewidth of the PL spectra at low temperatures reveal the color purity of the film appropriate for light-emitting and display applications. To understand the

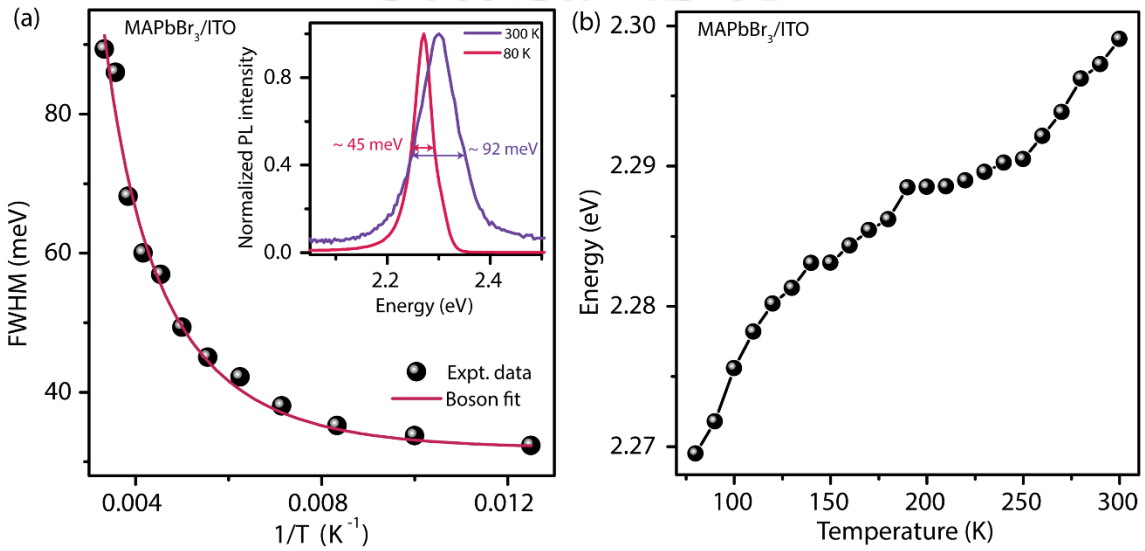

Fig. 2.16. (a) Variation of FWHM of the PL spectra of $MAPbBr_3$ film with measurement temperature. The experimental data is shown by the symbol and the solid line corresponds to the fitted data; the inset shows the comparison of the normalized PL spectra taken at 80 and 300 K. (b) Variation in PL peak position (energy) with measurement temperature for the 120 nm perovskite film.

exciton-phonon coupling, FWHM of the excitonic peak as a function of temperature is analyzed. It has been reported that the exciton-phonon coupling parameter is associated with the localized and delocalized electronic transition and it affects the PL spectral line width. The contribution of exciton-phonon coupling is quantified by fitting the FWHM vs. temperature data using the Boson model, as shown in **Fig. 2.16(a)**. The Boson model [54, 55] is given by,

$$\Gamma(T) = \Gamma_0 + \Gamma_{LO}/(exp(\hbar\omega_{LO}/k_B T) - 1) \qquad (2.2)$$

where, Γ_0, Γ_{LO}, $\hbar\omega_{LO}$, and k_B are the inhomogeneous broadening contribution, longitudinal exciton-phonon contribution, longitudinal optical phonon energy, and the Boltzmann constant. From the fitted data, the extracted parameters are as follows: Γ_0 = 32 meV, Γ_{LO} = 174 meV, $\hbar\omega_{LO}$ = 27 meV.

The longitudinal optical phonon energy is consistent with the earlier reports (25-42 meV) [56]. Note that there is an overall blue shift of the PL peak with the increase in measurement temperature, as shown in **Fig. 2.16(b)**. As the temperature increases from 80 to 300 K, the PL peak is blue-shifted by 30 meV due to exciton-phonon coupling and lattice expansion, since the perovskite semiconductors show positive thermal expansion coefficient for the bandgap.

The carrier lifetime of the vacuum deposited $MAPbBr_3$ film on ITO is investigated using the TRPL measurement under 405 nm pulsed laser excitation monitored at the corresponding PL peak (see **Fig. 2.17**). A comparison of the TRPL spectra of the films with thickness 10, 40, and 120 nm is shown in **Fig. 2.17**. In each case, the TRPL spectra of 10, 40 and 120 nm films are recorded by monitoring the decay at the corresponding PL peak positions, i.e., at 530, 532 and 540 nm for the films with thickness 10, 40, and 120 nm, respectively. The experimental data are fitted with tri-exponential decay function, since the PL emission peak primarily has the contributions from free exciton recombination, bound exciton recombination, and trap states. The tri-exponential decay function is given by, $I(T) = \sum_{i=1}^{3} A_i exp(-t/\tau_i)$, where A_i is the amplitude of the decay curve

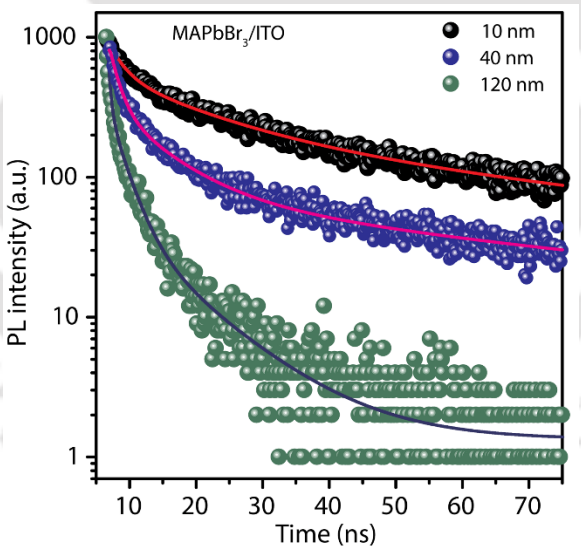

Fig. 2.17. Comparison of TRPL spectra of perovskite films with different thicknesses on ITO substrate.

corresponding to the lifetime τ_i. The average lifetime of the film is calculated using the relation [46]: $\tau_{avg} = \sum_{i=1}^{3} A_i \tau_i^2 / \sum_{i=1}^{3} A_i \tau_i$. Average lifetimes corresponding to the 10, 40, and 120 nm films are found to be ~45, ~6 and ~5 ns. The decrease in carrier lifetime with increasing thickness can be attributed to the higher contribution of non-radiative recombination in the thicker film

associated with trapping centers due to grain boundaries, and this is consistent with the lower PL intensity in the steady-state spectra. If the radiative and nonradiative lifetimes are expressed as τ_r and τ_{nr}, then the effective lifetime τ_{eff} is given by, $\frac{1}{\tau_{eff}} = \frac{1}{\tau_r} + \frac{1}{\tau_{nr}}$. Since, $\tau_{nr} \ll \tau_r$, the above equation reveals that $\tau_{eff} \approx \tau_{nr}$ and thus, $\tau_{eff} \ll \tau_r$. The presence of defects is also confirmed from the PL line shape analysis at low temperature. Thus, considering the moderate PL lifetime and high PL intensity in the 40 nm film grown at a substrate temperature of 50 ºC, this condition is considered optimum for the growth and fabrication of optoelectronic devices.

2.5. Summary and Conclusions

In this chapter, we have presented a thorough analysis on the growth kinetics and scaling behavior of vacuum deposited $MAPbBr_3$ thin film on ITO and SiO_2 substrates. Later, a direct correlation between the growth parameters and structural/optical characteristics of the film is established. These results may lead to a new path to engineer the device performance as we correlate the growth parameters to the optical and structural properties of the perovskite film, and we can precisely control various morphological parameters using the vacuum deposition method. The key findings of the chapter are summarized below.

1. Anomalous scaling behavior of the vacuum-deposited $MAPbBr_3$ hybrid perovskite thin film on different substrates at low thicknesses.
2. For the optimized thickness, the near-unity roughness exponent (α) of the film on both ITO and SiO_2 substrates indicate locally smooth surface.
3. The growth exponents, β, are found to be ~ 0.22 and ~ 0.90, and the thermal activation energies (E_a) are found to be ~ 0.10 and ~ 0.15 eV, for the films grown on ITO and SiO_2 substrates, respectively.
4. The higher values of β and E_a for the films grown on SiO_2 substrate as compared to the case of ITO suggest a higher step edge barrier resulting in a mound-like growth on the SiO_2 substrate and a steady lateral growth on the ITO substrate.
5. High exciton binding energy and high optical stability of the perovskite film on ITO substrate.
6. Optimized film thickness and substrate temperature are found to be 40 nm and 50 °C with high crystallinity and low surface roughness on the ITO substrate.

References

[1] X. Tang, W. Chen, Z. Liu, J. Du, Z. Yao, Y. Huang, C. Chen, Z. Yang, T. Shi, W. Hu, Z. Zang, Y. Chen, Y. Leng, Ultrathin, Core–Shell Structured SiO2 Coated Mn2+-Doped Perovskite Quantum Dots for Bright White Light-Emitting Diodes, Small, 15 (2019) 1900484.
[2] L. Zhang, Y. Liu, Z. Yang, S. Liu, Two Dimensional Metal Halide Perovskites: Promising Candidates for Light-Emitting Diodes, J ENERGY CHEM., 37 (2019) 97-110.
[3] X. Fu, Z. Peng, C. Zhang, Y. Xia, J. Zhang, W. Luo, L.J. Guo, H. Li, Y. Wang, D. Zhang, Controlled Synthesis of Brightly Fluorescent CH3NH3PbBr3 Perovskite Nanocrystals Employing Pb(C17H33COO)2 as the Sole Lead Source, RSC Adv., 8 (2018) 1132-1139.
[4] R.L.Z. Hoye, M.R. Chua, K.P. Musselman, G. Li, M.-L. Lai, Z.-K. Tan, N.C. Greenham, J.L. MacManus-Driscoll, R.H. Friend, D. Credgington, Enhanced Performance in Fluorene-Free Organometal Halide Perovskite Light-Emitting Diodes using Tunable, Low Electron Affinity Oxide Electron Injectors, Adv. Mater., 27 (2015) 1414-1419.
[5] L.-B. Luo, G.-A. Wu, Y. Gao, L. Liang, C. Xie, Z.-X. Zhang, X.-W. Tong, T. Wang, F.-X. Liang, A Highly Sensitive Perovskite/Organic Semiconductor Heterojunction Phototransistor and Its Device Optimization Utilizing the Selective Electron Trapping Effect, Adv. Opt. Mater, 7 (2019) 1900272.
[6] F. Chen, C. Xu, Q. Xu, Y. Zhu, F. Qin, W. Zhang, Z. Zhu, W. Liu, Z. Shi, Self-Assembled Growth of Ultrastable CH3NH3PbBr3 Perovskite Milliwires for Photodetectors, ACS Appl. Mater. Interfaces, 10 (2018) 25763-25769.
[7] H. Lu, W. Tian, F. Cao, Y. Ma, B. Gu, L. Li, A Self-Powered and Stable All-Perovskite Photodetector–Solar Cell Nanosystem, Adv. Funct. Mater., 26 (2016) 1296-1302.
[8] W. Tian, H. Zhou, L. Li, Hybrid Organic–Inorganic Perovskite Photodetectors, Small, 13 (2017) 1702107.
[9] J. Feng, X. Yan, Y. Liu, H. Gao, Y. Wu, B. Su, L. Jiang, Crystallographically Aligned Perovskite Structures for High-Performance Polarization-Sensitive Photodetectors, Adv. Mater. , 29 (2017) 1605993.
[10] Z.-X. Zhang, Z. Long-Hui, X.-W. Tong, Y. Gao, C. Xie, Y.H. Tsang, L.-B. Luo, Y.-C. Wu, Ultrafast, Self-Driven, and Air-Stable Photodetectors Based on Multilayer PtSe2/Perovskite Heterojunctions, J. Phys. Chem. Lett, 9 (2018) 1185-1194.
[11] Z. Yang, Y. Deng, X. Zhang, S. Wang, H. Chen, S. Yang, J. Khurgin, N.X. Fang, X. Zhang, R. Ma, High-Performance Single-Crystalline Perovskite Thin-Film Photodetector, Adv. Mater, 30 (2018) 1704333.
[12] J. Luan, J. Xu, J. Chen, X. Shi, B. Zhang, S. Dai, J. Yao, Efficient Planar CH3NH3PbBr3 Perovskite Solar Cells Prepared at Room Temperature with Ionic-Liquids/Fullerene as an Electron Transport Bilayer, J. Solid State Chem. , 270 (2019) 436-442.
[13] P. Zhang, F. Yang, M.A. Kamarudin, C.H. Ng, G. Kapil, T. Ma, S. Hayase, Performance Enhancement of Mesoporous TiO2-Based Perovskite Solar Cells by SbI3 Interfacial Modification Layer, ACS Appl. Mater. Interfaces, 10 (2018) 29630-29637.
[14] C.S. Ponseca Jr, T.J. Savenije, M. Abdellah, K. Zheng, A. Yartsev, T.r. Pascher, T. Harlang, P. Chabera, T. Pullerits, A. Stepanov, Organometal halide perovskite solar cell materials rationalized: ultrafast charge generation, high and microsecond-long balanced mobilities, and slow recombination, J. Am. Chem. Soc., 136 (2014) 5189-5192.
[15] M. Yi, W. Jang, J.S. Cho, D.H. Wang, Enhanced Interface of Polyurethane Acrylate via Perfluoropolyether for Efficient Transfer Printing and Stable Operation of Pedot:Pss in Perovskite Photovoltaic Cells, Applied Surface Science, 467-468 (2019) 168-177.
[16] B. Liu, S. Wang, Z. Ma, J. Ma, R. Ma, C. Wang, High-Performance Perovskite Solar Cells with Large Grain-Size Obtained by the Synergy of Urea and Dimethyl Sulfoxide, Applied Surface Science, 467-468 (2019) 708-714.

[17] H. Zhu, Y. Fu, F. Meng, X. Wu, Z. Gong, Q. Ding, M.V. Gustafsson, M.T. Trinh, S. Jin, X.Y. Zhu, Lead Halide Perovskite Nanowire Lasers with Low Lasing Thresholds and High Quality Factors, Nat. Mater, 14 (2015) 636-642.
[18] P. Liu, X. He, J. Ren, Q. Liao, J. Yao, H. Fu, Organic–Inorganic Hybrid Perovskite Nanowire Laser Arrays, ACS Nano, 11 (2017) 5766-5773.
[19] S.A. Veldhuis, P.P. Boix, N. Yantara, M. Li, T.C. Sum, N. Mathews, S.G. Mhaisalkar, Perovskite Materials for Light-Emitting Diodes and Lasers, Advanced Materials, 28 (2016) 6804-6834.
[20] Z. Li, J. Moon, A. Gharajeh, R. Haroldson, R. Hawkins, W. Hu, A. Zakhidov, Q. Gu, Room-Temperature Continuous-Wave Operation of Organometal Halide Perovskite Lasers, ACS Nano, 12 (2018) 10968-10976.
[21] S.I. Seok, M. Grätzel, N.-G. Park, Methodologies toward Highly Efficient Perovskite Solar Cells, Small, 14 (2018) 1704177.
[22] K. Lin, J. Xing, L.N. Quan, F.P.G. de Arquer, X. Gong, J. Lu, L. Xie, W. Zhao, D. Zhang, C. Yan, W. Li, X. Liu, Y. Lu, J. Kirman, E.H. Sargent, Q. Xiong, Z. Wei, Perovskite Light-Emitting Diodes with External Quantum Efficiency Exceeding 20 Per Cent, Nature, 562 (2018) 245-248.
[23] W. Xu, Q. Hu, S. Bai, C. Bao, Y. Miao, Z. Yuan, T. Borzda, A.J. Barker, E. Tyukalova, Z. Hu, M. Kawecki, H. Wang, Z. Yan, X. Liu, X. Shi, K. Uvdal, M. Fahlman, W. Zhang, M. Duchamp, J.-M. Liu, A. Petrozza, J. Wang, L.-M. Liu, W. Huang, F. Gao, Rational Molecular Passivation for High-Performance Perovskite Light-Emitting Diodes, Nat. Photonics, 13 (2019) 418-424.
[24] Y. Cao, N. Wang, H. Tian, J. Guo, Y. Wei, H. Chen, Y. Miao, W. Zou, K. Pan, Y. He, H. Cao, Y. Ke, M. Xu, Y. Wang, M. Yang, K. Du, Z. Fu, D. Kong, D. Dai, Y. Jin, G. Li, H. Li, Q. Peng, J. Wang, W. Huang, Perovskite Light-Emitting Diodes Based on Spontaneously Formed Submicrometre-Scale Structures, Nature, 562 (2018) 249-253.
[25] D. Tsamouras, G. Palasantzas, J.T.M. De Hosson, Growth front Roughening of Room-Temperature Deposited Oligomer Films, Appl. Phys. Lett., 79 (2001) 1801-1803.
[26] H. Sirringhaus, P.J. Brown, R.H. Friend, M.M. Nielsen, K. Bechgaard, B.M.W. Langeveld-Voss, A.J.H. Spiering, R.A.J. Janssen, E.W. Meijer, P. Herwig, D.M. de Leeuw, Two-Dimensional Charge Transport in Self-Organized, High-Mobility Conjugated Polymers, Nature, 401 (1999) 685-688.
[27] P.F. Van Hutten, V.V. Krasnikov, G. Hadziioannou, A Model Oligomer Approach to Light-Emitting Semiconducting Polymers, Acc. Chem. Res., 32 (1999) 257-265.
[28] B.C. Mohanty, H.R. Choi, Y.S. Cho, Fluctuations in Global Surface Scaling Behavior in Sputter-Deposited Zno Thin Films, EPL, 93 (2011) 26003.
[29] S.M. Obaidulla, P.K. Giri, Surface Roughening And Scaling Behavior Of Vacuum-Deposited Sncl2pc Organic Thin Films On Different Substrates, Appl. Phys. Lett., 107 (2015) 221910.
[30] S. Kowarik, A. Gerlach, S. Sellner, F. Schreiber, J. Pflaum, L. Cavalcanti, O. Konovalov, Anomalous Roughness Evolution of Rubrene Thin Films Observed in Real Time During Growth, Phys. Chem. Chem. Phys., 8 (2006) 1834-1836.
[31] D. Tsamouras, G. Palasantzas, Temperature Dependence of the Growth Front Roughening of Oligomer Films, Appl. Phys. Lett., 80 (2002) 4528-4530.
[32] Y. Liu, T. Zhou, M. Sun, D. Zhao, Q. Wei, Y. Sun, R. Wang, F. Jin, Q. Niu, Z. Su, Scaling Behavior and Morphology Evolution of CH3NH3PbI3 Perovskite Thin Films Grown by Thermal Evaporation, Mater. Res. Express, 4 (2017) 075510.
[33] S.K. Sinha, E.B. Sirota, S. Garoff, H.B. Stanley, X-Ray and Neutron Scattering from Rough Surfaces, Physical Review B, 38 (1988) 2297-2311.
[34] S. Yim, K.i. Kim, T.S. Jones, Growth Morphology of Perylene-3,4,9,10-tetracarboxylic Dianhydride (PTCDA) Thin Films: Influence of Intermolecular Interactions and Step-Edge Barriers, J. Phys. Chem. C, 111 (2007) 10993-10997.
[35] A.C. Dürr, F. Schreiber, K.A. Ritley, V. Kruppa, J. Krug, H. Dosch, B. Struth, Rapid Roughening in Thin Film Growth of an Organic Semiconductor (Diindenoperylene), Phys. Rev. Lett., 90 (2003) 016104.

[36] M. Kalff, P. Šmilauer, G. Comsa, T. Michely, No coarsening in Pt(111) homoepitaxy, Surf. Sci., 426 (1999) L447-L453.
[37] J.H. Jeffries, J.K. Zuo, M.M. Craig, Instability of Kinetic Roughening in Sputter-Deposition Growth of Pt on Glass, Phys. Rev. Lett., 76 (1996) 4931-4934.
[38] G. Palasantzas, J. Krim, Scanning Tunneling Microscopy Study of the Thick Film Limit of Kinetic Roughening, Phys. Rev. Lett., 73 (1994) 3564-3567.
[39] Y.P. Zhao, J.B. Fortin, G. Bonvallet, G.C. Wang, T.M. Lu, Kinetic Roughening in Polymer Film Growth by Vapor Deposition, Phys. Rev. Lett., 85 (2000) 3229-3232.
[40] G.W. Collins, S.A. Letts, E.M. Fearon, R.L. McEachern, T.P. Bernat, Surface Roughness Scaling of Plasma Polymer Films, Phys. Rev. Lett., 73 (1994) 708-711.
[41] R. Dalven, Empirical Relation between Energy Gap and Lattice Constant in Cubic Semiconductors, Phys. Rev. B, 8 (1973) 6033-6034.
[42] Z. Xiao, Y. Zhou, H. Hosono, T. Kamiya, N.P. Padture, Bandgap Optimization of Perovskite Semiconductors for Photovoltaic Applications, Chem. Eur. J., 24 (2018) 2305-2316.
[43] R. Prasanna, A. Gold-Parker, T. Leijtens, B. Conings, A. Babayigit, H.-G. Boyen, M.F. Toney, M.D. McGehee, Band Gap Tuning via Lattice Contraction and Octahedral Tilting in Perovskite Materials for Photovoltaics, J. Am. Chem. Soc., 139 (2017) 11117-11124.
[44] J.-H. Lee, N.C. Bristowe, J.H. Lee, S.-H. Lee, P.D. Bristowe, A.K. Cheetham, H.M. Jang, Resolving the Physical Origin of Octahedral Tilting in Halide Perovskites, Chem. Mater., 28 (2016) 4259-4266.
[45] C. Grote, R.F. Berger, Strain Tuning of Tin–Halide and Lead–Halide Perovskites: A First-Principles Atomic and Electronic Structure Study, J. Phys. Chem. C, 119 (2015) 22832-22837.
[46] S. Parveen, K.K. Paul, P.K. Giri, Precise Tuning of the Thickness and Optical Properties of Highly Stable 2D Organometal Halide Perovskite Nanosheets through a Solvothermal Process and Their Applications as a White LED and a Fast Photodetector, ACS Appl. Mater. Interfaces, 12 (2020) 6283-6297.
[47] E.Y. Tiguntseva, I.N. Saraeva, S.I. Kudryashov, E.V. Ushakova, F.E. Komissarenko, A.R. Ishteev, A.N. Tsypkin, R. Haroldson, V.A. Milichko, D.A. Zuev, S.V. Makarov, A.A. Zakhidov, Laser Post-Processing of Halide Perovskites for Enhanced Photoluminescence and Absorbance, J. Phys.: Conf. Ser., 917 (2017) 062002.
[48] Y. Tian, M. Peter, E. Unger, M. Abdellah, K. Zheng, T. Pullerits, A. Yartsev, V. Sundström, I.G. Scheblykin, Mechanistic Insights into Perovskite Photoluminescence Enhancement: Light Curing with Oxygen Can Boost Yield Thousandfold, Phys. Chem. Chem. Phys., 17 (2015) 24978-24987.
[49] E. Mosconi, D. Meggiolaro, H.J. Snaith, S.D. Stranks, F. De Angelis, Light-Induced Annihilation of Frenkel Defects in Organo-Lead Halide Perovskites, Energy Environ. Sci., 9 (2016) 3180-3187.
[50] S. Parveen, K.K. Paul, R. Das, P.K. Giri, Large Exciton Binding Energy, High Photoluminescence Quantum Yield and Improved Photostability of Organo-Metal Halide Hybrid Perovskite Quantum Dots Grown on a Mesoporous Titanium Dioxide Template, J. Colloid Interface Sci., 539 (2019) 619-633.
[51] J. Li, X. Yuan, P. Jing, J. Li, M. Wei, J. Hua, J. Zhao, L. Tian, Temperature-Dependent Photoluminescence Of Inorganic Perovskite Nanocrystal Films, RSC Adv., 6 (2016) 78311-78316.
[52] Z.-K. Tan, R.S. Moghaddam, M.L. Lai, P. Docampo, R. Higler, F. Deschler, M. Price, A. Sadhanala, L.M. Pazos, D. Credgington, F. Hanusch, T. Bein, H.J. Snaith, R.H. Friend, Bright Light-Emitting Diodes Based on Organometal Halide Perovskite, Nat Nanotechnol., 9 (2014) 687.
[53] G. Franssen, E. Litwin-Staszewska, R. Piotrzkowski, T. Suski, P. Perlin, Optical and Electrical Properties of Homoepitaxially Grown Multiquantum Well InGaN/GaN Light-Emitting Diodes, J. Appl. Phys., 94 (2003) 6122-6128.
[54] A.D. Wright, C. Verdi, R.L. Milot, G.E. Eperon, M.A. Pérez-Osorio, H.J. Snaith, F. Giustino, M.B. Johnston, L.M. Herz, Electron–Phonon Coupling in Hybrid Lead Halide Perovskites, Nat Commun, 7 (2016) 11755.

[55] S. Rudin, T.L. Reinecke, B. Segall, Temperature-Dependent Exciton Linewidths in Semiconductors, Phys. Rev. B, 42 (1990) 11218-11231.
[56] C. Quarti, G. Grancini, E. Mosconi, P. Bruno, J.M. Ball, M.M. Lee, H.J. Snaith, A. Petrozza, F. De Angelis, The Raman Spectrum of the CH3NH3PbI3 Hybrid Perovskite: Interplay of Theory and Experiment, J. Phys. Chem. Lett., 5 (2014) 279-284.

Chapter 3

Large Exciton Binding Energy, High Photoluminescence Quantum Yield and Improved Photostability of Organo-Metal Halide Hybrid Perovskite Quantum Dots Grown on a Mesoporous TiO_2 Template

In this chapter, we present a novel synthetic route to grow size-tunable hybrid perovskite ($CH_3NH_3PbI_3$ and $CH_3NH_3PbBr_3$) quantum dots (QDs) using a Fluorine-doped TiO_2 (F-TiO_2) mesoporous template and these QDs exhibit large exciton binding energy, high photoluminescence quantum yield and improved photostability. The pore size in F-TiO_2 template is tuned by varying the HF molar concentration during its solvothermal growth and size of the perovskite QDs embedded in F-TiO_2 pores is tuned in the range of 1.7-5.1 nm. As compared to its bulk counterpart the $CH_3NH_3PbI_3$ ($MAPbI_3$, MA= CH_3NH_3) QD with average size ~1.7 nm exhibits ~47 nm blue shift in the PL spectrum, ~43-fold enhancement in photoluminescence (PL) intensity and ~25 % PL quantum yield (QY). On the other hand, $MAPbBr_3$ QD of similar size exhibits dramatically enhanced (~124 times) PL emission with narrow line width and a PL QY of ~57 %, which is significant for the template-assisted growth of perovskite QDs film. Quantitative analysis of the PL emission energy vs QD size shows an excellent fit with the Brus equation confirming the strong quantum confinement effect in the perovskite QDs. Analysis of low-temperature PL spectra reveals high exciton binding energy (162-272 meV) of the QDs as compared to the bulk film (~32 meV) due to the high effective dielectric constant and high electron-hole recombination probability in the QDs, consistent with the high PL QY of the QDs. The blue shift of the PL peak energy with increasing temperature is explained on the basis of localization effect. The $MAPbBr_3$ QDs embedded in porous F-TiO_2 template maintain its initial PL intensity up to several hours ($\geq$10 h) under the UV laser exposure (18mW), while that of the bulk film decreases to <67 % of its initial value. Thus, template grown hybrid perovskite QDs exhibiting high photostability and very high PL QY are promising for the next generation optoelectronic applications.

3.1. Introduction

Organic-inorganic halide perovskites have fostered unprecedented research interest due to their rapidly achieved spectacular performance in the field of optoelectronic devices along with their remarkable characteristics, such as low cost, long-range charge transport, tunable optical bandgap, high absorption coefficient and photoluminescence quantum yield (PL QY)[1-9]. Currently, perovskite-based solar cells have achieved power conversion efficiency up to 22 % and LEDs have achieved quantum efficiency as high as 10 %[10]. Additionally, other applications of perovskite, such as sensors, amplified spontaneous emission and lasing, photodetectors, memory devices have also been realized[11-14]. In the last chapter, we have discussed about the growth kinetics of vacuum deposited 3D perovskite thin film whose emission intensity was not high enough to apply it devices. Hence, to improve the optoelectronic properties and stability, we have tried to synthesize perovskite nanocrystals (NCs).

In recent years, perovskite NCs have drawn great attention owing to their unique properties, such as large exciton binding energy, narrow emission bandwidth, high PL QY, decent stability along with the well-known properties of bulk perovskite[15-22]. Lead bromide based perovskite quantum dots (QDs) in colloidal solution have approached ~100 % PL QY, synthesized by colloidal method[23]. Schmidt and co-workers first demonstrated the synthesis of ~6 nm sized organic-inorganic halide perovskite NCs through a simple method using ammonium bromide with a medium-length alkyl chain[24]. Since then, perovskite NCs are being prepared by different methods for a wide range of optoelectronic applications. In the case of NCs synthesized by the colloidal method, the final product consists of NCs with some unwanted bulk structures. The as-synthesized colloidal perovskite NCs are ionic and essentially hygroscopic in nature, which makes them usually unstable in the ambient environment[25-28]. Perovskite solution may be incorporated in various mesoporous templates, confining the growth of perovskite in the pores, which results in the controlled growth of perovskite NCs guided by the mesoporous structure. Researchers have devoted great efforts to synthesize different templates, since in-situ fabrication process of perovskite NCs is preferable for device applications. Kojima et al. observed strong PL emission from nanocrystalline lead bromide perovskite synthesized by rapid self-organization on a mesoporous aluminum oxide film[29]. Di et al. demonstrated the formation of self-assembled perovskite NCs embedded in a solid organic matrix[30]. Malgras et al. described a simple method

to grow monodisperse 3.3 nm sized $MAPbBr_xI_{3-x}$ NCs inside mesoporous silica templates by the varying pore size of the templates[31]. Recently, Anaya et al. reported quantum confinement (QC) induced tunable emission over a wide range of energy (~0.34 eV) by embedding the perovskite NCs in thin metal oxide films[32]. Though the size-tunable perovskite nanoparticles (NPs) are successfully achieved in earlier works, very few studies discussed on the improvement of fluorescence intensity and their application in light-emitting devices. Demchyshyn et al. used nanoporous anodic alumina (npAAO) and nanoporus silicon (npSi) thin films for the growth of perovskite nanocrystals with very high PL QY (up to 25 % for $CH_3NH_3PbI_3$, 60 % for $CH_3NH_3PbBr_3$, 90 % for $CsPbBr_3$) and they also demonstrated blue emission from $CsPbBr_3$ in npSi and cyan EL in npAAO-based LEDs[33]. Recently, Ghosh et al. reported growth of $MAPbI_3$ NPs on a mesoporous Si nanowire template and they achieved ~12 fold enhancement in PL intensity with respect to bulk perovskite film and a PL QY of ~9 %[34]. The reported PL QY of template grown perovskite NCs is typically quite low and needs further improvement for device applications.

Herein, we demonstrate the growth of $MAPbI_3$ and $MAPbBr_3$ QDs inside a mesoporous Fluorine doped TiO_2 (F-TiO_2) template by a simple solution processed method. With the help of steady state and low-temperature PL study the origin of high emission efficiency of the QDs is investigated. This template grown perovskite QDs also exhibit much better photostability and air stability compared to bulk films, which is very promising for their practical applications, including the light emitting diodes.

3.2. Experimental Procedure

3.2.1. Materials

The starting materials for the present work are titanium (Ti) foil (99.7 %, Sigma Aldrich), hydrofluoric acid (HF, 48 %, Merck), hydrochloric acid (HCl, 37%, Merck), methylamine solution (CH_3NH_3, 33 wt% in absolute ethanol, Sigma-Aldrich), lead(II) iodide (PbI_2, 99 %, Sigma-Aldrich), lead(II) bromide ($PbBr_2$, 99.999 %, Sigma-Aldrich), hydroiodic acid (HI, 57 wt% in water, Sigma-Aldrich), hydrobromic acid (HBr, 48 wt% in water, Sigma-Aldrich), N,N-dimethylformamide (DMF, >99 %, Sigma-Aldrich), diethyl ether (>99 %, Merck) and Titania paste (Sigma-Aldrich).

3.2.2. Synthesis Procedures

3.2.2.1. Synthesis of Porous TiO_2 Nanostructures

Mesoporous 3D F-TiO_2 nanoflowers (NFs) with self-grown TiO_2 NCs were prepared using the procedure reported by Paul et al.[35]. In a typical synthesis, commercially available Ti foil was first cleaned by 18 % aqueous HCl solution at 90 °C for 20 min to remove impurities and oxide layers. Afterward, it was rinsed with deionized (DI) water vigorously and finally dried in the inert gas atmosphere. Cleaned Ti foil was taken into a Teflon-lined autoclave (Berghof, BR-100) with 50 mL of aqueous HF solution (20 mM-80 mM). The sealed autoclave was heated and maintained at 150 °C for 8 hours. After the hydrothermal treatment, the autoclave was allowed to cool down naturally and then the foil was gently washed with DI water and dried in an oven at 90 °C to get the mesoporous F-TiO_2 templates. The mesoporous F-TiO_2 templates grown with 20 mM, 40 mM, and 80 mM HF concentrations are named as F1, F2 and F3, respectively.

3.2.2.2. Synthesis of $MAPbI_3$

$MAPbI_3$ perovskite precursor solution was prepared using the well-established procedure[36]. To prepare CH_3NH_3I powder, 24 mL of methylamine solution was diluted with 50 mL of absolute ethanol and stirred for 15 min in 250 mL round-bottom flask. Then, 8 mL of HI was slowly added to the above solution at 0 °C with vigorous stirring at 1000 rpm for 2 h. Afterward, the solution was heated at 60 °C for 5 h with continuous stirring to evaporate the solvent. To remove impurities from the obtained white CH_3NH_3I powder, the crystals were washed several times with anhydrous diethyl ether and dried at 60 °C in a vacuum oven overnight. Then, CH_3NH_3I and PbI_2 were dissolved in DMF at 1:1 molar ratio to obtain the semi-transparent yellow $CH_3NH_3PbI_3$ perovskite solution with 30 wt%.

3.2.2.3. Synthesis of $MAPbBr_3$

We followed a similar procedure to obtain the $MAPbBr_3$ perovskite precursor solution. CH_3NH_3Br was first prepared by adding 8 mL methylamine and 2.83 mL HBr acid solution to 22 mL of absolute ethanol. For the elimination of impurities and recrystallization of CH_3NH_3Br, the same procedure has been followed, as discussed for the synthesis of CH_3NH_3I powder. The as-prepared

CH_3NH_3Br powder was dissolved together with $PbBr_2$ at a 2:1 molar ratio in DMF, to get a transparent colorless $MAPbBr_3$ solution with a concentration of 30 wt%.

3.2.2.4. Growth of Perovskite QDs on F-TiO_2

The syntheses of $MAPbI_3$ and $MAPbBr_3$ QDs were carried out by spin coating the as-synthesized perovskite solution on the F-TiO_2 template at 2500 rpm for 30 sec, followed by annealing at 80 °C for 20 min. The $MAPbI_3$ templates F1, F2, and F3 coated with $MAPbI_3$ are named as F1PI, F2PI and F3PI, respectively, and those coated with $MAPbBr_3$ are named as F1PB, F2PB and F3PB, respectively. **Fig. 3.1** illustrates the schematic of the template-assisted growth process of perovskite QDs. To compare the performance of perovskite QDs grown on F-TiO_2, commercially

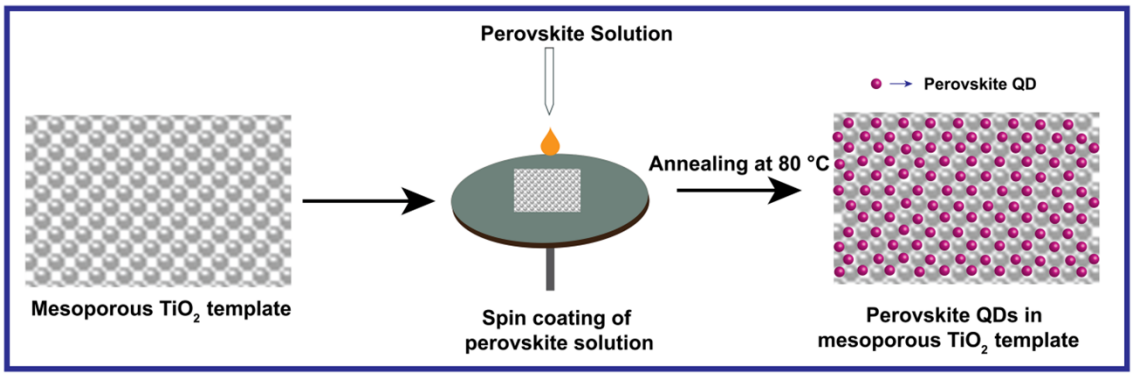

Fig. 3.1. Schematic of hydrothermally grown mesoporous F-TiO_2 template and growth of perovskite QDs on it by spin coating followed by annealing.

available mesoporous TiO_2 paste (m-TiO_2) was also used as a template to grow perovskite film/NPs. For this, commercial m-TiO_2 paste was first diluted in ethanol and then spin coated on ITO substrate and subsequently PI and PB solutions were deposited on m-TiO_2 layer. Note that the m-TiO_2 contains pores of much larger size than that of the mesoporous F-TiO_2, as discussed later.

3.3. Characterization Techniques

The morphology of TiO_2 templates before and after the deposition of perovskite QDs has been characterized using FESEM (Sigma, Zeiss). The high magnification surface morphologies of TiO_2 and perovskite QDs for different samples have been studied using a TEM (JEOL-JEM 2010) operated at 200 kV. High-angle annular dark field (HAADF) images were obtained using a

scanning transmission electron microscope (STEM) in aberration-correction mode (JEM 2100F, 200 kV) for high-resolution imaging. The surface area of TiO_2 nanoflower was determined using the multipoint Brunauer−Emmett−Teller (BET) method and the average pore size was determined using the Barett−Joyner−Halenda (BJH) model. UV−Vis absorption spectra were derived from the diffuse reflectance spectra (DRS) of the samples measured using a commercial spectrophotometer equipped with an integrating sphere (PerkinElmer, Lamda 950). The room temperature steady-state PL spectra of iodide and bromide-based perovskite NCs were recorded using 405 nm and 355 nm diode laser (CNI Laser) excitation, respectively with the help of a commercial fluorometer (Fluoromax-4, Horiba Scientific). The PL QY of the samples was measured in the thin film mode using an integrating sphere (FM-SPHERE, Horiba) attached with the fluorometer. Low temperature (80–300 K) PL measurements were carried out using a liquid nitrogen cooled optical cryostat (Optistat DNV, Oxford Instruments) attached to the above fluorometer. Time resolved PL (TRPL) measurements were performed using 405 nm/ 375 nm pulsed laser excitation for iodide/ bromide-based perovskite QDs, with an instrument response time of <50 ps (LifeSpecII, Edinburgh Instruments).

3.4. Results and Discussion

3.4.1. Morphology Studies

Surface morphology of as-synthesized F-TiO_2 template with arbitrary shaped TiO_2 NCs was investigated by FESEM and the low magnification images are shown in **Fig. 3.2(a-c)**. These images clearly reveal the nanoflowers (NF) type morphology of the F-TiO_2 nanostructures. **Fig. 3.2(d-f)** portray the enlarged view of pristine F-TiO_2 NF templates. It is evident from **Fig. 3.2(d)** that for sample F1 (grown with 20 mM HF), the self-grown TiO_2 NCs are observed to be uniformly decorated on the NF surface, due to the irregular surface etching by HF during the hydrothermal treatment. When the HF concentration increases from 20 mM to 40 mM, surface etching is more prominent and thus the size of the NCs is observed to be increased, as shown in **Fig. 3.2(e)**. For 80 mM HF concentration, the inter-particle separation is further increased, as shown in **Fig. 3.2(f)**. Histogram showing the separation between two consecutive NCs in F1 is depicted in **Fig. 3.2(g)** with an average separation of 3.2 nm. As a result of the intense surface etching, separation between consecutive NCs increases in F2 and it is estimated to be 4.8 nm, as shown in **Fig. 3.2(h)**. In F3, the average inter-particle separation is 6.4 nm, as shown in **Fig. 3.2(i)**. The inter-particle gap serves

as pore-like structure and acts as the template for the growth of perovskite QDs. In the course of spin coating of perovskite solution on the F-TiO_2 template, the PI or PB QDs are formed in the inter-particle gaps (voids/pores) of TiO_2 NCs. Due to the formation of perovskite QDs, the inter-

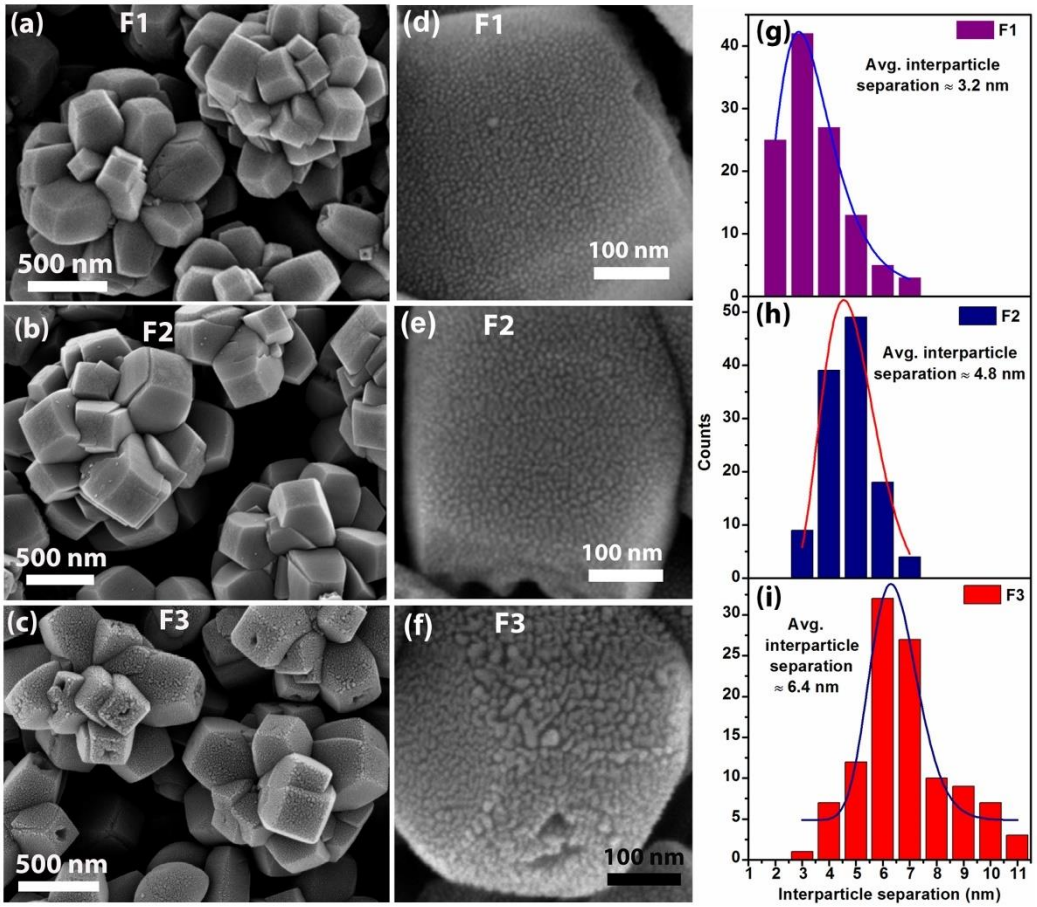

Fig. 3.2. FESEM images of mesoporous TiO_2 NFs grown at different HF concentrations: (a) 20 mM (F1), (b) 40 mM (F2) and (c) 80 mM (F3). Enlarged view of mesoporous F-TiO_2 petals grown at different HF concentrations: (d) 20 mM (F1), (e) 40 mM (F2) and (f) 80 mM (F3). (g-i) Histograms of inter-particle separation in corresponding mesoporous TiO_2 templates, respectively.

particle gap/voids in F-TiO_2 templates are observed to be filled, as shown in **Fig. 3.3(a-c)**, resulting in the uniform decoration of perovskite QDs in the pores of F-TiO_2 template. Due to the resolution limit of FESEM imaging, perovskite QDs are not clearly discernable here. However, the size of perovskite QDs increases from F1PI to F3PI, which is consistent with the pore size in the mesoporous F-TiO_2 NF template. To compare the performance of perovskite QDs grown on F-TiO_2, commercially procured mesoporous TiO_2 paste (m-TiO_2) was also used as a template to grow perovskite NPs. **Fig. 3.4(a,b)** shows the FESEM image of PI and PB deposited on m-TiO_2

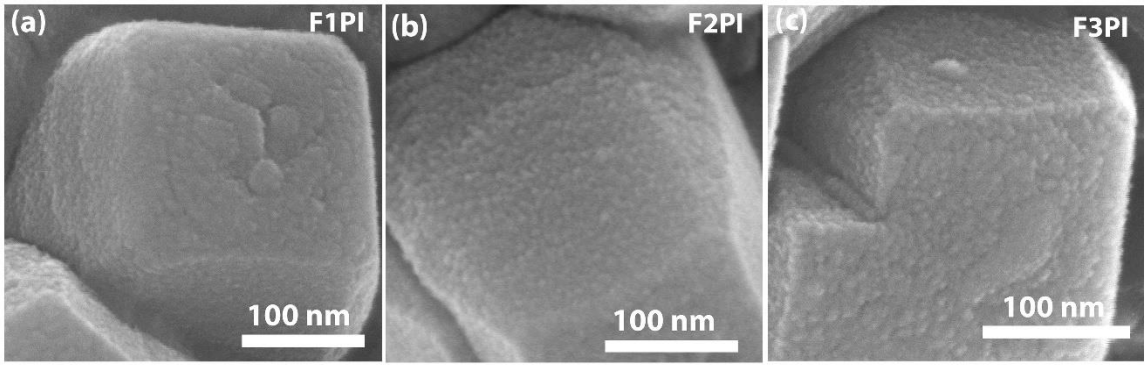

Fig. 3.3. FESEM images of PI perovskite layer coated on various F-TiO_2 templates: (a) F1PI, (b) F2PI, (c) F3PI.

coated substrates revealing bulk nature of the perovskite, since the pore sizes in m-TiO_2 is very large (>30 nm). EDX spectrum of the as-synthesized F-TiO_2 NF (F1) is shown in Fig. 3.4(c) confirming the presence of Ti, O, and F in the NF. The concentration of F is observed to be ≈8 at% with HF concentration 20 mM, which confirms the doping and surface adsorption of fluorine ion on F-TiO_2 NF surface[35]. In contrast, commercially procured m-TiO_2 paste does not have any fluorine doping (see **Fig. 3.4(d)**) and hence intrinsic in nature and it behaves differently for the light emission characteristic of the perovskite layer on it.

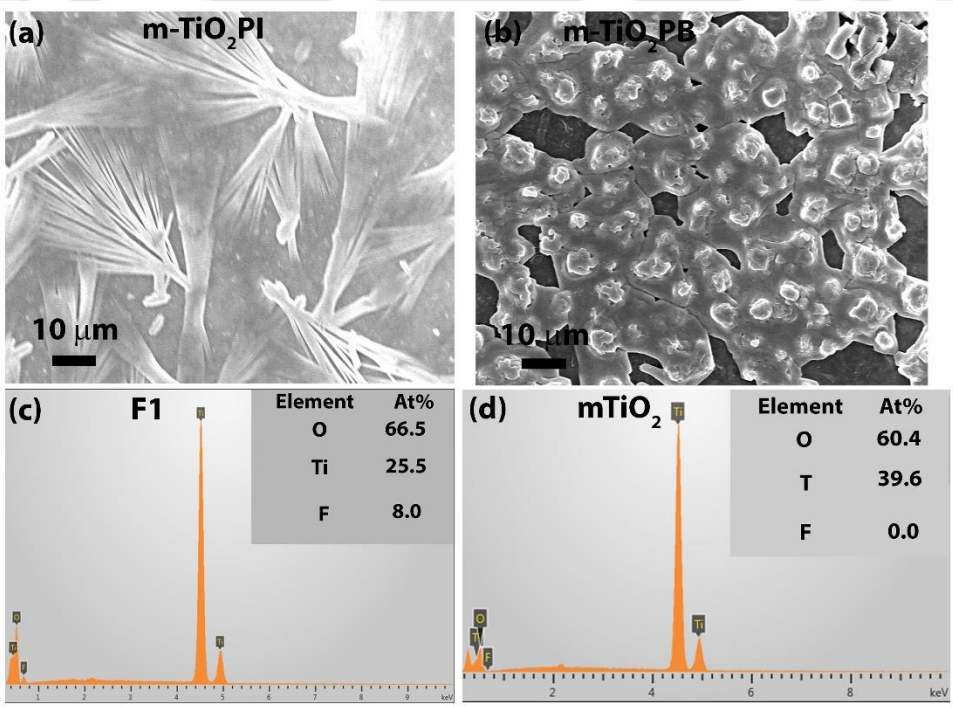

Fig. 3.4. FESEM images of (a) PI and (b) PB films deposited on mTiO_2 coated ITO substrates. EDX spectra and elemental composition of (c) F1 and (d) mTiO_2 paste.

With the help of Brunauer–Emmett–Teller (BET) process, we measured the surface area and pore size of the as-grown F-TiO_2 NF template and commercially available mesoporous m-TiO_2 paste. The N_2 adsorption-desorption isotherms of F3 are shown in **Fig. 3.5(a)** and the isotherms of F-TiO_2 NF exhibit an abrupt increase in the high-pressure region (>0.7 P/P_0 value), which can be related to the capillary condensation and multilayer adsorption of N_2 in the voids between F-TiO_2 NCs. The average pore size and corresponding size distribution was analyzed using Barrett-Joyner-Halenda (BJH) analysis. The BJH pore size distribution profile for F3 is shown in the inset of **Fig. 3.5(a)**. The mean surface area and average pore diameter of F3 are measured to be 13.836 m^2/g and 4.3 nm, respectively. Note that the pore diameter calculated from BET is less than the estimated inter-particle separation between TiO_2 NCs from FESEM image, which is primarily due to the resolution limit of the FESEM. The N_2 adsorption-desorption isotherms and the BJH pore size distribution profiles for commercially available mesoporous m-TiO_2 paste are shown in **Fig. 3.5(b)**. The average pore diameter of m-TiO_2 is ~32.9 nm, which is too large to grow perovskite QDs using it as a template.

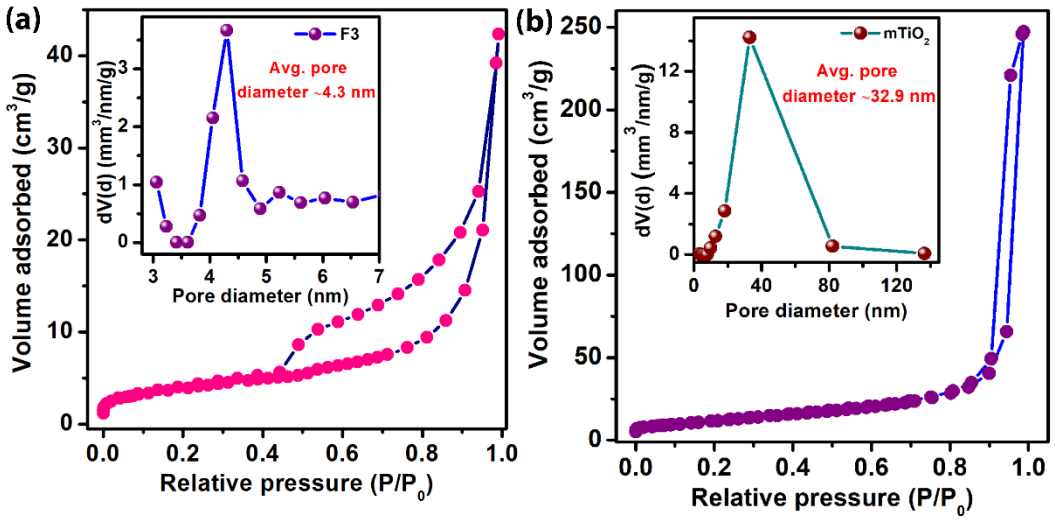

Fig. 3.5. (a) N_2 adsorption/desorption isotherms of F-TiO_2 NF template obtained from F3. The inset shows the corresponding BJH pore size distribution. (b) N_2 adsorption/desorption isotherms of commercial m-TiO_2 paste and the inset shows corresponding BJH pore size distribution.

TEM images of the PI QDs grown on F-TiO_2 templates were acquired to investigate the actual size and morphology of individual QD. To prepare the TEM sample, F-TiO_2 layer with the PI QD was scratched from the Ti foil (substrate) in the form of powder and then dispersed in toluene. Next, the dispersion was drop casted on the TEM grid and heated at ~45 °C to evaporate the solvent.

Fig. 3.6(a) shows the TEM image of the sample F1PI revealing the uniform decoration of PI QDs on the F-TiO_2 template. The corresponding size distribution of PI QDs with average size ~1.7 nm is shown in the inset of **Fig. 3.6(a)**. **Fig. 3.6(b)** shows the bright field high-resolution STEM image of F1PI discerning the discrete distribution of PI QDs on F-TiO_2 template. The uniform growth of PI QDs on the F-TiO_2 templates of F2 and F3 are shown in **Fig. 3.6(c,d)**, and the corresponding

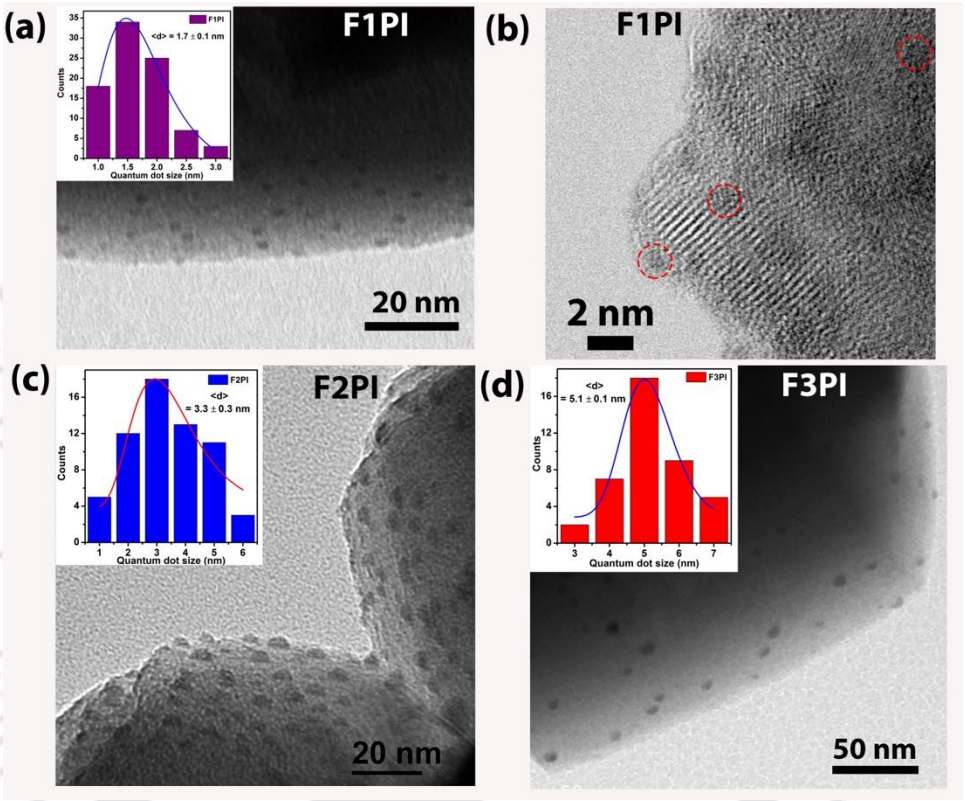

Fig. 3.6. (a) TEM image of PI QDs in F1PI and corresponding size distribution in the inset. (b) High resolution bright field STEM image of F1PI. TEM image of PI QDs in: (c) F2PI and (d) F3PI and the corresponding size distributions shown in the inset.

particle size distribution with an average diameter of ~3.3 nm and 5.1 nm are shown in the inset, respectively. Since the size of the QDs grown on F1 is smaller than that of F2 and F3, it facilitates stronger QC effect, which will be discussed later. It is evident from the TEM images that the size of the as-grown PI QDs on F-TiO_2 template becomes larger with the increase of the molar concentration of HF. The estimated size of the PI QDs from the TEM images is consistent with the average pore size or interparticle separation between F-TiO_2 NCs in different samples. We find that the average size of the QDs in F3PI is ~5.1 nm, which is marginally higher than the pore diameter of F3 (~4.3 nm) calculated using BJH analysis. Hence, ultra-small pores in the F-TiO_2

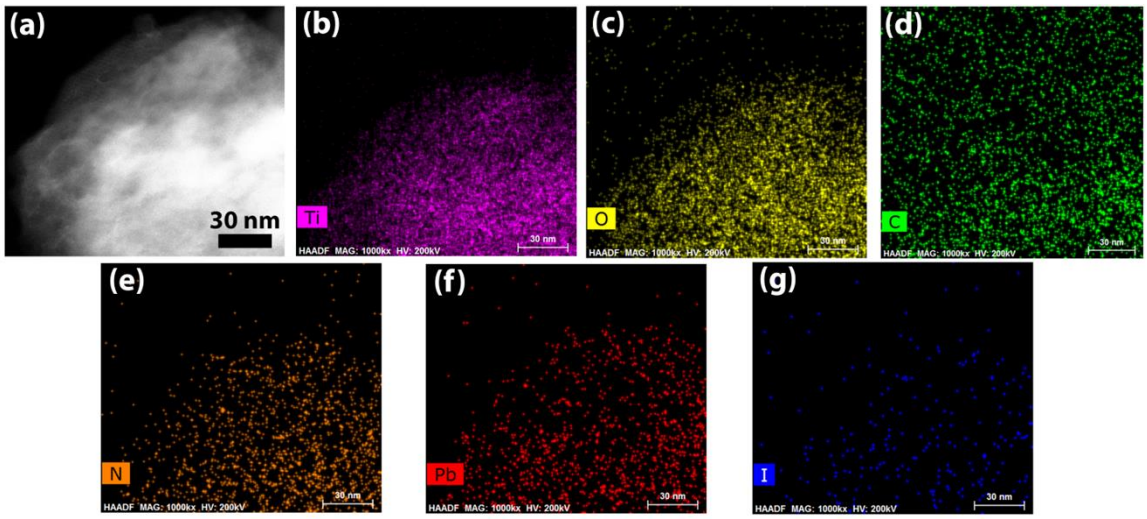

Fig. 3.7. (a) HAADF STEM image of F1PI and (b-g) the corresponding elemental mapping of titanium, oxygen, carbon, nitrogen, lead, iodine respectively, showing their spatial distribution.

template act as nucleation sites for the growth of perovskite QDs. Note that the perovskite QDs are partially embedded in the pores of the F-TiO_2 template and partially outside the pores, which is fully consistent with the TEM images. After spin coating and annealing of the perovskite solution, PI QDs become crystallized and exhibit superior properties. HAADF image of the elemental mapping for F1P1 is shown in **Fig. 3.7(a)**. The elemental mapping clearly shows the presence of C, N, Pb and I on F-TiO_2 template confirming the presence of PI QDs on F-TiO_2 template (see **Fig. 3.7(b-g)**). To compare the properties of QDs grown on F-TiO_2 template with

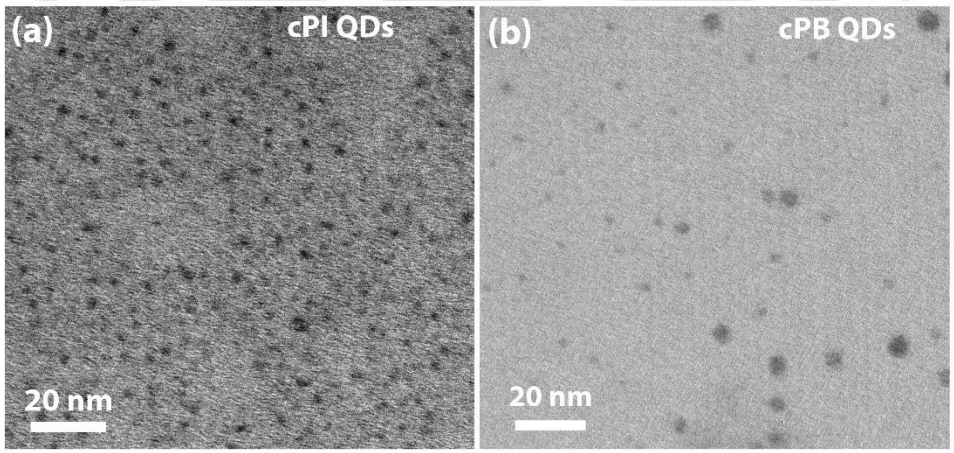

Fig. 3.8. TEM images of (a) cPI QDs and (b) cPB QD prepared by colloidal method [37].

that grown by colloidal method, we prepared colloidal QDs following the method reported by Huang et al.[37] and samples are termed as cPI and cPB corresponding to PI and PB precursors,

respectively. cPI and cPB QDs with average QD size ~2 nm were successfully synthesized, as shown in **Fig. 3.8(a,b)**, and utilized for the comparison of light emission properties along with stability.

3.4.2. XRD Analysis

In order to confirm the crystal structure and phase of the bulk perovskite films and PI/PB QDs, XRD pattern of each sample has been recorded and shown in **Fig. 3.9(a)**. Each characteristic diffraction peak of crystalline PI matches with the literature[38, 39]. No trace of the PbI_2 peak ($2\theta=12°$) is observed, which confirms the complete transformation of precursor materials (CH_3NH_3I and PbI_2) into PI. As evident from the XRD pattern, both the PI QDs and the F-TiO_2

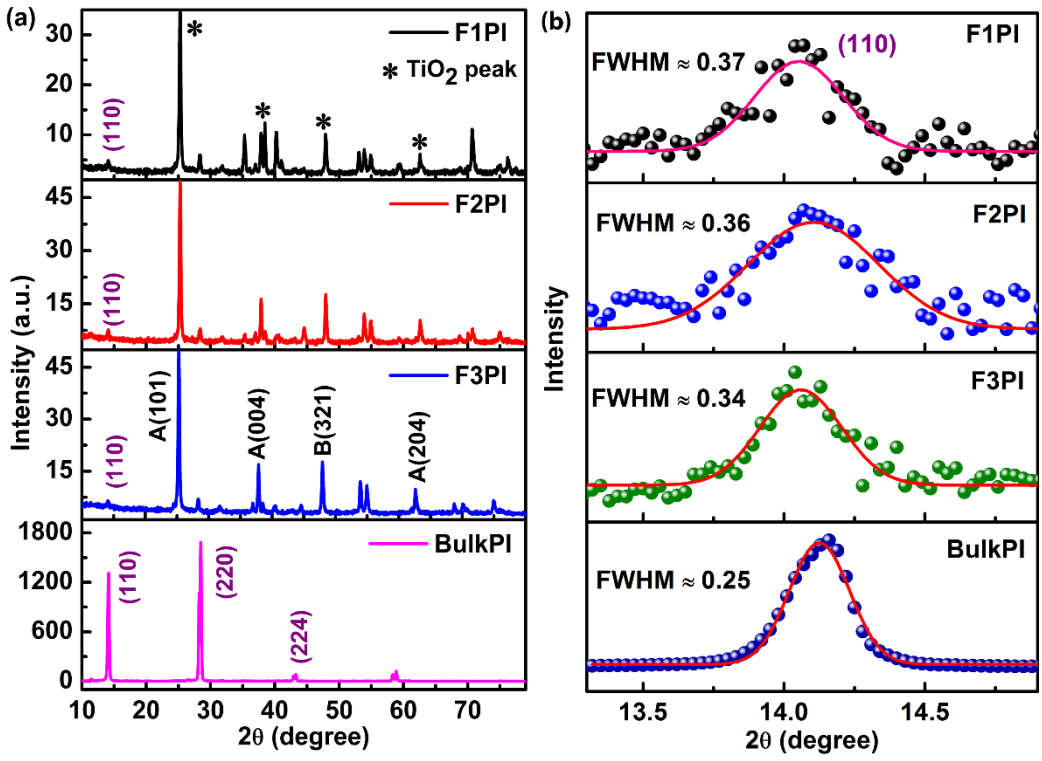

Fig. 3.9. (a) Comparison of the XRD pattern of F1PI, F2PI, F3PI and BulkPI. (b) Comparison of XRD pattern of (110) diffraction peak of different PI QDs.

template are highly crystalline in nature and the F-TiO_2 template is observed to be mostly in anatase phase (marked as "A" in the **Fig.3.9(a)**) with a small trace of brookite phase (marked as "B"). **Fig. 3.9(b)** shows the XRD pattern corresponding to (110) plane of PI QDs grown within the voids of F-TiO_2 template along with the bulk PI film grown on the ITO substrate. The intensity

of the characteristic (110) diffraction peak of PI QDs is much lower than the BulkPI film, which is due to the lower thickness/volume of PI QDs. With decreasing size of PI QDs, the line width of the XRD peak is observed to be broadened systematically, as evident from **Fig. 3.9(b)**. The (110) peak position slightly shifts to lower angle as the size of the PI QDs decreases, which indicates the presence of tensile strain in the QDs. The FWHM of (110) peak for the smallest PI QDs (F1PI) is estimated to be ~0.37°, which is ~1.5 times that of the BulkPI. Thus, the increase in FWHM is consistent with the formation of ultra-small size QDs. Though the Scherrer formula can predict the crystallite size of PI QDs grown on various F-TiO_2 templates, finer estimation of the QD size is difficult due to the low intensity of the diffraction peak. In this case, Scherrer formula gives a

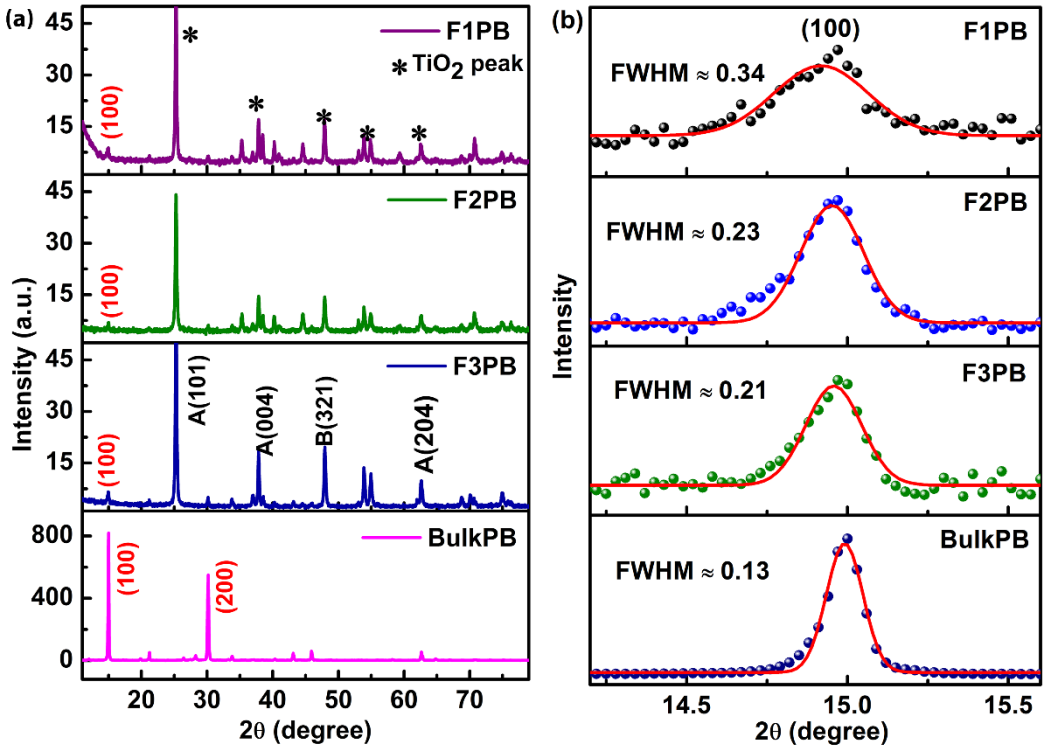

Fig. 3.10. (a) Comparison of the XRD pattern of F1PB, F2PB, F3PB and BulkPB. (b) (100) diffraction peak for PB QDs, grown on various F-TiO_2 templates.

higher estimate of the size of the QDs as compared to that measured from TEM, primarily due to their ultra-small sizes where the validity of the formula is questionable. **Fig. 3.10(a)** shows the XRD patterns of BulkPB and PB QDs grown on F-TiO_2 templates, suggesting a highly crystalline cubic phase of PB crystals. **Fig. 3.10(b)** shows the XRD pattern corresponding to (100) plane of PB NPs grown on various F-TiO_2 templates along with the BulkPB film. Similar to the PI NPs,

the (100) plane shifts to lower angle and the line width for F1PB increases systematically with decreasing the NP size and the FWHM is estimated to be ~2.6 times that of the BulkPB case. The possibility of ultra-thin capping layer of perovskite film on the F-TiO_2 NF is unlikely, since the XRD intensity is low and line width is relatively large for the QDs. To confirm the same, ultra-thin (~4 nm) PB film was deposited on ITO substrate by vapor deposition method and it showed ~3 times stronger XRD peak intensity compared to that of the QD case (**Fig. 3.11**). In the presence of any additional polycrystalline layer of perovskite film on the surface of the F-TiO_2, the intensity of XRD pattern would be more intense, which is contrary to our observation. Hence, the presence of any capping layer is ruled out in the present case.

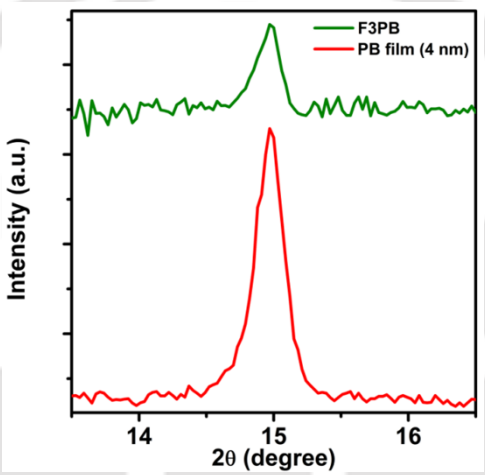

Fig. 3.11. Comparison of the XRD pattern of F3PB (QD size ~5 nm) and very thin PB film (4 nm) on ITO substrate. The curves are vertically shifted for clarity of presentation.

3.4.3. Optical Analysis

3.4.3.1. UV-vis Absorption Studies

DRS of the as-grown samples are studied to understand the change in the band structure due to the formation of perovskite NPs/QDs. From the DRS, Kubelka-Munk (K-M) function, F(R) is calculated which is related to the absorption coefficient (α) given by,

$$F(R) = (1 - R)^2/2R = \alpha/S \qquad (3.1)$$

where, R is the diffuse reflectance, S is the scattering coefficient. **Fig. 3.12(a)** exhibits the plot of the K-M function for PI QDs on various F-TiO_2 templates. A significant blue shift (up to 51 nm for F1PI) in the absorption edge of the PI QDs is observed with respect to that of the BulkPI film

on ITO substrate, which is clearly noticeable from the magnified view of plot for F1PI and BulkPI shown in the inset of **Fig. 3.12(a)**. Among different PI samples, the absorption edge of F1PI is observed maximally blue shifted, which may be due to the strong QC effect in the PI QDs in F1PI, since it contains the smallest size QDs. As the size of the QDs decreases below the exciton Bohr radius, there is a sharp transition in the absorption band due to excitonic transition, as observed in **Fig. 3.12(a)**[40]. To compare the optical properties of PB NPs/QDs grown in a similar way, F(R) for different samples was analyzed. **Fig. 3.12(b)** shows a comparison of F(R) of the sample F1PB,

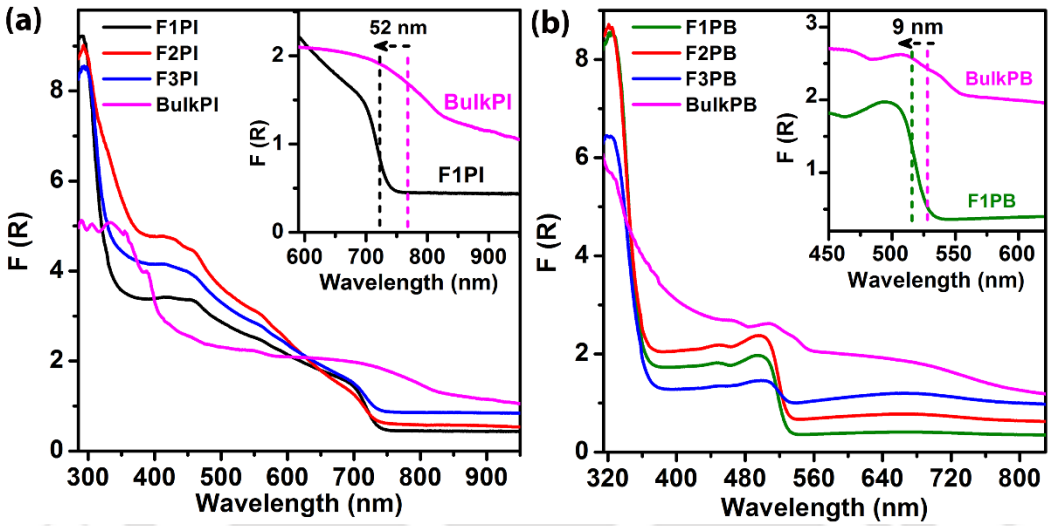

Fig. 3.12. (a) A plot of K-M function, F(R), for PI QDs grown on the different mesoporous F-TiO_2 template and the BulkPI film deposited on ITO substrate (BulkPI).The inset shows an enlarged view of absorption edge for F1PI and BulkPI indicating the blue shift of the absorption edge in F1PI with respect to the BulkPI film. (b) A comparison of the K-M functions for the samples F1PB, F2PB, F3PB and BulkPB film. The inset shows the blue shift of the absorption edge in F1PB as compared to that of BulkPB.

F2PB, F3PB, and BulkPB film. Though, a similar blue shift is observed for PB QDs compared to its bulk counterpart, PB QDs exhibit much lesser blue shift than PI QDs. In both the cases, the absorption spectra of perovskite QDs exhibit sharp band edge step indicating their direct bandgap nature. The F(R) value of bulk films is observed to be higher than the perovskite QDs, may be because of higher thickness of bulk perovskite film than the QDs. The contribution of F-TiO_2 absorption is observed at ~350 nm with a sharp edge and at a higher wavelength (> 400 nm) it possesses negligible absorbance[41, 42]. Thus, the measured absorbance of different samples observed in the visible region has a negligible contribution from the F-TiO_2 template and the observed features are characteristics of the PI/PB QDs.

3.4.3.2. Steady State Photoluminescence Studies

Due to the ultra-small size of the QDs, QC effect is expected to be prominent in PL spectrum, since quantization of energy levels and enlargement of the bandgap are the most prominent consequences of the confinement of carriers in semiconductor QDs. PL spectra for the PI QDs were recorded using a 405 nm laser excitation in ambient condition. **Fig. 3.13(a)** shows a comparison of PL spectra for pristine F1, BulkPI and F1PI. Note that pristine F1 does not show any measurable PL intensity in the visible region for the 405 nm excitation, while the BulkPI film possesses a relatively sharp PL peak centered at 762 nm, due to the direct band to band transition. The PI QDs grown on F1 template shows dramatically high PL intensity as compared to that of the bare F1 and BulkPI. **Fig. 3.13(b)** exhibits comparative PL spectra of PI QDs grown over the various F-TiO_2 templates with different pore sizes under identical conditions of measurement. PL intensity of PI QDs is observed to remarkably increased when the size of the QDs decreased, as depicted in the inset of **Fig. 3.13(b)**. As compared to the BulkPI film, the PL intensities of F1PI, F2PI, and F3PI are observed to be enhanced by ~41, 22 and 19 times, respectively, due to the reduced size of the QDs. The normalized PL spectra corresponding to **Fig. 3.13(b)** is displayed in **Fig. 3.13(c)** showing a systematic blue shift in PL peak position from F3PI to F1PI with the decrease in the size of the PI QDs, which is fully consistent with the absorption spectra. This strongly indicates the QC effect in the perovskite QDs confined in the pores of mesoporous F-TiO_2 templates. PI QDs grown within the mesoporous F-TiO_2 template display sharp PL peaks at 716 nm (F1PI), 721 nm (F2PI) and 737 nm (F3PI), which are observed to be blue-shifted from that of BulkPI (764 nm). The PL spectrum for F1PI is maximally blue shifted (47 nm) with respect to the BulkPI film.

This gradual shift of PL peak towards the higher energy is an indication of enlargement of the optical bandgap due to the quantum size effect[31]. Each PL spectrum for PI QDs possesses relatively broader line width (FWHM ~86 nm) as compared to the BulkPI film (~47 nm), which may be associated with the size distribution of PI QDs on the F-TiO_2 template. Additionally, Förster resonance energy transfer process from smaller to the larger QDs is reported to be prominent for the size distribution of QDs. Thus, the higher energy emission from smaller QDs may contribute to the overall broadening of the PL emission[43]. In order to quantify the quantum size effect of PB based perovskite QDs, comparative PL spectra were recorded for the PB QDs

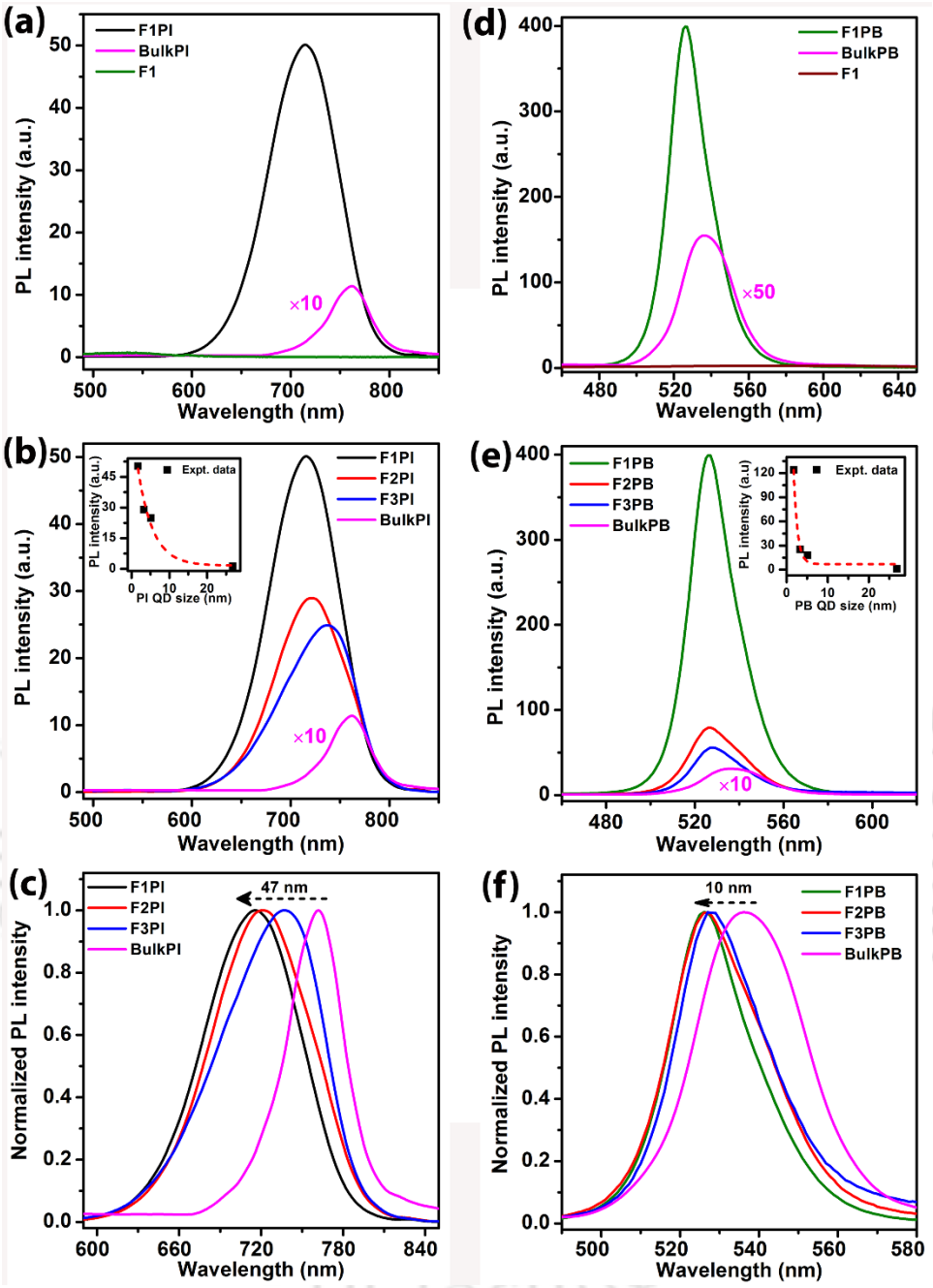

Fig. 3.13. (a) A comparison of PL spectra of pristine F1, BulkPI and F1PI, (b) comparison of PL spectra of F1PI, F2PI, F3PI and BulkPI film and the inset shows a variation of PL intensity with PI QD size, (c) the corresponding normalized PL spectra showing the blue shift of the PL peak up to 47 nm. (d) Comparison of PL spectra of pristine F1, BulkPB and F1PB, (e) comparison of PL spectra of various PB QDs with BulkPB, while inset shows the variation of PL intensity with PB QD size and (f) the corresponding normalized PL spectra. To enable comparison of intensities, some of the spectra are multiplied by the factors mentioned in respective image.

using a 355 nm laser excitation in ambient condition. **Fig. 3.13(d)** shows a comparison of PL spectra for the pristine F1, BulkPB film and PB QDs grown on F1, which depicts dramatically

enhanced PL intensity from F1PB compared to both the pristine F1 and BulkPB film. **Fig. 3.13(e)** shows a comparison of PL spectra of PB QDs grown on different F-TiO_2 templates and BulkPB film. As evident from the inset of **Fig. 3.13(e)**, the PL emission from F1PB is exceptionally intense and estimated to be ~124 fold higher than that of the BulkPB film. The corresponding normalized PL spectra are shown in **Fig. 3.13(f)**, which reveals a small blue shift (~10 nm) for the smallest size PB QDs (F1PB) as compared to the BulkPB film. FWHM of PL spectra for F1PB, F2PB, and F3PB are observed to be ~24 nm, 28 nm and 26 nm, respectively, while that for the BulkPB film is estimated to be ~31 nm. Thus, the reduction in line width of PL spectra for the PB QDs indicates their better color purity in emission, which is promising for the fabrication of efficient green LEDs. Note that the F-TiO_2 NFs template possesses very low oxygen vacancy defects and thus have very minor absorption in the visible-NIR region.

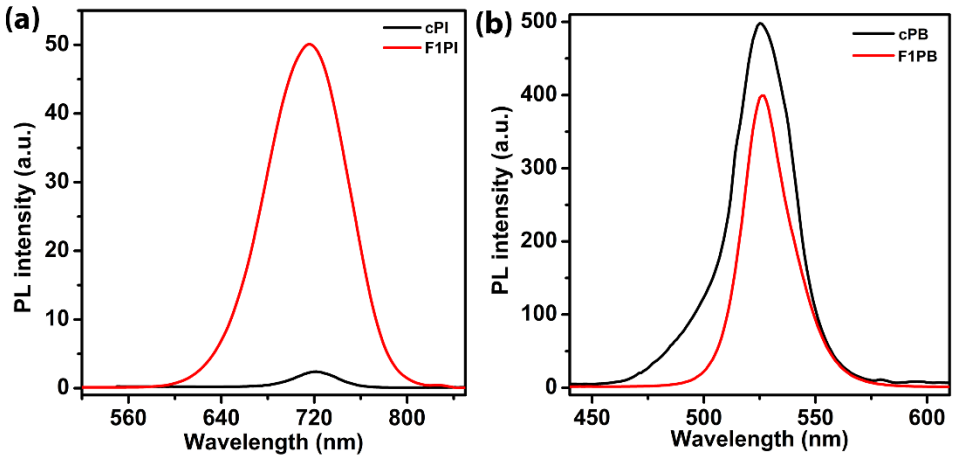

Fig. 3.14. (a) Comparison of PL spectra of cPI QDs and F1PI. (b) Comparison of PL spectra between cPB QDs and F1PB.

Since the absorption intensity of the F-TiO_2 template in the visible-NIR region is extremely low, the emission from the perovskite QDs is minimally affected by the reabsorption. Emission properties of PI and PB QDs grown on F-TiO_2 templates are compared with perovskite QDs synthesized using the top down method. PL emission of cPI QDs is found to be centered at ~ 721 nm (see **Fig. 3.14(a)**). PL intensity of F1PI is ~20 times higher than that of the cPI QD film, for similar concentration. **Fig. 3.14(b)** shows the PL spectrum of cPB QDs with excitonic emission centered at ~ 525 nm and FWHM ~31 nm. Though cPB QDs show slightly higher (~1.2 times) PL intensity than the F1PB, the line width of PL spectrum is higher for cPB QDs than that of PB QDs grown on F-TiO_2 template indicating high color purity of perovskite QDs grown in case of F1PB.

Again, for comparison, PL spectra of PI and PB film deposited on m-TiO_2 are compared with BulkPI and BulkPB film (see **Fig. 3.15**). For both the cases, the PL emission is less for m-TiO_2 template, which may be due to the well-known electron accepting nature of the m-TiO_2 layer[44]. In the present case, F-TiO_2 template is Fluorine doped (as confirmed from EDX) and Fluorine acts as n-type donor in TiO_2, which increases its electron concentration and reduces the probability of electron transfer from perovskite layer causing high radiative recombination. Seo et al. reported that Fluorine passivates the oxygen vacancy defects and acts as an extrinsic n-type donor for F-TiO_2 by increasing the concentration of free electrons in the conduction band of F-TiO_2[45]. This also leads to increase in surface electron concentration and enhanced catalytic activity by electron

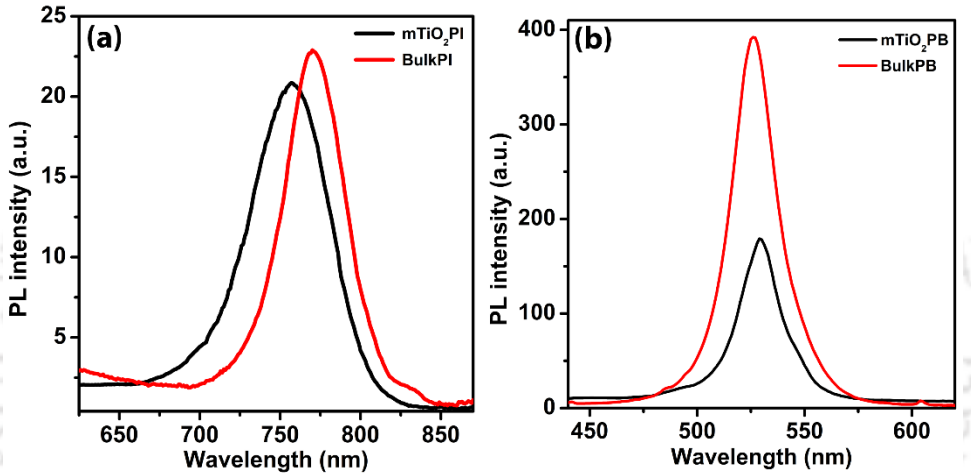

Fig. 3.15. (a) Comparison of PL spectra of PI NPs deposited on commercially available mesoporous TiO_2 and BulkPI film. (b) Comparison of PL spectra between PB NPs deposited on mesoporous TiO_2 and BulkPB film.

spill-over effect [46]. In our case, since the F-TiO_2 layer is electron rich, it minimizes the possibility of electron injection from the perovskite QDs to the F-TiO_2 layer. Using XPS analysis, it was reported that hydrothermally grown F-TiO_2 NCs contain two major peaks related to physical adsorption of F ions on the surface of the F-TiO_2 flowers and substitution of F atoms in the F-TiO_2 lattice[35]. This leads to the electron rich F-TiO_2 layer in the present case and strongly enhanced PL emission, compared to the commercial m-TiO_2 case.

A quantitative analysis of the blue shift with QD size and the origin of lower blue shift in PB QDs than the PI QDs are investigated using the well-known Brus equation[47]. In semiconductor QDs, the enlargement of the optical bandgap is usually explained by quantum confinement effect using

'particle in a box' model. The effective bandgap (E^*) of QDs due to QC effect was first calculated by Brus considering the Coulomb contribution[47] and is given by:

$$E^* = E_g + h^2/8\mu d^2 - 1.786e^2/4\pi\varepsilon_0\varepsilon_r d \qquad (3.2)$$

This relation was obtained by solving the Hamiltonian for the cluster's lowest excited state assuming the Hydrogen-like model to describe the interaction between electron and hole. Here, E^* is the energy of the lowest excited state of the exciton inside the QD, E_g is the energy of bandgap of the bulk perovskite, h is the Planck's constant, μ is the reduced exciton mass, d is the radius of the QD, e is the electronic charge, ε_0 and ε_r are the dielectric constants of vacuum and perovskite, respectively. The second term in **equation (3.2)** increases as d^{-2}, which corresponds to the first energy level of a pseudoparticle of reduced mass μ confined within a spherical well of radius d.

Table 3.1. *Details of sizes and the PL characteristics of the $CH_3NH_3PbI_3$ (PI) QDs.*

Sample	QD size (nm)	Peak position (nm)	Intensity enhancement factor	PL QY (%)
F1PI	1.7	716	41	25
F2PI	3.3	721	22	13
F3PI	5.1	737	19	11
BulkPI	--	764	1	1

Table 3.2. *Details of the PL characteristics of the $CH_3NH_3PbBr_3$ (PB) QDs.*

Sample	Peak position (nm)	Intensity enhancement factor	PL QY (%)
F1PB	526	124	57
F2PB	527	25	13
F3PB	528	18	11
BulkPB	536	1	5

The third term of the **equation (3.2)** represents the Coulomb attraction, which decreases as d^{-1} and this term is very prominent for smaller size/large bandgap material[47]. The bulk bandgap of PB is larger than that of PI and dielectric constant of PB is reported to be smaller than PI [48]. In the present case, the Coulomb interaction term is more prominent for larger bandgap PB (BulkPB

≈2.37 eV) than lower bandgap PI (BulkPB ≈1.62 eV) due to Coulomb screening effect, resulting in a smaller increase in the bandgap in PB film due to the confinement effect [49].

A summary of room temperature PL features with the size distribution of perovskite QDs is shown in **Table 3.1** and **Table 3.2**. **Fig. 3.16(a)** shows the variations of PL QY for the samples PI QDs and BulkPI, while **Fig. 3.16(b)** shows the comparison of PL QY for PB QDs along with BulkPB. The PL QY of PI and PB QDs grown on the F1 template are measured to be ~25% and 57%, respectively, which are significantly high compared to the bulk film as well as the other reported works in template-assisted growth of perovskite NPs[31, 32, 34]. High PL QY of perovskite QDs indicates low non-radiative recombination of excitons in QDs. Note that higher QY reported for the PB QDs is usually obtained with colloidal QDs solution, while the present results correspond to QD film on F-TiO_2 substrate/template. Hence, the observed high PL QY is considered to be

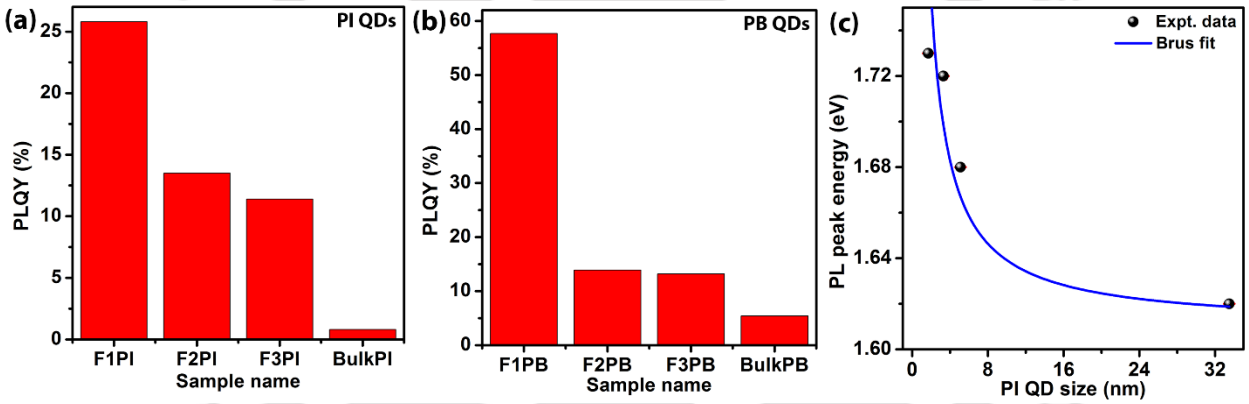

Fig. 3.16. A comparison of PL QY of various (a) PI QDs and (b) PB QDs with their bulk counterparts. (c) The spectral position of the PL peak maxima with respect to the particle size of PI QDs grown on the different F-TiO_2 templates. The points fitted to Brus equation is shown by a blue solid line.

significant for the development of QD thin film-based LEDs and display devices. The increase in PL intensity and high PL QY in case of perovskite QDs may be due to the high exciton binding energy which prevents the dissociation of excitons prior to radiative decay, increasing the emission probability [50]. The excitons in bulk perovskite with binding energy 28-75 meV are reported to be 3D Wannier type, which facilitates strong delocalization as it is close to the thermal energy at room temperature (RT) (~26 meV), tending to dissociate into free carriers before recombining radiatively, which results in low PL QY in bulk film[24, 36, 49, 51]. In contrast, the perovskite QDs or NCs possess sufficiently high exciton binding energy (~100 meV), which prevents their easy dissociation at RT, resulting in the enhanced PL emission. Additionally, efficient radiative

recombination of photogenerated charge carriers and passivation of non-radiative recombination may be one of the boosting factors for the high PL QY of perovskite QDs, which is further confirmed from the TRPL analysis (discussed later). F1PI sample contains uniformly decorated ultra-small size PI QDs (~1.7 nm), facilitating the extraordinary enhancement in PL emission. It is reported that the exciton Bohr radius (R_B) of $MAPbI_3$ is ~3 nm and thus to realize the strong QC, the condition $d/R_B < 2$ should be obeyed [32, 52-54]. In the present case, the size of the QDs for all the samples satisfies the above condition to exhibit the strong confinement effect.

In order to analyze further the QC effect quantitatively, the dependence of the size of the PI QDs on their PL properties has been analyzed. Fig. **3.16(c)** shows a plot of PL peak energy vs the size of the corresponding PI QDs estimated from the TEM analysis and the fitting with the Brus equation (solid line). From the fitted parameters, exciton reduced mass (μ) and dielectric constant (ε_r) were estimated as $0.19m_0$ and 8.9, respectively, where m_0 is electron rest mass. Considering these parameters, Bohr radius (R_B) is calculated as ~2.5 nm using the relation: $R_B = (m_0\varepsilon_r/\mu)(0.053)(nm)$. The estimated values of μ, ε_r, and R_B match fairly well with the reported values for BulkPI at RT [32, 54] and it validates the use of Brus equation for strong confinement effect observed here.

3.4.3.3. Low-Temperature Photoluminescence Studies

To investigate the effect of temperature on luminescence and excitonic properties of perovskite QDs, temperature dependent PL spectra were acquired for F1PI and F1PB in the range of 80-300 K (see **Fig. 3.17**). **Fig. 3.17(a)** shows the temperature-dependent PL spectra of F1PI QDs. With the lowering of temperature, the PL peak intensity increases monotonically and is the highest at 80 K. The inset of **Fig. 3.17(a)** shows the systematic decrease in PL intensity with increasing temperature. When the temperature increases from 80 K to 300 K, we observed a systematic blue shift in PL peak position (from 739 nm to 717 nm) and significant line width broadening for F1PI. The broadening of the PL peak at higher temperature can be explained on the basis of the expansion of the unit cell of perovskite crystal that increases the crystal strain, which in turn enhances the exciton-phonon interaction resulting into peak broadening[55]. The broadening of the PL peak at higher temperature was reported to be caused by the coupling of the excitons to acoustic phonons and to longitudinal optical (LO) phonons in GaN[56]. It has been reported that under non-resonant

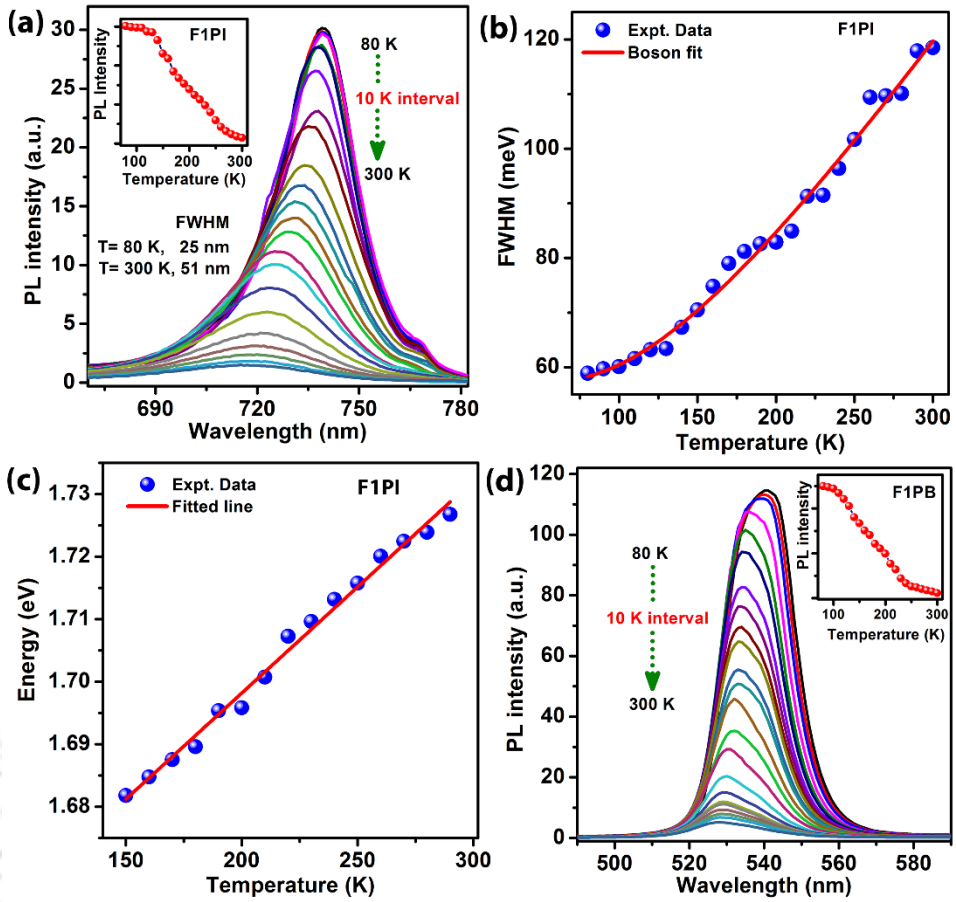

Fig. 3.17. (a) Temperature dependent PL spectra of F1PI; the inset shows the change in PL intensity with temperature. (b) Variation of FWHM of PL peak with temperature fitted with the Boson model. The symbols represent experimental data, while the solid line corresponds to fitted data. (c) Variation of PL peak energy of F1PI with respect to temperature. The symbols represent experimental data, while the solid line corresponds to fitted data. (d) Temperature dependent PL spectra of F1PB; the inset shows the variation of PL intensity with temperature.

factors including size distribution of the QDs may be responsible for the broadening of PL peak. The electron-phonon coupling of the QDs in F1PI is studied by plotting temperature-dependent PL spectral width, as shown in **Fig. 3.17(b)**. The experimental data of FWHM (Γ) are fitted using the Boson model given by, $\Gamma(T) = \Gamma_0 + \Gamma_{LO}/(exp(\hbar\omega_{LO}/k_BT) - 1)$, where, Γ_0 is the inhomogeneous broadening contribution, Γ_{LO} is the longitudinal exciton-optical phonon contribution to the FWHM and $\hbar\omega_{LO}$ is the LO phonon energy. From the fitted data, the obtained parameters are as follows: Γ_0 = 57.0 meV, Γ_{LO} = 168.3 meV, $\hbar\omega_{LO}$= 33.8 meV. Our result is fully consistent with reported value of optical phonon energy (25-42 meV) derived from the Raman scattering from $MAPbI_3$[57]. Note that no additional PL peak is observed at low-temperature regime, which discards the possibility of phase change in F1PI QDs at low temperature. **Fig.**

3.17(c) illustrates the temperature dependence of PL peak energy of F1PI QDs. F1PI QDs exhibit a blue shift of ~57 meV in PL peak position as the temperature increases from 80 K to 300 K. The experimental data of peak energy of F1PI in the temperature range 150-290 K is fitted with the equation[58], $E_g(T) = E_0 + A_{TE}T + A_{EP}(1 + 2/(exp(\hbar\omega/k_BT) - 1))$, where, E_0 is the bandgap at T=0 K, A_{TE} and A_{EP} are the weight of the thermal expansion (TE) and electron-phonon (EP) interaction terms. $\hbar\omega$ is the optical phonon energy. From the fitted data, the derived parameters are E_0= 1.63 eV, A_{TE}= 0.33 meV/K, A_{EP}= 4.96 meV and $\hbar\omega$= 42.3 meV. These values match well with the literature [58, 59]. Hence, the linear increase in PL peak energy with temperature may be attributed to the dominating contribution of TE, while the contribution of EP is negligible in this temperature range. **Fig. 3.17(d)** shows temperature-dependent PL spectra of F1PB QDs in the

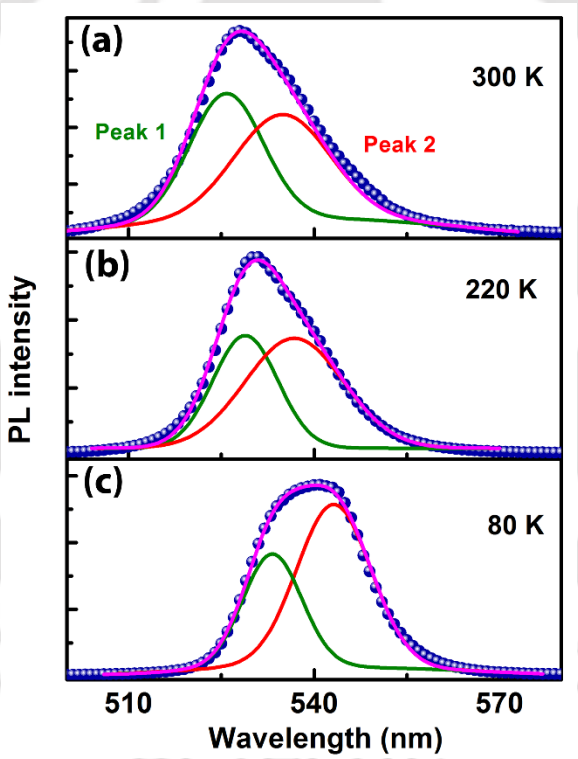

Fig. 3.18. PL spectra with Gaussian deconvolution for F1PB recorded at different temperatures: (a) 300 K, (b) 220 K and (c) 80 K.

range 80-300 K. Similar to the F1PI case, the PL intensity is observed to be decreased with increasing temperature due to thermal quenching along with a systematic blue shift. The phase transition induced change in PL peak (i.e. reversal of PL shift) is not observed in case of F1PB QDs[60], which discards the possibility of phase change in F1PB QDs. The room temperature (300

K) PL spectrum for F1PB shows an asymmetry in lower energy region, indicating a trace of bound excitonic emission. The deconvulated PL spectra of F1PB QDs at 300 K, 220 K, and 80 K are shown in **Fig. 3.18(a-c)**, respectively. At 300 K, the spectral weight of Peak 1 at ~525 nm arising due to the free exciton recombination dominates over the bound exciton recombination (peak 2 at ~535 nm), as shown in **Fig. 3.18(a)**. With the lowering of temperature, the bound excitonic emission increases and at 80 K, it dominates over the free excitonic recombination, as shown in **Fig. 3.18(c)**. **Fig. 3.19(a)** shows the variation in PL peak energy of F1PB QDs with temperature. On the other hand, F1PB QDs show relatively small blue shift for both the peaks (~33 meV for peak 1 and ~30 meV for peak 2) at a rate ~0.13 meV/K in the temperature range 80-300 K. This blue shift may be attributed to the electron-phonon coupling[61]. Exciton binding energy (E_b) for the various QDs is estimated from temperature-dependent PL spectra. The temperature dependence of the integrated PL intensity of F1PB and F1PI QDs are shown in **Fig. 3.19(b)** and the experimental data are fitted using the Arrhenius equation, given by, $I(T) = I_0/(1 + A\,exp(-E_b/K_BT))$, where, *I(T)* and I_0 are the integrated PL intensities at temperatures T and 0 K, respectively. *A* is a constant. In order to estimate the E_b of partially embedded perovskite QDs, the experimental data are fitted in the higher temperature region (250-300 K). From the fitting of the Arrhenius equation above keeping the parameters free, the E_b is estimated to be 162.1±22.2 meV and 271.1±34.1 meV for F1PI and F1PB QDs, respectively. Thus, the exciton binding energy of perovskite QDs is very high in the present case as compared to the reported values for QDs as well as the bulk counterpart (~32 meV)[61]. Note that there are some characteristic differences in PL evolution with temperature for F1PI and F1PB. For example, the decrease in PL intensity with temperature is faster in F1PI as compared to F1PB due to lower exciton binding energy value. The shift in PL peak position with increasing temperature is also larger in F1PI in contrast to F1PB. Also, asymmetry is observed in F1PB at low temperature due to the dominant contribution of bound excitons. Higher exciton binding energy of PB based QDs compared to the PI based QDs originates from lower dielectric constant, larger bandgap energy and stable cubic crystal structure in F1PB.

Note that size dependent exciton binding energy has been reported for conventional semiconductor QDs. Using electron-hole explicitly correlated Hartree-Fock (eh-XCHF) method, it is reported that electron-hole recombination probability and exciton binding energy for CdSe QDs follows a scaling relationship with QD size as $\sim d^{-n}$. As the size of the particle increases by 16.1 times and

the exciton binding energy and recombination probability decreases by a factor of 12.9 and 4.55×10^5, respectively[62]. In our case, for the F1PI QDs, as the size decreased by ~19.4 times (from ~33 nm in bulk to 1.7 nm in QDs), the exciton binding energy increases by a factor of ~5.1, which is quite consistent with the above prediction, which had an error bar of 28 %. For F1PB QDs, the factor comes out to be ~8.5 times. The large increase in exciton binding energy is

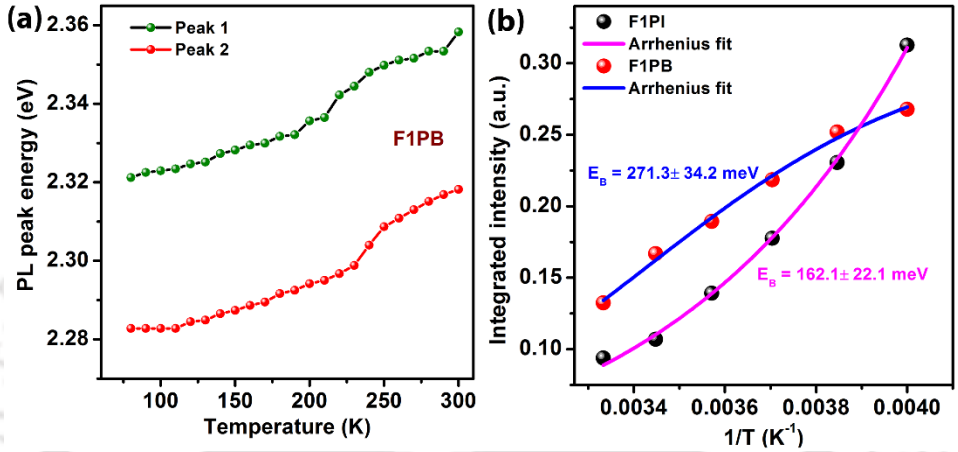

Fig. 3.19. (a) Variation in PL peak energy of F1PB with temperature. In the case of F1PB, two peaks (peak 1, peak 2) are fitted. (b) PL integrated intensity vs inverse of temperature for F1PI and F1PB. The experimental data are fitted with the Arrhenius equation. The symbols represent experimental data, while the solid line corresponds to fitted data.

explained on the basis of strong confinement effect in the small QDs, where the binding energy varies as d^{-1}[51]. Thus, due to the increase in the exciton binding energy, the perovskite QDs show stronger QC effect than their bulk counterparts. Higher exciton binding energy for perovskite QDs supports higher PL QY for QDs compared to bulk films, resulting in stable and outstandingly enhanced PL emission at room temperature[61]. Higher exciton binding energy of PB based QDs compared to the PI based QDs originates from lower dielectric constant and larger bandgap energy in F1PB[49]. Exciton binding is calculated theoretically from electron-hole interaction energy V_{eh} which is calculated from the electron-hole pair density using the expression[63], $V_{eh} = \int d\vec{r_e} d\vec{r_h} \rho_{eh}(\vec{r_e}, \vec{r_h}) r_{eh}^{-1} \varepsilon^{-1}(\vec{r_e}, \vec{r_e})$, where ρ_{eh} is the electron-hole pair density function and ε^{-1} is the inverse dielectric function. Hence, higher dielectric function corresponds to lower exciton binding energy. Exciton binding energy of perovskite QDs grown on F-TiO_2 templates is quite high compared to the other reported values for colloidal-based perovskite NP films, which makes it a very good candidate for stable light emitting and other optoelectronic device applications at room temperature[64].

3.4.3.4. Time-Resolved Photoluminescence Studies

In order to investigate lifetime and recombination kinetics of carriers, TRPL measurement was performed on PI QDs on various F-TiO_2 templates and BulkPI film using a 405 nm laser excitation. The TRPL decay transients fitted with bi-exponential decay function can be expressed as follows: $I(t) = \sum_{i=1}^{2} A_i exp(-t/\tau_i)$, where A_i is the amplitude of the TRPL decay curve corresponding to

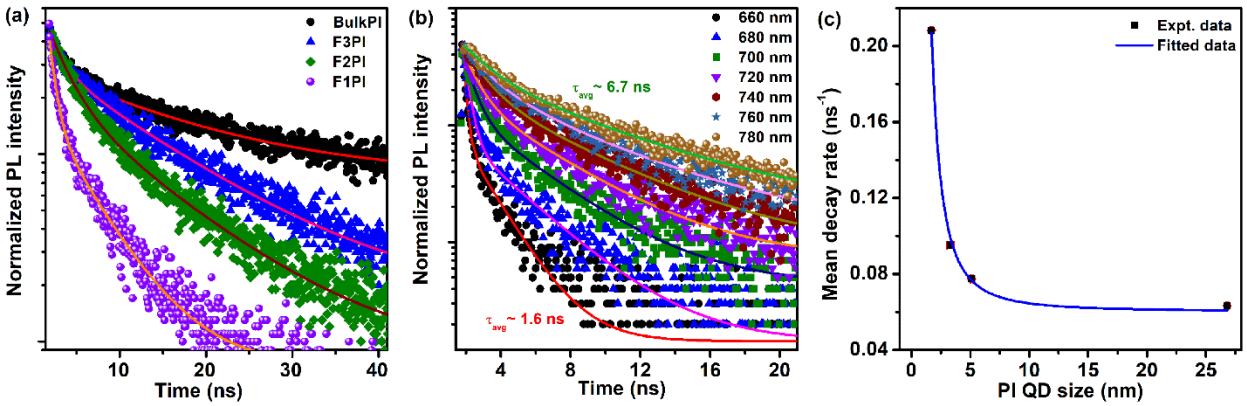

Fig. 3.20. (a) A comparison of TRPL spectra of BulkPI film, F1PI, F2PI and F3PI with 405 nm laser excitation and monitored at their respective peak position. (b) PL decay of sample F1PI monitored at different emission wavelengths. (c) PL decay rate as a function of PI QD size. Blue solid line shows the best fit curve following an inverse quadratic dependence with QD size.

the lifetime τ_i. The average lifetime (τ_{avg}) is calculated considering the following relation: $\tau_{avg} = (A_1\tau_1^2 + A_2\tau_2^2)/(A_1\tau_1 + A_2\tau_2)$. **Fig. 3.20(a)** shows the TRPL decay profiles of BulkPI film and various PIQDs monitoring the emission at their respective PL peak positions. The details of the individual components of BulkPI film and PI QDs are given in **Table 3.3**. The average life times are estimated to be ~15.8 ns, 12.9 ns, 10.5 ns and 4.9 ns for BulkPI film, F3PI, F2PI, and F1PI, respectively. Thus, the τ_{avg} reduces systematically with the reduction of QD size, consistent with

Table 3.3. *The details of the TRPL decay time constants for the $CH_3NH_3PbI_3$ QDs.*

Sample	τ_1 (ns)	A_1 (%)	τ_2 (ns)	A_2 (%)	τ_{avg} (ns)
BulkPI	1.34	12.92	16.02	87.08	15.84
F3PI	1.78	9.91	13.08	90.09	12.91
F2PI	2.00	27.68	11.13	73.32	10.47
F1PI	0.74	38.59	5.21	61.41	4.85

the previous reports[18, 65]. The smallest size PI QDs (F1PI) possesses ~3 fold faster recombination or short average lifetime compared to the BulkPI film. Shorter lifetime of PI QDs implies faster recombination and thus higher PL QY, suggesting the PL decay of PI QDs mainly through the exciton recombination and suppression of non-radiative recombination. TRPL spectra of F1PI monitored at different emission wavelengths (660-780 nm at 20 nm intervals) are obtained under 405 nm laser excitation and the results are shown in **Fig. 3.20(b)**. Each spectrum is fitted with bi-exponential decay function and the fitted curve is shown by the solid line. At lower emission wavelengths, the PL decay times are observed to be shortened systematically (from 6.75 ns at 780 nm to 1.60 ns at 669 nm) confirming the QC effect of PI QDs. Thus, the broad PL spectrum for F1PI is mainly due to the variation in the PI QDs size and faster emission occurs at higher energies[47]. Since the mean decay rate (Γ) is related to the PL QY by the equation: $PL\ QY = \Gamma_r/\Gamma = \Gamma_r/(\Gamma_{nr} + \Gamma_r)$, where, Γ is inversely proportional to τ, Γ_r and Γ_{nr} are the radiative and non-radiative decay rates, respectively. In our case, the PL QY of PI QDs is very high, hence the radiative recombination can be considered to be dominant over non-radiative recombination even at room temperature. Thus, the PL QY corresponding to the PI QDs may proportionally vary with Γ_r. The dependence of PL decay rate on the PI QDs size is plotted in Fig. **3.20(c)**.

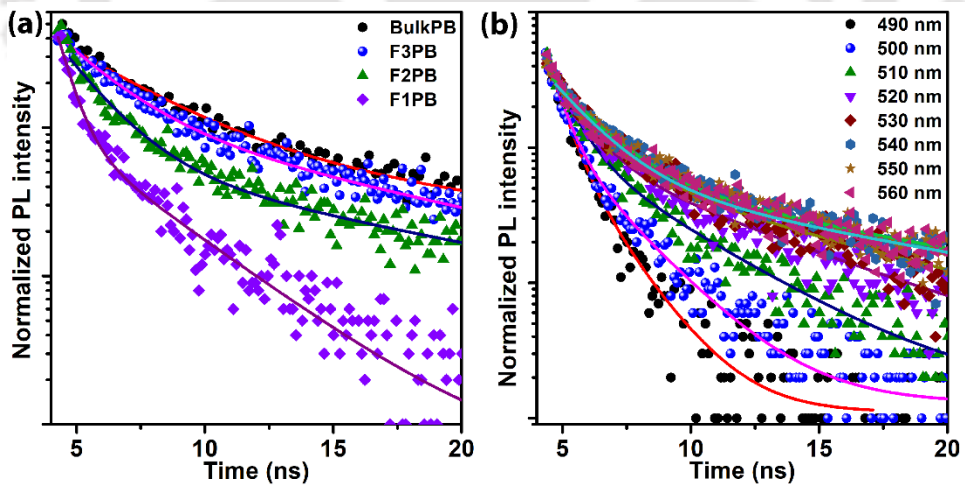

Fig. 3.21. (a) Comparison of the TRPL spectra of BulkPB film, F3PB, F2PB and F1PB with 375 nm excitation monitored at their respective emission peak, (b) TRPL decay of F1PB monitored at different emission wavelengths.

The experimental data (Γ) can precisely be fitted with the relation, $\Gamma \sim 1/d^2$. This is fully consistent with the expected behavior that the radiative decay rate is inversely proportional to the surface area of the QDs and the number of radiative decay path increases as the QDs size decreases. For

comparison, TRPL study was also performed on various PB QDs and BulkPB film with 375 nm laser excitation, as shown in **Fig. 3.21(a)**. Similar to the PI QDs, τ_{avg} of F1PB, F2PB, F3PB, and BulkPB are found to be ~3.3 ns, 7.2 ns, 9.9 ns and 20.2 ns, respectively, demonstrating faster decay for PB QDs than the BulkPB film. PL emission corresponding to the QDs is reported to be confined in the bimolecular regime where decay rate is mainly due to radiative recombination resulting in the faster decay than the bulk film, which possesses longer decay time in the monomolecular regime due to the influence of non-radiative trap filling[66]. As the size of QD enters in the quantum regime, the confinement of electron and hole wave functions is observed to be enhanced facilitating the greater radiative transition probability, which results in faster radiative decay[67]. TRPL spectra for F1PB recorded at different emission wavelengths (490-560 nm) at an interval of 10 nm with 375 nm laser excitation are shown in **Fig. 3.21(b)**. PL decay time is observed to be

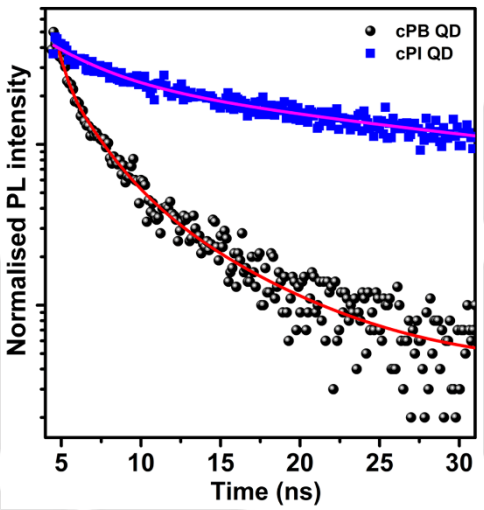

Fig. 3.22. Comparison of TRPL decay profiles of cPI and cPB QDs.

systematically shortened with the lowering of the emission wavelength. At higher emission wavelengths, the TRPL decay profiles are observed to be overlapped, confirming the narrow size distribution of PB QDs (absence of large PB QDs), further verified by the sharp PL emission (FWHM ~24 nm). TRPL decay profiles of cPI and cPB QDs on ITO substrates are shown in **Fig. 3.22**. The average lifetime of cPB and cPI QDs are ~3.8 ns and ~27.1 ns, respectively. Average carrier lifetime for F1PB and cPB QDs are nearly equal, which is consistent with their emission behavior. It reveals the fact that cPB QDs possess high radiative recombination similar to that of F1PB QDs. In contrast, the average lifetime of carriers in cPI QDs is larger than even the BulkPI film, which reveals the presence of non-radiative decay paths in it.

3.4.3.5. Photostability Studies

Despite the tremendous efforts to prepare the air and photo stabilized perovskites, it is still one of the major challenges for the commercialization of perovskite QD based devices. In order to test the photostability, each as-grown sample was exposed to continuous UV irradiation (360 nm laser, 18 mW at source) for several hours and PL emission was recorded as a function of time at a regular interval. As shown in **Fig. 3.23(a)**, the PL emission of BulkPI and BulkPB films are observed to be drastically reduced to 25 % and 67 % after 10 h of UV irradiation, respectively. As compared to the bulk counterpart, both the PI QDs and PB QDs show significantly improved photostability. Even after 10h of UV irradiation, F1PB preserves ~99 % of its PL intensity, while F1PI shows ~86 %. The lower stability of F1PI is due to the fact that iodide-based NPs are known to be highly vulnerable to moisture and UV light. Stability of F1PI and F1PB QDs are compared with cPI and

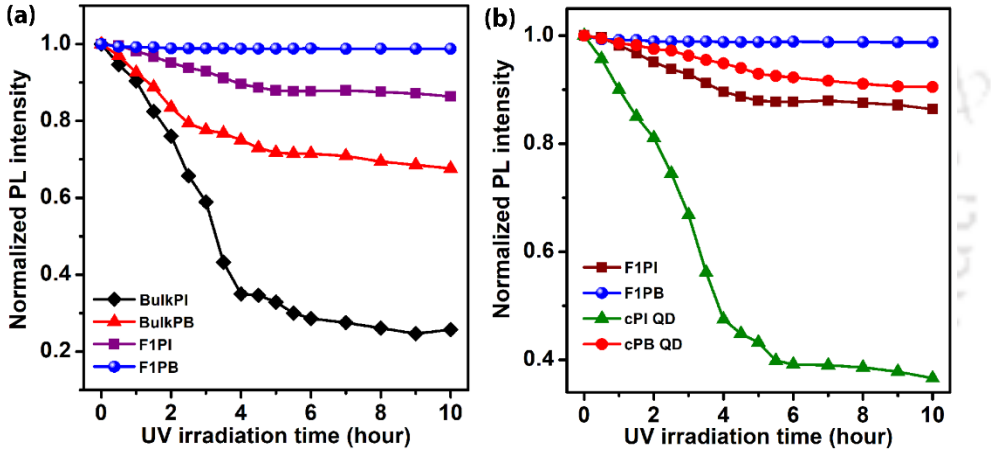

Fig. 3.23. (a) Optical stability test of perovskite QDs (PI and PB) with 360 nm UV laser (power 18 mW at source) exposure up to 10 h. (b) Optical stability test among perovskite QDs (PI and PB) synthesized using top down method, F1PI and F1PB with 360 nm UV laser (power 18 mW at source) exposure up to 10 h.

cPB QDs (see **Fig. 3.23(b)**). It's evident that cPI QDs degrade very fast under UV irradiation and PL emission reduces to ~36 % of initial value after 10 h of UV irradiation. cPB QDs show better stability than the cPI QDs and it restores 90 % of its initial PL intensity after 10 h of UV light exposure. Hence, perovskite QDs grown on F-TiO_2 template show superior stability compared to the QDs prepared using colloidal method. In the present case, the mesoporous sites of the F-TiO_2 flower act as the nucleation sites for the growth of perovskite QDs and these QDs are surrounded and partly covered by the F-TiO_2 NCs, which restricts the perovskite QDs from the complete exposure to moisture and UV irradiation, preventing its fast degradation. We have observed that

the as-grown perovskite QDs are quite stable in the ambient atmosphere and maintains its initial PL intensity for more than a month. For the fully embedded QDs, stability is expected to be much better and would be suitable for the fabrication of stable devices.

3.5. Summary and Conclusions

In this chapter, we have reported a cost-effective and reproducible method to grow perovskite QDs partially embedded inside the pores on F-TiO_2 template with high optical quality in ambient condition. A comparative analysis of the structural and photo-physical properties of Iodine and Bromine based perovskite QDs is presented. Our study offers a novel template-assisted synthesis route for perovskite QDs with very high photo and air stability, which is promising for various optoelectronic applications including light emitting devices. The highlights of the chapter are summarized below.

1. Mesoporous F-TiO_2 template assisted growth of stable hybrid perovskite QDs is demonstrated here.
2. The smallest sized $MAPbBr_3$ QDs exhibit sharp and dramatically enhanced (more than two orders of magnitude) PL emission with extremely high PL QY of 57 %, while the iodide-based perovskite shows ~25 % PL QY, which are the highest among the reported values for the template assisted growth of perovskite QD films.
3. Quantitative analysis of the PL data reveals strong confinement effect validated by fitting the experimental data with canonical expressions derived for the quantum regime.
4. A careful analysis of the low-temperature PL spectra reveals very high exciton binding energy (162-272 meV) for the QDs as compared to the bulk film (32 meV) due to high effective dielectric constant, and high electron-hole recombination probability in the QDs, which supports extremely high PL QY and stable emission from the QDs.
5. The blue shift of the PL peak with increasing temperature is quantitatively explained on the basis of thermal expansion effect.
6. The strongly enhanced PL of perovskite QDs is ascribed to enhanced radiative recombination probability and QC effect, as revealed from the TRPL analysis.
7. The perovskite QDs embedded in porous TiO_2 template are photostable as it maintains its initial PL intensity up to several hours (≥10 h) under the UV laser exposure (18 mW), while that of bulk film decreases to <67 %.

References

[1] J.-P. Correa-Baena, A. Abate, M. Saliba, W. Tress, T.J. Jacobsson, M. Grätzel, A. Hagfeldt, The rapid evolution of highly efficient perovskite solar cells, Energy Environ. Sci., 10 (2017) 710-727.
[2] Z. Zhu, Y. Bai, X. Liu, C.C. Chueh, S. Yang, A.K.Y. Jen, Enhanced Efficiency and Stability of Inverted Perovskite Solar Cells Using Highly Crystalline SnO2 Nanocrystals as the Robust Electron-Transporting Layer, Adv. Mater., 28 (2016) 6478-6484.
[3] N.-G. Park, M. Grätzel, T. Miyasaka, K. Zhu, K. Emery, Towards stable and commercially available perovskite solar cells, Nat. Energy., 1 (2016) 16152.
[4] C.S. Ponseca Jr, T.J. Savenije, M. Abdellah, K. Zheng, A. Yartsev, T.r. Pascher, T. Harlang, P. Chabera, T. Pullerits, A. Stepanov, Organometal halide perovskite solar cell materials rationalized: ultrafast charge generation, high and microsecond-long balanced mobilities, and slow recombination, J. Am. Chem. Soc., 136 (2014) 5189-5192.
[5] C. Wehrenfennig, G.E. Eperon, M.B. Johnston, H.J. Snaith, L.M. Herz, High charge carrier mobilities and lifetimes in organolead trihalide perovskites, Adv. Mater., 26 (2014) 1584-1589.
[6] G. Xing, N. Mathews, S. Sun, S.S. Lim, Y.M. Lam, M. Grätzel, S. Mhaisalkar, T.C. Sum, Long-Range Balanced Electron-and Hole-Transport Lengths in Organic-Inorganic CH3NH3PbI3, Science, 342 (2013) 344-347.
[7] S.D. Stranks, G.E. Eperon, G. Grancini, C. Menelaou, M.J. Alcocer, T. Leijtens, L.M. Herz, A. Petrozza, H.J. Snaith, Electron-hole diffusion lengths exceeding 1 micrometer in an organometal trihalide perovskite absorber, Science, 342 (2013) 341-344.
[8] A. Kojima, K. Teshima, Y. Shirai, T. Miyasaka, Organometal halide perovskites as visible-light sensitizers for photovoltaic cells, J. Am. Chem. Soc., 131 (2009) 6050-6051.
[9] H.-S. Kim, C.-R. Lee, J.-H. Im, K.-B. Lee, T. Moehl, A. Marchioro, S.-J. Moon, R. Humphry-Baker, J.-H. Yum, J.E. Moser, Lead iodide perovskite sensitized all-solid-state submicron thin film mesoscopic solar cell with efficiency exceeding 9%, Sci. Rep., 2 (2012) 591.
[10] W.S. Yang, B.-W. Park, E.H. Jung, N.J. Jeon, Y.C. Kim, D.U. Lee, S.S. Shin, J. Seo, E.K. Kim, J.H. Noh, Iodide management in formamidinium-lead-halide–based perovskite layers for efficient solar cells, Science, 356 (2017) 1376-1379.
[11] S. Zhuo, J. Zhang, Y. Shi, Y. Huang, B. Zhang, Self-Template-Directed Synthesis of Porous Perovskite Nanowires at Room Temperature for High-Performance Visible-Light Photodetectors, Angew. Chem. Int. Ed., 54 (2015) 5693-5696.
[12] F. Wang, J. Mei, Y. Wang, L. Zhang, H. Zhao, D. Zhao, Fast Photoconductive Responses in Organometal Halide Perovskite Photodetectors, ACS Appl. Mater. Interfaces, 8 (2016) 2840-2846.
[13] G. Kakavelakis, E. Gagaoudakis, K. Petridis, V. Petromichelaki, V. Binas, G. Kiriakidis, E. Kymakis, Solution Processed CH3NH3PbI3–xClx Perovskite Based Self-Powered Ozone Sensing Element Operated at Room Temperature, ACS Sens., 3 (2018) 135-142.
[14] H. Zhu, Y. Fu, F. Meng, X. Wu, Z. Gong, Q. Ding, M.V. Gustafsson, M.T. Trinh, S. Jin, X.Y. Zhu, Lead Halide Perovskite Nanowire Lasers with Low Lasing Thresholds and High Quality Factors, Nat. Mater, 14 (2015) 636-642.
[15] Y. Hassan, Y. Song, R.D. Pensack, A.I. Abdelrahman, Y. Kobayashi, M.A. Winnik, G.D. Scholes, Structure-Tuned Lead Halide Perovskite Nanocrystals, Adv. Mater., 28 (2016) 566-573.
[16] J.A. Sichert, Y. Tong, N. Mutz, M. Vollmer, S. Fischer, K.Z. Milowska, R. García Cortadella, B. Nickel, C. Cardenas-Daw, J.K. Stolarczyk, Quantum Size Effect in Organometal Halide Perovskite Nanoplatelets, Nano Lett., 15 (2015) 6521-6527.

[17] J. Cho, Y.-H. Choi, T.E. O'Loughlin, L. De Jesus, S. Banerjee, Ligand-Mediated Modulation of Layer Thicknesses of Perovskite Methylammonium Lead Bromide Nanoplatelets, Chem. Mater., 28 (2016) 6909-6916.
[18] F. Zhang, H. Zhong, C. Chen, X.-g. Wu, X. Hu, H. Huang, J. Han, B. Zou, Y. Dong, Brightly Luminescent and Color-Tunable Colloidal CH3NH3PbX3 (X= Br, I, Cl) Quantum Dots: Potential Alternatives for Display Technology, ACS nano, 9 (2015) 4533-4542.
[19] P. Tyagi, S.M. Arveson, W.A. Tisdale, Colloidal Organohalide Perovskite Nanoplatelets Exhibiting Quantum Confinement, J. Phys. Chem. Lett., 6 (2015) 1911-1916.
[20] L. Protesescu, S. Yakunin, M.I. Bodnarchuk, F. Krieg, R. Caputo, C.H. Hendon, R.X. Yang, A. Walsh, M.V. Kovalenko, Nanocrystals of cesium lead halide perovskites (CsPbX3, X= Cl, Br, and I): novel optoelectronic materials showing bright emission with wide color gamut, Nano Lett., 15 (2015) 3692-3696.
[21] H. Huang, F. Zhao, L. Liu, F. Zhang, X.-g. Wu, L. Shi, B. Zou, Q. Pei, H. Zhong, Emulsion Synthesis Of Size-Tunable CH3NH3PbBr3 Quantum Dots: An Alternative Route Toward Efficient Light-Emitting Diodes, ACS Appl. Mater. Interfaces, 7 (2015) 28128-28133.
[22] V. Malgras, J. Henzie, T. Takei, Y. Yamauchi, Hybrid methylammonium lead halide perovskite nanocrystals confined in gyroidal silica templates, ChemComm, 53 (2017) 2359-2362.
[23] S. Gonzalez-Carrero, L. Francés-Soriano, M. González-Béjar, S. Agouram, R.E. Galian, J. Pérez-Prieto, The luminescence of CH3NH3PbBr3 perovskite nanoparticles crests the summit and their photostability under wet conditions is enhanced, Small, 12 (2016) 5245-5250.
[24] L.C. Schmidt, A. Pertegás, S. González-Carrero, O. Malinkiewicz, S. Agouram, G. Mínguez Espallargas, H.J. Bolink, R.E. Galian, J. Pérez-Prieto, Nontemplate Synthesis of CH3NH3PbBr3 Perovskite Nanoparticles, J. Am. Chem. Soc., 136 (2014) 850-853.
[25] T. Leijtens, G.E. Eperon, N.K. Noel, S.N. Habisreutinger, A. Petrozza, H.J. Snaith, Stability of metal halide perovskite solar cells, Adv. Energy Mater., 5 (2015).
[26] L. Loo, P. Patel, Perovskite photovoltaics: David Mitzi addresses the promises and challenges, MRS Bull., 40 (2015) 636.
[27] J. Pan, S.P. Sarmah, B. Murali, I. Dursun, W. Peng, M.R. Parida, J. Liu, L. Sinatra, N. Alyami, C. Zhao, Air-stable surface-passivated perovskite quantum dots for ultra-robust, single-and two-photon-induced amplified spontaneous emission, J. Phys. Chem. Lett., 6 (2015) 5027-5033.
[28] S. Yang, F. Zhang, J. Tai, Y. Li, Y. Yang, H. Wang, J. Zhang, Z. Xie, B. Xu, H. Zhong, A detour strategy for colloidally stable block-copolymer grafted MAPbBr 3 quantum dots in water with long photoluminescence lifetime, Nanoscale, 10 (2018) 5820-5826.
[29] A. Kojima, M. Ikegami, K. Teshima, T. Miyasaka, Highly Luminescent Lead Bromide Perovskite Nanoparticles Synthesized with Porous Alumina Media, Chem. Lett., 41 (2012) 397-399.
[30] D. Di, K.P. Musselman, G. Li, A. Sadhanala, Y. Ievskaya, Q. Song, Z.-K. Tan, M.L. Lai, J.L. MacManus-Driscoll, N.C. Greenham, Size-dependent photon emission from organometal halide perovskite nanocrystals embedded in an organic matrix, J. Phys. Chem. Lett., 6 (2015) 446-450.
[31] V. Malgras, S. Tominaka, J.W. Ryan, J. Henzie, T. Takei, K. Ohara, Y. Yamauchi, Observation of Quantum Confinement in Monodisperse Methylammonium Lead Halide Perovskite Nanocrystals Embedded in Mesoporous Silica, J. Am. Chem. Soc., 138 (2016) 13874-13881.
[32] M. Anaya, A. Rubino, T.C. Rojas, J.F. Galisteo-López, M.E. Calvo, H. Míguez, Strong Quantum Confinement and Fast Photoemission Activation in CH3NH3PbI3 Perovskite Nanocrystals Grown within Periodically Mesostructured Films, Adv. Opt. Mater., 5 (2017).
[33] S. Demchyshyn, J.M. Roemer, H. Groiß, H. Heilbrunner, C. Ulbricht, D. Apaydin, A. Böhm, U. Rütt, F. Bertram, G. Hesser, M.C. Scharber, N.S. Sariciftci, B. Nickel, S. Bauer, E.D. Głowacki, M. Kaltenbrunner, Confining metal-halide perovskites in nanoporous thin films, Sci. Adv, 3 (2017).

[34] J. Ghosh, R. Ghosh, P.K. Giri, Mesoporous Si Nanowire Templated Controlled Fabrication of Organometal Halide Perovskite Nanoparticles with High Photoluminescence Quantum Yield for Light-Emitting Applications, ACS Appl. Nano Mater., 1 (2018) 1551-1562.
[35] K.K. Paul, S. Jana, P. Giri, Tunable and High Photoluminescence Quantum Yield from Self-Decorated TiO2 Quantum Dots on Fluorine Doped Mesoporous TiO2 Flowers by Rapid Thermal Annealing, Part. Part. Syst. Charact., (2018) 1800198.
[36] Z.-K. Tan, R.S. Moghaddam, M.L. Lai, P. Docampo, R. Higler, F. Deschler, M. Price, A. Sadhanala, L.M. Pazos, D. Credgington, F. Hanusch, T. Bein, H.J. Snaith, R.H. Friend, Bright Light-Emitting Diodes Based on Organometal Halide Perovskite, Nat Nanotechnol., 9 (2014) 687.
[37] H. Huang, Q. Xue, B. Chen, Y. Xiong, J. Schneider, C. Zhi, H. Zhong, A.L. Rogach, Top-Down Fabrication of Stable Methylammonium Lead Halide Perovskite Nanocrystals by Employing a Mixture of Ligands as Coordinating Solvents, Angew. Chem., 56 (2017) 9571-9576.
[38] B. Lei, V.O. Eze, T. Mori, Effect of Morphology Control of Light Absorbing Layer on CH3NH3PbI3 Perovskite Solar Cells, J. Nanosci. Nanotechnol, 16 (2016) 3176-3182.
[39] X. Guo, C. McCleese, C. Kolodziej, A.C. Samia, Y. Zhao, C. Burda, Identification and characterization of the intermediate phase in hybrid organic–inorganic MAPbI 3 perovskite, Dalton Trans., 45 (2016) 3806-3813.
[40] Y.-H. Qiu, F. Nan, Q. Wang, X.-D. Liu, S.-J. Ding, Z.-H. Hao, L. Zhou, Q.-Q. Wang, Tuning the Competitive Recombination of Free Carriers and Bound Excitons in Perovskite CH3NH3PbBr3 Single Crystal, J. Phys. Chem. C, 121 (2017) 6916-6923.
[41] K.K. Paul, P.K. Giri, Role of Surface Plasmons and Hot Electrons on the Multi-Step Photocatalytic Decay by Defect Enriched Ag@TiO2 Nanorods under Visible Light, J. Phys. Chem. C, 121 (2017) 20016-20030.
[42] K.K. Paul, R. Ghosh, P.K. Giri, Mechanism of strong visible light photocatalysis by Ag 2 O-nanoparticle-decorated monoclinic TiO 2 (B) porous nanorods, Nanotechnology, 27 (2016) 315703.
[43] P. Kumar, C. Muthu, V.C. Nair, K.S. Narayan, Quantum Confinement Effects in Organic Lead Tribromide Perovskite Nanoparticles, J. Phys. Chem. C, 120 (2016) 18333-18339.
[44] P. Zhang, F. Yang, M.A. Kamarudin, C.H. Ng, G. Kapil, T. Ma, S. Hayase, Performance Enhancement of Mesoporous TiO2-Based Perovskite Solar Cells by SbI3 Interfacial Modification Layer, ACS Appl. Mater. Interfaces, 10 (2018) 29630-29637.
[45] H. Seo, L.R. Baker, A. Hervier, J. Kim, J.L. Whitten, G.A. Somorjai, Generation of Highly n-Type Titanium Oxide Using Plasma Fluorine Insertion, Nano Lett., 11 (2011) 751-756.
[46] L.R. Baker, A. Hervier, H. Seo, G. Kennedy, K. Komvopoulos, G.A. Somorjai, Highly n-Type Titanium Oxide as an Electronically Active Support for Platinum in the Catalytic Oxidation of Carbon Monoxide, J. Phys. Chem. C, 115 (2011) 16006-16011.
[47] L. Brus, Electronic Wave Functions in Semiconductor Clusters: Experiment and Theory, J. Phys. Chem., 90 (1986) 2555-2560.
[48] Q. Lin, A. Armin, R.C.R. Nagiri, P.L. Burn, P. Meredith, Electro-optics of perovskite solar cells, Nat. Photonics, 9 (2015) 106.
[49] K. Tanaka, T. Takahashi, T. Ban, T. Kondo, K. Uchida, N. Miura, Comparative study on the excitons in lead-halide-based perovskite-type crystals CH3NH3PbBr3 CH3NH3PbI3, Solid State Commun., 127 (2003) 619-623.
[50] K. Zheng, Q. Zhu, M. Abdellah, M.E. Messing, W. Zhang, A. Generalov, Y. Niu, L. Ribaud, S.E. Canton, T.n. Pullerits, Exciton Binding Energy and the Nature of Emissive States in Organometal Halide Perovskites, J. Phys. Chem. Lett., 6 (2015) 2969-2975.
[51] Y.H. Kim, H. Cho, J.H. Heo, T.S. Kim, N. Myoung, C.L. Lee, S.H. Im, T.W. Lee, Multicolored Organic/Inorganic Hybrid Perovskite Light-Emitting Diodes, Adv. Mater., 27 (2015) 1248-1254.
[52] M. Hirasawa, T. Ishihara, T. Goto, K. Uchida, N. Miura, Magnetoabsorption of the lowest exciton in perovskite-type compound (CH3NH3) PbI3, Physica B Condens Matter., 201 (1994) 427-430.

[53] A. Buin, R. Comin, A.H. Ip, E.H. Sargent, Perovskite quantum dots modeled using ab initio and replica exchange molecular dynamics, J. Phys. Chem. C, 119 (2015) 13965-13971.
[54] V. D'Innocenzo, G. Grancini, M.J.P. Alcocer, A.R.S. Kandada, S.D. Stranks, M.M. Lee, G. Lanzani, H.J. Snaith, A. Petrozza, Excitons Versus Free Charges in Organo-Lead Tri-Halide Perovskites, Nat. Commun., 5 (2014) 3586.
[55] S. Zhuang, D. Xu, J. Xu, B. Wu, Y. Zhang, X. Dong, G. Li, B. Zhang, G. Du, Temperature-dependent photoluminescence on organic inorganic metal halide perovskite CH3NH3PbI3–x Cl x prepared on ZnO/FTO substrates using a two-step method, Chin.Phys.B, 26 (2017) 017802.
[56] G. Franssen, E. Litwin-Staszewska, R. Piotrzkowski, T. Suski, P. Perlin, Optical and Electrical Properties of Homoepitaxially Grown Multiquantum Well InGaN/GaN Light-Emitting Diodes, J. Appl. Phys., 94 (2003) 6122-6128.
[57] C. Quarti, G. Grancini, E. Mosconi, P. Bruno, J.M. Ball, M.M. Lee, H.J. Snaith, A. Petrozza, F. De Angelis, The Raman spectrum of the CH3NH3PbI3 hybrid perovskite: interplay of theory and experiment, J. Phys. Chem. Lett., 5 (2013) 279-284.
[58] K. Wei, Z. Xu, R. Chen, X. Zheng, X. Cheng, T. Jiang, Temperature-dependent excitonic photoluminescence excited by two-photon absorption in perovskite CsPbBr3 quantum dots, Opt. Lett, 41 (2016) 3821-3824.
[59] B. Ai, C. Liu, Z. Deng, J. Wang, J. Han, X. Zhao, Low temperature photoluminescence properties of CsPbBr3 quantum dots embedded in glasses, Phys. Chem. Chem. Phys., 19 (2017) 17349-17355.
[60] J. Dai, H. Zheng, C. Zhu, J. Lu, C. Xu, Comparative investigation on temperature-dependent photoluminescence of CH3NH3PbBr3 and CH(NH2)2PbBr3 microstructures, J. Mater. Chem. C, 4 (2016) 4408-4413.
[61] J. Li, X. Yuan, P. Jing, J. Li, M. Wei, J. Hua, J. Zhao, L. Tian, Temperature-Dependent Photoluminescence Of Inorganic Perovskite Nanocrystal Films, RSC Adv., 6 (2016) 78311-78316.
[62] J.M. Elward, A. Chakraborty, Effect of Dot Size on Exciton Binding Energy and Electron–Hole Recombination Probability in CdSe Quantum Dots, Journal of Chemical Theory and Computation, 9 (2013) 4351-4359.
[63] J.M. Elward, A. Chakraborty, Effect of Dot Size on Exciton Binding Energy and Electron–Hole Recombination Probability in CdSe Quantum Dots, J. Chem. Theory Comput., 9 (2013) 4351-4359.
[64] K. Wu, A. Bera, C. Ma, Y. Du, Y. Yang, L. Li, T. Wu, Temperature-dependent excitonic photoluminescence of hybrid organometal halide perovskite films, Phys. Chem. Chem. Phys., 16 (2014) 22476-22481.
[65] M. Zhang, H. Yu, M. Lyu, Q. Wang, J.-H. Yun, L. Wang, Composition-dependent photoluminescence intensity and prolonged recombination lifetime of perovskite CH3NH3PbBr3−xClx films, Chem. Commun., 50 (2014) 11727-11730.
[66] S.D. Stranks, V.M. Burlakov, T. Leijtens, J.M. Ball, A. Goriely, H.J. Snaith, Recombination kinetics in organic-inorganic perovskites: excitons, free charge, and subgap states, Phys. Rev. Appl., 2 (2014) 034007.
[67] V.K. Ravi, A. Swarnkar, R. Chakraborty, A. Nag, Excellent green but less impressive blue luminescence from CsPbBr3 perovskite nanocubes and nanoplatelets, Nanotechnology, 27 (2016) 325708.

भारतीय प्रौद्योगिकी संस्थान गुवाहाटी
Indian Institute of Technology Guwahati

Chapter 4

Precise Tuning of the Thickness and Optical Properties of Highly Stable 2D Organometal Halide Perovskite Nanosheets Through a Solvothermal Process and Its Applications as a White LED and a Fast Photodetector

In this chapter, a novel, highly reproducible and facile solvothermal route is presented to synthesize and tailor the thickness and optical bandgap of the organic-inorganic halide perovskite nanosheets (NS). Our study reveals that self-assembly of randomly oriented perovskite nanorods leads to the growth of multilayered perovskite NS at ~100 °C, while at higher temperature large area few-layer to bilayer 2D NS ($CH_3NH_3PbBr_3$) are obtained through lattice expansion and layer separation depending precisely on the temperature. Interestingly, the thickness of the 2D NS shows a linear dependence on the reaction temperature and thus enables precise tuning of the thickness from 14 layers to 2 layers giving rise to a systematic increase in the bandgap and appearance of excitonic absorption bands. Quantitative analysis of the change in the bandgap with thickness revealed strong quantum confinement effect in the 2D layers. The perovskite 2D NS exhibits tunable color and high photoluminescence (PL) quantum yields (QY) up to 84 %. Through a careful analysis of the steady-state and time-resolved PL spectra, the origin of the lower PL QY in thinner NS is traced to surface defects in the 2D layers, for the first time. A white light converter was fabricated using the composition tuned 2D $CH_3NH_3PbBrI_2$ NS on a blue LED chip. The 2D perovskite photodetector exhibits a stable and very fast rise/fall time (24 µs/103 µs) along with high responsivity and detectivity of ~1.93 A/W and 1.04×10^{12} Jones, respectively. Storage, operational and temperature dependent stability studies reveal high stability of the 2D perovskite NS under the ambient condition with high humidity. The reported method is highly promising for the development of large-area stable 2D perovskite layers for various cutting-edge optoelectronic applications.

4.1. Introduction

Low dimensional organic-inorganic halide perovskites nanostructures have recently aroused a great deal of interest due to their low cost, easy solution processing, good stability, and outstanding optoelectronic properties[1-8]. Intensive research is being conducted especially on 2D nanoplatelet or nanosheet (NS) in comparison to their bulk, 1D and 0D counterparts for its appealing features, such as large lateral size, narrow band absorption and emission spectra, long diffusion length and long carrier lifetime, excellent charge transport properties, which makes it a promising material for the applications in photovoltaics and optoelectronics[9-18]. Interestingly, organic-inorganic halide perovskite ($MAPbBr_3$, MA= CH_3NH_3) nanocrystals (NCs) have gained much attention and are widely used in various devices as compared to the inorganic $CsPbBr_3$ or $FAPbBr_3$ (FA = $CH(NH_2)_2$), since it can be synthesized at room temperature with low cost due to its low formation energy[19-21].

In the literature, very few reports have addressed on the synthesis of colloidal 2D organic-inorganic halide perovskite nanoplatelets due to lack of control in the growth of pure 2D NSs[10, 12, 15, 22]. Gonzalez-Carrero et al. prepared a blue luminescent 2D perovskite using $C_{18}H_{40}BrN$ as the organic component[23]. Dou et al. used $C_4H_{11}NHBr$ and CH_3NH_3Br for the growth of single- and few-unit-cell-thick single-crystalline 2D hybrid perovskite $(C_4H_9NH_3)_2PbBr_4$[24]. Sichert et al. tuned the thickness and photoluminescence properties of the perovskite by varying the ratio of organic cations (CH_3NH_3Br and $C_{32}H_{68}BrN$)[10]. Cho et al. modulated the layer thickness of the perovskite nanoplatelet by changing the chain length and concentration of the added alkylammonium cations[12]. Similarly, Yuan et al. used different organic ammonium bromide salts to tune the color of highly luminescent quasi-2D layered structured perovskite ($(C_6H_5CH_2NH_3)_2PbBr_4$)[22]. Levchuk et al. realized the thickness-tunability of perovskite nanoplatelet using the ligand-assisted re-precipitation method by varying the oleylamine and oleic acid ligand ratio[15]. In these reports, different kinds of organic amine salts and different ratios of capping ligands have been used to tune the thickness of the 2D perovskite. However, precise tuning of the thickness of 2D layer through temperature control and the long-term stability of the 2D layer are least addressed in the literature, and such a control is highly desirable for its exploitation in various demanding applications.

Interestingly, the solvothermal method is a very easy and facile route to tune the morphology of NSs due to the high pressure/temperature inside the closed environment of the autoclave. Although plenty of works have been done on tuning the morphology of the inorganic based perovskites ($CsPbBr_3$) using the solvothermal method, there is hardly any report on the effect of solvothermal treatment on the morphology of the organic-inorganic halide perovskites[25-34]. Zhang et al. demonstrated the preparation of mixed halide perovskite $CH_3NH_3Pb(Br_{1-x}Cl_x)_3$ single crystals by the solvothermal growth of stoichiometric $PbBr_2$ and $[(1-y)CH_3NH_3Br+yCH_3NH_3Cl]$ DMF precursor solutions[26]. Xia et a. developed a hydrothermal method using $Pb(CH_3COO)_2.3H_2O$, HBr and CH_3NH_2 alcohol solution to prepare $CH_3NH_3PbBr_3$ cluster, which was used as active material in lithium batteries[29]. Recently, Zhang et al. fabricated a hybrid material via the encapsulation of perovskite $MAPbBr_3$ NCs in europium-based metal-organic frameworks, which has been used in multistage anti-counterfeiting[25]. Note that all the reported solvothermal methods required a long duration (12-48 hours) of synthesis, which is not time and cost-efficient. In the literature, tuning of the thickness or optical properties of the nanoplatelet is achieved mostly by varying the number of ligands or organic salts. However, a fast and cost effective synthesis of 2D perovskite with tunable thickness and optical properties is highly desirable and worth interesting. Interestingly, we achieved layer controlled growth of 2D perovskite by a solvothermal method of reaction simply by controlling the growth temperature.

Herein, we demonstrate a facile, fast, controlled solvothermal method to tailor the thickness of the ultra-stable organic-inorganic halide perovskite ($MAPbBr_3$) NS with excellent tunable light absorption/ emission and photodetector performance. The growth mechanism of the NSs is qualitatively discussed based on the classical theory of self-assembly and exfoliation. Through the control of the thickness of the 2D NS, bandgap tuning is achieved from green luminescent nanorods (NRs) to cyan luminescent quantum dots (QDs). The real-life application of the 2D NSs was demonstrated by fabricating a white LED device by depositing the orange emitting $CH_3NH_3PbBr_1I_2$ NS on a blue LED. Next, we fabricated a photodetector device using the 2D perovskite NS that shows very high stability, fast response time and high responsivity. The efficacy of the current solvothermal method for fast, convenient and controllable synthesis of the large area, stable 2D perovskite layers and their uses in various optoelectronic devices are demonstrated here.

4.2. Experimental Details

4.2.1. Materials

The starting materials for the present synthesis are methylamine solution (CH_3NH_3, 33 wt% in absolute ethanol, Sigma-Aldrich), lead(II) iodide (PbI_2, 99 %, Sigma-Aldrich), lead(II) bromide ($PbBr_2$, 99.999 %, Sigma-Aldrich), hydroiodic acid (HI, 57 wt% in water, Sigma-Aldrich), hydrobromic acid (HBr, 48 wt% in water, Sigma-Aldrich), N,N-dimethylformamide (DMF, >99%, Sigma-Aldrich), diethyl ether (>99 %, Merck), toluene (Merk), Oleic acid ($CH_3(CH_2)_7CH=CH(CH_2)_7COOH$, Merk) and Oleylamine (≥98 % (primary amine), Sigma-Aldrich).

4.2.2. Synthesis Procedures

4.2.2.1. Synthesis of CH_3NH_3Br

CH_3NH_3Br (MABr) powder was prepared by diluting the 8 mL of CH_3NH_3 solution with 50 mL of absolute ethanol while stirring the solution for 15 min in a round-bottom flask. Then, 2.83 mL HBr was slowly added to the solution in an ice bath with vigorous stirring at 900 rpm for 2 h. The solution was then heated at 70 °C for several hours with continuous stirring till the solvent evaporates. To remove impurities from the MABr powder and as well as to recrystallize it, the powder was washed several times with anhydrous diethyl ether and finally dried at 60 °C in a vacuum oven overnight.

4.2.2.2. Synthesis of Ultrathin 2D Perovskite NS

To prepare the precursor solution, MABr and $PbBr_2$ were first mixed in DMF, and then Oleic acid was added to the solution. Next, 60 µl OAm was added to the solution and then transferred into a Teflon lined autoclave without any pretreatment and heated it at different temperatures (60-180 °C) for only 30 min. The synthesis procedure is schematically illustrated in **Fig. 4.1**. Note that reported solvothermal methods usually adopted long-duration reactions (12-48 hrs), in contrast to our fast reaction method. After the solvothermal process, the crude solution was cooled down naturally, and 400 µl of the solution was added into 10 ml toluene. The as-prepared NSs were separated from the solution by centrifugation for 15000 rpm for 15 min. The supernatant was discarded, and the precipitate was redispersed in 5 ml toluene for further characterization. No additional washing was adopted for purification. The samples are named as PB60, PB100, PB120,

etc. according to the reaction temperatures as detailed in **Table 4.1**. To prepare the $MAPbCl_3$, $MAPbI_3$, and mixed halide NSs, the same protocol was followed by replacing the $PbBr_2$ with $PbCl_2$, PbI_2 or mixed halide precursors (i.e., $PbCl_2/PbBr_2$ and $PbI_2/PbBr_2$), respectively. To illustrate the robustness of the method and the stability of the 2D perovskites, all the experiments were carried out in ambient air with relatively high humidity (~70 %) without the use of a glove box.

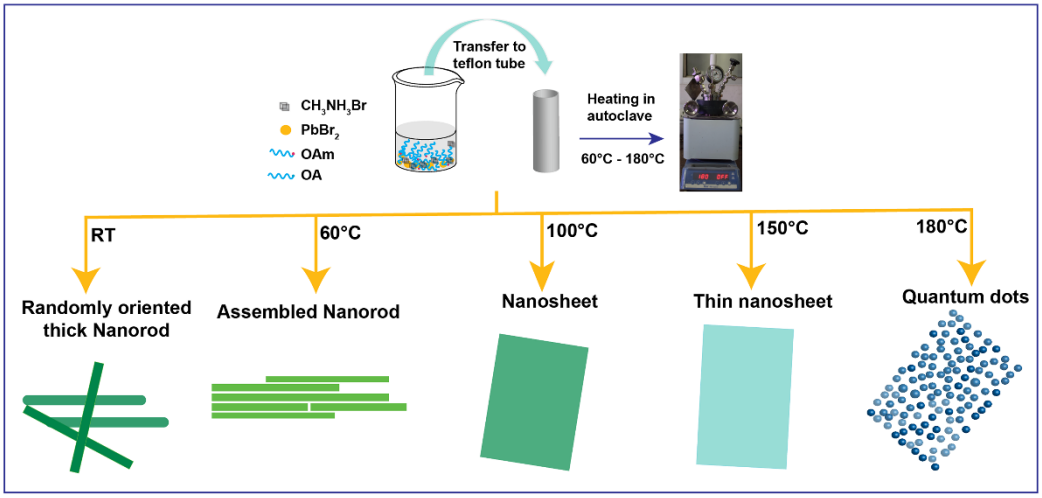

Fig. 4.1. Schematic illustration of the synthesis procedure of $MAPbBr_3$ nanostructures and its structural evolution with solvothermal reaction temperature.

Table 4.1. *Details of the NS samples with 2D layer thickness and their PL characteristics. For all the cases, the OAm amount is 60 µl except for PB100/200 where it is 200 µl.*

Sample code	Solvothermal Temperature (°C)	Duration (min)	Thickness of 2D NS (nm)	PL peak position (nm)	PL QY (%)
PB60	60	30	18.5	525	64
PB100	100		8.4	518	78
PB120	120		6.4	515	59
PB130	130		4.8	512	43
PB140	140		3.2	508	38
PB150	150		1.2	499	32
PB180	180		1.2	488	30
PB100/200	100		-	458	84

4.2.2.3. Fabrication of Photodetector

First, Si/SiO_2 (300 nm) substrates were cleaned by ultra-sonication using acetone, iso-propanol, water sequentially each for 10 min, followed by drying/heating at 150 ºC for 1 h on the hot plate. The substrate was then treated by UV-Ozone for 20 min to remove any residue. To avoid the degradation of the material while depositing the electrodes, the Al electrodes were first deposited on the wafers using a shadow mask by a thermal evaporation method. Then the PB140 NS solution was drop cast between the gap of two electrodes and dried at 60 ºC. We use a planar geometry of the device for simplicity of fabrication.

4.3. Characterization Techniques

The morphology of perovskite NSs has been characterized using FESEM (Sigma, Zeiss) imaging. The high magnification surface morphologies for different samples have been studied using a TEM (JEOL-JEM 2010) operated at 200 kV. AFM (Cypher, Oxford Instruments) images were acquired to determine the thickness of the perovskite NSs. UV-vis absorption spectra of the samples were measured using a commercial spectrophotometer (PerkinElmer, Lamda 950). XRD pattern was recorded with Rigaku RINT 2500 TTRAX-III using Cu Kα radiation with a scanning speed of 3°/min. The room temperature steady-state photoluminescence (PL) spectra were recorded using a commercial fluorimeter using 400 nm excitation using a Xenon lamp (Fluoromax-4, Horiba Scientific). PL quantum yield (QY) of the samples was measured in solution made using an integrating sphere (FM-SPHERE, Horiba) attached with the fluorimeter. Low temperature (80–300 K) PL measurements were carried out using a liquid nitrogen-cooled optical cryostat (Optistat DNV, Oxford Instruments) attached to the above fluorimeter using 405 nm laser excitation. TRPL measurements were performed using a 405 nm pulsed laser excitation for perovskite NSs, with an instrument response time of <50 ps (LifeSpecII, Edinburgh Instruments). Photodetector measurement was carried out using an assembled setup consisting of a microprobe station (Ecopia, Korea), a 405 nm diode laser, a source meter (Keithley 2400, Germany), a pulse generator (Agilent) and a digital storage oscilloscope (Agilent). The spectral response and external quantum efficiency were measured using a 150 W Xe lamp (Newport, USA), a monochromator (Newport, USA) and a power meter (Newport, USA).

4.4. Results and Discussions

4.4.1. Morphology and Microstructural Analyses

A schematic illustration of the synthesis procedure and the structural evolution of perovskite NSs with the variation of the solvothermal temperature (T_s) was depicted in **Fig. 4.1**. Here, the solvothermal synthesis process is conducted inside an autoclave, which is placed inside a preheated oven and the reaction is initiated soon after the autoclave is placed inside the oven. Pressure in the liquid inside the close chamber is moderate to high, which favors the crystal nucleation while the surfactant is adsorbed onto the sidewalls of the autoclave, preventing the agglomeration of NS[35]. **Fig. 4.2.** represents the FESEM images of the perovskite NSs prepared at different T_s. Prior to the solvothermal treatment, narrow and long NR with width ~210 nm and length ~8 µm is observed from the reaction at room temperature (RT), as shown in **Fig. 4.2(a)**; the inset shows a magnified

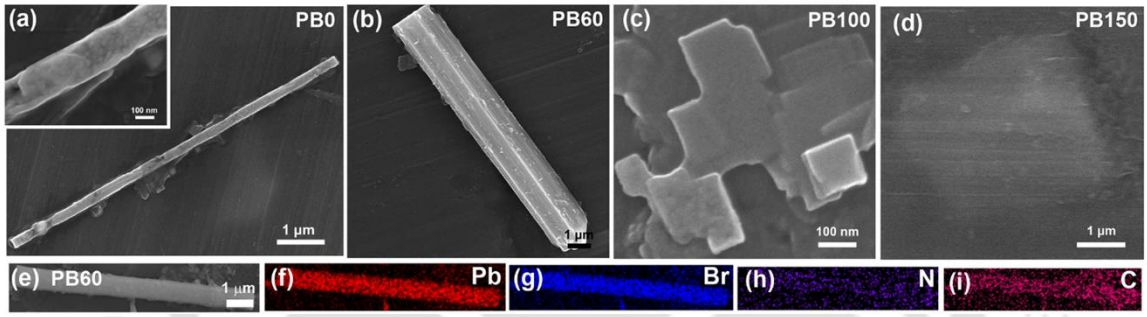

Fig. 4.2. (a) FESEM images of $MAPbBr_3$ sample for (a) PB0, (b) PB60, (c) PB100 and (d) PB150. (e) FESEM image of PB60, and (f-i) the corresponding elemental mapping for Pb, Br, C and N, respectively, showing their spatial distribution.

view of the NR. At T_s = 60 °C (PB60), the width of NR is dynamically increased from 210 nm to ~2 µm due to the lateral self-assembly of thin NRs (**Fig. 4.2(b)**). **Fig. 4.2(c)** depicts the formation of thick NS for PB100 (T_s = 100 °C) as a result of the lateral attachment of the NRs. Interestingly, at T_s = 150 °C, the thinner NS is formed, as shown in **Fig. 4.2(d)** for PB150, due to hindrance in the vertical growth of the sheet in the presence of surface ligands. Note that the ultrathin NSs for PB150 cannot be fully discerned in the FESEM image due to its resolution limit. **Fig. 4.2(e)** shows the FESEM image of PB60 on which the elemental mapping was performed. **Fig. 4.2(f-i)** depict the corresponding elemental mapping of Pb, Br, N, and C, respectively, showing the spatial distribution of each element in the NR. The images represent the uniform distribution of all the elements of $MAPbBr_3$ throughout the NRs and hence the formation of perovskite NS with a distinct shape is confirmed.

To understand the structural evolution of perovskite NS with the solvothermal treatment, TEM images were recorded at different stages of solvothermal growth. For the sample PB0, synthesized by simply mixing the precursors at RT without any special treatment, randomly oriented NRs are observed. At T_s = 60 °C (PB60), lateral self-assembly of NRs occurs in the presence of an optimum concentration of capping ligand, as shown in **Fig. 4.3(a)**. The corresponding HRTEM lattice fringe pattern for PB60 with lattice spacing 0.32 nm is shown in **Fig. 4.3(b)** and the inset shows the corresponding inverse fast Fourier transform (IFFT) image. Further increase in T_s to 100 °C results into the compact attachment of the self-assembled NRs to form large-area 2D nanosheet (NS), as revealed in **Fig. 4.3(c)**. **Fig. 4.3(d)** depicts the HRTEM lattice fringe pattern of well crystalline perovskite NS in PB100. The calculated lattice spacing of 0.26 nm and 0.31 nm corresponds to the

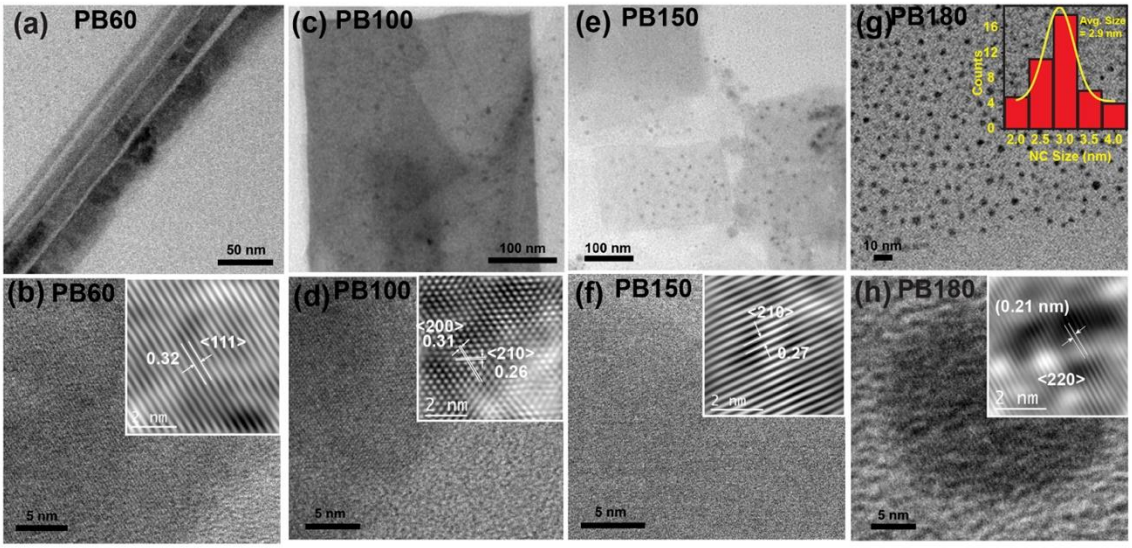

Fig. 4.3. (a,b) TEM image of self-assembled 2D perovskite NRs in PB60 and the corresponding HRTEM lattice image; the inset in (b) shows the corresponding IFFT image with an interplanar spacing of 0.32 nm. (c,d) The TEM image of 2D perovskite NS in PB100 and the corresponding HRTEM image; the inset shows the corresponding IFFT image. (e,f) TEM images of ultrathin 2D perovskite NS in PB150 and the corresponding HRTEM image; the inset shows the corresponding IFFT image. (g,h) The TEM image of 2D perovskite QDs in PB180 and the HRTEM lattice image of a 2D QD. The insets of (g,h) show the size distribution QDs in PB180 and IFFT image of the lattice fringe, respectively.

(210) and (200) planes, respectively, of the $MAPbBr_3$ crystals (see the inset of **Fig. 4.3(d)**), suggesting the cubic structure corresponding to the space group Pm3m (221). For PB150, perovskite NS along with QDs is observed due to the higher temperature (T_s = 150 °C), as shown in **Fig. 4.3(e)**. Interestingly, the thickness of the NS is much reduced in PB150 as compared to that of PB100, which is evident from the image contrast and it will be more evident from the AFM

analysis discussed later. **Fig. 4.3(f)** demonstrates the HRTEM lattice fringe pattern of PB150, and the calculated lattice spacing is 0.27 nm corresponding to (210) plane. Finally, for PB180, the 2D NSs are disintegrated into 2D QDs, as shown in **Fig. 4.3(g)**, revealing the uniform distribution of QDs and the corresponding size distribution with an average size of 2.9 nm is shown in the inset. **Fig. 4.3(h)** shows the HRTEM lattice fringe pattern of a 2D QD, implying its highly crystalline nature with a lattice spacing of 0.21 nm, which corresponds to (220) plane of $MAPbBr_3$. Since the lateral size of the NSs is comparable/less than the exciton Bohr radius in bromide-based perovskite (~ 4 nm), these are termed as 2D QDs.

The current solvothermal method enables us to successfully tailor the morphology/thickness of the perovskite NSs from thick NRs to ultrathin 2D NS and finally to 2D QDs. The key factors in controlling the morphology are the solvothermal temperature, duration, and surfactant concentration. Inside the autoclave, the solvent cannot evaporate, and when the temperature and pressure of the solvent are increased above a critical point, the solvent becomes a supercritical fluid phase, which shows the characteristics of both the liquid and gas phases and this supercritical fluid exhibits high viscosity and easily dissolve the chemical compounds that are insoluble under ambient conditions[36]. To optimize the growth and tune the perovskite NSs, the concentration of OAm and the time duration of solvothermal treatment were varied for PB100 sample (i.e., at T_s = 100 °C) keeping all other parameters unchanged (see **Fig. 4.4**). Randomly oriented NRs along with

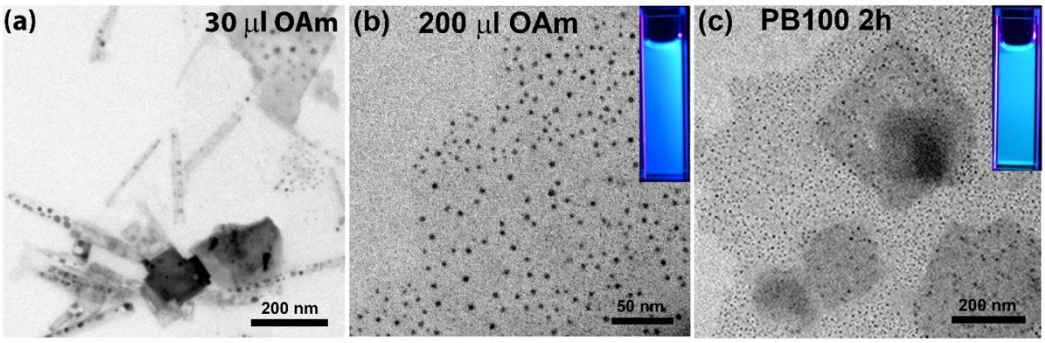

Fig. 4.4. TEM image of solvothermally grown perovskite nanostructures synthesized with (a) 30 µl (b) 200 µl OAm at 100 °C for 30 min. (c) TEM image of perovskite NCs for PB100, solvothermally treated for 2h duration.

small area thick NSs are observed at 30 µl OAm content as shown in **Fig. 4.4(a)**. For 200 µl OAm concentration, the NSs are fully disintegrated to QDs with very high blue emission under UV light, as revealed from **Fig. 4.4(b)** and its inset. Thus, it can be concluded that the OAm concentration

has a strong impact on controlling the morphology of the perovskite NS. Next, by keeping the OAm concentration and T_s fixed at 60 µl and 100 °C, respectively, an extension of the solvothermal treatment duration from 30 min to 2h results into the formation of 2D NS decorated with QDs, as shown in **Fig. 4.4(c)**. When the solution is solvothermally treated with a high concentration of surface ligand, more nuclei are formed, and its growth is dynamically controlled in all the directions, resulting in smaller nuclei[14]. Further, as the solvothermal reaction time is increased, keeping the temperature constant, the ligands get more time to react with the precursor nuclei and disintegrate the NSs resulting in the formation of QDs/NCs. Hence, OAm is key to control the kinetics of crystallization and controls the thickness of the nanostructure, while OA suppresses the NS aggregation and increases the colloidal stability[3]. Note that the synthesis process with only 1-octadecene resulted into the formation of non-uniform nanostructures, and tuning of the morphology and the optical band gap was not achievable with the variation of reaction time and temperature. In contrast, the combination of OAm and OA allowed us to successfully tune the thickness, morphology and the optical properties of the NS systematically. Thus, at an optimum growth condition (60 µl OAm and 30 min solvothermal treatment), the self-assembly process of NRs and nanoplatelet have been observed to take place due to the destabilization of the surface ligands caused by the elevated autoclave pressure and temperature. Without any pretreatment, the DMF solution slowly reacted with the capping ligands inside the autoclave and arranged in a specific direction. It has been reported that high pressure inside the closed chamber of the autoclave is a key factor in assembling the randomly oriented NRs in a specific direction[30]. At elevated pressure and temperature, controlled evaporation of the solvent in solvothermal method increase the viscosity of the growth medium which facilitates the lateral oriented attachment of the NRs and platelets to form NSs due to lack of free volume and spatial constraints[37]. Interestingly, we observe a dramatic change in the structural parameter in the perovskite crystal at T_s = 150 ºC (discussed later). At this temperature, the as-grown NSs consist of bilayer perovskite.

Note that pressure-induced phase transition and self-assembly of NR to from 2D NS have been reported earlier for perovskite material[7, 18, 30, 37-39]. The self-assembly of NRs can also be explained by considering the interaction energies between the NRs. According to the classical theory of interaction between nanoparticles, two dominating forces responsible for the self-assembly process of NSs are the van der Waals force, and electrostatic interaction. The repulsion

forces arise from the net charges and the steric repulsion of organic ligands[21]. The electrostatic repulsion force between two interacting $MAPbBr_3$ NRs and nanoplatelet dominates at large separation, while the attractive van der Waals force dominates at a short distance, and for the self-assembly of two NRs, they have to overcome an energy barrier of ~$0.25k_BT$[21]. Hence, at room temperature, it is very difficult for the NSs to be self-organized in a particular direction. In the solvothermal method, high pressure and controlled temperature play crucial roles in supplying the required energy to the NRs, and they attach laterally to each other to form large-area NSs. At higher reaction temperature, due to the increased thermal energy liquid-phase exfoliation of layers occurs giving rise to the thinning of the 2D layers down to 1.2 nm (bilayer perovskite) at 150 ºC (discussed below).

In order to estimate the thickness of the 2D perovskite NS precisely, AFM images were recorded in the tapping mode. **Fig. 4.5(a)** shows the AFM image and the corresponding height profile of PB0, revealing the thickness of the NR as ~67 nm. **Fig. 4.5(b)** exhibits the AFM image of PB60,

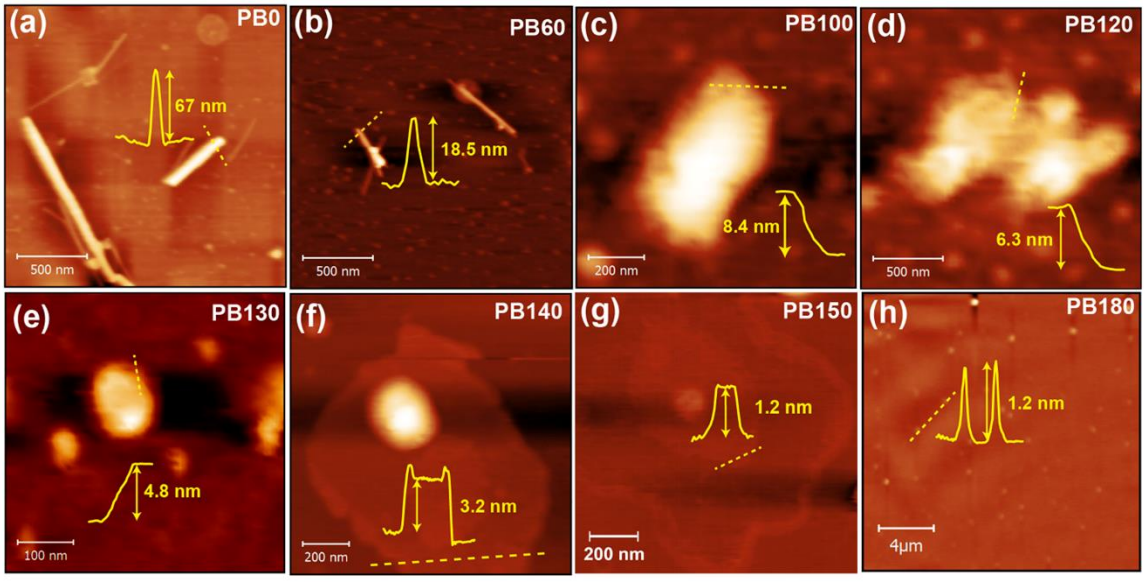

Fig. 4.5. AFM topography images of 2D NS in (a) PB0, (b) PB60, (c) PB100, (d) PB120, (e) PB130, (f) PB140, (g) PB150, and (h) PB180. The corresponding height profiles of the 2D NS are shown in the respective images, which essentially represent the thickness of the 2D layers in each case.

and the thickness of the NR is found to be ~18.5 nm. **Fig. 4.5(c)** demonstrates the formation of thin NS in PB100 and the average thickness of the NS is found to be ~8.4 nm. The AFM images of thin NSs in PB120 and PB130 are shown in **Fig. 4.5(d,e)** and the corresponding thicknesses are

found to be ~6.3 nm and ~4.8 nm, respectively. **Fig. 4.5(f,g)** depict the AFM images of PB140 and PB150 NS, respectively. Interestingly, the thicknesses of PB140 and PB150 NS are further reduced to ~3.2 nm and ~1.2 nm, respectively, as depicted in their respective height profiles. For PB180, a uniform distribution of QDs is observed as seen in the AFM image shown in **Fig. 4.5(h)** and the corresponding thickness of the QDs is estimated to be ~1.2 nm. Considering the unit cell size of $MAPbBr_3$ as 5.93 Å, the number of unit cell layers (n) was estimated from the thickness of the NSs/QDs to be: n ≈ 14, 10, 8, 5, 2 and 2 for the samples grown at 100, 120, 130, 140, 150 and 180 °C, respectively[15]. Thus, we have successfully tuned the thickness of the NS precisely from 14 layers (14L) to 2L by systematically increasing the solvothermal reaction temperature. The thickness of the NS and QDs is comparable to or less than the 3D exciton Bohr radius of $MAPbBr_3$ (~ 4.4 nm); hence a strong QC effect can be expected in the optical properties of the NSs. It is reported that oleic acid is densely packed in an ordered layer on the NS surface, thus helps in stabilizing the 2D NS growth[40]. Here, tuning the thickness of 2D NS is achieved by the increased reactivity of OAm due to the high pressure and temperature inside the autoclave. At low temperature where the interplanar spacing is less, the surface ligands can't enter between the layers and exfoliation of layer can't occur. But, at high temperatures the interplanar spacing is enlarged (discussed from XRD analysis), and the surface ligands can successfully exfoliate the NS layer giving rise to thinner NS[41]. Hence, the surface ligands are attached to the surface of the NSs and selectively exfoliate the layers of the NSs along the vertical direction, promoting thinner sheets at higher temperature. Thus, the control of growth and morphology of colloidal NSs are achieved by a kinetically controlled process, governed by the temperature-dependent dynamic surface−ligand interaction.

4.4.2. Structural and Compositional Analyses

Results of XRD measurements presented in **Fig. 4.6(a)** exhibit that the initial cubic structure of the perovskite solution is retained in the course of the self-assembly process in solvothermal treatment. XRD patterns of $MAPbBr_3$ NSs indicate a pure cubic phase, perfectly assigned to Pm-3m space group (**Fig. 4.6(a)**). The XRD (130) peak is dominant in PB180 and diffraction peak intensity of (110) plane is greater than (100) plane in PB180 indicating 2D QDs. The comparison of interplanar spacing corresponding to (100) diffraction peak for different growth temperatures is shown in **Fig. 4.6(b)**. It is worth noting that there is a systematic increase in lattice spacing (*d*-

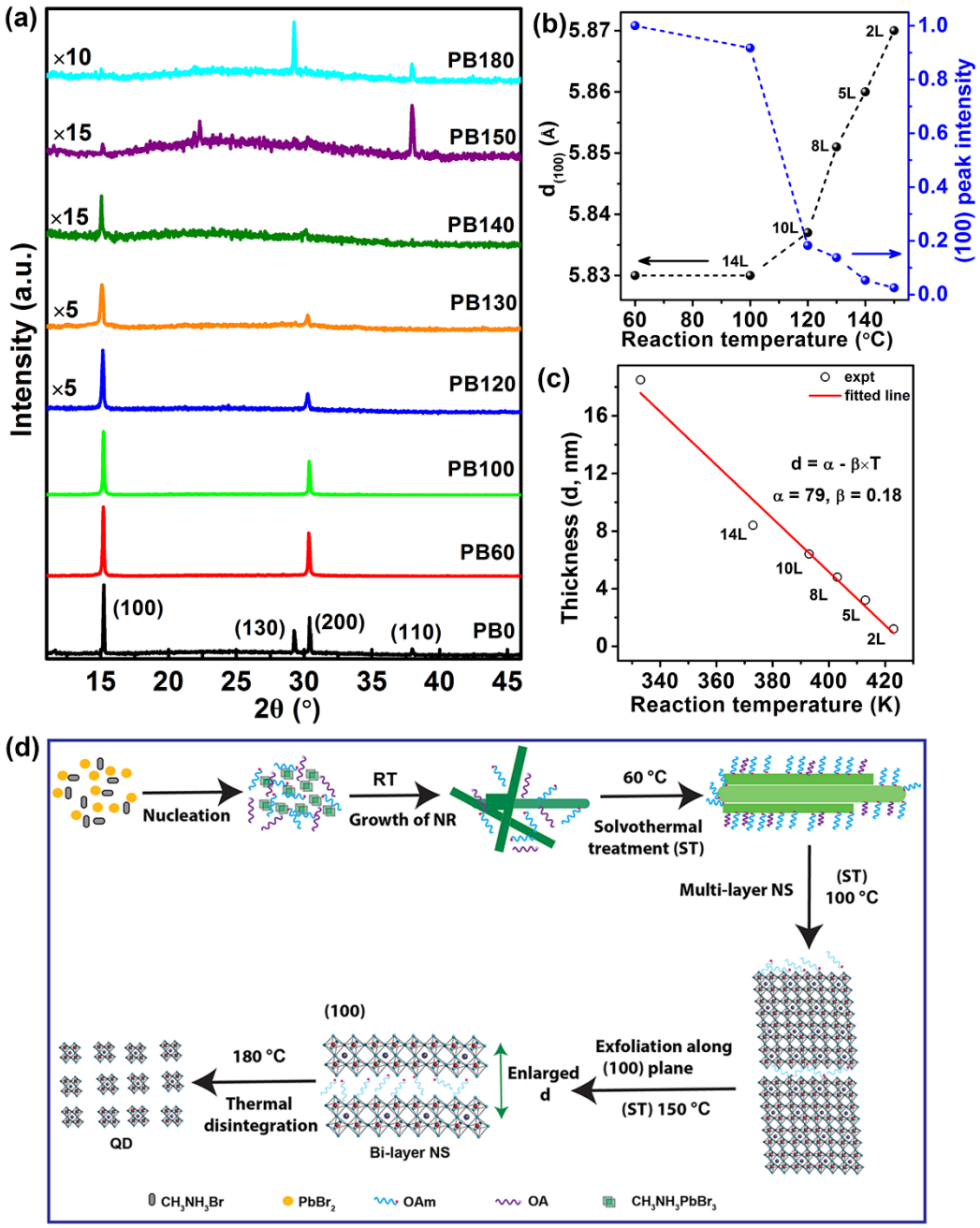

Fig. 4.6. (a) A comparison of XRD patterns of perovskite NS prepared at different solvothermal temperatures. (b) Change in (100) interplanar spacing and (100) peak intensity with solvothermal temperature. (c) Change in the thickness of the 2D NS with solvothermal reaction temperature. (d) A schematic illustration of the growth mechanism and shape evolution of the perovskite NSs during different stages of solvothermal reaction at different temperatures.

spacing) (from 5.82 Å at RT to 5.89 Å at 180 °C) with increasing temperature and reduction in sheet thickness. Note that with the increase in T_s the morphology of the NS is changed from thick NR to ultra-thin NS to ultrathin QDs and thus, the (100) diffraction peak position is observed to

be shifted towards lower angle (~0.18° shift), indicating lattice expansion and marginal broadening in full width at half maxima (FWHM) (0.079 to 0.108°). Since the NSs are highly anisotropic, the Scherrer equation cannot be employed to determine the dimension from the observed FWHM. Hence, the thickness of the NSs is measured directly from AFM height profile analysis. The right Y-axis of **Fig. 4.6(b)** displays the comparison of (100) diffraction peak intensity with the increase in T_s, reaction temperature. Characteristic XRD peak intensity (100) systematically decreases with increasing T_s; especially at 150 °C the (100) peak intensity reduces largely indicating exfoliation of the sheets perpendicular to (100) direction leading to bilayer perovskite (thickness, ~1.2 nm). The (100) oriented 2D perovskite can be categorized as Ruddlesden-Popper phase[42]. **Fig. 4.6(c)** shows the variation in NS thickness with T_s. This shows a linear decrease in thickness (*d*) with increasing temperature (T) (as shown by the linear fit). The negative coefficient of the temperature term indicates dissociation energy, which is obviously proportional to T. We believe that as the d-spacing increases with increasing temperature, more of OAm enters in between the two layers of perovskite NS and results into exfoliation/separation of layers to thinner layers down to 1.2 nm thin 2D layer. A schematic of the possible growth mechanism and shape evolution from randomly oriented NR to 2D QDs is presented in **Fig. 4.6(d)**. It is interesting to note the systematic decrease

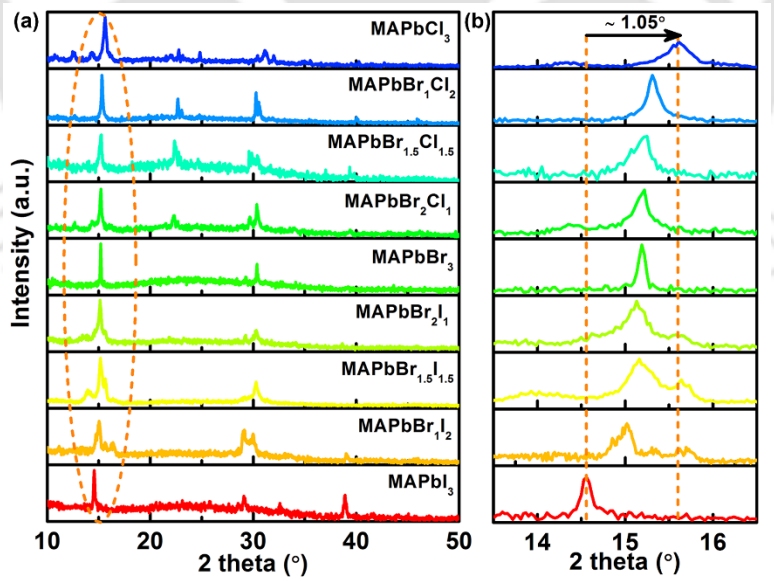

Fig. 4.7. (a) A comparison of XRD pattern of pure and mixed halide perovskite NS in PB100, (b) enlarged view of the XRD pattern of the marked region showing a systematic upshift in the peak position with compositional tuning.

in intensity of (100) peak in XRD pattern with increasing T_s due to the thinner layers cleaved from the cleavage (100) plane. The XRD patterns of pure $MAPbX_3$ (X= I, Br and Cl) and mix halide

perovskite NSs synthesized at 100 °C are shown in **Fig. 4.7(a,b)**. When the halide composition is changed from iodide to bromide and towards chloride, the characteristic XRD peaks systematically shift towards higher diffraction angles (see **Fig. 4.7(b)**), which can be attributed to the decrease in radii of halide ions from iodide to bromide and chloride[14].

The chemical valence state, composition, and surface properties of PB100 and PB150 NSs were investigated using the XPS analysis. The XPS spectrum of Br 3d is presented in **Fig. 4.8(a)**, which is deconvulated with two peaks centered at 68.9 ($3d_{5/2}$) and 70.6 eV ($3d_{3/2}$), corresponding to the inner and surface Br ions, respectively. In **Fig. 4.8(b)**, the XPS spectrum of Br 3d corresponding to PB150 NS is presented with Gaussian deconvulated peaks centered at 68.6 and 70.0 eV. Hence,

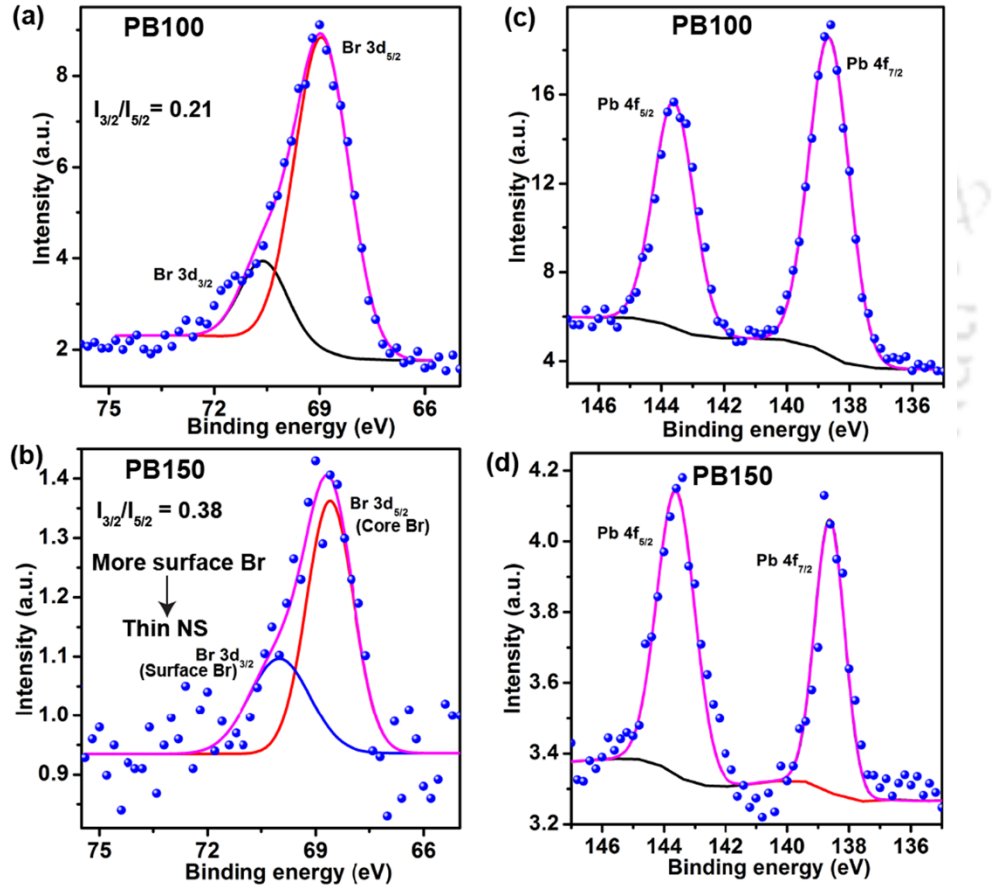

Fig. 4.8. Deconvolution of the XPS spectra corresponding to Br 3d in (a) PB100, (b) PB150. Deconvolution of the XPS spectra corresponding to Pb 4f in (c) PB100, (d) PB150, considering a Shirley background.

there is a marginal shift (~0.3 eV and ~0.6 eV) in binding energy (BE) in thinner PB150 NS corresponding to Br $3d_{5/2}$ and Br $3d_{3/2}$ respectively, revealing good surface properties even for

higher reaction temperature. Note that the intensity ratio of Br $3d_{3/2}$ peak to $3d_{5/2}$ peak is marginally higher for PB150 (~0.38) than that in PB100 (~0.21) suggesting a Br rich surface in case of thinner NSs. This is consistent with the decrease in the thickness of the NS in PB150 as compared to PB100. In **Fig. 4.8(c,d)**, the XPS spectrum of Pb^{2+} (Pb 4f) for PB100 and PB150 exhibit two symmetric peaks, which are attributed to Pb $4f_{7/2}$ and Pb $4f_{5/2}$ levels at BE of 138.7 eV and 143.6 eV, respectively. The spin-orbit split between the Pb $4f_{7/2}$ and Pb $4f_{5/2}$ levels for both the NSs was found to be 4.9 eV, which matches well with the reported value (4.8 eV)[2]. In our system, the contribution of metallic Pb at a lower binding energy (136.8 eV) is not observed, indicating no partial reduction/oxidation of Pb.

4.4.3. Optical Analysis

4.4.3.1. UV-vis Absorption and Photoluminescence Studies

UV-vis absorption and PL emission spectra of various perovskite NSs are shown in **Fig. 4.9(a)** and the inset shows the corresponding photographs of the $MAPbBr_3$ NS suspensions in toluene excited by UV light. PL emission spectra were recorded with 400 nm excitation. The apparent emission color of the solutions systematically changed from green (PB0) via blue-green (PB150) to cyan (PB180). Correspondingly, there is a systematic blue shift of the absorption edge and PL peak (from 530.0 nm in PB0 to 488.2 nm in PB180) in the respective spectrum with the increase in reaction temperature. The systematic blue shift can be attributed to the systematic reduction in the thickness of the NS down to 1.2 nm. PL spectrum for PB180 QDs possesses relatively broader PL linewidth (41.6 nm) as compared to that of 2D NS in PB150 (22.8 nm), which may be associated with the size distribution of the perovskite QDs. Note that PL peak energy is successfully tuned by ~200 meV (~42 nm) by tailoring the thickness of the NSs. Tuning of PL emission peak from green (530.0 nm) to cyan (488.2 nm) region may be caused by the strong QC effect due to the reduced thickness of the 2D NS down to 2 layers and its final disintegration to 2D QDs. Note that PB150 and PB180 show excitonic features in the absorption spectra due to the transition to higher excited states (see **Fig. 4.9(b)**). The excitonic peaks shift towards higher energy region (~10 nm) for QDs in PB180 compared to NS in PB150 due to an increase in the bandgap caused by the lateral confinement in QDs. Further tuning of the PL emission to the blue region is achieved by changing the OAm concentration while keeping the reaction temperature fixed at 100 °C. As the OAm amount is increased from 60 µL to 200 µL, the PL peak position is tuned from

518 nm to 458 nm, i.e., a large blue shift of 60 nm is observed (see **Fig. 4.9(c)**). Increase in the OAm concentration results into the formation of 2D QDs (discussed earlier), which in turn results into the shift in PL peak position to blue region due to strong confinement effect. Hence, using the solvothermal method, we could successfully synthesize the bright blue-emitting perovskite QDs. Similarly, by increasing the reaction duration to 2 hrs, the PL peak of PB100 NS is blue-shifted by ~28 nm (see **Fig. 4.9(d)**).

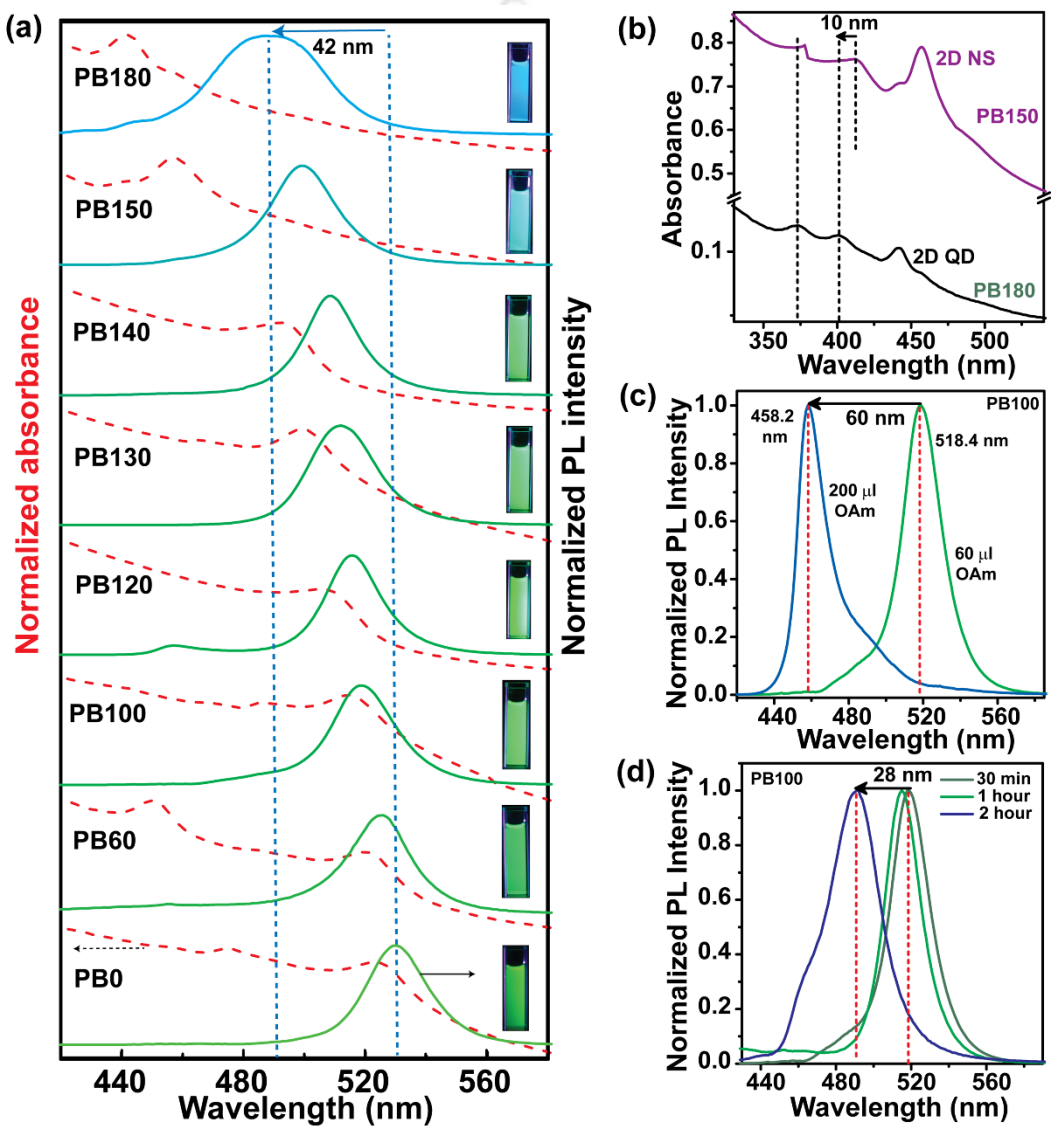

Fig. 4.9. (a) UV-vis absorption (dashed lines) and PL spectra (solid lines) of various perovskite NSs; the inset in each case shows the corresponding photograph of the sample under UV light irradiation. (b) Comparison of absorption spectra for 2D perovskite NS in PB150 and PB180. Excitonic peaks are marked with vertical dashed lines. (c) Normalized PL spectra of perovskite NS in PB100 prepared with 60 µl and 200 µl OAm. (d) Comparison of PL spectra of perovskite NS synthesized at 100 ºC with 60 µl OAm for different time durations.

Variation in PL intensity with excitation wavelength for NS in PB100 and PB140 is shown in **Fig. 4.10(a)** revealing maximum intensity of PL at 466 nm and 400 nm excitation wavelength for PB100 and PB140, respectively. However, PL peak position does not change with excitation wavelength. Excitation spectra of PB100 with emission at 518 nm and PB140 with emission at 508 nm are shown in **Fig. 4.10(b,c)** along with absorbance data at the right axis showing the identical behavior of excitation spectra and absorption spectra.

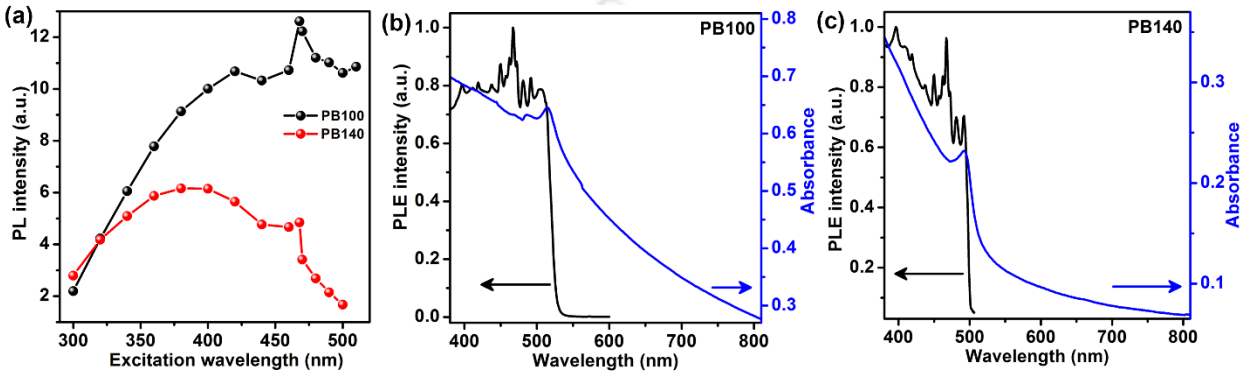

Fig. 4.10. (a) Variation in PL intensity with respect to excitation wavelength for PB100 and PB140. Comparison of PL excitation spectra and absorbance for (b) PB100 (emission at 518 nm) and (c) PB140 (emission at 508 nm).

Interestingly, this simple solvothermal synthesis technique can be easily extended to fabricate colloidal PB100 NSs through halide substitutions. A series of colloidal $MAPbX_3$ NSs with tunable compositions were fabricated by the solvothermal treatment at 100 ºC using different combinations of PbX_2 salts, as shown in **Fig. 4.11(a)**, and the inset shows the evolution of emission color under UV light excitation upon forming mixed-halide NSs (X = Br, Cl, and I). The absorption and PL spectra are finely tuned over the full visible range (450 to 656 nm) by varying the composition of cations. Band structure of halide perovskite is greatly influenced by the p-orbitals of lead and halogen (X = Cl, Br or I) atoms. Thus, a change in the halide composition of the perovskite from Cl to Br to I results into the change in the valence orbital of halide from 3p to 4p to 5p, respectively, causing a systematic reduction in the bandgap[43]. This can be clearly observed from the change in absorption edge from 443 nm for $MAPbCl_3$ to 514 nm for $MAPbBr_3$ to 643 nm for $MAPbI_3$. The systematic increase in optical bandgap from 1.8 eV to ~2.8 eV with halide exchange from I to Cl is exhibited in **Fig. 4.11(b)**. Hence, the band structure of halide perovskite is successfully tuned by our solvothermal method using a different combination of halide salts.

The tunable optical properties of the NS can be explained by considering the perovskite crystal structure. The ultrathin NS is comprised of layers of corner-sharing $PbBr_6$ octahedra, with the capping ligand around the NS, leading to the confinement of electrons giving rise to discrete energy levels[10]. Exciton Bohr radius of bromide perovskite is reported to be ~4.4 nm, which is higher than the thickness of NS in PB140 (5 layers). Hence, we consider the perovskite NS in PB140,

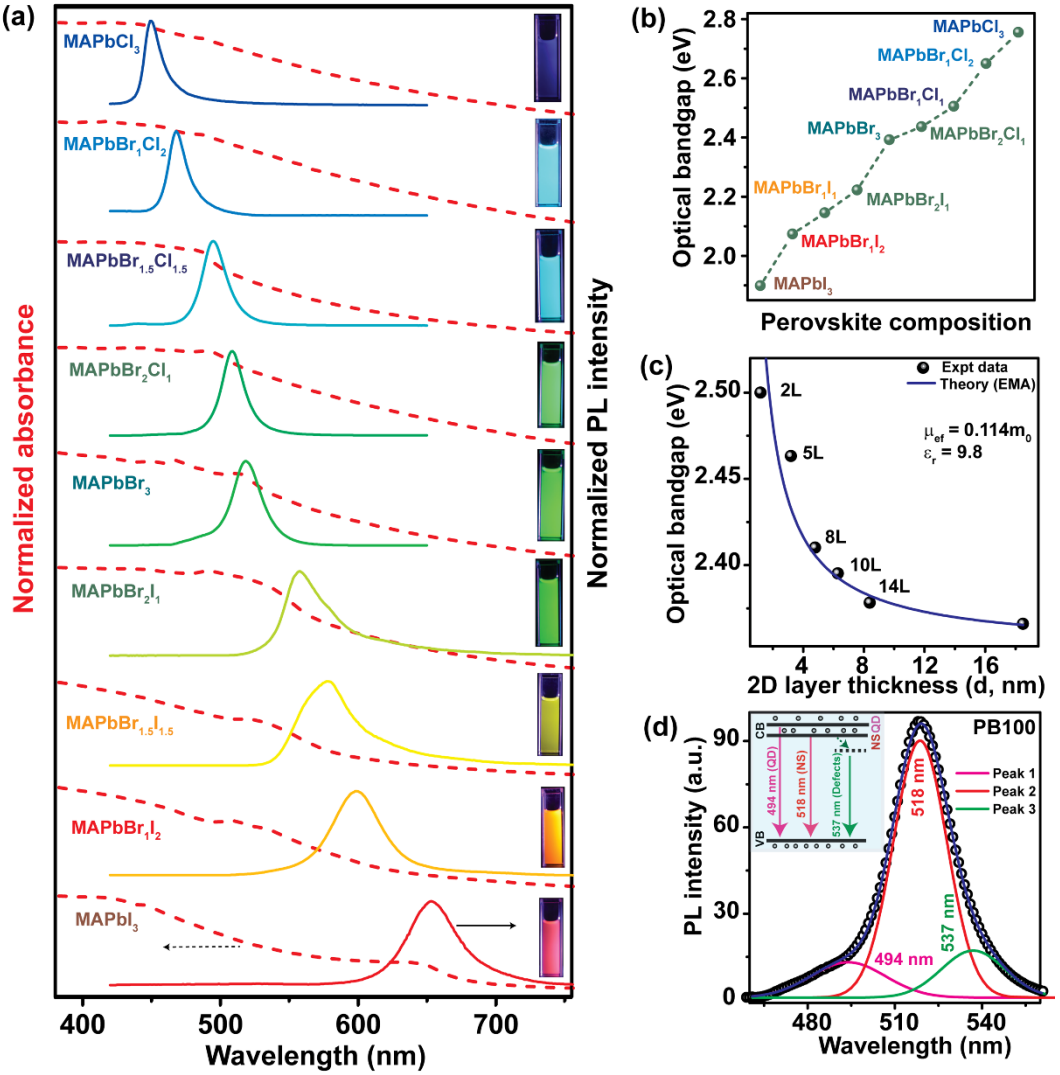

Fig. 4.11. (a) UV-Vis absorption and PL emission spectra of pure and mixed halide perovskite NSs for PB100 obtained by anion exchange. (b) Variation of optical bandgap with halide exchange of multilayered perovskite NS. (c) Variation of the optical bandgap as a function of the thickness of 2D layers. The experimental data are fitted with the quantum confinement model. The data points labeled with xL, where x represents the number of layers. (d) Deconvulated PL spectra of PB100 NS and inset showing band diagram corresponding to each PL peak.

PB150, and PB180 to be in the strong confinement regime resulting in cyan emitting NS and QDs under UV light. Note that the increase in the bandgap in perovskite has also been associated with

the lattice contraction/distortion. However, we observed a systematic expansion of the lattice with increasing reaction temperature i.e. with reduced thickness (see **Fig. 4.11(c)**). In general, lattice expansion is expected to give rise to a red shift of the bandgap. However, a systematic blue shift in the absorption edge and PL peak is observed in our case, which is contrary to the behavior expected from lattice expansion. This confirms the fact that the systematic blue shift in the absorption edge is not related to change in the lattice constant, but it is due to the ultra-small thickness of the layers that gives rise to the QC effect. To assess the QC effect quantitatively, we have plotted the optical bandgap vs NS thickness in **Fig. 4.11(c)**. The optical band gap was calculated from the absorption spectra of different samples. Interestingly, thickness dependence of the optical bandgap data follows the Brus model of QC using the effective mass approximation (EMA)[44]:

$$E_g = E_0 + h^2/8\mu_{ef}d^2 - 1.786e^2/4\pi\varepsilon_0\varepsilon_r d \qquad (4.1)$$

Where E_0 is the bulk bandgap, d is the 2D layer thickness, h is the Planck's constant, μ_{ef} is the effective reduced mass of exciton, and ε_r is the dielectric constant. From the fitting of E_g vs. d plot, the extracted parameters are: $\mu_{ef} = 0.114m_0$, $\varepsilon_r = 9.8$, which match well with earlier reports[45, 46]. Here m_0 is the free electron mass. Taking the above values, the Bohr radius (R_B) of $MAPbBr_3$ is calculated using the relation,

$$R_B = m_0\varepsilon_r R_H/\mu_{ef} \qquad (4.2)$$

Where, R_H is Bohr radius of a hydrogen atom (0.053 nm). Exciton Bohr radius of $MAPbBr_3$ is found to be 4.6 nm, which closely matches with the reported values[46, 47]. Hence, the change in the optical bandgap of the 2D perovskite layers with the 2D layer thickness clearly follows the QC model and thus the 2D NS can act as ideal platform for exploiting quantum effects in perovskite materials.

Importantly, the absolute PL QYs of the perovskite NSs are measured to be high and these are tabulated in **Table 4.1**. The highest PL QY (78 %) was achieved for the NS grown at T_s = 100 ºC. However, a further increase in T_s leads to thinning of the layers, and it affects the non-radiative/ radiative transition channels of photons indirectly, which in turn results in the reduction of the PL QYs of the NSs[48]. A closer look at the PL spectral features, including its asymmetry, reveals that each peak contains three emission peaks. Deconvulated PL spectra of PB100 NS with three

peaks is shown in **Fig. 4.11(d)**. As the position of peak 1 closely matches with the QDs emission peak (see **Fig. 4.11(d)**), the peak 1 is believed to originate from the 2D perovskite QDs that are simultaneously present along with the 2D NSs. Peak 2, which is dominant and coincides with the absorption edge peaks is originated from NS band to band transition or band-edge emission[49]. Peak 3 is believed to be defect-related emission, including surface defect which is more dominant in thinner NS, such as PB150. The summary of the PL features is summarized with a band diagram showing the respective transitions in the inset of **Fig. 4.11(d)**. The deconvulated PL peaks of other samples are shown in **Fig. 4.12**. The details of the fitting parameters of all samples are given in

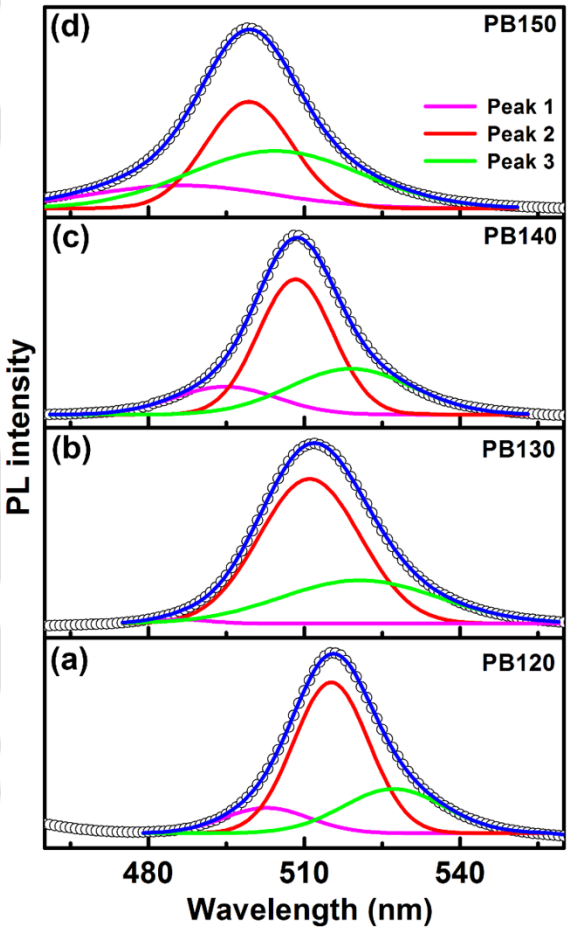

Fig. 4.12. Comparison of deconvulated PL spectra of various NS samples, such as (a) PB120, (b) PB130, (c) PB140, (d) PB150. The symbols are experimental data and the lines are fitted peaks (Gaussian).

Table 4.2. It is clear that the contribution of additional two peaks (1, 3) is significant for thinner NS such as PB150 as compared to that of PB100. It is quite expected, as with the decrease in the thickness of the NS, the presence of surface related defects and presence of QDs are prominent.

From XPS analysis, it is inferred that PB 150 NS has more surface Br than PB100, which results into more surface defects in thinner NS. Note that PB100 shows much higher PL QY than that of PB150. As the reaction temperature is increased, the contribution of band edge emission decreased (see **Table 4.2**) and the contribution of defect-related emissions is increased, due to lower thickness of NS. This in turn results in the overall decrease in PL QY in thinner NS. Post-growth processing may be required to eliminate the influence of surface defects in the 2D NS for improving the overall PL QY.

Table 4.2. *Details of the PL peak parameters deconvulated with Gaussian peaks.*

Sample	Peak 1 (nm) (%)	Peak 2 (nm) (%)	Peak 3 (nm) (%)
PB100	494 (13)	518 (72)	537 (15)
PB120	503 (12)	515 (63)	527 (25)
PB130	486 (1)	511 (68)	521 (31)
PB140	495 (15)	508 (55)	519 (30)
PB150	486 (18)	499 (40)	504 (42)

4.4.3.2. Low-Temperature Photoluminescence Studies

The temperature-dependent PL spectra of PB100 NS were investigated in the range of 80-300 K to study the origin of high PL QY and the excitonic properties. **Fig. 4.13(a)** shows the temperature-dependent PL spectra of PB100 NS, revealing the systematic increase in PL intensity with decreasing temperature. The inset of **Fig. 4.13(a)** shows the dependence of integrated PL intensity on temperature. **Fig. 4.13(b)** shows the temperature-dependent integrated PL intensity, and the experimental data are fitted using the Arrhenius equation, given by,

$$I(T) = I_0/\left(1 + Aexp(-E_B/k_BT)\right), \qquad (4.3)$$

where, $I(T)$ and I_0 are the integrated PL intensities at temperatures T and 0 K, respectively. A is a constant, and E_B is the exciton binding energy. To estimate the exciton binding energy of NS, the experimental data are fitted in the higher temperature region (160-300 K). From the fitting, E_B is found to be ~225±21 meV for PB100. Thus, the exciton binding energy in our 2D NS is ~4 times higher than that of its 3D bulk counterpart (30-76 meV) and it is consistent with the result presented

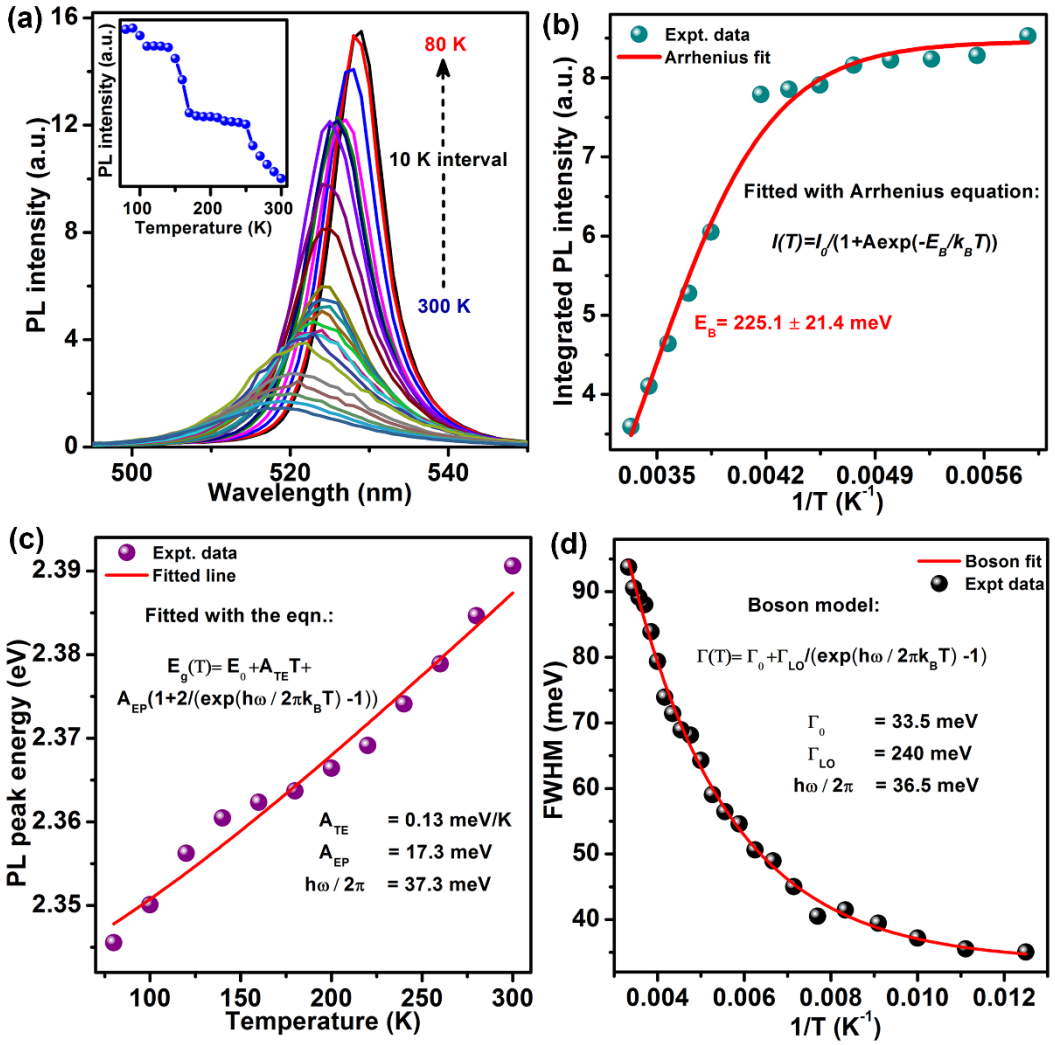

Fig. 4.13. (a) Temperature-dependent PL spectra of 2D NS in PB100 in the range 80 K- 300 K. The inset shows the variation of PL intensity with measurement temperature (T). (b) Integrated PL intensity vs. inverse of temperature for PB100. The experimental data are fitted with the Arrhenius equation. (c) Variation of PL peak energy and (d) FWHM with measurement temperature for PB100.

in the previous chapter on perovskite QDs[50]. It also matches well with the theoretical limit[51]: $E_B^{2D} = 4 \times E_B^{3D}$. In 2D NS, due to its ultralow thickness, the Coulomb interaction between electron and hole is less screened, which in turn increases the exciton binding energy[51]. Though the exciton binding energy of bulk perovskite is large enough to show the excitonic effect at room temperature, the recombination is mainly dominated by the recombination of free electrons and holes, which may have resulted into the overestimation of exciton binding energy based on low-temperature experiments[52]. Hence, the exciton binding energy extracted from the fitted data in high-temperature regime may be taken as an actual one, which is ~7 fold higher than the bulk one.

This confirms that the PL emission in NS is from the exciton recombination due to enhanced exciton stability[52]. High exciton binding energy in PB100 NS supports the stable and high PL QY. The variation in PL peak energy with temperature is shown in **Fig. 4.13(c)**, revealing ~45.8 meV upshift in PL peak with the increase in temperature. In perovskite semiconductor, the increase in bandgap with temperature is attributed to the electron-phonon coupling[53]. The exciton–phonon coupling leads to the shrinkage in band gap, which induces the PL spectral red shift with decreasing temperature. Hence, perovskite has a positive thermal expansion coefficient of the band gap. In order to estimate the electron-phonon coupling, the experimental data of PL peak position vs temperature is fitted with the equation[50],

$$E_g(T) = E_0 + A_{TE}T + A_{EP}(1 + 2/(exp(\hbar\omega/k_BT) - 1)) \quad (4.4)$$

Where E_0 is the bandgap at 0 K, $\hbar\omega$ is the phonon energy, A_{TE} and A_{EP} are the factors accounting for thermal expansion and electron-phonon interaction, respectively. The parameters extracted from the fitting are: A_{TE}= 0.13 meV/K, A_{EP}= 17 meV, $\hbar\omega$= 37 meV, which match well with the literature[4]. Temperature-dependent linewidth ($\Gamma(T)$) of PL spectra is displayed in **Fig. 4.13(d)**. A broadening in PL peak at higher temperature is observed, which may be caused by the coupling of the excitons to acoustic phonons and to longitudinal optical (LO) phonons[54]. To quantify the exciton-phonon interaction in the 2D NS, experimental data are fitted using Boson model given by:

$$\Gamma(T) = \Gamma_0 + \Gamma_{LO}/(exp(\hbar\omega_{LO}/K_BT) - 1) \quad (4.5)$$

where Γ_0 is the inhomogeneous broadening contribution, Γ_{LO} is the longitudinal exciton-optical phonon contribution to the FWHM, and $\hbar\omega_{LO}$ is the LO phonon energy. The values of the fitted parameters are: Γ_0 = 33 meV, Γ_{LO} = 240 meV, $\hbar\omega_{LO}$= 36 meV, which are consistent with the unresolved vibration energy in the Raman spectrum[55]. Interestingly, the optical phonon energy extracted from Boson fit matches very well with that obtained from the fitted data using **equation (4.5)**. High optical phonon energy indicates strong exciton-phonon interactions, which is expected in a quantum confined system.

4.4.3.3. Time-Resolved Photoluminescence Studies

TRPL measurement was performed on various perovskite NSs using a 405 nm pulsed laser excitation. The PL decay curves shown in **Fig. 4.14** are fitted with triexponential decay function given by, $I(t) = \sum_{i=1}^{3} A_i exp(-t/\tau_i)$ where A_i is the amplitude of the PL decay component corresponding to the lifetime τ_i. The average lifetime (τ_{avg}) is calculated using the relation: $\tau_{avg} = \sum_{i=1}^{3} A_i \tau_i^2 / \sum_{i=1}^{3} A_i \tau_i$. Based on the deconvolution of steady state PL spectrum with three peaks, the PL decay is fitted with triexponential decay function. The corresponding fitting parameters

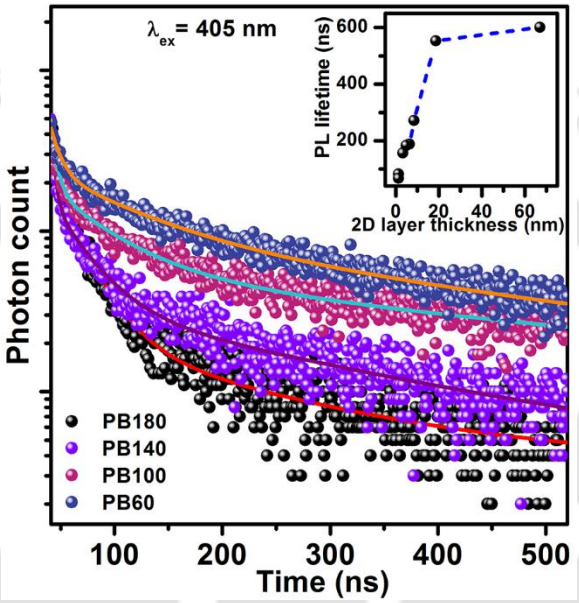

Fig. 4.14. A comparison of TRPL spectra of various 2D perovskite NS (PB60-PB180); the symbols corresponds to experimental data and the solid lines correspond to the fitted data. The inset shows the variation of the PL lifetime with 2D layer thickness.

(see **Table 4.3**) including the evolution of the amplitude of each peak with solvothermal temperature is consistent with the steady state PL results. The contributions from three different states of different origin essentially suggest different time constants of each component. Slow component with high amplitude of the TRPL decay corresponds to the main PL contribution, i.e., band edge emission, while the faster lifetime component corresponds to the presence of QDs along with NS and defect states. As shown in **Table 4.3**, the average lifetime changes from 601.3 ns in PB0 to 67.0 ns PB180. Hence, a 9-fold decrease in PL lifetime is observed for the QDs due to the reduction in thickness/size. The variation in PL lifetime with the thickness of the 2D NS is presented in the inset of **Fig. 4.14**, demonstrating a longer lifetime of carriers for the thicker NS

grown at lower temperature suggesting a reduction in nonradiative recombination paths, which in turn yields high PL QY, suitable for optoelectronic device applications[56].

Table 4.3. *TRPL decay components fitted with tri-exponential function.*

Sample	τ_1 (ns) (A_1 %)	τ_2 (ns) (A_2 %)	τ_3 (ns) (A_3 %)	τ_{avg} (ns)
PB60	5.7(3)	696.7(85)	78.3(12)	601.3
PB100	5.4 (8)	382.2 (67)	54.4 (25)	271.3
PB120	5.2 (9)	277.8 (64)	40.7 (27)	188.5
PB130	5.4 (11)	288.7 (59)	42.9 (30)	183.8
PB140	3.1 (15)	258.9 (57)	32 (28)	156.2
PB150	4.5 (24)	225 (29)	34.2 (47)	82.5
PB180	6.4(20)	167.5(31)	28.8(49)	67.0

4.4.4. Stability of the 2D NS

Stability of 2D NS is studied under different conditions. In order to evaluate the stability of the NS under prolonged laser irradiation, we have recorded the PL spectra of PB140 NS at room temperature at a regular interval under continuous laser irradiation (405 nm, 15 mW at source). The variation of PL emission intensity with time under continuous laser irradiation for 7 hours in the ambient condition is shown in **Fig. 4.15(a)**. We observe first a gradual increase in PL intensity with laser exposure up to 2.5 hours of the laser irradiation of PB140 and then it marginally decreased followed by constant intensity, which is higher than its initial intensity. It is likely that due to local heating caused by the laser exposure, the structural and optical properties of the NS are improved resulting in higher PL intensity after prolonged laser exposure. However, prolonged exposure leads to more stable performance of the NS. Hence, the 2D NS exhibits excellent optical stability under UV laser exposure for long duration. Effect of laser irradiation on the PL intensity is better understood by deconvolution of PL spectra for PB140 NS sample with three Gaussian peaks before and after laser irradiation for 3 hrs (see **Fig. 4.15(b)**). These three peaks are attributed to the presence of QDs, NS band-edge emission and defect-related emissions, as discussed earlier. Before laser irradiation, the contribution of defect emission is prominent. However, after laser

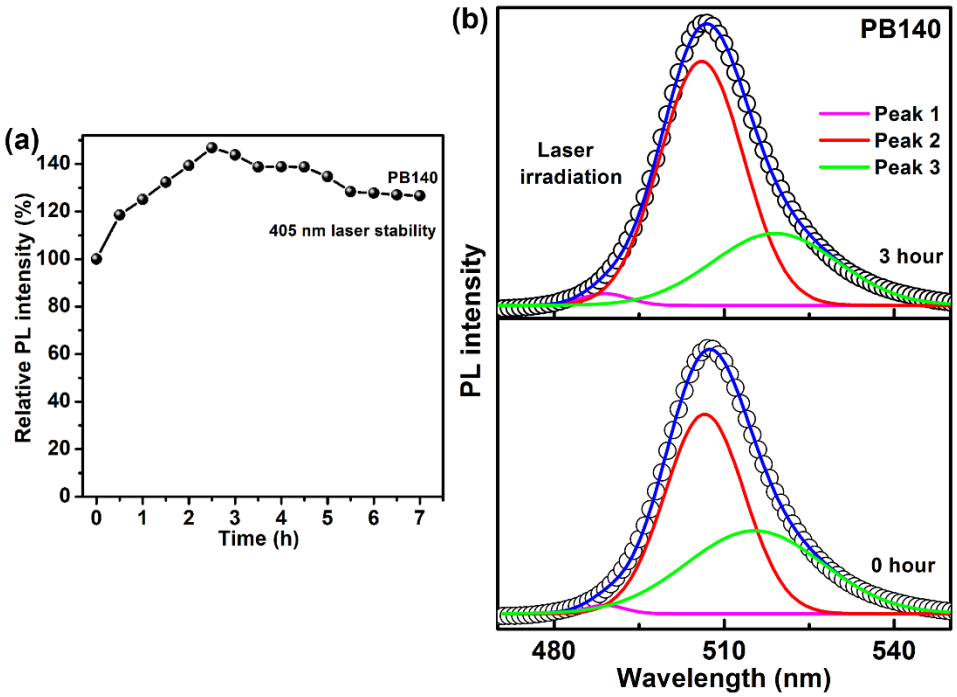

Fig. 4.15. (a) Variation of PL intensity for PB140 as a function of laser (CW) irradiation time. (b) Comparison of PL spectra of PB140 before and after laser irradiation for 3 hrs. The symbols represent the experimental data and the solid lines represent the fitted peaks.

irradiation, the contribution of band edge emission peak is substantially increased as compared to that of defect, which in turn results into the higher intensity of emission. Tiguntseva et al. reported 130 % improved PL emission in $CH_3NH_3PbI_3$ by laser post processing[57]. Gentle laser heating is reported to reduce the defect concentration in the perovskite film[57]. Tian et al. reported thousand fold enhancement in PL intensity and proposed that the trapping sites which are responsible for non-radiative charge recombination can be de-activated in the course of light curing process[58]. Mosoconi et al. reported the increase in PL lifetime and total intensity which eventually stabilize, due to reduction of an initial trap density of $\sim 10^{17}$ cm^{-3} to a stabilized trap density of $\sim 10^{16}$ cm^{-3}[59].

Long-term storage stability of 2D NS in PB140 is also tested in the ambient environment. The sample was stored in the ambient condition with high humidity without any protection. **Fig. 4.16(a)** exhibits the PL spectra of PB140 taken for a freshly prepared sample and that of after 8 months of storage. The PL intensity of PB140 is observed to be marginally reduced after 8 months of storage, indicating its high stability. Thus, the NS retains its initial PL emission even after the storage for several months in high humidity ambient, which is the most unique property of 2D Ruddelson

proper perovskite compared to its 3D counter part due to high formation energy, hydrophobic organic cations, strong Van-der Waals interaction between the capping organic molecules and the [PbI_6] units.[60, 61] However, PL intensity of PB150 NS decreases by >90 % after storing it in ambient condition for 8 months, as shown in **Fig. 4.16(b)**. The NSs in PB150 is of bilayer thickness, hence it may disintegrate into QDs in ambient condition, as QD peak is prominent in the PL spectra after 8 months of storage. Further processing may be needed to increase the stability of bilayer NS.

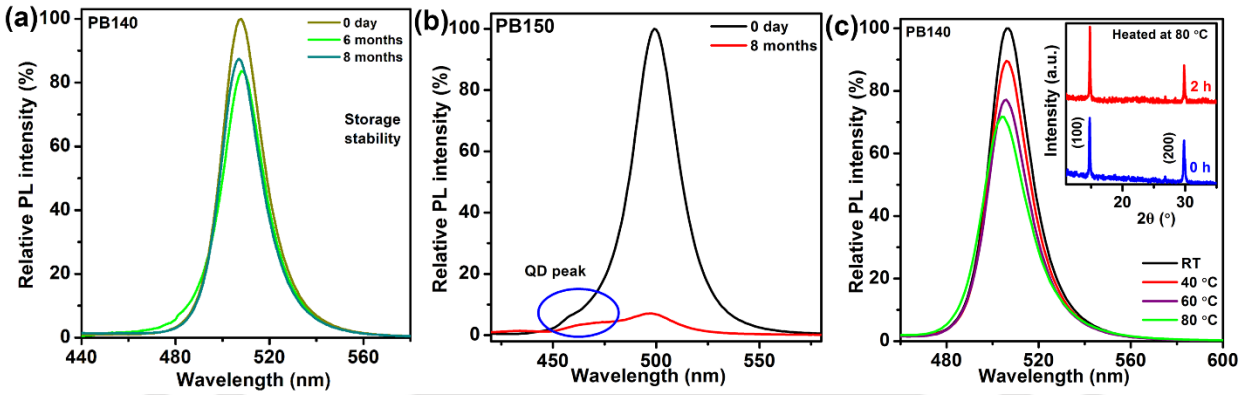

Fig. 4.16. Comparison of PL spectra of (a) PB140 and (b) PB150 for freshly prepared sample and after storing it for 8 months in ambient condition. (c) Heating temperature dependent stability of PL emission in PB140. The inset shows the comparison of XRD pattern of PB140 before and after heating at 80 ºC for 2 h.

Temperature dependent stability of PB140 NS is investigated by heating the sample at different temperatures and recording its PL spectra at each temperature. There is a systematic decrease in PL intensity with increasing temperature of heating (see **Fig. 4.16(c)**), which is consistent with the thermal quenching behaviour of PL. To assess its structural stability after heating, XRD pattern was recorded before and after heating the sample at 80 ºC for 2 hours. The XRD pattern intensity is increased after heating, as shown in the inset of **Fig. 4.16(c)**, and it implies the improved crystal structure of the NS after heating. Hence, the synthesized NS shows excellent structural and optical stability at higher temperature up to 80 ºC.

4.4.5. Performance of 2D Perovskite NS as White LED

Practical application of the as-grown 2D NS is demonstrated by fabricating a white LED using a blue LED chip and $MAPbBr_1I_2$ layer. Mixed halide perovskite solution having emission peak at ~600 nm is first mixed with polymer and then it was used as an orange emissive layer on top of

blue LED to fabricate the white LED. The electroluminescence spectra of the optimized white LED driven by bias voltage 2.35 V is shown in **Fig. 4.17(a)**, with upper inset showing the digital photograph of the device. The CIE coordinates of the device are found to be (0.33,0.30) with CCT

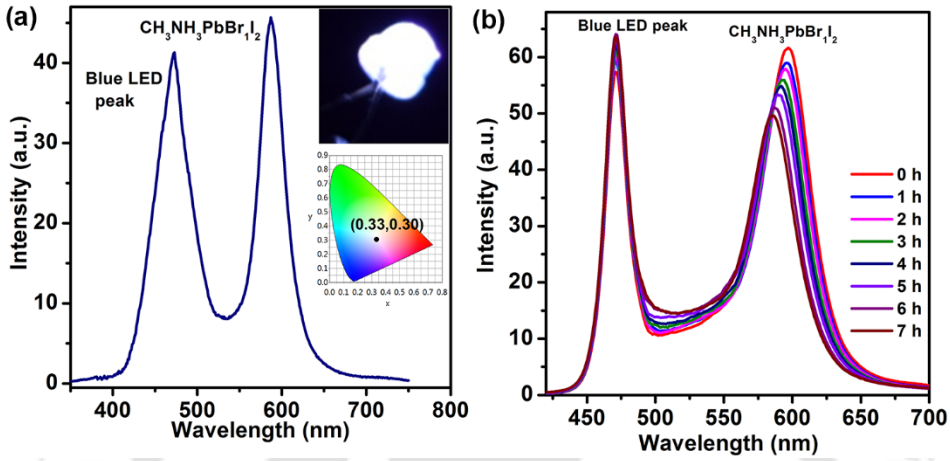

Fig. 4.17. (a) EL spectra of white light-emitting NS device fabricated with blue LED chip and $MAPbBr_1I_2$ NSs. The upper inset shows a digital photograph of the emitting device and the lower inset shown the CIE chromaticity coordinates of the white LED device. (b) Operational stability of white light-emitting NS device.

5263 and CRI 55 (see lower inset of **Fig. 4.17(a)**). The CIE coordinates of the fabricated white LED is closely matched with the pure white light (0.33, 0.33). The performance and color purity of the orange luminescent perovskite coated white LED are comparable or better than other reported orange luminescent phosphor coated white LEDs using carbon dots, silicon dots and other 2D materials[62-66]. Hence, mixed halide perovskite can be considered as a promising candidate for the high color quality, low cost white light production and in the solid-state lighting field. Operational stability of fabricated LED is measured after 7 h of continuous illumination. After 7 hours of continuous operation at 2.35 V, the blue LED peak remains constant, however $MAPbBr_1I_2$ peak is slightly (~1.2 times) decreased as shown in **Fig. 4.17(b)**. Hence, white LED shows very good stability without any protection and encapsulation of the device will increase the stability further.

4.4.6. Performance of 2D Perovskite NS Based Photodetector

The 2D perovskite NSs with high lateral size (surface area) and long diffusion length are reported to be promising for various photovoltaic and optoelectronic applications[7, 9, 67]. Accordingly, a photodetector device was fabricated based on PB140 NSs in order to demonstrate its potential

application. The schematic representation of the planar device structure and the energy band diagram are portrayed in **Fig. 4.18(a)**. Aluminum electrodes with an interdigital spacing of 100 μm were first deposited on the Si/SiO_2 substrate by thermal evaporation through a shadow mask.

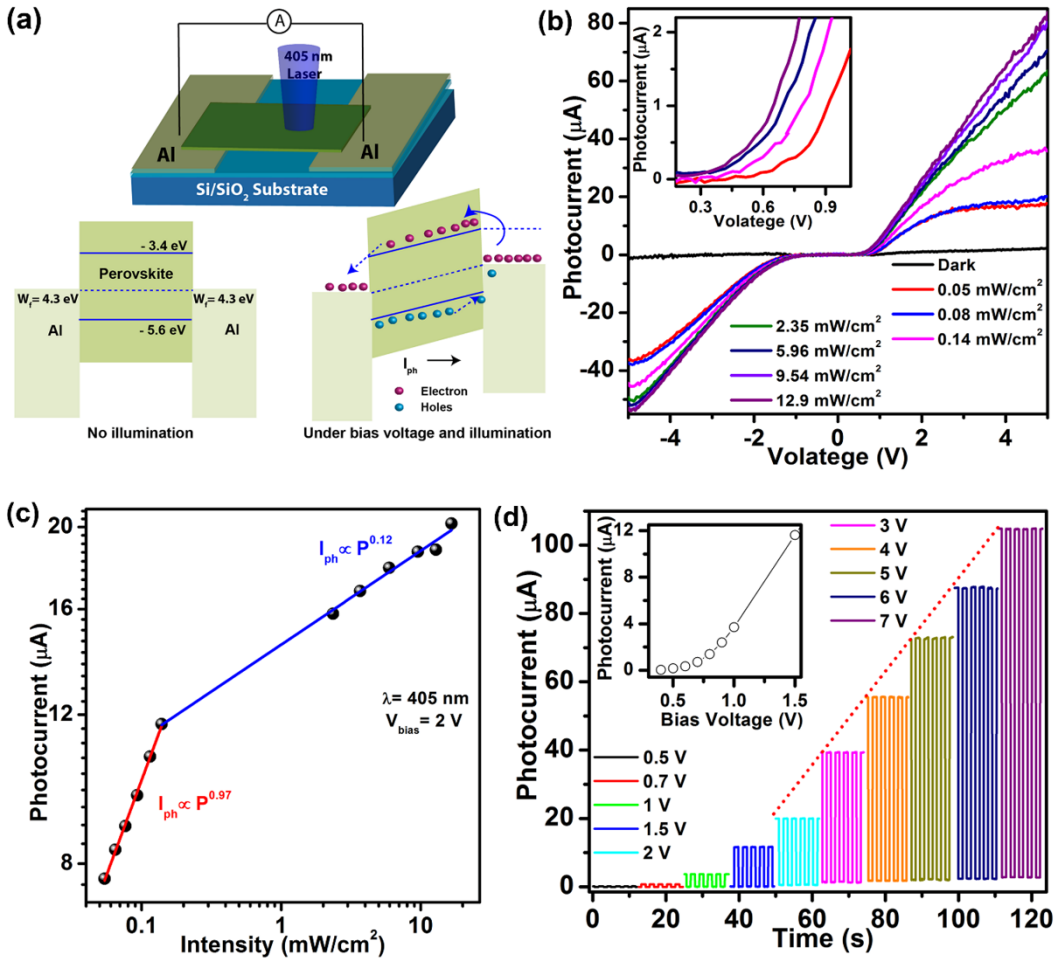

Fig. 4.18. (a) Schematic diagram of a photodetector device fabricated with PB140 NS and the energy band diagram of the Al/$MAPbBr_3$/Al structure before light illumination (no bias) and after light illumination (under bias). (b) I–V characteristics of the photodetector in the dark and under illumination with 405 nm laser for different light irradiation intensities; the inset shows the magnified I–V curve at lower bias voltages. (c) Logarithmic plot of the photocurrent as a function of the light intensity at a bias voltage of 2 V and the data are fitted with a power law. (d) Time-dependent photoresponse of PB140 NS under 405 nm light illumination (5.96 mW/cm^2) recorded at different bias voltages. The inset shows the photocurrent vs. bias voltage for a fixed intensity of illumination.

Subsequently, the NS solution was drop cast between the gap of two electrodes and dried at 60 °C. In the dark, very low current (dark current, I_{dark}) flows between two electrodes under an applied bias voltage. When the device was exposed to light (405 nm laser), it results in the generation of electron-hole pairs with an energy higher than the bandgap of the perovskite NS. The electron and

holes are then rapidly drifted in different directions under bias voltage and collected by the electrodes leading to a dramatic increase in current (photocurrent, I_{ph}) between the metal electrodes. **Fig. 4.18(b)** shows the I-V characteristics of the device obtained in the dark and under different intensities of light illumination (405 nm). Under the dark condition, nearly linear current-voltage (*I–V*) behavior is observed. Under illumination, the current is abruptly increased, implying good sensitivity of the device to light. The photocurrent is highly dependent on the light intensity, and it is systematically increased with the increase in the light intensity because the number of photogenerated carriers is proportional to the absorbed photon flux. The inset of **Fig. 4.18(b)** shows the magnified view of I-V characteristic in the low bias region, indicating that the turn-on voltage of the device is very low (~0.4 V). **Fig. 4.18(c)** demonstrates the dependence of the photocurrent on light intensities under 2 V bias. This dependence can be understood better by fitting the data of photocurrent vs intensity by the well-known power law: $I_{Ph} \alpha P^{\theta}$, where I_{ph} is the photocurrent, P is the light intensity and θ is an empirical value reflecting the recombination of photocarriers, as shown in **Fig. 4.18(c)**[68]. In the low-intensity range, exponent θ=0.97 was obtained, which is close to 1.0, suggesting a low recombination loss. In contrast, in the high-intensity range, non-unity $\theta=0.12$ was observed, implying a strong recombination loss due to the presence of high carrier density and some trap states in the bandgap region[69]. Typical temporal photoresponse of the device under pulsed laser illumination at different bias voltages is shown in **Fig. 4.18(d)**. The photoresponse of the device is observed to be highly stable and reproducible over the long operational duration as well as ambient storage. The rise and fall edges of the photoresponse curve are very steep, indicating the very fast response of the device.[68] The photocurrent increases linearly with increasing the bias voltage due to the efficient transport of photocarriers and the suppression of the recombination loss at higher bias voltage. In the low bias region (0 to 1.5 V), the photocurrent increases very rapidly following a nonlinear behavior, as shown in the inset of **Fig. 4.18(d)**.

To calculate the fast response speed of the device, temporal response curve was recorded in a digital storage oscilloscope at a bias voltage of 5 V using the 405 nm pulsed laser driven by a TTL pulse, as shown in **Fig. 4.19(a)**. Since the direct measurement of the photocurrent is inherently slow in an ammeter, a 100 kΩ load resistance is added in series to the circuit, and the voltage across the load is measured in the oscilloscope. The rise/fall time of the device is found to be very

Table 4.4: *Comparison of the performance and stability of the perovskite NS-based photodetectors reported in the literature with the present work.*

Active material	Measurement condition (voltage, wavelength)	Rise time/ Fall time (ms)	R (A/W)	Stability (days of storage)	Ref
$MAPbBr_3$ QDs	2 V, 405 nm	320, 280	0.223	20 (30 % decrease in I_{ph})	[49]
$MAPbBr_3$ milliwire	2 V, 532 nm	407, 895	0.525	225*	[5]
$CsPbBr_3$ nanoplatelet	1.5 V, 442 nm	0.6, 0.9	34	47 (34 % decrease in R)	[70]
$CsPbCl_3$ NS	8 V, 405 nm	70, 45	-	2	[27]
$CsPbBr_3$ microplatelet	5 V, 405 nm	20.9, 24.6	1.33	210 (10 % decrease in I_{ph})	[71]
$MAPbBr_3$ NS	5 V, 405 nm	0.024, 0.103	1.93	180 (15 % decrease$^{\#}$ in PL)	*This work*

*I_{ph}=photocurrent, R=responsivity, * ~30 % decrease in PL intensity after 140 min in 75% humidity, $^{\#}$under 70% humidity*

fast 24 μs/103 μs. Note that the photocurrent response of our photoconductor is much faster than those reported earlier on perovskite NS (see **Table 4.4**). This may be due to high crystalline quality and high mobility of the carriers in the as-grown 2D NS. **Fig. 4.19(b)** presents the long-term stability of the photodetector device. The temporal photoresponse curve of the freshly fabricated sample is presented in the first five cycles in **Fig. 4.19(b)**. The second and third five cycles in **Fig. 4.19(b)** correspond to the temporal photoresponse curve recorded after 15 days and one month of storage, respectively, without any encapsulation. It is clear that a very marginal decay in photocurrent (~10.7 %) is observed after one month of storage, implying that the device retains its photodetection capability even under the ambient condition with high humidity. Thus, it can be concluded that the as-synthesized perovskite NSs have high ambient stability even under high humidity. Note that most of the reported perovskite photodetectors exhibit poor stability[72, 73]. **Fig. 4.19(c)** summarizes the evolution of the photocurrent under the continuous illumination of 405 nm laser light in ambient condition (relative humidity: 60–70 %, temperature ~23 °C) without any encapsulation/protection for 7 h operation under bias voltage of 5 V. The photocurrent remains almost constant throughout the measurement period, indicating its outstanding repeatability and

long term operational stability. To characterize the performance of the as-fabricated photodetector, responsivity, external quantum efficiency (EQE) and detectivity (D) were calculated in the spectral

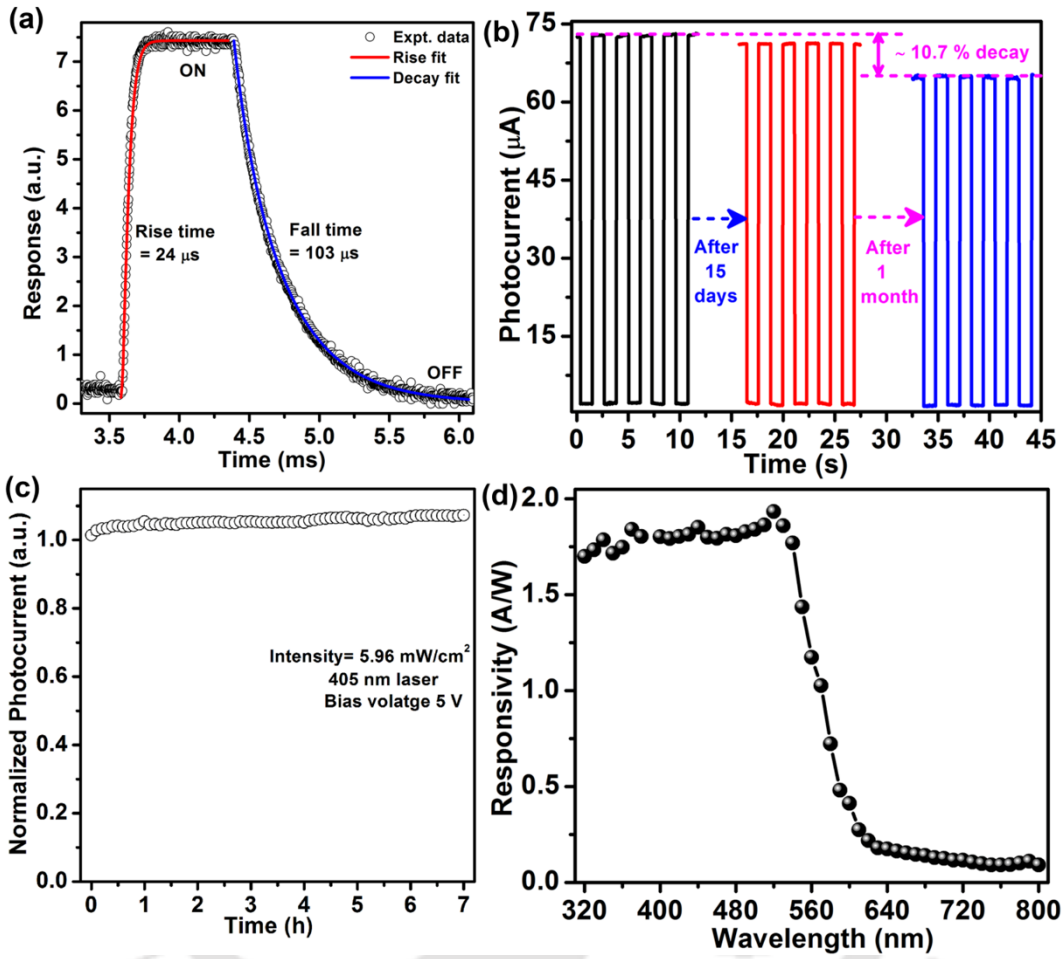

Fig. 4.19. (a) Temporal response of the photocurrent for PB140 NS photodetector measured at a bias of 5 V along with the exponential fits. (b) Photoresponse curve of PB140 NS photodetector device after long-term storage in humid ambient. (c) Normalized photocurrent of PB140 NS photodetector (without encapsulation) as a function of operation time at a bias voltage of 5 V. (d) Spectral responsivity of the NS photodetector recorded at 5 V bias.

range 310−800 nm. The efficiency of a photodetector is expressed in terms of spectral responsivity since it is directly proportional to the internal gain. Responsivity (R) of a photodetector can be defined as the photocurrent generated in the photodetector per unit power of the light incident on its effective area and can be expressed as,

$$R = \frac{I_{ph} - I_{dark}}{PA} \qquad (4.6)$$

Here, A is the effective illuminated area (0.02 cm^2). As shown in **Fig. 4.19(d)**, the NS detector displays a good spectral selectivity with a reasonably flat response in the range 310-560 nm consistent with its absorption behavior. Interestingly, the present device shows high responsivity in the UV region and can be exploited as a UV photodetector. The detectivity and *EQE* are also calculated using the following equations to express the figure of merits of the photodetector device,

$$D = R \times \left(\frac{A}{2qI_{dark}}\right)^{1/2} \quad (4.7)$$

$$EQE = R\frac{hc}{q\lambda} \quad (4.8)$$

Where A is the effective area of the photodetector, q is the electronic charge, h is the Planck's constant, c is the light velocity in vacuum and λ is the wavelength of the incident light.

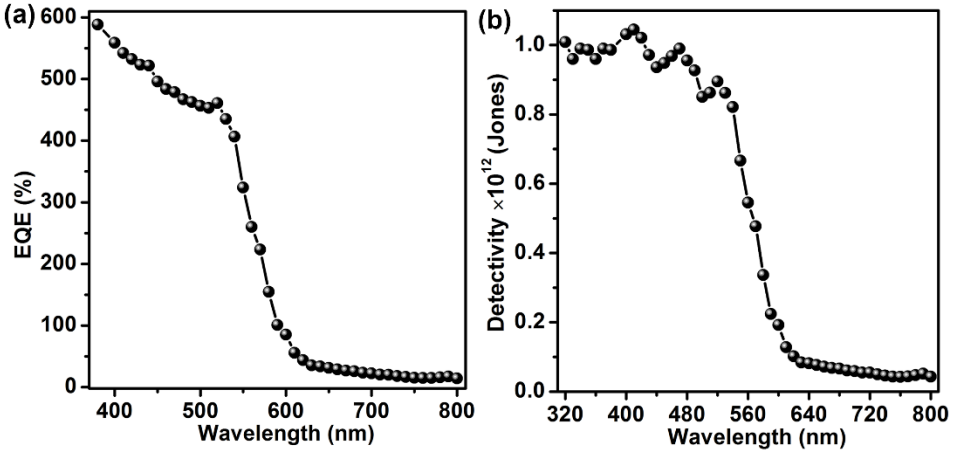

Fig. 4.20. (a) External quantum efficiency, and (b) detectivity of the 2D perovskite photodetector (with PB140) over a broad spectral range under a bias voltage of 5 V.

Hence, to achieve high detectivity of the device, high responsivity and low dark current are necessary. **Fig. 4.20(a)** shows the EQE of the device under 5 V bias. **Fig. 4.20(b)** depicts the detectivity in the spectral range of 310-800 nm under 5 V bias. Both the parameters demonstrate spectral trend similar to the responsivity data since they are proportional to responsivity. The peak detectivity and EQE of PB140 NS are observed to be 1.04×10^{12} Jones and 658 %, respectively. Note that the EQE of the device is very high (>100 %), which may be partly due to the tunneling of the carriers in the ultra-thin 2D NS. Perovskite photodetector reported to produce very EQE ($>10^5$ %) which is defined as photoconductive gain[74]. In general, trap states are beneficial to

achieve high gain. In the trap states, minority charge carriers are captured by traps, thus allowing the majority carriers to flow through the external circuit. The thinner nanosheet has more defect/trap states which may help in trapping minority charge carriers. High electron mobility of layered perovskite allows easy transport of electrons to the contacts. The 2D material-based UV-visible photodetector is applicable in numerous fields, such as imaging sensing, optical communication, optical storage, electric arc detection in factories, etc.

4.5. Summary and Conclusions

In this chapter, a simple, reproducible and novel solvothermal synthesis route is presented to successfully grow large-area 2D perovskite nanosheets with precisely tunable thickness and high optical quality and colloidal stability. In contrast to the methods reported mostly for inorganic perovskites, which are time consuming and tedious, we have demonstrated a precise control of the thickness of 2D hybrid organic perovskite layer from 14 layers to 2 layers simply by the control of temperature of the solvothermal process and our method is very facile and versatile. The resulting properties of the 2D NS are highly tunable and these are further successfully applied for the fabrication of a fast photodetector and a white LED. The present method is very promising for the development of large-area stable 2D perovskite layers for various cutting edge optoelectronic and imaging applications. The novelties of the work presented in the chapter are summarized below.

1. A fast solvothermal synthesis of 2D perovskite with precise control of thickness only by temperature control and an empirical relation showing linear relationship between growth temperature and the thickness of the 2D NS is established.
2. Without any pretreatment of the precursors, simple solvothermal treatment at various temperatures (100-150 °C) allowed us to tailor the thickness of the large-area (several micrometers) 2D NSs from 14 layers down to a bilayer thickness (1.2 nm), as revealed by systematic TEM and AFM analyses.
3. The temperature-dependent thickness evolution is quantitatively analyzed based on the supplied thermal energy, leading to the enlarged interlayer spacing and accelerated crystal growth along the lateral direction.
4. The band gap of the NS is effectively tuned from 2.34 to 2.54 eV owing to the strong QC effect in the 2D NSs.

5. We have also demonstrated bright blue-emitting QDs by increasing the OAm concentration with a very high PL QY of 84 % and a large spectral blue shift of ~60 nm.
6. Through a careful analysis of the steady-state and time-resolved PL spectra, the origin of the lower PL QY in thinner NS is traced to nonradiative recombination centers in the 2D layers.
7. The NS exhibits excellent optical and long-term stability including high temperature (up to 80 °C) stability, retaining its initial PL intensity for more than 8 months.
8. A white LED is fabricated with the orange luminescent 2D $CH_3NH_3PbBrI_2$ NS, with a CIE coordinate of (0.33, 0.30).
9. The 2D perovskite photodetector exhibits a very fast rise/fall time (24 µs/103 µs) along with high responsivity of ~1.93 A/W.

References

[1] H. Huang, F. Zhao, L. Liu, F. Zhang, X.-g. Wu, L. Shi, B. Zou, Q. Pei, H. Zhong, Emulsion Synthesis Of Size-Tunable CH3NH3PbBr3 Quantum Dots: An Alternative Route Toward Efficient Light-Emitting Diodes, ACS Appl. Mater. Interfaces, 7 (2015) 28128-28133.
[2] S. Gonzalez-Carrero, R.E. Galian, J. Pérez-Prieto, Maximizing the Emissive Properties of CH3NH3PbBr3 Perovskite Nanoparticles, J. Mater. Chem. A, 3 (2015) 9187-9193.
[3] F. Zhang, H. Zhong, C. Chen, X.-g. Wu, X. Hu, H. Huang, J. Han, B. Zou, Y. Dong, Brightly Luminescent and Color-Tunable Colloidal CH3NH3PbX3 (X= Br, I, Cl) Quantum Dots: Potential Alternatives for Display Technology, ACS nano, 9 (2015) 4533-4542.
[4] K. Zheng, Q. Zhu, M. Abdellah, M.E. Messing, W. Zhang, A. Generalov, Y. Niu, L. Ribaud, S.E. Canton, T.n. Pullerits, Exciton Binding Energy and the Nature of Emissive States in Organometal Halide Perovskites, J. Phys. Chem. Lett., 6 (2015) 2969-2975.
[5] F. Chen, C. Xu, Q. Xu, Y. Zhu, F. Qin, W. Zhang, Z. Zhu, W. Liu, Z. Shi, Self-Assembled Growth of Ultrastable CH3NH3PbBr3 Perovskite Milliwires for Photodetectors, ACS Appl. Mater. Interfaces, 10 (2018) 25763-25769.
[6] P. Kumar, C. Muthu, V.C. Nair, K.S. Narayan, Quantum Confinement Effects in Organic Lead Tribromide Perovskite Nanoparticles, J. Phys. Chem. C, 120 (2016) 18333-18339.
[7] J. Liu, K. Song, Y. Shin, X. Liu, J. Chen, K.X. Yao, J. Pan, C. Yang, J. Yin, L.-J. Xu, H. Yang, A.M. El-Zohry, B. Xin, S. Mitra, M.N. Hedhili, I.S. Roqan, O.F. Mohammed, Y. Han, O.M. Bakr, Light-Induced Self-Assembly of Cubic CsPbBr3 Perovskite Nanocrystals into Nanowires, Chem. Mater., (2019).
[8] J. Xing, X.F. Liu, Q. Zhang, S.T. Ha, Y.W. Yuan, C. Shen, T.C. Sum, Q. Xiong, Vapor Phase Synthesis of Organometal Halide Perovskite Nanowires for Tunable Room-Temperature Nanolasers, Nano Lett., 15 (2015) 4571-4577.

[9] S.T. Ha, X. Liu, Q. Zhang, D. Giovanni, T.C. Sum, Q. Xiong, Synthesis of Organic–Inorganic Lead Halide Perovskite Nanoplatelets: Towards High-Performance Perovskite Solar Cells and Optoelectronic Devices, Adv. Opt. Mater, 2 (2014) 838-844.
[10] J.A. Sichert, Y. Tong, N. Mutz, M. Vollmer, S. Fischer, K.Z. Milowska, R. García Cortadella, B. Nickel, C. Cardenas-Daw, J.K. Stolarczyk, Quantum Size Effect in Organometal Halide Perovskite Nanoplatelets, Nano Lett., 15 (2015) 6521-6527.
[11] P. Tyagi, S.M. Arveson, W.A. Tisdale, Colloidal Organohalide Perovskite Nanoplatelets Exhibiting Quantum Confinement, J. Phys. Chem. Lett., 6 (2015) 1911-1916.
[12] J. Cho, Y.-H. Choi, T.E. O'Loughlin, L. De Jesus, S. Banerjee, Ligand-Mediated Modulation of Layer Thicknesses of Perovskite Methylammonium Lead Bromide Nanoplatelets, Chem. Mater., 28 (2016) 6909-6916.
[13] J. Song, L. Xu, J. Li, J. Xue, Y. Dong, X. Li, H. Zeng, Monolayer and Few-Layer All-Inorganic Perovskites as a New Family of Two-Dimensional Semiconductors for Printable Optoelectronic Devices, Adv. Mater, 28 (2016) 4861-4869.
[14] M. Chen, Y. Zou, L. Wu, Q. Pan, D. Yang, H. Hu, Y. Tan, Q. Zhong, Y. Xu, H. Liu, B. Sun, Q. Zhang, Solvothermal Synthesis of High-Quality All-Inorganic Cesium Lead Halide Perovskite Nanocrystals: from Nanocube to Ultrathin Nanowire, Adv. Funct. Mater., 27 (2017) 1701121.
[15] I. Levchuk, P. Herre, M. Brandl, A. Osvet, R. Hock, W. Peukert, P. Schweizer, E. Spiecker, M. Batentschuk, C.J. Brabec, Ligand-Assisted Thickness Tailoring of Highly Luminescent Colloidal CH3NH3PbX3 (X = Br and I) Perovskite Nanoplatelets, ChemComm, 53 (2017) 244-247.
[16] J. Shamsi, Z. Dang, P. Bianchini, C. Canale, F. Di Stasio, R. Brescia, M. Prato, L. Manna, Colloidal Synthesis of Quantum Confined Single Crystal CsPbBr3 Nanosheets with Lateral Size Control up to the Micrometer Range, J. Am. Chem. Soc., 138 (2016) 7240-7243.
[17] Q.A. Akkerman, S.G. Motti, A.R. Srimath Kandada, E. Mosconi, V. D'Innocenzo, G. Bertoni, S. Marras, B.A. Kamino, L. Miranda, F. De Angelis, A. Petrozza, M. Prato, L. Manna, Solution Synthesis Approach to Colloidal Cesium Lead Halide Perovskite Nanoplatelets with Monolayer-Level Thickness Control, J. Am. Chem. Soc., 138 (2016) 1010-1016.
[18] Y. Nagaoka, K. Hills-Kimball, R. Tan, R. Li, Z. Wang, O. Chen, Nanocube Superlattices of Cesium Lead Bromide Perovskites and Pressure-Induced Phase Transformations at Atomic and Mesoscale Levels, Adv. Mater., 29 (2017) 1606666.
[19] W.S. Subhani, K. Wang, M. Du, X. Wang, N. Yuan, J. Ding, S. Liu, Anti-Solvent Engineering for Efficient Semitransparent CH3NH3PbBr3 Perovskite Solar Cells for Greenhouse Applications, J ENERGY CHEM, 34 (2019) 12-19.
[20] J. Luan, J. Xu, J. Chen, X. Shi, B. Zhang, S. Dai, J. Yao, Efficient Planar CH3NH3PbBr3 Perovskite Solar Cells Prepared at Room Temperature with Ionic-Liquids/Fullerene as an Electron Transport Bilayer, J. Solid State Chem. , 270 (2019) 436-442.
[21] W. Wang, Y. Zhang, W. Wu, X. Liu, X. Ma, G. Qian, J. Fan, Quantitative Modeling of Self-Assembly Growth of Luminescent Colloidal CH3NH3PbBr3 Nanocrystals, J. Phys. Chem. C, 123 (2019) 13110-13121.
[22] Z. Yuan, Y. Shu, Y. Xin, B. Ma, Highly Luminescent Nanoscale Quasi-2d Layered Lead Bromide Perovskites with Tunable Emissions, ChemComm, 52 (2016) 3887-3890.
[23] S. Gonzalez-Carrero, G.M. Espallargas, R.E. Galian, J. Pérez-Prieto, Blue-Luminescent Organic Lead Bromide Perovskites: Highly Dispersible and Photostable Materials, J. Mater. Chem. A, 3 (2015) 14039-14045.
[24] L. Dou, A.B. Wong, Y. Yu, M. Lai, N. Kornienko, S.W. Eaton, A. Fu, C.G. Bischak, J. Ma, T. Ding, N.S. Ginsberg, L.-W. Wang, A.P. Alivisatos, P. Yang, Atomically Thin Two-Dimensional Organic-Inorganic Hybrid Perovskites, Science, 349 (2015) 1518.

[25] D. Zhang, W. Zhou, Q. Liu, Z. Xia, CH3NH3PbBr3 Perovskite Nanocrystals Encapsulated in Lanthanide Metal–Organic Frameworks as a Photoluminescence Converter for Anti-Counterfeiting, ACS Appl. Mater. Interfaces, 10 (2018) 27875-27884.
[26] T. Zhang, M. Yang, E.E. Benson, Z. Li, J. van de Lagemaat, J.M. Luther, Y. Yan, K. Zhu, Y. Zhao, A Facile Solvothermal Growth of Single Crystal Mixed Halide Perovskite CH3NH3Pb(Br1−xClx)3, ChemComm, 51 (2015) 7820-7823.
[27] W. Zhai, J. Lin, C. Li, S. Hu, Y. Huang, C. Yu, Z. Wen, Z. Liu, Y. Fang, C. Tang, Solvothermal Synthesis of Cesium Lead Halide Perovskite Nanowires with Ultra-High Aspect Ratios for High-Performance Photodetectors, Nanoscale, 10 (2018) 21451-21458.
[28] M. Chen, H. Hu, Y. Tan, N. Yao, Q. Zhong, B. Sun, M. Cao, Q. Zhang, Y. Yin, Controlled Growth of Dodecapod-Branched CsPbBr3 Nanocrystals and Their Application in White Light Emitting Diodes, NANO ENERGY, 53 (2018) 559-566.
[29] H.-R. Xia, W.-T. Sun, L.-M. Peng, Hydrothermal Synthesis of Organometal Halide Perovskites for Li-Ion Batteries, ChemComm, 51 (2015) 13787-13790.
[30] Z.-J. Li, E. Hofman, A.H. Davis, M.M. Maye, W. Zheng, General Strategy for the Growth of CsPbX3 (X = Cl, Br, I) Perovskite Nanosheets from the Assembly of Nanorods, Chem. Mater., 30 (2018) 3854-3860.
[31] W. Zhai, J. Lin, Q. Li, K. Zheng, Y. Huang, Y. Yao, X. He, L. Li, C. Yu, C. Liu, Y. Fang, Z. Liu, C. Tang, Solvothermal Synthesis of Ultrathin Cesium Lead Halide Perovskite Nanoplatelets with Tunable Lateral Sizes and Their Reversible Transformation into Cs4PbBr6 Nanocrystals, Chem. Mater., 30 (2018) 3714-3721.
[32] L.-J. Chen, C.-R. Lee, Y.-J. Chuang, Z.-H. Wu, C. Chen, Synthesis and Optical Properties of Lead-Free Cesium Tin Halide Perovskite Quantum Rods with High-Performance Solar Cell Application, J. Phys. Chem. Lett, 7 (2016) 5028-5035.
[33] D. Chen, X. Chen, J. Li, X. Li, J. Zhong, Ultrathin CsPbX3 (X = Cl, Br, I) Nanoplatelets: Solvothermal Synthesis and Optical Spectroscopic Properties, Dalton Trans., 47 (2018) 9845-9849.
[34] L.-J. Chen, J.-H. Dai, J.-D. Lin, T.-S. Mo, H.-P. Lin, H.-C. Yeh, Y.-C. Chuang, S.-A. Jiang, C.-R. Lee, Wavelength-Tunable and Highly Stable Perovskite-Quantum-Dot-Doped Lasers with Liquid Crystal Lasing Cavities, ACS Appl. Mater. Interfaces, 10 (2018) 33307-33315.
[35] G. Gadea, A. Morata, A. Tarancon, Chapter Five - Semiconductor Nanowires for Thermoelectric Generation, in: S. Mokkapati, C. Jagadish (Eds.) SEMICONDUCT SEMIMET, Elsevier, 2018, pp. 321-407.
[36] H. Zhong, T. Mirkovic, G.D. Scholes, 5.06 - Nanocrystal Synthesis, in: D.L. Andrews, G.D. Scholes, G.P. Wiederrecht (Eds.) Comprehensive Nanoscience and Technology, Academic Press, Amsterdam, 2011, pp. 153-201.
[37] R.K. Mallavajula, L.A. Archer, Nanocrystal Self-Assembly Assisted by Oriented Attachment, Angew. Chem. Int. Ed., 50 (2011) 578-580.
[38] V. Schettino, R. Bini, Constraining Molecules at the Closest Approach: Chemistry at High Pressure, Chem. Soc. Rev., 36 (2007) 869-880.
[39] T. Yin, Y. Fang, W.K. Chong, K.T. Ming, S. Jiang, X. Li, J.-L. Kuo, J. Fang, T.C. Sum, T.J. White, J. Yan, Z.X. Shen, High-Pressure-Induced Comminution and Recrystallization of CH3NH3PbBr3 Nanocrystals as Large Thin Nanoplates, Adv. Mater, 30 (2018) 1705017.
[40] T. Udayabhaskararao, M. Kazes, L. Houben, H. Lin, D. Oron, Nucleation, Growth, and Structural Transformations of Perovskite Nanocrystals, Chem. Mater., 29 (2017) 1302-1308.
[41] M. Jian, H. Liu, T. Williams, J. Ma, H. Wang, X. Zhang, Temperature-Induced Oriented Growth of Large Area, Few-Layer 2d Metal–Organic Framework Nanosheets, Chem. Commun., 53 (2017) 13161-13164.
[42] L. Mao, C.C. Stoumpos, M.G. Kanatzidis, Two-Dimensional Hybrid Halide Perovskites: Principles and Promises, J. Am. Chem. Soc., 141 (2019) 1171-1190.

[43] M. Roy, Vikram, S. Banerjee, A. Mitra, A. Alam, M. Aslam, Composition-Controlled Synthesis of Hybrid Perovskite Nanoparticles by Ionic Metathesis: Bandgap Engineering Studies from Experiments and Theoretical Calculations, Chem. Eur. J., 25 (2019) 9892.
[44] L. Brus, Electronic Wave Functions in Semiconductor Clusters: Experiment and Theory, J. Phys. Chem., 90 (1986) 2555-2560.
[45] V. D'Innocenzo, G. Grancini, M.J.P. Alcocer, A.R.S. Kandada, S.D. Stranks, M.M. Lee, G. Lanzani, H.J. Snaith, A. Petrozza, Excitons Versus Free Charges in Organo-Lead Tri-Halide Perovskites, Nat. Commun., 5 (2014) 3586.
[46] K. Galkowski, A. Mitioglu, A. Miyata, P. Plochocka, O. Portugall, G.E. Eperon, J.T.-W. Wang, T. Stergiopoulos, S.D. Stranks, H.J. Snaith, R.J. Nicholas, Determination of the Exciton Binding Energy and Effective Masses for Methylammonium and Formamidinium Lead Tri-Halide Perovskite Semiconductors, Energy Environ. Sci., 9 (2016) 962-970.
[47] Q. Wang, X.-D. Liu, Y.-H. Qiu, K. Chen, L. Zhou, Q.-Q. Wang, Quantum Confinement Effect and Exciton Binding Energy of Layered Perovskite Nanoplatelets, AIP Adv., 8 (2018) 025108.
[48] H. Xu, J. Wang, T. Xuan, C. Lv, J. Hou, L. Zhang, Y. Dong, J. Shi, Convenient and Large-Scale Synthesis of High-Quality, All-Inorganic Lead Halide Perovskite Nanocrystals for White Light-Emitting Diodes, CHEM ENG J, 364 (2019) 20-27.
[49] J. Ghosh, R. Ghosh, P.K. Giri, Strong Cathodoluminescence and Fast Photoresponse from Embedded CH3NH3PbBr3 Nanoparticles Exhibiting High Ambient Stability, ACS Appl. Mater. Interfaces, 11 (2019) 14917-14931.
[50] S. Parveen, K.K. Paul, R. Das, P.K. Giri, Large Exciton Binding Energy, High Photoluminescence Quantum Yield and Improved Photostability of Organo-Metal Halide Hybrid Perovskite Quantum Dots Grown on a Mesoporous Titanium Dioxide Template, J. Colloid Interface Sci., 539 (2019) 619-633.
[51] J. Shamsi, A.S. Urban, M. Imran, L. De Trizio, L. Manna, Metal Halide Perovskite Nanocrystals: Synthesis, Post-Synthesis Modifications, and Their Optical Properties, Chem. Rev., 119 (2019) 3296-3348.
[52] Z.-K. Tan, R.S. Moghaddam, M.L. Lai, P. Docampo, R. Higler, F. Deschler, M. Price, A. Sadhanala, L.M. Pazos, D. Credgington, F. Hanusch, T. Bein, H.J. Snaith, R.H. Friend, Bright Light-Emitting Diodes Based on Organometal Halide Perovskite, Nat Nanotechnol., 9 (2014) 687.
[53] J. Li, X. Yuan, P. Jing, J. Li, M. Wei, J. Hua, J. Zhao, L. Tian, Temperature-Dependent Photoluminescence Of Inorganic Perovskite Nanocrystal Films, RSC Adv., 6 (2016) 78311-78316.
[54] G. Franssen, E. Litwin-Staszewska, R. Piotrzkowski, T. Suski, P. Perlin, Optical and Electrical Properties of Homoepitaxially Grown Multiquantum Well InGaN/GaN Light-Emitting Diodes, J. Appl. Phys., 94 (2003) 6122-6128.
[55] C. Quarti, G. Grancini, E. Mosconi, P. Bruno, J.M. Ball, M.M. Lee, H.J. Snaith, A. Petrozza, F. De Angelis, The Raman Spectrum of the CH3NH3PbI3 Hybrid Perovskite: Interplay of Theory and Experiment, J. Phys. Chem. Lett., 5 (2014) 279-284.
[56] X. Tang, W. Chen, Z. Liu, J. Du, Z. Yao, Y. Huang, C. Chen, Z. Yang, T. Shi, W. Hu, Z. Zang, Y. Chen, Y. Leng, Ultrathin, Core–Shell Structured SiO2 Coated Mn2+-Doped Perovskite Quantum Dots for Bright White Light-Emitting Diodes, Small, 15 (2019) 1900484.
[57] E.Y. Tiguntseva, I.N. Saraeva, S.I. Kudryashov, E.V. Ushakova, F.E. Komissarenko, A.R. Ishteev, A.N. Tsypkin, R. Haroldson, V.A. Milichko, D.A. Zuev, S.V. Makarov, A.A. Zakhidov, Laser Post-Processing of Halide Perovskites for Enhanced Photoluminescence and Absorbance, J. Phys.: Conf. Ser., 917 (2017) 062002.
[58] Y. Tian, M. Peter, E. Unger, M. Abdellah, K. Zheng, T. Pullerits, A. Yartsev, V. Sundström, I.G. Scheblykin, Mechanistic Insights into Perovskite Photoluminescence Enhancement: Light Curing with Oxygen Can Boost Yield Thousandfold, Phys. Chem. Chem. Phys., 17 (2015) 24978-24987.
[59] E. Mosconi, D. Meggiolaro, H.J. Snaith, S.D. Stranks, F. De Angelis, Light-Induced Annihilation of Frenkel Defects in Organo-Lead Halide Perovskites, Energy Environ. Sci., 9 (2016) 3180-3187.

[60] Y. Zheng, T. Niu, X. Ran, J. Qiu, B. Li, Y. Xia, Y. Chen, W. Huang, Unique Characteristics Of 2d Ruddlesden–Popper (2drp) Perovskite For Future Photovoltaic Application, J. Mater. Chem. A, 7 (2019) 13860-13872.
[61] L. Zhang, Y. Liu, Z. Yang, S. Liu, Two Dimensional Metal Halide Perovskites: Promising Candidates for Light-Emitting Diodes, J ENERGY CHEM., 37 (2019) 97-110.
[62] X. Li, Y. Liu, X. Song, H. Wang, H. Gu, H. Zeng, Intercrossed Carbon Nanorings with Pure Surface States as Low-Cost and Environment-Friendly Phosphors for White-Light-Emitting Diodes, Angew. Chem. Int. Ed., 54 (2015) 1759-1764.
[63] J. Ren, X. Sun, Y. Wang, R. Song, Z. Xie, S. Zhou, P. Chen, Controllable Photoluminescent and Nonlinear Optical Properties of Polymerizable Carbon Dots and Their Arbitrary Copolymerized Gel Glasses, Adv. Opt. Mater, 6 (2018) 1701273.
[64] A.K. Mandal, M. Ray, I. Rajapaksa, S. Mukherjee, A. Datta, Xylene-Capped Luminescent Silicon Nanocrystals: Evidence of Supramolecular Bonding, J. Phys. Chem. C, 116 (2012) 14644-14649.
[65] Y. Wang, Z. Yin, Z. Xie, X. Zhao, C. Zhou, S. Zhou, P. Chen, Polysiloxane Functionalized Carbon Dots and Their Cross-Linked Flexible Silicone Rubbers for Color Conversion and Encapsulation of White LEDs, ACS Appl. Mater. Interfaces, 8 (2016) 9961-9968.
[66] S.C. Huang, J.K. Wu, W.-J. Hsu, H.H. Chang, H.Y. Hung, C.L. Lin, H.-Y. Su, N. Bagkar, W.-C. Ke, H.T. Kuo, R.-S. Liu, Particle Size Effect on the Packaging Performance of YAG:Ce Phosphors in White LEDs, Int. J. Appl. Ceram. Technol., 6 (2009) 465-469.
[67] G. Xing, N. Mathews, S. Sun, S.S. Lim, Y.M. Lam, M. Grätzel, S. Mhaisalkar, T.C. Sum, Long-Range Balanced Electron-and Hole-Transport Lengths in Organic-Inorganic CH3NH3PbI3, Science, 342 (2013) 344-347.
[68] L.-B. Luo, G.-A. Wu, Y. Gao, L. Liang, C. Xie, Z.-X. Zhang, X.-W. Tong, T. Wang, F.-X. Liang, A Highly Sensitive Perovskite/Organic Semiconductor Heterojunction Phototransistor and Its Device Optimization Utilizing the Selective Electron Trapping Effect, Adv. Opt. Mater, 7 (2019) 1900272.
[69] Z.-X. Zhang, Z. Long-Hui, X.-W. Tong, Y. Gao, C. Xie, Y.H. Tsang, L.-B. Luo, Y.-C. Wu, Ultrafast, Self-Driven, and Air-Stable Photodetectors Based on Multilayer PtSe2/Perovskite Heterojunctions, J. Phys. Chem. Lett, 9 (2018) 1185-1194.
[70] X. Liu, D. Yu, F. Cao, X. Li, J. Ji, J. Chen, X. Song, H. Zeng, Low-Voltage Photodetectors with High Responsivity Based on Solution-Processed Micrometer-Scale All-Inorganic Perovskite Nanoplatelets, Small, 13 (2017) 1700364.
[71] Y. Li, Z. Shi, L. Lei, F. Zhang, Z. Ma, D. Wu, T. Xu, Y. Tian, Y. Zhang, G. Du, C. Shan, X. Li, Highly Stable Perovskite Photodetector Based on Vapor-Processed Micrometer-Scale CsPbBr3 Microplatelets, Chem. Mater., 30 (2018) 6744-6755.
[72] W. Tian, H. Zhou, L. Li, Hybrid Organic–Inorganic Perovskite Photodetectors, Small, 13 (2017) 1702107.
[73] H. Lu, W. Tian, F. Cao, Y. Ma, B. Gu, L. Li, A Self-Powered and Stable All-Perovskite Photodetector–Solar Cell Nanosystem, Adv. Funct. Mater., 26 (2016) 1296-1302.
[74] X. Zhao, L. Huang, Y. Wang, X. Zhu, L. Li, G. Li, W. Sun, Interface Engineering for Gain Perovskite Photodetectors with Extremely High External Quantum Efficiency, RSC Adv., 10 (2020) 32976-32983.

Chapter 5

Stable Deep Blue Emission with Unity Quantum Yield in Organic-Inorganic Halide Perovskite 2D Nanosheets Doped with Cerium and Terbium at High Concentrations

In this chapter, we have developed a novel strategy to achieve stable and deep blue emission with absolute unity photoluminescence (PL) quantum yield (QY) through Ce^{3+} and Tb^{3+} doping at high concentration in 2D $CH_3NH_3PbBr_3$ nanosheet (NS) using a solvothermal method. Our studies reveal that with Ce/Tb doping, the thickness of the NS systematically goes down from 10 layers to bilayer (1.4 nm) perovskite at high doping level and the bandgap of the 2D perovskite layer increases from 2.394 eV to 2.981 eV. The measured bandgap widening with doping is analyzed and explained on the basis of quantum confinement effect and lattice contraction. Interestingly, by incorporating 70 mol% $CeBr_3$ in the perovskite crystal, we achieved a deep blue emitting nanoplatelet with 100 % QY, narrow linewidth (~24 nm), and a color coordinate of (0.145, 0.054) closely matching with the standard color Rec. 2020 (0.131, 0.046) specification, making it one of the most efficient perovskite blue light emitters reported to date. We also demonstrate much improved storage stability of the Ce and Tb doped NS, fully consistent with the density functional theory (DFT) calculations. Low temperature PL study reveals the coexistence of ordered and disordered orthorhombic phases. We investigated the role of dopants in the achieving the high QY and deep blue emission in 2D perovskite using DFT based calculation of its electronic structure. From DFT calculation, we show that the dopants stabilize the structure with lower formation energy and it enrich the conduction band edge states without introducing deep trap states, which is responsible for the high PL QY. The calculation also reveals that Tb doping leads to substantial increase in bandgap, which is fully consistent with our experimental results. Finally, Ce^{3+} doped $CH_3NH_3PbBr_3$ blue-emitting nanoplatelet is used as a white light LED with CIE coordinates (0.334, 0.326). This work demonstrates a versatile approach to develop rare-earth doped deep blue-emitting 2D perovskites with exceptionally high PL QY and provides new insights into the structural stability and electronic structure of rare-earth doped 2D perovskites.

5.1. Introduction

Over the past decade, lead halide-based perovskites having the general formula $APbX_3$ (where A= CH_3NH_3, Cs, etc.; X= Br, Cl, and I) have emerged as an outstanding class of material for the fundamental scientific and technological application-based research[1-5]. Despite having several advantages, such as tunable bandgap, superior optoelectronic properties, excellent photovoltaic efficiency, the commercialization of lead halide perovskites is still facing hindrance due to its toxicity and poor stability in ambient environment[1, 6-9]. Hence, there is an intense search for developing Pb free perovskite with improved optoelectronic performance due to the toxicity of Pb. Tremendous efforts have been devoted to incorporate transition metals (Mn^{2+}, Cu^{2+}, Fe^{2+}, Zn^{2+}), metalloids (Sn^{2+}, Bi^{3+}) and lanthanide materials (Ce^{3+}, Eu^{3+}, Yb^{3+}, etc.), etc. in the perovskite crystal[9-17]. However, doping-related studies are still far from satisfactory, since the substitution of Pb^{2+} often deteriorates the remarkable optoelectronic performance of lead halide perovskites[18]. Sn was the first metal to be considered as a replacement of Pb[12, 13]. However, Sn doped perovskite crystal is found to be very unstable in nature, since Sn^{2+} quickly oxidizes to Sn^{4+} upon exposure to atmosphere[9, 19]. Bi^{3+} doping in $CH_3NH_3PbBr_3$ ($MAPbBr_3$, MA= CH_3NH_3) or $CsPbBr_3$ crystal significantly quenches the photoluminescence quantum yield (PL QY), since it includes non-radiative recombination centers in the crystal, though it improves the stability[11, 20, 21]. Mn-doped $CsPbCl_3$ nanocrystal (NC) is one of the most intensively studied system, as it introduces a new electronic energy level resulting in low energy electronic transition due to strong exchange interaction between d electron of Mn^{2+} and perovskite[22, 23]. However, the PL QY and doping efficiency was much lower than the anticipated value in the most synthesis procedure, since the perovskite crystal structure was affected by the high doping concentration[10, 18, 24-26].

Interestingly, rare-earth dopants in perovskites are considered very promising due to its remarkable optical properties[27]. Octahedral site ($PbBr_6$) in perovskite crystals perfectly matches the doping criteria of lanthanide materials, as it prefers a higher coordination number (≥ 6). The energy levels of rare-earth elements are not very sensitive to the lattice environment, as its partially filled 4f shell ($4f^{n-1}$) is shielded from external by $5s^2$ and $6p^6$ electrons, which makes it comparatively more stable in ambient condition[28]. Song and coworkers first reported the rare-earth codoped (Ce^{3+} and Yb^{3+}; Yb^{3+} and Er^{3+}) $CsPbCl_{1.5}Br_{1.5}$ NCs and explored it as a downconverter of commercial silicon solar

cell resulting into an improvement of the power conversion efficiency from 18.1 to 21.5 %[14]. The same group presented doping of various other lanthanide materials (Ln^{3+} = Ce^{3+}, Sm^{3+}, Eu^{3+}, Tb^{3+}, Dy^{3+}, Er^{3+}, and Yb^{3+}) into the $CsPbCl_3$ crystal lattice following a modified hot injection method, which exhibits a blue shift in the absorption spectra in the doped NC with the increase in the atomic number of dopant lanthanide ions[29]. However, PL QY decreases substantially in the blue region. Though Ce^{3+} doped $CsPbCl_3$ yeilds blue emission at 430 nm, the QY decreases to 24.3 %[29]. Even with Tb^{3+} doping, Song et al. achieved PL emission at 550 nm with PL QY 31.2 %[29]. Zhang et al. reported enhancement of total (excitonic + dopant) PL QY from 5 to 127.8 % with Yb^{3+} and Yb^{3+}/Er^{3+} doped $CsPbCl_3$ NC[30]. Gamelin et al. reported an exceedingly high PL QY of 190 %, even in bulk like thin films of Yb^{3+} doped $CsPbCl_3$[31]. High PL QY in Yb^{3+} doped $CsPbCl_3$ is due to an efficient quantum-cutting phenomenon, where the high absorption coefficient of $CsPbCl_3$ allows it to transfer the excitonic energy to Yb^{3+} ions upon photoexcitation.

However, the incorporation of rare-earth ions using direct synthesis process is quite challenging in the narrow bandgap variants of perovskite i.e., $CsPbBr_3$ and $CsPbI_3$[32]. Few groups have reported the doping of rare-earth ions following modified synthesis techniques or post-synthesis strategies. Yao et al. reported enhancement of the photo/electroluminescence efficiency of $CsPbBr_3$ NCs through doping of heterovalent Ce^{3+} ions via a facile hot-injection method[33]. However, they achieved green emission with Ce^{3+} doping at 515 nm, and the bandgap couldn't be tuned much with doping concentration. Duan et al. incorporated RE^{3+} (RE = La, Ce, Nd, Sm, Eu, Gd, Tb, Ho, Er, Yb, and Lu) into $CsPbBr_3$ films via a multistep solution-processed technique for solar cell application[34]. Mir et al. followed a post-synthesis doping procedure to dope Mn and Yb in $CsPbX_3$ (X= Cl, Br, and I) NC with bandgaps covering the entire visible region[35]. However, the relative intensity of dopant emission is sharply quenched in $CsPbBr_3$ and $CsPbI_3$ NCs as compared to $CsPbCl_3$ NC. Wang et al. introduced Eu^{3+} in the $CsPbI_3$ crystal by reversible redox cycle, where Pb^0 is oxidized by Eu^{3+} ions and I^0 is reduced by Eu^{2+} ions[16]. Though several reports discussed doping-induced blue emission from $CsPbCl_3$ nanocrystal, very few studies discussed about the bandgap tuning of Br based perovskite towards the blue region with high emission efficiency. Recently, blue emission was achieved with doping of metal ions (Sb^{3+} and Nd^{3+}) in $CsPbBr_3$ with 73.8 % and 90 % PL QY[36, 37]. Deep blue emission from bromide-based perovskite has been reported without doping by changing the synthesis condition, but the PL QY was found to be pretty low compared to green luminescent perovskite. All-bromide-based cesium

lead perovskite nanocrystals with deep blue emission at 405 (±1) nm was synthesized by Shi et al., however PL QY could be achieved up to 22 (±3)%[38]. Gao and co-workers reported deep blue emission (435 nm) from $CsPbBr_3$ nanoribbons of two-unit-cell thickness with PL QY up to 10 %[39]. Hence, the reported PL QYs are still quite low as compared to unity QY of perovskite nanomaterials in the green region. With growing uses of blue LED in the modern technology, there is an emergent need for achieving stable blue emission. Though rare-earth doping in all-inorganic halide perovskite ($CsPbX_3$) shows excellent optoelectronic and photovoltaic performance, incorporation of rare-earth dopants in organic-inorganic hybrid perovskite ($MAPbX_3$) is quite challenging due to its volatile nature in an exposed environment. To our knowledge, to date only one report demonstrated rare-earth doping in organic-inorganic halide perovskite for solar cell application. Wu et al. incorporated anhydrous EuI_2 as a dopant into the $MAPbI_3$ thin film to increase the grain size and they achieved improved stability of the solar cell, though the device efficiency was not improved significantly[40]. However, higher grain size usually results in lower PL QY. To the best of our knowledge, there is no report on the doping of rare-earth ions on $MAPbBr_3$ nanostructure, particularly by the solvothermal method to incorporate the dopants in ultrathin two-dimensional (2D) lead halide perovskites. Due to the versatility of the solvothermal method, it is imperative to explore this method for doping of rate-earth atoms in the ultrathin perovskite layers. In the previous chapter, we have demonstrated the efficacy of the solvothermal process to precisely tune the thickness and optical properties of highly stable 2D organometal halide perovskite nanosheets and their applications in white LED and fast photodetector[41].

Here, we develop a facile and fast solvothermal synthesis process for doping of Ce and Tb ions into $MAPbBr_3$ 2D nanosheet (NS). This method allows us to tune the optical properties of the host $MAPbBr_3$ NS by changing the doping concentrations of Ce and Tb. TEM imaging was utilized to study the systematic change in NS dimension with increasing doping concentrations. AFM images were recorded to estimate the thickness of the perovskite NSs and NPLs. XRD analysis is utilized to characterize the 2D diffraction peaks in Ce and Tb doped 2D perovskite layers. Optical absorption studies enable us to monitor the systematic change in the bandgap with doping concentrations. Room temperature and low-temperature PL analyses were carried out to study the effect of doping concentrations on the light emission characteristics of the doped 2D NS. TRPL study is carried out to understand the contribution of non-radiative recombination and defects on doped $MAPbBr_3$ NS. The origin of high PL quantum yield and large blue shift of the PL peaks is

studied thoroughly using various experimental tools and our conclusions are fully supported by the density functional theory (DFT) calculation of its electronic structure and formation energy of the dopants. Finally, we fabricate a downconverter white light-emitting diode (LED) by depositing 2D $MAPb_{1-x}Ce_xBr_3$ nanoplatelet (NPL) on Rhodamine B coated commercially available UV LED.

5.2. Experimental Procedure

5.2.1. Materials

Methylamine solution (CH_3NH_3, 33 wt% in absolute ethanol, Sigma-Aldrich), lead(II) bromide ($PbBr_2$, 99.999 %, Sigma-Aldrich), hydrobromic acid (HBr, 48 wt % in water, Sigma-Aldrich), N, N-dimethylformamide (DMF, >99 %, Sigma-Aldrich), diethyl ether (>99 %, Merck), toluene (Merk), oleic acid ($CH_3(CH_2)_7CH=CH(CH_2)_7COOH$, Merk), oleylamine (OAm) (≥98 % (primary amine), Sigma-Aldrich), cerium(III) bromide ($CeBr_3$, 99.9 %, Sigma-Aldrich), terbium(III) chloride hexahydrate ($TbCl_3.6H_2O$, 99.9 %, Sigma-Aldrich), and poly(methyl methacrylate) (PMMA) powder (Sigma Aldrich) were used to synthesis the doped and undoped perovskite NSs. All the materials were used as received without any further purification.

5.2.2. Synthesis Procedures

5.2.2.1. Synthesis of CH_3NH_3Br

The organic part of the hybrid perovskite is synthesized by diluting the 8.2 mL of CH_3NH_3 solution with 30 mL of absolute ethanol and stirred the solution in a round-bottom flask. Afterward, 3 mL HBr was slowly added to the previous solution in an ice bath with vigorous stirring at 1000 rpm for 3 h. To evaporate the solvents, the solution was heated at 70 °C for several hours with continuous stirring. Once the solvents completely evaporate, the remaining MABr salt was washed several times with ethanol to remove impurities. Then, the powder was washed with anhydrous diethyl ether to recrystallize. The powder was dried at 70 °C in a vacuum oven.

5.2.2.2. Synthesis of Undoped and Ce, Tb Doped 2D Perovskite NS

2D perovskite NS was synthesized by a solvothermal method following the procedure described in Chapter 4 with minor modifications[41]. The precursor solution was prepared by mixing equal moles of MABr and $PbBr_2$ in DMF, and then oleic acid and 60 µl OAm were added, and the

solution was then transferred into a Teflon lined autoclave without any pretreatment and solvothermal treatment at 120 °C for 30 min. After the solvothermal process, the crude solution was allowed to cool down naturally for 30 min in the ambient environment. The autoclave was then opened and 180 µl of the product solution was added into 10 ml toluene while stirring. To wash the as-prepared NS and separate it from the crude solution, it is centrifuged two times at 10000 rpm for 10 min. The supernatant was discarded each time, and the precipitate was re-dispersed in 10 ml toluene for further characterization. Note that all the syntheses procedures were carried out in ambient environment without the use of a glove box.

To synthesize the Ce and Tb doped 2D perovskite NS, different amounts of $PbBr_2$ was replaced by $CeBr_3$ and $TbCl_3$ according to the desired doping concentrations. Typically, for 20 mol% doping concentration of $CeBr_3$, 0.1 mM MABr, 0.02 mM $CeBr_3$, and (0.1-0.02) = 0.08 mM $PbBr_2$ were first mixed and afterward same solvothermal procedure was followed, as discussed earlier. We varied the concentrations of $CeBr_3$ and $TbCl_3$ from 0 to a maximum of 70 mol%. The 0, 20, 50 and 70 mol% $CeBr_3$/$TbCl_3$ doped samples are named as Ce0/Tb0, Ce20/Tb20, Ce50/Tb50, Ce70/Tb70, respectively.

5.3. Characterization Techniques

The high magnification surface morphology of the undoped and doped perovskite NSs have been characterized using a field-effect TEM (JEOL-JEM 2010) operated at 200 kV. AFM (Cypher, Oxford Instruments) images were taken to calculate the thicknesses. XRD (Rigaku RINT 2500 TRAX–III, Cu-Kα radiation) patterns were recorded to determine the crystal structure of different samples. X-ray photoelectron spectroscopy (XPS) measurement was carried out using a PHI X-tool automated photoelectron spectrometer (ULVAC-PHI, Japan) with an Al Kα X-ray beam (1486.6 eV) at a beam current of 20 mA for the analysis of the chemical compositions and chemical environment. UV−Vis absorption spectra of the 2D NSs were measured using a commercial spectrophotometer (PerkinElmer, Lamda 950). The room temperature steady-state PL spectra were recorded using 350 nm lamp excitation using a commercial fluorimeter (Fluoromax-4, Horiba Scientific). PL QY of the samples was measured in solution mode using an integrating sphere (FM-SPHERE, Horiba) attached to the fluorimeter. Low temperature (80–300 K) PL measurements were carried out using a liquid nitrogen-cooled optical cryostat (Optistat DNV, Oxford Instruments) attached to the above fluorimeter under 405 nm laser excitation in thin-film

mode. TRPL measurements were performed using a 375 nm pulsed laser excitation for perovskite NSs, with an instrument response time of <50 ps (LifeSpecII, Edinburgh Instruments).

5.4. Computational Methodology

To envisage the electronic and optical properties of pristine, Ce and Tb-doped 2×2×2 super-cell of $CH_3NH_3PbBr_3$, we have performed first-principles electronic structure calculations within the framework of DFT[42]. Throughout the work, we have used Vienna Ab-initio Simulation Package (VASP) code[43], where projector augmented wave (PAW)[44] formalism has been implemented. We have used Perdew-Burke-Ernzerhof (PBE)[45] form of Generalized gradient approximation (GGA) as the exchange-correlation functional, whereas the converged energy cut off has been chosen to be 500eV. The Brillouin zone has been sampled using 3×3×3 Monkhorst-pack scheme[46] for the ionic relaxation of the systems. After finding the minimum energy configuration of the pristine system, the pristine system has been doped with Cerium (Ce) and Terbium (Tb) with a concentration of 12.5 % for an individual doped system, while minimum energy configuration is achieved through the full ionic relaxations of the atoms. Further, we have determined the projected density of states (PDOS) to analyze the elemental orbital contribution of the constituent atoms in the valence band and conduction band regime. The self-consistency has been achieved with 10^{-3} eV energy convergence and 1×10^{-2} eV/Å force convergence criteria in all the geometry optimization calculations. In order to compliment the experimental outcome of stability enhancement in the doped system as compared to the pristine $CH_3NH_3PbBr_3$, we have estimated the formation energy of the individual systems from the total energy calculations.

5.5. Results and Discussions

5.5.1. Morphology Studies

5.5.1.1. FETEM Analysis

The effect of Ce/Tb doping on the morphology of as-synthesized 2D $MAPbBr_3$ NS was characterized using TEM analysis. The doping concentration in 2D perovskite NS is varied by replacing $PbBr_2$ with $CeBr_3$/$TbCl_3$ during the solvothermal synthesis. It is observed that doping of Ce^{3+} and Tb^{3+} has quite a significant effect on the morphology of the 2D perovskite NSs, as shown in **Fig. 5.1**. **Fig. 5.1(a)** represents the image of an undoped perovskite NS revealing typically

rectangular shaped large area NS of width ~346 nm and length ~890 nm. Interestingly, after doping of 20 mol% $CeBr_3$, the dimension of the NS decreases and shape of the NS is observed to be changed from rectangular to square shape with a lateral dimension of ~546 nm × 507 nm (see **Fig. 5.1(b)**). As the doping concentration further increased to 50 mol%, a uniform distribution of NSs of perfectly square shape is observed with a lateral size ~ 240 nm in Ce50 (see **Fig. 5.1(c)**). With

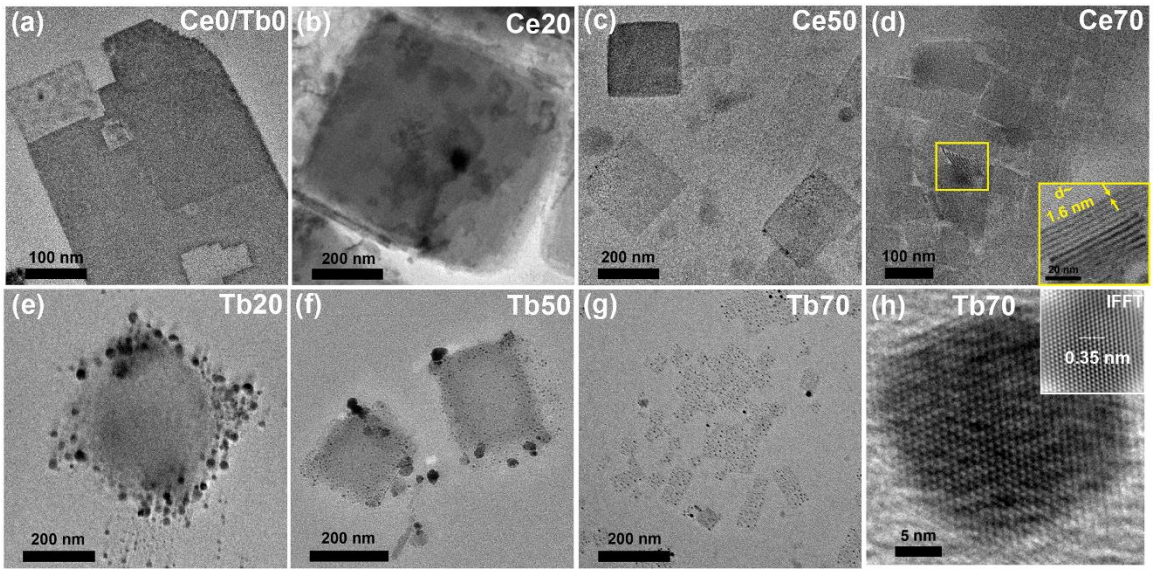

Fig. 5.1. TEM images of (a) undoped 2D perovskite, and Ce^{3+} doped perovskite NSs with $CeBr_3$ concentrations: (b) 20 mol%, (c) 50 mol% and (d) 70 mol%. The inset in (d) shows the vertically aligned 2D NSs. TEM images of Tb^{3+} doped NSs at $TbCl_3$ concentrations: (e) 20 mol%, (f) 50 mol% and (g) 70 mol%. (h) HRTEM lattice images of the Tb70 NS; the inset shows the corresponding IFFT image.

70 mol% $CeBr_3$ doping, the NS dimension is further decreased, which is termed as nanoplatelet (NPL). The NPLs are observed to be uniformly grown and vertical stacking of NPLs can be seen in some regions, as marked with a yellow square in **Fig. 5.1(d)**. Inset of **Fig. 5.1(d)** shows the high-resolution TEM image of self-assembled vertically stacked NPLs in Ce70, revealing the thickness of ~1.6 nm for each layer, which corresponds to ~2 monolayers of cubic perovskite phase, since the unit cell size of $MAPbBr_3$ perovskite is 5.93 Å. Interestingly, both the lateral size and thickness are successfully tuned with Ce^{3+} doping at different concentrations, which induces an extraordinary improvement in the optical properties of the host lattice (discussed later). **Fig. 5.1(e)** represents the TEM image of 2D perovskite NS doped in $MAPb_{0.8}Tb_{0.2}Br_{2.4}Cl_{0.6}$ showing square-shaped NS of width ~ 378 nm. Interestingly, the TEM image of Tb20 reveals the presence of nanoparticles (NPs) attached at the edges of NS (see **Fig. 5.1(e)**). As the $TbCl_3$ doping

concentration increases to 50 mol%, the lateral size of the NSs decreases and it is uniformly decorated with tiny NPs appearing like dots at the edges, as shown in **Fig. 5.1(f)**. In Tb70, the lateral size of NSs is further decreased, which is considered as NPL of average lateral size ~ 36 nm with uniformly decorated 2D NCs over it (see **Fig. 5.1(g)**). Hence, the incorporation of rare-earth dopants in the $MAPbBr_3$ crystal inhibits the lateral as well as vertical growth of NSs and it

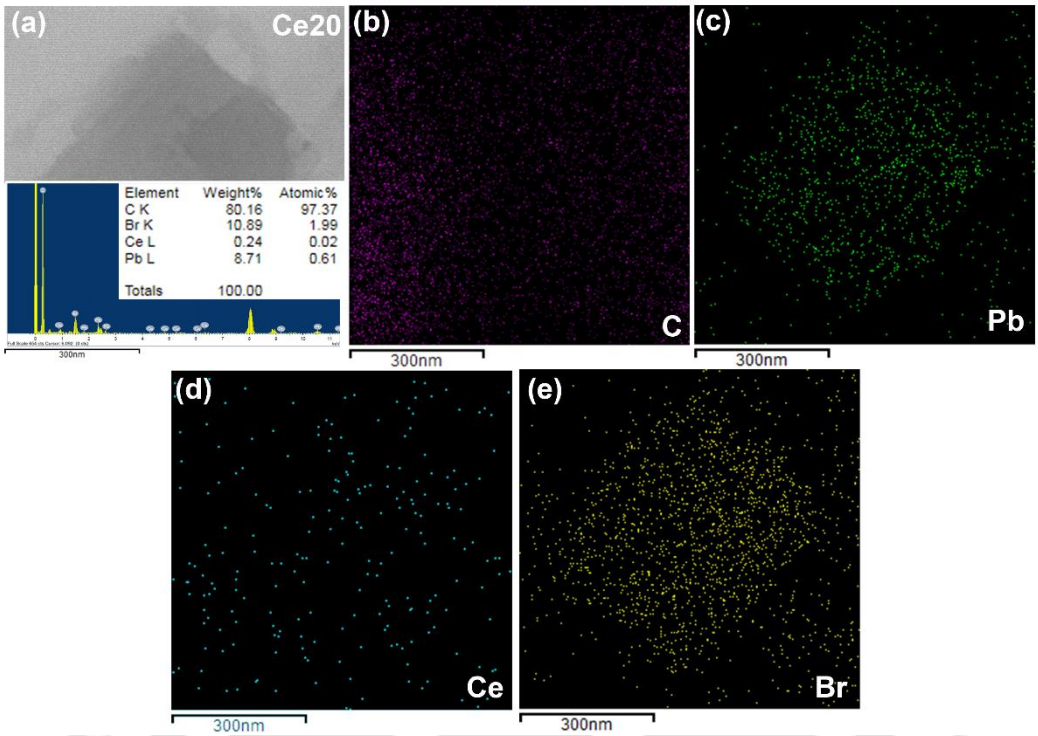

Fig. 5.2. (a) TEM image of Ce doped perovskite nanoplatelets in Ce20; the inset shows the corresponding EDX spectrum. (b-e) Corresponding elemental mapping images of C, Pb, Ce and Br in Ce20.

results in the decrease in thickness and lateral size of the NSs and eventually, the NSs break into large number of uniformly distributed NPLs under the solvothermal condition. **Fig. 5.1(h)** shows the high-resolution TEM (HRTEM) lattice fringe pattern of perovskite NPL and the inset shows the corresponding inverse fast Fourier transform (IFFT) image, in Tb70, revealing lattice spacing of 0.35 nm related to the (002) plane of the perovskite phase[47]. To verify the incorporation of dopant ion Ce^{3+} inside the $MAPbBr_3$ crystal, energy dispersive X-ray spectroscopy (EDX) was performed on the 2D doped NS. **Fig. 5.2(a)** shows the STEM image of NS in Ce20. The inset of **Fig. 5.2(a)** shows the quantification of the EDX spectrum revealing a Ce/Pb atomic ratio of 0.03 for Ce20. This indicates a low doping concentration (~ 3.3 %) of Ce^{3+} inside $MAPbBr_3$ crystal consistent with the previous report on the doping of Ce^{3+} inside $CsPbBr_3$ host[33]. Thus, the actual

concentration of doped atoms is about six times lower than the reactant amount. On this basis, Ce70 is expected to contain ~11.6 % Ce^{3+} inside $MAPbBr_3$ crystal. Considering this, we have taken 12.5 % as the dopant concentration for the theoretical DFT calculation to understand the stability and electronic structure of the doped system (discussed later). Uniform distribution of different elements in $MAPbBr_3$ perovskite structure and as well as the dopant Ce on NS is shown in elemental mapping images, shown in **Fig. 5.2**. EDX analysis on Tb20 revealed the inclusion of guest Tb^{3+} ion in the $MAPbBr_3$ crystal, as shown in the inset of **Fig. 5.3(a)**. **Fig. 5.3** depicts the elemental mapping of 2D NS in Tb20, showing the uniform spatial distribution of each component in $MAPb_{1-x}Tb_xCl_{3x}Br_{3(1-x)}$.

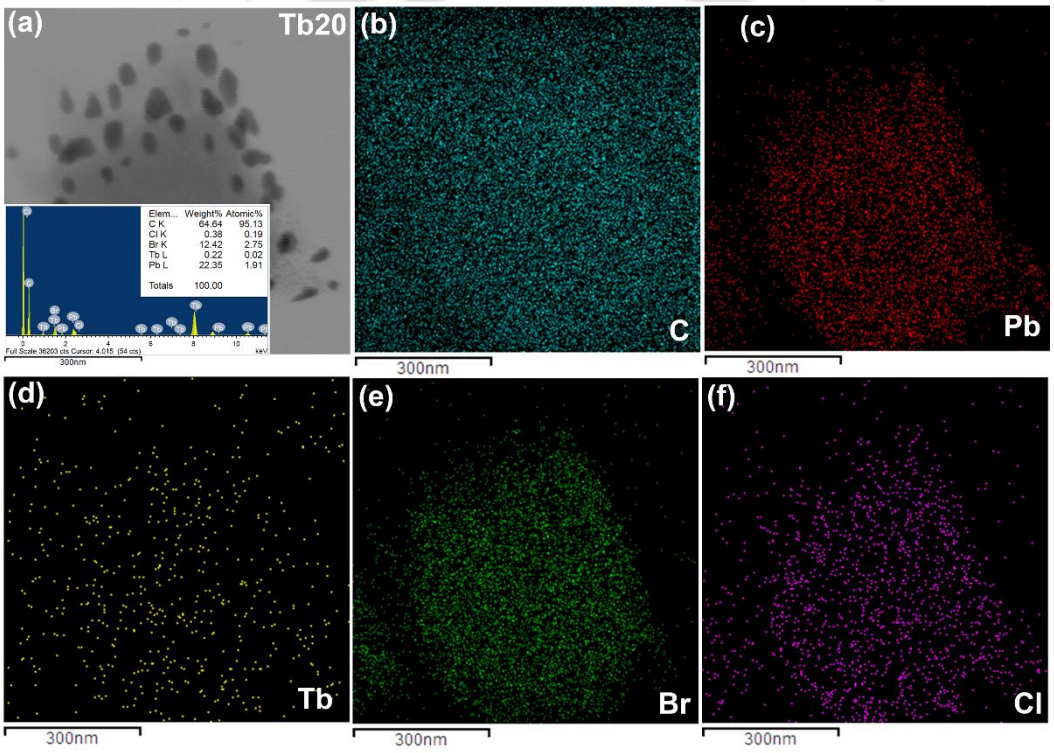

Fig. 5.3. (a) TEM image of Tb doped perovskite nanoplatelets in Tb20; the inset shows the corresponding EDX spectrum. (b-f) Corresponding elemental mapping images of C, Pb, Tb, Br and Cl in Tb20.

5.5.1.2. AFM Analysis

To provide a more direct evidence of the evolution of the thickness the 2D $MAPbBr_3$ NS with the inclusion of Ce^{3+} ion, AFM topography images were acquired in the tapping mode, as shown in Fig. 2. To record the AFM images, the NS solution were first diluted and drop casted on a SiO_2 substrate. The solution was then allowed to dry at room temperature to avoid any agglomeration.

Fig. 5.4(a) represents the AFM topography image of the undoped $MAPbBr_3$ NS. The thickness of the NS is found to be ~ 5.6 nm calculated from the AFM height profile, as shown in **Fig. 5.4(b)**. **Fig. 5.4(c,d)** exhibit the AFM image and the corresponding height profile of the marked region of Ce20 indicating thickness of the NS to be ~ 4 nm. With further increase in doping concentration, i.e., in Ce50, the thickness and width of the NS are further decreased to ~1.8 nm and ~133 nm, respectively, as depicted from the AFM image and the corresponding height profile in **Fig. 5.4(e,f)**. Interestingly, for Ce70, uniform distribution of NPLs is observed, as shown in the AFM image in

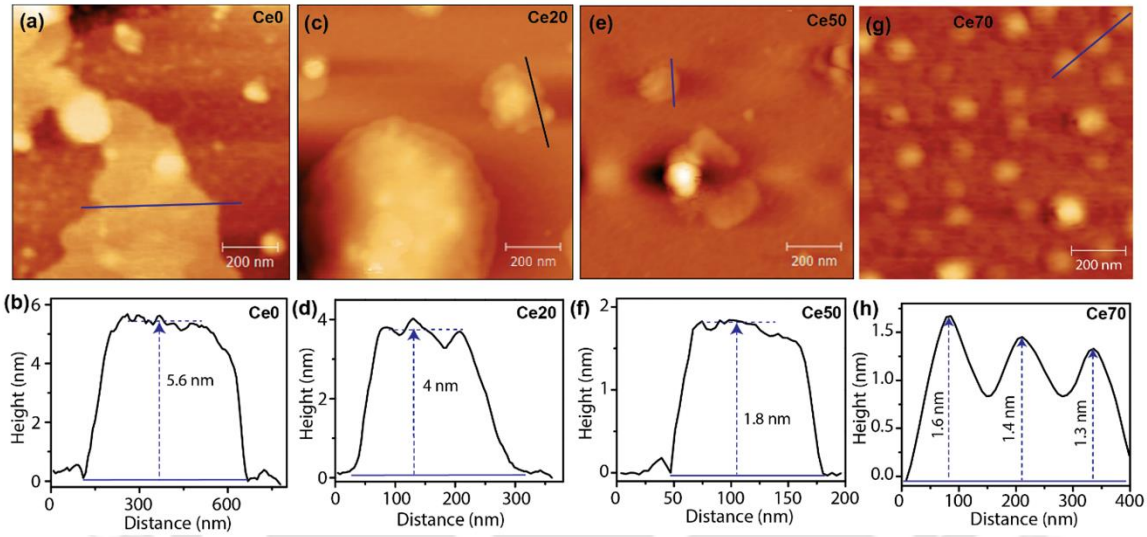

Fig. 5.4. AFM topography images of undoped and Ce doped $MAPbBr_3$ NS in (a) Ce0, (c) Ce20, (e) Ce50 and (g) Ce70 and the corresponding height profiles are shown in (b), (d), (f) and (h), respectively.

Fig. 5.4(g). **Fig. 5.4(h)** shows the corresponding height profile indicating the average thickness of the NPLs to be ~ 1.4 nm, which closely matches with the thickness estimated from the TEM imaging. In case of 2D NS/NPL, single layer (1L) $MAPbBr_3$ sheet consists of 2D arrangement of corner-sharing $(PbBr_6)^{4-}$ octahedra with a thickness of 0.593 nm[48]. Therefore, the measured thicknesses in Ce0, Ce20, Ce50, and Ce70 correspond to 10L, 7L, 3L, and 2L, respectively. Hence, the Ce^{3+} doping by solvothermal method enables us to tune the thickness of the 2D perovskite NS from ten layers (10L) to bilayer (2L), which may trigger strong quantum confinement effect in the NPL. A similar change in thickness is expected with Tb^{3+} doping in $MAPbBr_3$. The mechanism behind the change in thickness of NS with doping may be the replacement of Pb^{2+} ions with smaller size Ce^{3+} ions. In addition, the dopant atoms ($CeBr_3$/$TbCl_3$) may act as an inorganic ligand or an intercalating agent, which stimulates the exfoliation of the 2D NS. Presence of large number of

inorganic ligands helps in exfoliation of inorganic sheet layer promoting thinner NS. Here, large dopant concentration may also increase the reactivity of OAm because of the high pressure and high temperature inside the autoclave[41]. Elevated pressure and temperature inside the autoclave increase the reactivity of any material, which may be insoluble at room temperature[41]. Therefore, solvothermal process results in a stronger effect of doping on the dimensions of the perovskite nanosheets as compared to other methods. This resulted into the systematic decrease in thickness and lateral dimension of the 2D NSs at higher doping concentration. Note that the measured doping concentration in Ce20 and Tb20 is much less than the desired one, which supports the assertion that a small fraction of the dopants occupy the substitutional sites in perovskite and rest of the dopants help in the exfoliation of the NS by a kind of intercalation process similar to the commonly used layered 2D materials.

5.5.2. Structural Analysis

To acquire more insights into the structural quality of doped perovskite NS, the crystal structure of various doped and undoped samples were characterized using the XRD technique. **Fig. 5.5(a,b)** show the comparison of XRD patterns of Ce and Tb doped samples i.e., $MAPb_{1-x}Ce_xBr_{1-x}$ and $MAPb_{1-x}Tb_xCl_xBr_{1-x}$. **Fig. 5.5(a)** reveals the characteristic (001) diffraction plane of a cubic

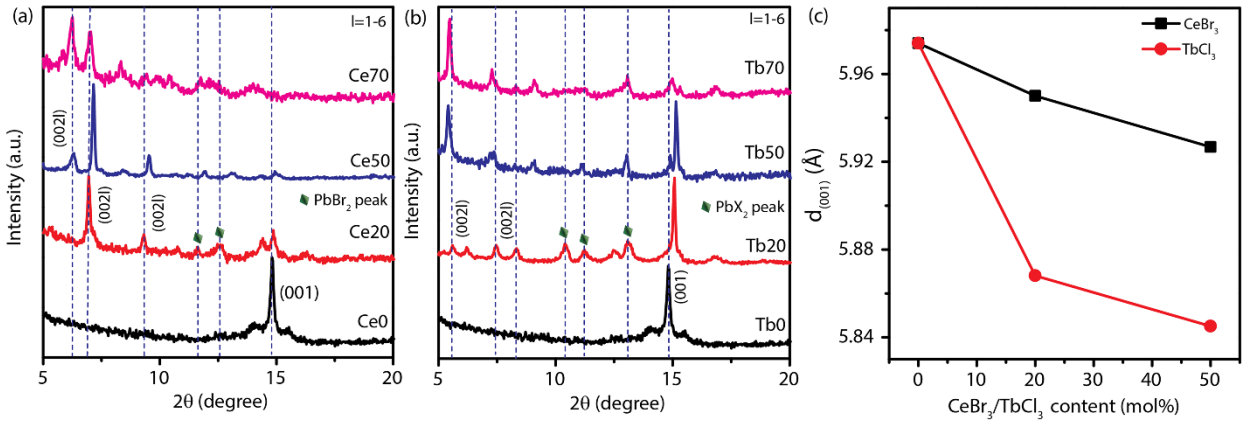

Fig. 5.5. A comparison of XRD patterns of perovskite NS before and after the doping with (a) Ce^{3+} and (b) Tb^{3+} at different molar concentrations.

structure at ~14.81° in undoped 2D NS, confirming the formation of pure perovskite phase without any impurity. Interestingly, with the substitution of Pb^{2+} by Ce^{3+}, diffraction peaks (002l) (l=1-6) at low angles ($2\theta<14.81°$) are observed, which is a signature of the layered structure, as shown in

Fig. 5.5(a). It is reported that there is an increase in *d*-spacing in 2D perovskite phase due to the insertion of inorganic octahedral sheet ($PbBr_6$) and, as a result several low diffraction angle peaks are emerged[49]. XRD pattern of Ce20 exhibits the diffraction peaks at 11.50º and 12.53º corresponding to disparate layered structure with inorganic sheets combined with corner-sharing octahedral containing Pb and Ce ion, respectively[50]. The (001) diffraction peak shifts monotonically towards higher angle in Ce20 and Ce50 as compared to the undoped sample due to the decrease in layer distance between the inorganic sheets as Pb ions (ionic radius 119 pm) are partially substituted by smaller size Ce ions (ionic radius 115 pm). In addition, the splitting of two peaks at 14.87º in Ce20 indicates phase transition from higher symmetry cubic phase to lower symmetry tetragonal phase[51]. Interestingly, the (001) diffraction peak is completely disappeared in Ce70 confirming fully transformed pure 2D perovskite phase. Similarly, XRD patterns of Tb doped samples represent the evolution of diffraction peaks at low angles ($2\theta<14.81º$), which are the characteristic features of 2D perovskite structure, suggesting the formation of an extremely thin $MAPb_{1-x}Tb_xCl_{3x}Br_{3(1-x)}$ layer (see **Fig. 5.5(b)**)[52]. The (001) diffraction peak systematically shifts towards higher angle with the increase in Tb doping concentration, which gives direct evidence of the inclusion of smaller radius Tb ion (ionic radius 106.2 pm) in place of Pb ion (ionic radius 119 pm). Besides the effect of Tb ions, halide mixing of Cl (ionic radius 167 pm) and Br ion (ionic radius 182 pm) in the 2D perovskite phase results into the shrinkage of the size of unit cell. Similar to Ce doped case, Tb doped samples exhibits diffraction peaks at ~ 11.24º and ~ 13.07º, which further confirms its 2D layered structure[50]. This indicates an in-plane orientation of BX_6 (B= Pb/Tb, X= Br/Cl) sheets. With the increase in Ce^{3+} and Tb^{3+} doping concentrations, the (100) diffraction peak shifts towards higher angle from 14.81º to 14.93º and 15.32º, respectively, indicating the lattice contraction. Interplanar spacing (d_{001}) decreases with increasing doping concentration from 5.97 Å to 5.93 Å and 5.84 Å for Ce and Tb doped NS, respectively revealing lattice contraction, as shown in **Fig. 5.5(c)**. In addition, significant broadening in the diffraction peaks of doped samples implies a reduction in the NS thickness upon inclusion of doped ions. Hence, with the incorporation of Ce/Tb ion in the 2D perovskite crystal, the subsequent change in the lattice spacing and structural phase transition from cubic to lower symmetry tetragonal phase are observed due to rotation and distortion of inorganic octahedral. Note that the lattice distortion is expected at high doping concentration, which is consistent with our experiment.

XPS analysis was conducted to further confirm the successful incorporation of Tb ion in $MAPbBr_3$ host as shown in **Fig. 5.6(a-d)**. **Fig. 5.6(a-d)** exhibited XPS peaks of Br 3d, Pb 4f, Cl 3p, Br 3p and Tb 3d. The broad Br 3d XPS spectrum of Tb20 is deconvulated with two peaks centered at 68.9 ($3d_{5/2}$) and 70.0 eV ($3d_{3/2}$), corresponding to the inner and surface Br ions, respectively (see **Fig. 5.6(a)**). The doublet peaks of Pb 4f are observed at 143.6 ($4f_{5/2}$) and 138.8 eV ($4f_{7/2}$) with spin orbit split of 4.8 eV (see **Fig. 5.6(b)**). The presence of metallic Pb contribution is not seen at lower energy confirming no reduction of Pb. Cl 2p peak is fitted with two peaks at 198.4 and 200 eV corresponding to $2p_{3/2}$ and $2p_{1/2}$ as shown in **Fig. 5.6(c)**. The doublet peaks shown in **Fig. 5.6(c)** at

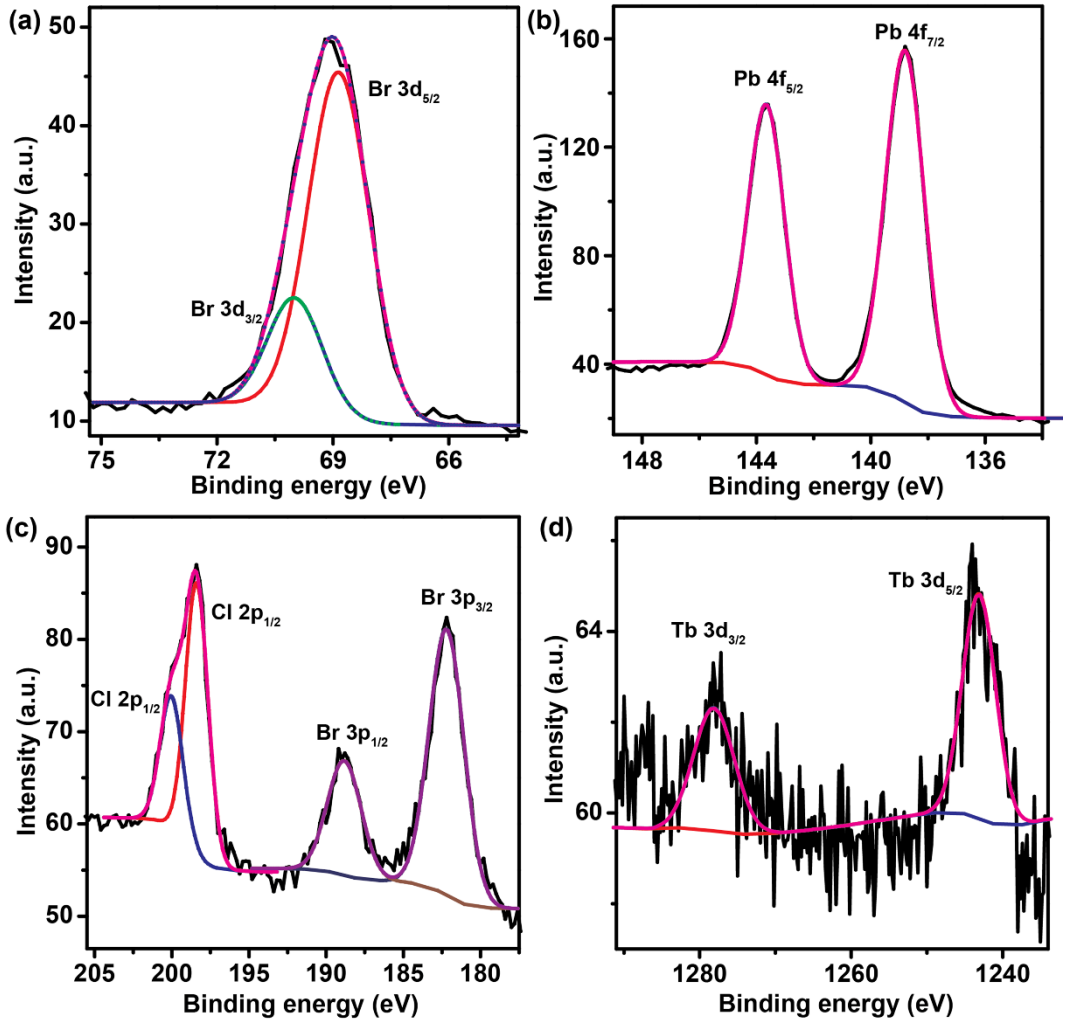

Fig. 5.6. (a-d) Deconvulated XPS spectra of Br 3d, Pb 4f, Cl 3p, Br 3p and Tb 3d in Tb20.

182.2 and 188.8 eV corresponds to Br $3p_{3/2}$ and Br $3p_{1/2}$. The peaks at 1243.1 and 1278.1 eV correspond to Tb $3d_{5/2}$ and $3d_{3/2}$, as shown in **Fig. 5.6(d)**.The presence of Cl 3p and Tb 3d peaks

confirms the successful incorporation of $TbCl_3$ in $MAPbBr_3$ NS. Tb/Pb ratio is found to be 0.014 in Tb20, which indicates a doping concentration of ~1.4 %.

5.5.3. Optical Analysis

5.5.3.1. UV-vis Absorption and Photoluminescence Studies

The effect of lanthanide doping on the absorption and emission spectra of the 2D perovskite was studied using synthetic spectroscopic tools. **Fig. 5.7(a,b)** shows the absorption and PL spectra of Ce^{3+} and Tb^{3+} doped samples demonstrating a systematic blue shift in the absorption edges with the increase in doping concentration. With respect to the undoped sample, we observe blue shifts up to of 42 nm and 86 nm in the excitonic absorption peak in 70 mol% Ce and Tb doped samples, respectively (see **Fig. 5.7(a,b)**). Therefore, a significant enlargement in bandgap (~0.25 eV and ~0.54 eV in Ce and Tb, respectively) is observed with doping of rare-earth ions in 2D $MAPbBr_3$ NS indicating successful incorporation of dopant ions in the crystal lattice[20]. Furthermore, a sharper excitonic peak is observed in the doped NS, which may be attributed to enhanced dielectric confinement effect in thinner 2D layered NS/NPLs. Urbach tail is weakened with the introduction of rare-earth ions suggesting an increase in the exciton binding energy to the extent that thermal energy at room temperature is insufficient to dissociate the excitons. Weaker Urbach tail in doped NS compared to the undoped one also implies less disorder in the doped NS[53]. Distinct and narrow excitonic emission peak implies efficient excitonic recombination responsible for efficient light emission. Note that Tb doping induces larger enlargement in bandgap compared to Ce doping case due to the incorporation of both metal and halide ions in the host lattice, i.e., with $TbCl_3$ doping, both Pb and Br are partially replaced by Tb and Cl, respectively. In contrast, for Ce doping, only Pb^{2+} is replaced by Ce^{3+}. Valence state of halide ions changes from *4p* to *3p* when Br is replaced by Cl resulting into an increase in the bandgap. Insets of **Fig. 5.7(a,b)** show the digital photographs of all the solutions under UV excitation depicting tuning of the color from green to deep blue after Ce and Tb doping. To quantify the tuning in emission color in Ce^{3+} and Tb^{3+} doped $MAPbBr_3$ NS, steady-state PL spectra are plotted in **Fig. 5.7(a,b)**. PL measurements of all the samples were performed under 350 nm lamp excitation. A strong green emission peak located at 518 nm is observed in undoped $MAPbBr_3$ NS. With the increase in $CeBr_3$ concentration, the PL peak is gradually blue shifted and emission intensity systematically increased by 6 times with respect to the undoped NS. When x reaches to 0.7 in $MAPb_{1-x}Ce_xBr_3$, the strong blue fluorescence

peak centered at 454 nm with narrow FWHM (full width at half maxima) of ~24 nm is observed at room temperature, which is much narrower than that of the conventional blue QDs[54]. This is significant and it indicates an effective modulation in the electronic structure of the 2D NS at high doping concentration[33]. The PL peak of Ce70 coincides with the excitonic absorption peak

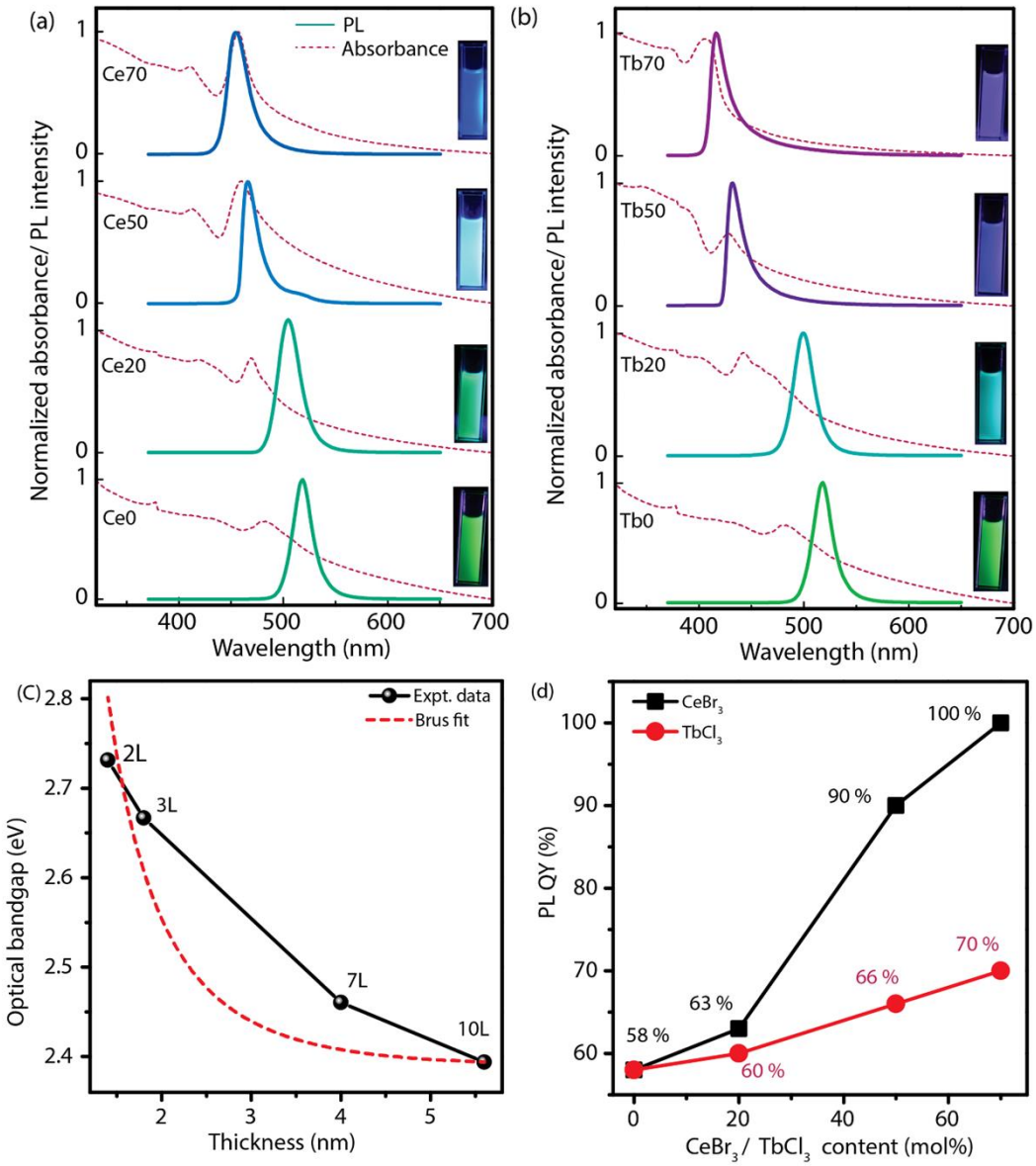

Fig. 5.7. Optical absorption (dashed line) and PL (solid line) spectra of undoped 2D perovskite NS and (a) Ce^{3+} and (b) Tb^{3+} doped 2D perovskite NS at different molar concentrations. The inset in each case shows the digital photographs of the corresponding perovskite NSs under UV illumination. (c) Optical bandgap energy as a function of thickness (*d*) of the Ce doped 2D perovskite NSs. (d) Comparison of PL QY of as-synthesized 2D perovskite NS with Ce^{3+} and Tb^{3+} doping.

without any stokes shift, indicating absence of any disorder or defects. The pure blue emission peaked at 454 nm from Ce70 has a color coordinate of (0.145, 0.054) very close to the Rec. 2020 (0.131, 0.046) specifications[54]. In case of Tb doping, the PL peak blue shifts from 518nm to 414 nm (deep blue), indicating a larger change in bandgap (~0.587 eV) with Tb doping than the Ce doping case (~0.337 eV). The PL intensity in the Tb doped NS increased by 3.5 time as compared to the undoped NS. The deep blue emission in Tb50 provides a color coordinate of (0.160, 0.0441), approaching the standard color Rec. 2020 (0.131, 0.046) specification[54]. In addition, the emission peak in Tb50 has a FWHM of 18 nm at room temperature, which is much smaller than the other conventional deep blue-emitting quantum dots, indicating its high color purity[54].

We find that doping concentration higher than 70 mol% leads to the quenching of the PL emission in the NS, which implies that 70 mol% of $CeBr_3$ is the highest limit and optimum for Ce doping in 2D $MAPbBr_3$ NS, and this appears to be the highest doping concentration of rare-earth ions reported till date. Note that the dopant concentration is proportional to the amount of $CeBr_3$ precursor added during synthesis, since the optical properties are systematically improved with doping in our samples, which rules out the presence of any impurity or self-crystalized phases unlike earlier reports[33]. Various factors may be responsible for the large PL spectral shift and enlargement of the bandgap. One of the factors accountable for the shift is the quantum confinement effect since lateral and vertical dimensions of the NS are systematically decreased with increase in doping concentration, as observed from TEM and AFM images. With doping, the thickness of the NS decreases from 10 layers to 2 layer (1.4 nm) NPL, which may impose the quantum confinement effect on the carriers and it may be responsible for the significant enlargement of the bandgap. However, thickness vs bandgap plot does not obey the well-known Brus equation[55] for various reasons, as shown from the fitting in **Fig. 5.7(c)**. Simple effective mass approximation of infinite quantum well strongly overestimates the bandgap with respect to the experimental values, as reported earlier[3, 56-58]. Note that in our case the change in the bandgap is slower than that predicted by the Brus fit, as shown in **Fig. 5.7(c)**, since other factors have competing effect on the bandgap variation. Interestingly, in the present case, the doping causes lattice contraction, and it results in the reduction of the bandgap in perovskite. However, in our system we observed an overall increase in the bandgap with doping, indicating dominating effect of quantum confinement[5, 59]. It may be noted that in case of 2D perovskite NS, additional factors need to be taken into account to accurately predict the bandgap variation with thickness.

Exciton binding energy is an important factor in 2D perovskite, since with decreasing thickness dielectric screening becomes minimal, as large number of electric field lines between the charge carriers are outside the perovskite layer[3]. This enhances the exciton binding energy of the NS, which in turns decreases the blue-shift in the bandgap[3]. Also, electron and hole effective mass is considered to be constant in effective mass approximation method; however, in 2D materials this strongly depends on the width of the well and correction factor needs to be added considering second order perturbation theory[58, 60]. In our case, there is a competing effect of strong increase of bandgap due to the reduction in the thickness, while a decrease in bandgap due to the lattice contraction and considering the other factors, it finally results in a slower increase in bandgap than that expected from the QC effect alone (see **Fig. 5.7(c)**).

The change in the PL QY with doping concentration is shown in **Fig. 5.7(d)**. PL QY is observed to be increased dramatically from 58 % to 100 % with Ce^{3+} doping, and in case of Tb doped NPLs it is enhanced to 70 % (see **Table 5.1**). Hence, we have remarkably achieved absolute unity quantum yield in deep blue-emitting perovskite NPLs with Ce^{3+} doping by a novel solvothermal

Table 5.1. *Details of the PL characteristics of the undoped and rare-earth doped $MAPbBr_3$ nanosheets.*

Rare-earth dopants	*Sample code*	*PL peak wavelength (nm)*	*PL QY (%)*
Undoped	Ce0, Tb0	518	58
20 mol% $CeBr_3$	Ce20	504	63
50 mol% $CeBr_3$	Ce50	465	90
70 mol% $CeBr_3$	Ce70	454	100
20 mol% $TbCl_3$	Tb20	500	60
50 mol% $TbCl_3$	Tb50	432	66
70 mol% $TbCl_3$	Tb70	416	70

process, rendering them as a highly efficient source of blue light. It has been predicted from theoretical calculation that Ce^{3+} has very small formation energy in perovskite (less than 2 eV at Pb site for any growth condition), which makes it easy for the incorporation of the Ce^{3+} dopants in the $MAPbBr_3$ lattice[20]. Interestingly, the Ce^{3+} dopant does not create any deep trap states, but

it enhances the lattice order when it is introduced in the $MAPbBr_3$ host lattice. The dominant dopant (Ce^{3+}) is reported to have a transition level ~0.2 eV bellow the conduction band, thus it introduces shallow transition features, which enhances the emission properties[20]. Additional transition states are created near the conduction band edge due to hybridization between Ce-*d* and Br-*p* states, which enrich the conduction band states causing the PL enhancement[20, 61]. Considering theoretical calculations and experimental results reported till date, the primary reasons for improved PL QY in doped (Ce^{3+}, Mg^{2+}, Cd^{2+}, Nd^{2+}) perovskite nanomaterials are considered to be the introduction of shallow energy levels and reduction in the structural disorder with doping[20, 37, 61, 62]. Also, radiative recombination rate increases significantly with doping due

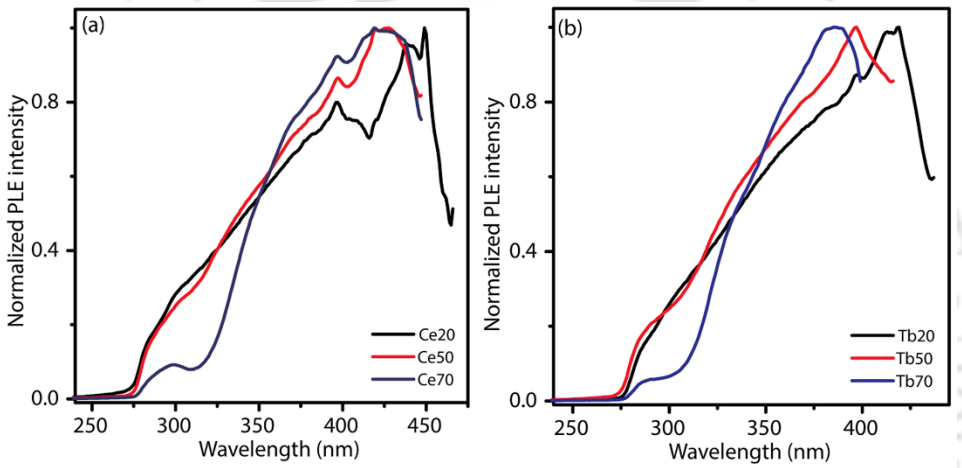

Fig. 5.8. Normalized PL excitation spectra of (a) Ce^{3+} and (b) Tb^{3+} doped NSs at different doping concentrations.

to the flattening of the conduction and valence band and lattice contraction upon doping due to overlap between the wave function of electron and hole states form the exciton[37]. Upon light excitation, an electron can transfer along the Pb-Br bond towards the Pb ion, while holes remain delocalized and hence electron-hole wave function overlap increases as the Pb-Br bond length decreases[37, 62]. Therefore, lattice contraction is another important factor for the enhancement in PL QY in the doped NSs. In addition, if there are any surface Ce atoms, which were unsuccessful in being incorporated into the bulk lattice, they provide additional electronic states near the conduction band rather than non-radiative trapping center[20]. In our system, the thickness of the NPLs in Ce70 is ~1.4 nm (bilayer). Hence, in case of high doping concentrations, most of the dopants are on the surface or very close to the surface, which contribute to create emissive channels near the conduction band. This is fully supported by our DFT calculation (discussed later). Strong

quantum confinement effect in the 2D NS is also an important factor for the PL enhancement in our system. The achievement of unity quantum yield in solvothermally grown Ce doped perovskite is very significant for their large-scale production and application in deep blue emitters.

PL excitation (PLE) spectra of Ce^{3+} doped $MAPbBr_3$ NS monitored at their respective emission peaks are shown in **Fig. 5.8(a)**, demonstrating a blue-shift in the PLE peak with increasing doping concentration, consistent the absorption spectra, which is a reflection of bandgap widening due to

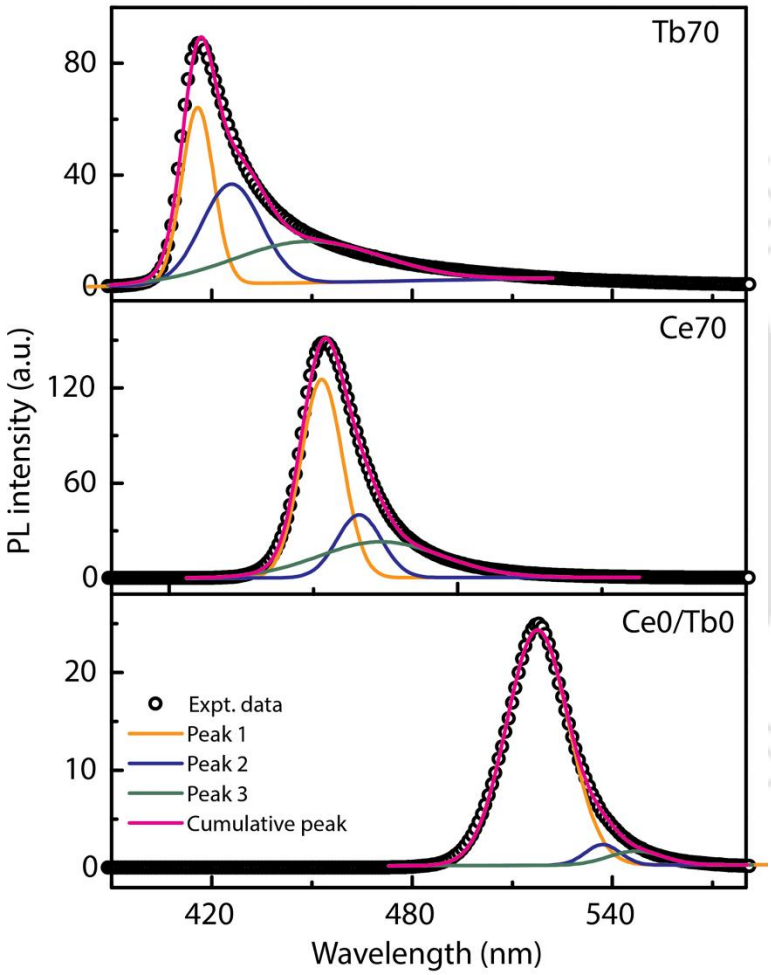

Fig. 5.9. Deconvulated PL spectra of Ce0, Ce70 and Tb70.

the successful incorporation of the Ce^{3+} ion in the host crystal. The PL excitation spectra of Tb doped 2D NS monitored at their respective emission peak is shown in **Fig. 5.8(b)**, demonstrating again a gradual blue shift with increasing doping concentration consistent with the emission spectrum. Intense excitonic absorption peak, negligible stokes shift, narrow and single PL emission

peak indicate negligible inhomogeneity and nearly monodisperse thickness of the NS/NPL. To ascertain the influence of band tail states in high doping concentration case, the PL spectra of Ce0, Ce70 and Tb70 are deconvulated with three Gaussian peaks, as shown in **Fig. 5.9**. It is clear that the excitonic peak (peak 1) has the highest contribution in all the three cases. However, the contribution of higher wavelength peaks (peak 2 and 3) is higher in Ce70 and Tb70 as compared to the undoped system. The higher wavelength peaks originates from the shallow states present just below the conduction band (~0.1 eV) in the doped system[20]. This could arise from the surface states as well the bulk states of the doped atoms[20]. Previously, these kind of tail states were observed in the blue emissive perovskite QDs due to carrier transition between low and high lying tail states[63].

5.5.3.2. Low-Temperature Photoluminescence Studies

The temperature-dependent PL spectra were studied to understand the excitonic trap and photonic properties of the doped and undoped NS. **Fig. 5.10(a)** shows the temperature-dependent PL spectra of undoped NS in the temperature range 80-300 K demonstrating multiple peaks at lower temperatures along with its excitonic peak. It can be noted that 2D perovskite shows strikingly different behavior in the low-temperature region depending on the number of layers, which is of great interest for the fundamental research and their optoelectronic application and this aspect remains largely unexplored. The evolution of PL spectra of Ce0 with lowering of temperatures suggests that it has multiple recombination channels, which get activated in the low temperature region (<260 K) (See **Fig. 5.10(a)**). Temperature-dependent PL spectra of Ce20 shows three shoulder peaks in the lower wavelength region (493, 483 and 468 nm) along with its excitonic peak below 110 K. The peaks at 483 and 468 nm in Ce20 disappear at 160 and 260 K, respectively, without showing any spectral shift when the temperature is increased from 80 K to 300 K (**Fig. 5.10(b)**). Similarly, Tb doped $MAPbBr_3$ 2D NS reveals three prominent shoulder peaks along with excitonic PL peak at low temperatures (see **Fig. 5.10(c)**). In case of Tb20, three shoulder peaks emerge at ~ 474 nm, ~457 nm and ~442 nm below 160 K, 220 K and 260 K, respectively, as shown in **Fig. 5.10(c)**. The positions of the peaks do not vary significantly with temperature, though their intensity gradually decreases with increasing temperature. No new PL peak appears in the lower energy region, which rules out the possibility of any impurity or defect states in the samples[64, 65]. The higher energy peaks in doped and undoped 2D NS at the low-temperature region may be

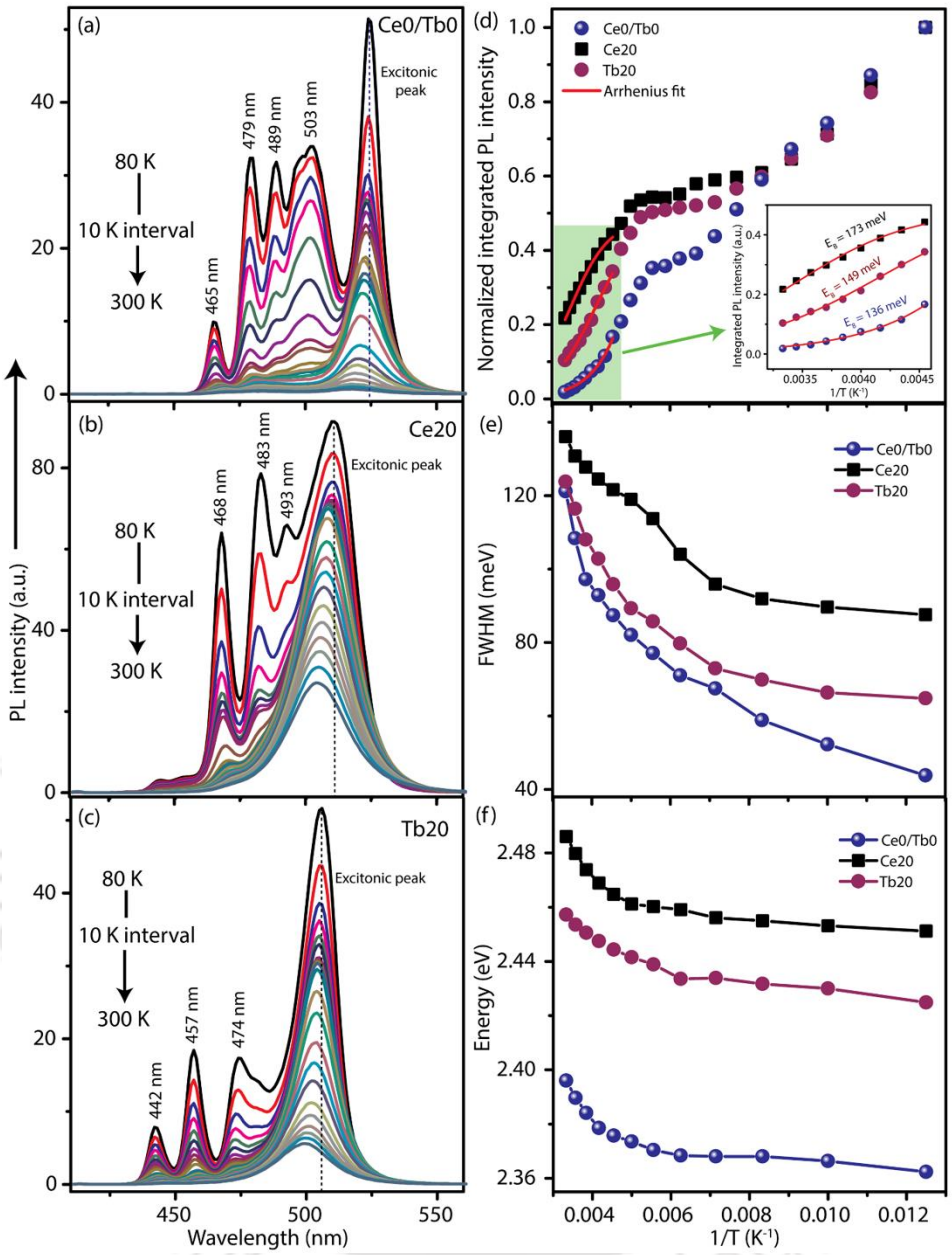

Fig. 5.10. Temperature-dependent PL spectra of 2D NS of (a) Ce0, (b) Ce20 and (c) Tb20 in the range 80 K - 300 K. (d) Integrated PL intensity vs. inverse of temperature for Ce0, Ce20 and Tb20. The experimental data in the range 220 - 300 K are fitted with the Arrhenius equation for each case shown in the expanded view in the inset. Temperature dependence of (e) FWHM and (f) PL peak energy for the excitonic peak in Ce0, Ce20 and Tb20.

originated due to phase transition or the coexistence of different phases of perovskite. $MAPbBr_3$ is reported to have orthorhombic (<145 K) and tetragonal phase (145-237 K) in the low-temperature region, and with increasing temperature it stabilizes to more symmetric cubic phase (>237 K) resulting into PL peaks at different positions[64, 66].

Dar et al. assigned the origin of additional PL peaks in MA-based perovskites at high energy region to the presence of molecularly disordered orthorhombic domains using density functional theory[67]. With decreasing temperature, the MA cations are kinetically trapped in a disordered domain along with ordered orthorhombic phase[67]. The disordered MA cation produces a strong local electric field resulting into an increase in bandgap of the ordered orthorhombic phase due to Stark-like effect which eventually splits the PL peaks[67]. The thickness of the NS is atomically thin in our system (<10 layers) and due to ultrathin 2D structure the crystal lattice is very vulnerable to the change in environmental temperature. The $PbBr_6$ octahedra are arranged on the surface with MA cation between them making it very feasible to orient in different directions resulting into a change in overall perovskite structure with environmental change. The shoulder peaks may also originate from bound exciton or multiple exciton-effects[41, 68, 69]. Broad PL peak due to intrinsic electronic transitions ($5d \rightarrow 4f$) of Ce^{3+} ions is reported to occur at ~450 nm[70]. Though at room temperature, the intrinsic transition features do not appear in PL spectra, it may get activated at low temperature resulting into high energy PL peaks. To distinguish the possible origin of the shoulder peaks, a detailed analysis of the evolution of the PL intensity, FWHM and PL peak energy of the samples with temperature was carried out. **Fig. 5.10(d)** shows the temperature-dependent integrated PL intensity of Ce0, Ce20 and Tb20 in the temperature range 80-300 K. It can be seen that the variation in the integrated intensity of PL with temperature has different slopes in different regions of temperature. As shown in **Fig. 5.10(d)**, the integrated PL intensities do not change significantly in the temperature range 150-180 K, 120-190 K and 140-190 K for Ce0, Ce20 and Tb20, respectively, which may be due to the phase transition. Note that the decrease in integrated PL intensity with increasing temperature is less prominent in Ce20 and Tb20 as compared to the undoped 2D NS (Ce0). As the temperature is increased from 80K to 300K, the integrated PL intensities decrease by 98 %, 78 % and 90 % for Ce0, Ce20 and Tb20, respectively, indicating enhanced excitonic recombination with the incorporation of Ce^{3+} in $MAPbBr_3$ NS. Comparatively less quenching of the PL intensity in the doped NS implies the presence of fewer non-radiative recombination centers, which are activated at lower temperatures. Note that, the excitonic PL intensity of undoped $MAPbBr_3$ NS decreases by a factor of ~54 with increase in temperature from 80 K to 300 K. In contrast, for the Ce and Tb doped NS, it decreases only by ~4.6 and ~9.6 times, respectively. This proves that carrier trapping and non-radiative channels are very few in the doped NS. Inset of **Fig. 5.10(d)** shows the temperature-dependent

integrated PL intensity in the range 220-300 K and the experimental data are fitted using the Arrhenius equation, given by,

$$I(T) = I_0/\left(1 + Aexp(-E_B/k_BT)\right) \quad (5.1)$$

where, *I(T)* and I_0 are the integrated PL intensities at temperatures *T* and 0 K, respectively[41]. *A* is a constant and E_B is the exciton binding energy. Exciton binding energy is calculated in the high-temperature region since $MAPbBr_3$ has a stable cubic phase at room temperature. From the fitting parameters, exciton binding energy is estimated to be 136 meV, 173 meV and 149 meV in Ce0, Ce20 and Tb20 NS, respectively. Thus, the E_B is the highest for the 20 % Ce doped NS. To the best of our knowledge exciton binding energy of Ce and Tb doped 2D $MAPbBr_3$ NS is not reported yet and these values are consistent with the other reported 2D perovskite structures[68]. Higher binding energy of excitons in doped NS implies better excitonic stability and high recombination rate consistent with its ultrahigh PL QY, highlighting the strong potential of such materials in exciton-related optoelectronic devices[65]. Therefore, at room temperature non-radiative decay processes and the dissociation of excitons is less probable in the Ce doped NS resulting into 100 % absolute PL QY. The spectral line width or FWHM of the excitonic PL peak is plotted as a function of temperature for Ce0, Ce20 and Tb20 in **Fig. 5.10(e)**. The linewidth gradually increases with increasing temperature due to strong exciton phonon coupling, which resulted into the overlap of close energy bands. The spectral line width of the PL peak in Ce20 varies at a slower rate compared to the undoped and Tb doped NS. Above 160 K, the line width of the excitonic PL peak broadens with increasing temperature at a faster rate implying wider thermal distribution of carriers in the discrete energy levels and intense exciton phonon interaction. A comparison of the temperature evolution of bandgap of the undoped and doped NS is shown in **Fig. 5.10(f)**. Below 160 K, the PL peak energies of the samples do not vary much with the temperature and above 160 K the peak energy increased with increasing temperature, which is contrary to the behavior of the conventional semiconductors. The sudden change/discontinuity in the peak energy with temperature mostly arise from the structural phase transition of the perovskite phase, as reported earlier[71]. At the transition point (160 K), the lattice phase in the NS transforms from orthorhombic to tetragonal to final cubic phase resulting into sudden shifts in the emission energy. The reason behind the unusual blue shift in the PL peak energy with increasing temperature is still not well understood. However, it is reported that the pseudocubic lattice constant of the perovskite

crystal increases with temperature[72]. The valence band maximum (VBM) of $MAPbBr_3$ is primarily constituted by antibonding hybrid states of the Br(*p*) and Pb(*s*) orbitals, while the conduction band minimum (CBM) is determined by a hybrid of Pb(*p*) and Br(*p*) orbitals and bonding between Pb(*s*) and Pb(*d*) states[59, 73]. CBM is much less affected by any external factors like structural distortion, however VBM is highly vulnerable to the lattice distortion[59]. Any change in the lattice constant destabilizes the VBM by increasing the Pb-Br overlap, which in turn results into the shift of the VBM to the higher energy levels[59]. This effect contributes to the enlargement of the bandgap in perovskites resulting into the blue shift of the PL peak energy with the rise in temperature contrary to the conventional semiconductor.

5.5.3.3. Time-Resolved Photoluminescence Studies

TRPL measurement was performed on undoped and doped perovskite NSs using a 405 nm pulsed laser excitation to study the decay kinetics. **Fig. 5.11(a)** shows the PL decay behavior of $MAPb_{1-x}Ce_xBr_3$ NS, fitted with triexponential decay function given by, $I(t) = \sum_{i=1}^{3} A_i exp(-t/\tau_i)$, where

Table 5.2. *Details of time resolved PL decay components of various samples fitted with a tri-exponential decay function.*

Sample	τ_1 *(ns)*	A_1 *%*	τ_2 *(ns)*	A_2 *%*	τ_3 *(ns)*	A_3 *%*	τ_{avg} *(ns)*
Ce0/Tb0	7.68	14.76	34.30	38.48	166.20	46.76	92.01
Ce20	3.70	19.77	14.77	43.28	76.09	36.95	35.25
Ce50	0.29	42.29	9.88	26.08	32.80	31.63	13.07
Ce70	-	-	6.28	100	-	-	6.28
Tb20	3.13	16.70	22.47	41.79	118.59	41.51	59.14
Tb50	0.57	30.79	7.28	11.45	57.98	57.76	34.44
Tb70	0.58	54.97	8.48	45.03	-	-	4.14

A_i is the amplitude of the PL decay component corresponding to the lifetime τ_i. The average lifetime (τ_{avg}) of the samples is calculated using the following relation: $\tau_{avg} = \sum_{i=1}^{3} A_i\tau_i^2 / \sum_{i=1}^{3} A_i\tau_i$. The faster component of the decay function corresponds to the non-radiative recombination of charge carriers, while the slower components are associated with radiative

recombination of free charge carriers[29]. Details of the decay components of the samples are tabulated in **Table 5.2**. It is observed that the carrier lifetime decreases from 92.01 to 6.28 ns with

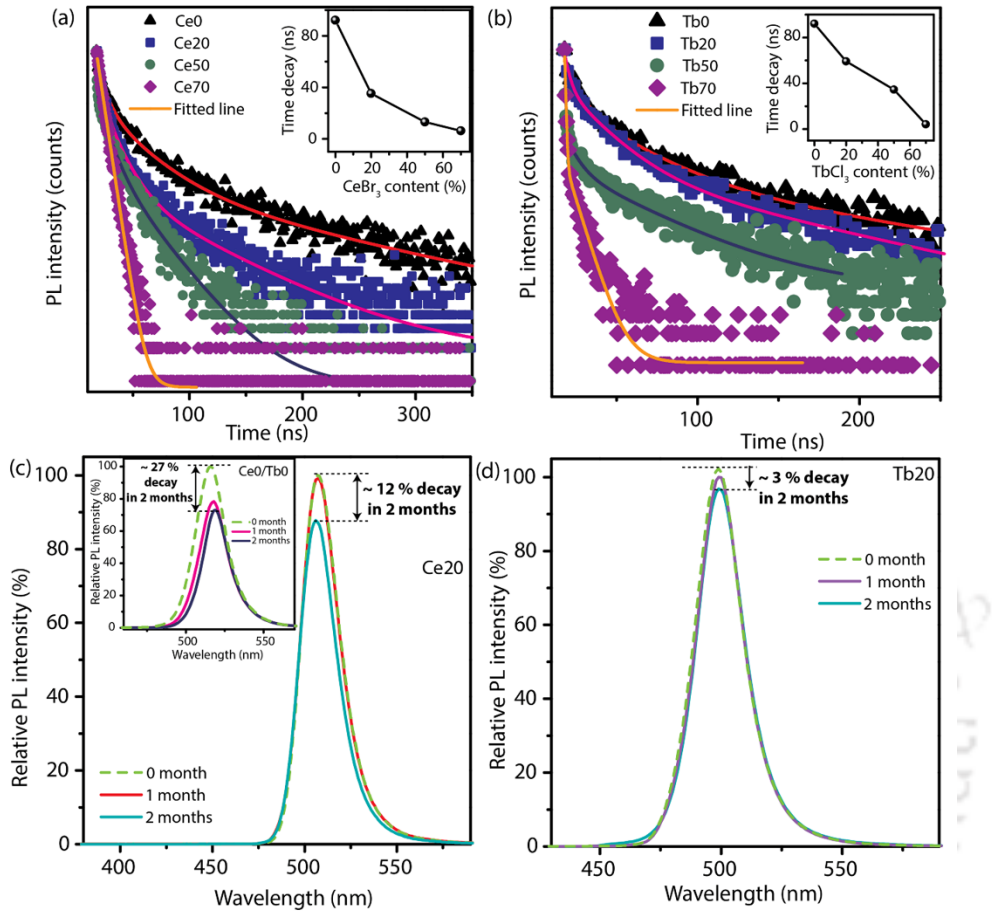

Fig. 5.11. A comparison of TRPL spectra of undoped 2D perovskite NS and (a) Ce^{3+} and (b) Tb^{3+} doped 2D perovskite NS at different doping concentrations. The insets in the corresponding figures show the variation in lifetime with the doping concentrations. Comparison of relative PL intensity of the (c) Ce^{3+} and (d) Tb^{3+} doped 2D perovskite NS taken at different time intervals after storing the samples in ambient conditions with relatively high humidity. The inset of (c) shows the change in PL intensity with storage time for the undoped perovskite sample.

increase in Ce^{3+} doping concentration, as shown in the inset of **Fig. 5.11(a)**. The decrease in lifetime is accompanied by the enhancement in the PL QY suggesting the partial elimination of non-radiative decay paths due to the incorporation of Ce^{3+} ions in perovskite lattice. 2D NPLs in Ce70 is better fitted with a single exponential function suggesting a very homogeneous electronic transition environment for the Ce^{3+} ions promoting 100 % PL QY[24, 29]. **Fig. 5.11(b)** shows the PL decay curves of $MAPb_{1-x}Tb_xCl_xBr_{1-x}$ 2D NS demonstrating a downward shift in decay time constant with increasing doping concentrations. The corresponding lifetimes are calculated to be

92.01, 59.14, 34.44, and 4.14 ns for Tb0, Tb20, Tb50, and Tb70, respectively. Hence, a 22-fold decrease in lifetime is observed after Tb^{3+} doping, as shown in the inset of **Fig. 5.11(b)**. Interestingly, the Tb70 data one fitted well with a bi-exponential decay function, while that of Tb0, Tb20 and Tb50 are fitted with tri-exponential decay functions indicating absence of the non-radiative decay channel with the incorporation of Tb^{3+} lanthanide ions. Decrease in carrier life time corresponds to increase in the recombination rate due to increasing carrier density, consistent with the quantum confinement effect and lattice contraction discussed earlier[37, 74]. Therefore, doping of Ce^{3+} and Tb^{3+} lanthanide ions introduce new emissive channels near the conduction band rather than non-radiative trapping channels promoting significant improvement of the PL emission characteristics of the host $MAPbBr_3$ crystal[75]. These conclusions are further supported by electronic structure calculations, discussed later.

5.5.4. Stability of the 2D NS

The stability of the doped 2D NS is studied to understand its efficacy in different environments. Evolution of PL emission spectra of Ce and Tb doped $MAPbBr_3$ NS under 370 nm excitation is monitored during long-term storage in ambient condition without any encapsulation. We found that PL spectra of Ce20 were nearly unchanged for at least one month, as shown in **Fig. 5.11(c)**. PL peak intensity in Ce20 decreases by ~ 12 % after 2 months of storage (see **Fig. 5.11(c)**). Inset of **Fig. 5.11(c)** shows the decrease in PL intensity of undoped NS by ~27 % after 2 months. In contrast, Tb doped NS shows only ~ 3 % quenching in PL intensity after 2 months of storage, as shown in **Fig. 5.11(d)**. These observations indicate that the trivalent rare-earth ions (Ce^{3+} and Tb^{3+}) provides good support to the 2D $MAPbBr_3$ NS framework with excellent storage stability under ambient condition, which makes them suitable for the use in various applications as environmentally friendly Pb-free halide perovskite. Note that Ce and Tb doped 2D NS prepared by our method show superior stability as compared to other metal-doped samples[25, 76]. Yao et al. reported 40 % decrease in PL QY after 30 days of storage in Ce doped $CsPbCl_3$ NCs[33]. In our case, the Tb doped 2D $MAPbBr_3$ NS shows better optical and storage stability compared to the Ce doped sample, which may be due to stronger bonding of the Tb^{3+} ion with the host lattice. Also, ionic radius of Tb (106 pm) is lower than Ce (115 pm) resulting into more lattice contraction induced by Tb^{3+} doping giving rise to better stability.

5.5.5. Electronic Structure Calculation

In order to comprehend the effect of Ce and Tb doping in the bandgap and electron density of pristine $MAPbBr_3$ system, we have performed first-principles electronic structure calculations within the framework of DFT in collaboration with IIT Indore[42]. To investigate the structural changes and corresponding stability in the pristine system under the influence of Ce and Tb doping, we have also determined the formation energy of the individual systems. The crystal structures of doped and undoped system are shown in **Fig. 5.12**. We have analysed the projected density of states (PDOS) of all three systems, as depicted in **Fig. 5.13**. This analysis provides a clear picture

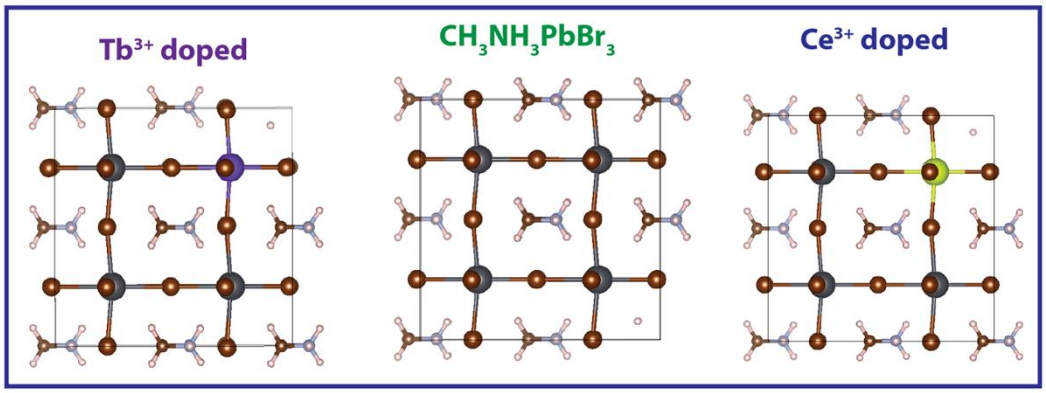

Fig. 5.12. Crystal structure of undoped and doped (12.5 %) $CH_3NH_3PbBr_3$ perovskites taken for DFT calculations.

of the electronic structure while describing the elemental orbital contribution of the constituting elements and their corresponding hybridization. The PDOS of the pristine $MAPbBr_3$ system shows the semiconducting nature with a bandgap of 1.76 eV (see **Fig. 5.13(a)**). A strong hybridization between *Pb-6p* and *Br-4p* is observed near the Fermi level of the valence band as well as in the higher energy range in the conduction band regime. The contribution of the organic cation, which consists of carbon (C), hydrogen (H) and nitrogen (N) is negligible near the Fermi level. In the case of Ce-doped $MAPbBr_3$, though the pretty negligible contribution near the fermi level of the valance band has been observed corresponding to *Ce-4f*, however, it contributes substantially in the conduction band regime along with *Pb-6p* and *Br-4p* (see **Fig. 5.13(b)**). Hence, *Ce-4f* is hybridized with *Pb-6p* and *Br-4p* in the conduction band and contributes to the enhancement of total DOS in the conduction band regime around 2 eV. Since we do not observe the presence of *Ce-5d* in the valance band, the well-known *5d-4f* rare-earth transition is not expected from Ce^{3+} in $MAPbBr_3$ host, which is consistent with the absence of Ce^{3+} emission peak in the PL spectra. Deep trap states corresponding to dopant defects are not observed in case of Ce doped $MAPbBr_3$, which

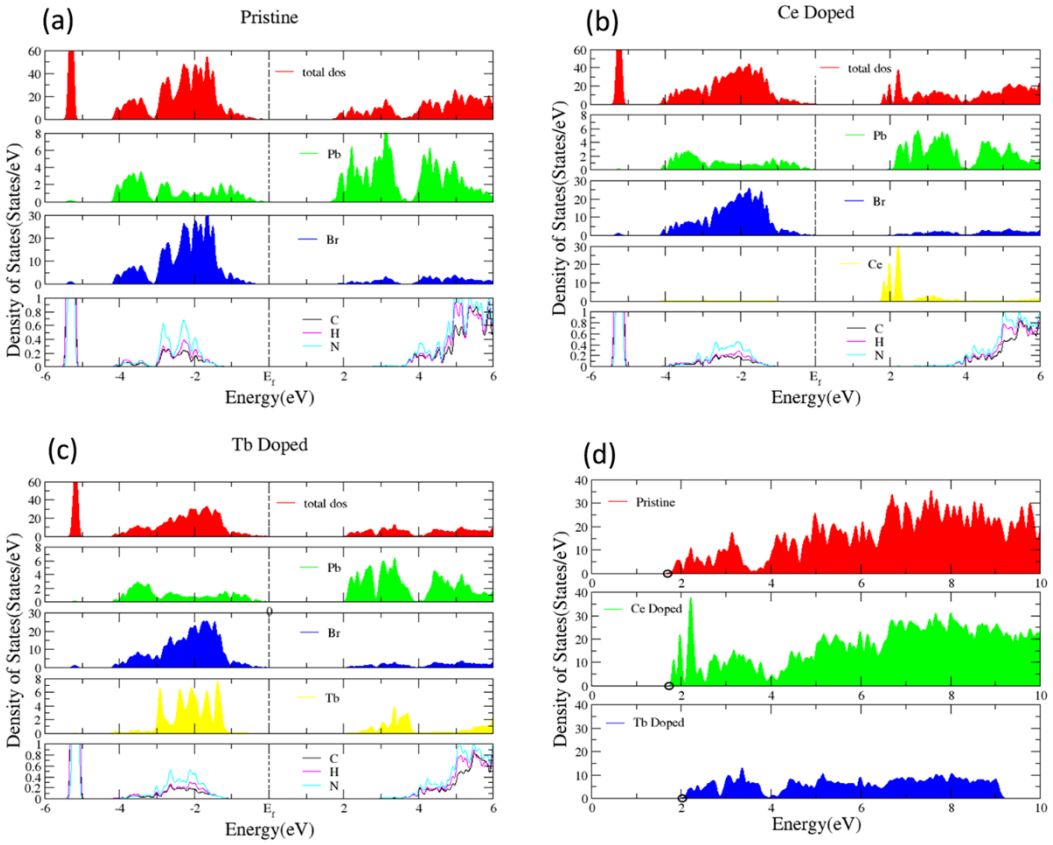

Fig. 5.13. Projected density of states (DOS) of (a) pristine, (b) Ce, (c) Tb doped $MAPbBr_3$. (d) Comparative analysis of total DOS in the conduction band regime for pristine and doped systems. The small circle depicts shift of the conduction band edge, which is much larger in Tb doped case than the Ce doped system.

may lead to non-radiative recombination, as seen in earlier reported Bi^{3+} doped $CsPbBr_3$ system[20]. Instead, it can be seen from **Fig. 5.13(b)** that in Ce doped system shallow transition levels are introduced approximately ~0.1 eV below the conduction band that act as new emissive channels, as discussed earlier. We can also infer from the PDOS of Ce doped $MAPbBr_3$ system that the total electron density in the conduction band regime substantially increases after Ce doping than the pristine one, which would lead to the possible modulation of the exciton relaxation and recombination. This supports the large enhancement in PL emission intensity post Ce^{3+} doping. Interestingly, the electronic structure analysis provides ~0.1 eV enlargement in the bandgap post Ce doping, whereas experimentally, the value is ~0.25 eV since quantum confinement effect and lattice contraction together contribute to the overall change in the bandgap.

Similar to Ce doped system, Tb does not play a major role in the valance band regime, as shown in **Fig. 5.13(c)**. The contribution in the conduction band regime is mainly due to the synergistic

hybridization of *Tb-4f, Pb-6p and Br-4p* orbitals. Therefore, in the Tb doping case also, the intrinsic transition due to Tb is not possible. Tb is contributing to the overall rearrangement of band positions. The density of state calculation shows an increment of bandgap of ~0.3 eV due to Tb doping in $MAPbBr_3$, which is larger than the Ce doped case. This is fully consistent with our experimental observation, which shows a total $\Delta E_g \sim 0.54$ eV in Tb70 as compared to $\Delta E_g \sim 0.25$ eV in Ce70. From the total PDOS of Tb doped $MAPbBr_3$, it can be seen that the inclusion of Tb decreased the electron density. However, the enhancement in PL QY may be due to quantum confinement effect and lattice contraction in Tb doped NS. We have also compared the total DOS in the conduction band regime of the pristine and doped cases, as reflected in **Fig. 5.13(d)** in a magnified scale. We can observe the small circle depicting the conduction band edge that has been shifted differently in case of Ce and Tb doped systems, where the shift is not very substantial in Ce doped $MAPbBr_3$, whereas Tb doping shifted the conduction band edge far from the Fermi level. Thus, there is a substantial increase in the bandgap in Tb doped case, which is fully consistent with the experimental results. Thus, the DFT calculation correctly predicts that Ce doping leads to major improvement in the PL emission yield, while the Tb doping causes a substantial increase in the bandgap along with increase in PL emission yield.

Further, from our calculation of the formation energy to theoretically predict the relative stability of the undoped and rare-earth doped system, we have found the pristine system is having a value of -6.85 eV, which is comparable to the earlier reported value[77]. This formation energy becomes lower with Ce and Tb doping, where it attains the value -7.06 eV and -7.25 eV, respectively. As more negative value of formation energy asserts the stability enhancement of a system, we can infer that the decrease in formation energy by ~0.21 eV and ~0.4 eV in case of Ce and Tb doped systems, respectively, signifies higher stability in the doped systems. This is fully consistent with our experimental data on improved stability of doped systems. Hence, the following major aspects can be inferred from our theoretical calculations: (a) the stability enhancement under the influence of Ce and Tb doping in $MAPbBr_3$, (b) bandgap increment after doping of Ce and Tb in $MAPbBr_3$, and (c) substantial enhancement of the electron density in the conduction band in Ce doped system giving rise to high emission yield. These results are fully consistent with our experimental observation and it complements our understanding of the electronic structure of the doped system.

5.5.6. Application of Ce Doped NSs for White LED

We have shown that $MAPb_{0.3}Ce_{0.7}Br_3$ possesses excellent light emission properties and to demonstrate its practical application, we have fabricated a down-converting white light-emitting diode with Ce doped $MAPbBr_3$, as shown in **Fig. 5.14(a)**. To fabricate the white LED, Ce70 and Rhodamine B were mixed with PMMA solution separately and sequentially deposited on a low cost commercial UV emitting chip (400 nm). The layers were kept to dry in ambient condition without any heating. The electroluminescence spectrum of the as-prepared white LED represents

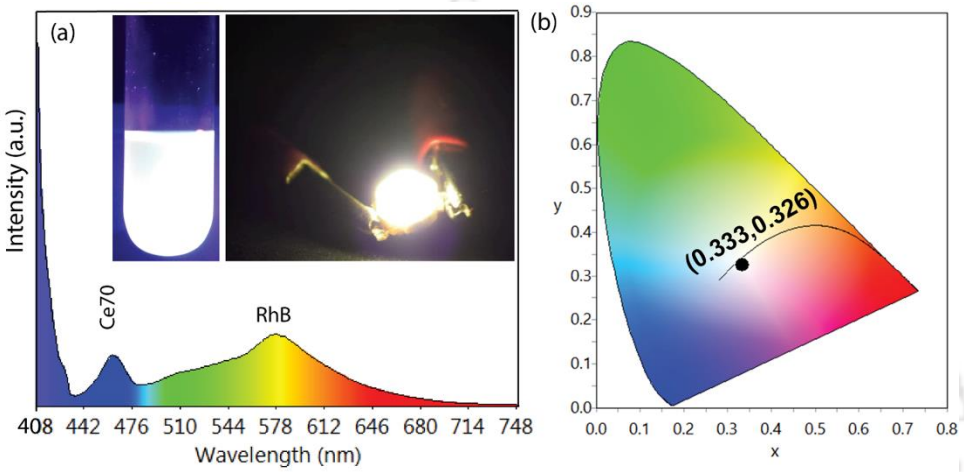

Fig. 5.14. (a) EL spectra of white light-emitting Ce doped 2D perovskite NS device fabricated with UV LED chip, Ce70, and Rhodamine B. The inset shows white light emission from colloidal solution under UV excitation and digital photograph of the white light converter. (b) CIE chromaticity coordinates of the Ce doped 2D perovskite white light converter.

a blue emission peak centered at 462 nm corresponding to Ce70 and a broad orange emission peak at 578 nm corresponding to Rhodamine B under the excitation of UV LED operating at 2.45 V (**Fig. 5.14(a)**). At an optimized ratio of the solutions, bright, warm, pure white emission is achieved, which can be seen from the photograph of a working white LED shown in the inset of **Fig. 5.14(a)**. White light emission from the colloidal solution of the mixture can be seen under the UV excitation as shown in the inset of **Fig. 5.14(a)**. CIE coordinates of (0.334, 0.326) for the white light converter is remarkably close to the standard white light (0.33,0.33) (see **Fig. 5.14(b)**). The white light converter demonstrates CCT of 5437 K, CRI of 73 and luminescence efficiency of 79.6 lm/W at 2.74 V. A mixture of sky-blue $MAPb(Br_{0.6}Cl_{0.4})_3$ and orange-red Rhodamine 6G was previously used as the emissive layer for the fabrication of perovskite white LEDs[78]. It was reported that the chance for electron–hole recombination increases due to decrease in crystallite/grain size in the Rhodamine B and perovskite mixture[78]. With the application of bias,

electron can be injected from perovskite layer into the conduction band of Rhodamine 6B, leading to a higher electroluminescence intensity[78]. The CIE coordinates of the white LED are very close to Planckian locus, as shown in **Fig. 5.14(b)** indicating that the color temperature is very pleasant and soothing to human eyes[17]. The quality of white light is determined by how well the CIE coordinates align with the black body radiation curve and accordingly it can be chosen as next-generation white LEDs[15]. CRI of a light source apparently indicates the ability of the light source to reveal the actual color of the object. Hence, high CRI is expected to recognize the natural color of any object under the light source. High luminescence efficiency of the fabricated white light converter using Ce doped $MAPbBr_3$ is very promising as highly energy-efficient LEDs and it can broaden the range of their potential applications in cutting-edge optoelectronic and imaging devices.

5.6. Summary and Conclusions

In conclusion, we have demonstrated a facile, reproducible solvothermal method to synthesize Ce and Tb doped $MAPbBr_3$ 2D perovskite nanosheets possessing deep blue emission with 100 % PL QY. Our analysis expanded the family of perovskite nanomaterials with $MAPb_{1-x}Ce_xBr_3$ and $MAPb_{1-x}Tb_xCl_{3x}Br_{3(1-x)}$ adding to the list having extremely high PL QY blue emission. The layered structure of 2D perovskite NS allows easy substitution of Pb^{2+} with Ce^{3+}/Tb^{3+} enabling the doping concentration up to 70 mol% $CeBr_3/TbCl_3$, which is believed to be the highest among the rare-earth dopants reported till date. Hence, successful doping of Ce and Tb ions in 2D $MAPbBr_3$ NS by the versatile solvothermal method may bestow the other perovskite system with highly efficient, narrow, stable blue emission, which illustrates its great potential in the fabrication of blue laser, LEDs, display, photodetectors, and medical devices. The key findings of the chapter are summarized below.

1. The introduction of rare-earth dopants significantly tuned the lateral size and thickness of the 2D NS to uniformly distributed ultrathin (bilayer) 2D NPLs.
2. Characteristic 2D diffraction peaks are observed at low diffraction angles in doped NS and NPLs signifying the formation of pure 2D perovskite phase.
3. The PL peak energy could be successfully tuned by ~0.337 eV and 0.587 eV to deep blue region in Ce and Tb doped $MAPbBr_3$ NS, respectively. From the qualitative and theoretical

analyses, it was revealed that the bandgap widening mainly results from the quantum confinement effect.

4. Post doping, the PL QY of the Ce and Tb doped NS significantly improved. Strong deep blue emission with 100 % PL QY is achieved with 70 mol% $CeBr_3$ concentration by our solvothermal method, which is very significant.
5. Our experimental results are fully supported by the electronic structure calculations using DFT method. Our calculation results reveal that Tb doping allows enlargement of bandgap by larger amount than the Ce doping, while the PL QY is highest for the Ce doped case.
6. Multiple PL peaks emerge at low temperatures due to the coexistence of different lattice phases as atomically thin NS structure allows easy orientation of perovskite structure.
7. The highly luminescent NPLs are further demonstrated as a down converter white LED with CIE coordinates (0.334, 0.326), closely matching with the pure white light and thus indicating their promising application in solid-state lightning field.

References

[1] A. Kojima, K. Teshima, Y. Shirai, T. Miyasaka, Organometal halide perovskites as visible-light sensitizers for photovoltaic cells, J. Am. Chem. Soc., 131 (2009) 6050-6051.
[2] V. D'Innocenzo, G. Grancini, M.J.P. Alcocer, A.R.S. Kandada, S.D. Stranks, M.M. Lee, G. Lanzani, H.J. Snaith, A. Petrozza, Excitons Versus Free Charges in Organo-Lead Tri-Halide Perovskites, Nat. Commun., 5 (2014) 3586.
[3] J.A. Sichert, Y. Tong, N. Mutz, M. Vollmer, S. Fischer, K.Z. Milowska, R. García Cortadella, B. Nickel, C. Cardenas-Daw, J.K. Stolarczyk, Quantum Size Effect in Organometal Halide Perovskite Nanoplatelets, Nano Lett., 15 (2015) 6521-6527.
[4] Y. Nagaoka, K. Hills-Kimball, R. Tan, R. Li, Z. Wang, O. Chen, Nanocube Superlattices of Cesium Lead Bromide Perovskites and Pressure-Induced Phase Transformations at Atomic and Mesoscale Levels, Adv. Mater., 29 (2017) 1606666.
[5] S. Parveen, S.M. Obaidulla, P.K. Giri, Growth Kinetics of Hybrid Perovskite Thin Films on Different Substrates at Elevated Temperature and Its Direct Correlation with the Microstructure and Optical Properties, Appl. Surf. Sci., 530 (2020) 147224.
[6] J.H. Jeffries, J.K. Zuo, M.M. Craig, Instability of Kinetic Roughening in Sputter-Deposition Growth of Pt on Glass, Phys. Rev. Lett., 76 (1996) 4931-4934.

[7] A. Kojima, M. Ikegami, K. Teshima, T. Miyasaka, Highly Luminescent Lead Bromide Perovskite Nanoparticles Synthesized with Porous Alumina Media, Chem. Lett., 41 (2012) 397-399.
[8] S.D. Stranks, G.E. Eperon, G. Grancini, C. Menelaou, M.J. Alcocer, T. Leijtens, L.M. Herz, A. Petrozza, H.J. Snaith, Electron-hole diffusion lengths exceeding 1 micrometer in an organometal trihalide perovskite absorber, Science, 342 (2013) 341-344.
[9] H.-C. Wang, W. Wang, A.-C. Tang, H.-Y. Tsai, Z. Bao, T. Ihara, N. Yarita, H. Tahara, Y. Kanemitsu, S. Chen, R.-S. Liu, High-Performance CsPb1−xSnxBr3 Perovskite Quantum Dots for Light-Emitting Diodes, Angew. Chem. Int. Ed., 56 (2017) 13650-13654.
[10] W. Liu, Q. Lin, H. Li, K. Wu, I. Robel, J.M. Pietryga, V.I. Klimov, Mn2+-Doped Lead Halide Perovskite Nanocrystals with Dual-Color Emission Controlled by Halide Content, J. Am. Chem. Soc., 138 (2016) 14954-14961.
[11] P.K. Nayak, M. Sendner, B. Wenger, Z. Wang, K. Sharma, A.J. Ramadan, R. Lovrinčić, A. Pucci, P.K. Madhu, H.J. Snaith, Impact of Bi3+ Heterovalent Doping in Organic–Inorganic Metal Halide Perovskite Crystals, J. Am. Chem. Soc., 140 (2018) 574-577.
[12] F. Hao, C.C. Stoumpos, R.P.H. Chang, M.G. Kanatzidis, Anomalous Band Gap Behavior in Mixed Sn and Pb Perovskites Enables Broadening of Absorption Spectrum in Solar Cells, J. Am. Chem. Soc., 136 (2014) 8094-8099.
[13] H.-J. Feng, T.R. Paudel, E.Y. Tsymbal, X.C. Zeng, Tunable Optical Properties and Charge Separation in CH3NH3SnxPb1–xI3/TiO2-Based Planar Perovskites Cells, J. Am. Chem. Soc., 137 (2015) 8227-8236.
[14] D. Zhou, D. Liu, G. Pan, X. Chen, D. Li, W. Xu, X. Bai, H. Song, Cerium and Ytterbium Codoped Halide Perovskite Quantum Dots: A Novel and Efficient Downconverter for Improving the Performance of Silicon Solar Cells, Adv. Mater., 29 (2017) 1704149.
[15] G.C. Adhikari, S. Thapa, H. Zhu, P. Zhu, Mg2+-Alloyed All-Inorganic Halide Perovskites for White Light-Emitting Diodes by 3D-Printing Method, Adv. Optical Mater., 7 (2019) 1900916.
[16] L. Wang, H. Zhou, J. Hu, B. Huang, M. Sun, B. Dong, G. Zheng, Y. Huang, Y. Chen, L. Li, Z. Xu, N. Li, Z. Liu, Q. Chen, L.-D. Sun, C.-H. Yan, A Eu3+-Eu2+ Ion Redox Shuttle Imparts Operational Durability to Pb-I Perovskite Solar Cells, Science, 363 (2019) 265.
[17] S. Thapa, G.C. Adhikari, H. Zhu, A. Grigoriev, P. Zhu, Zn-Alloyed All-Inorganic Halide Perovskite-Based White Light-Emitting Diodes with Superior Color Quality, Sci Rep, 9 (2019) 18636.
[18] B. Luo, F. Li, K. Xu, Y. Guo, Y. Liu, Z. Xia, J.Z. Zhang, B-Site Doped Lead Halide Perovskites: Synthesis, Band Engineering, Photophysics, and Light Emission Applications, J. Mater. Chem. C, 7 (2019) 2781-2808.
[19] A.B.F. Vitoreti, S. Agouram, M. Solis de la Fuente, V. Muñoz-Sanjosé, M.A. Schiavon, I. Mora-Seró, Study of the Partial Substitution of Pb by Sn in Cs–Pb–Sn–Br Nanocrystals Owing to Obtaining Stable Nanoparticles with Excellent Optical Properties, J. Phys. Chem. C, 122 (2018) 14222-14231.
[20] J. Yin, G.H. Ahmed, O.M. Bakr, J.-L. Brédas, O.F. Mohammed, Unlocking the Effect of Trivalent Metal Doping in All-Inorganic CsPbBr3 Perovskite, ACS Energy Lett., 4 (2019) 789-795.
[21] R. Begum, M.R. Parida, A.L. Abdelhady, B. Murali, N.M. Alyami, G.H. Ahmed, M.N. Hedhili, O.M. Bakr, O.F. Mohammed, Engineering Interfacial Charge Transfer in CsPbBr3 Perovskite Nanocrystals by Heterovalent Doping, J. Am. Chem. Soc., 139 (2017) 731-737.
[22] R. Buonsanti, D.J. Milliron, Chemistry of Doped Colloidal Nanocrystals, Chem. Mater., 25 (2013) 1305-1317.
[23] N. Pradhan, S. Das Adhikari, A. Nag, D.D. Sarma, Luminescence, Plasmonic, and Magnetic Properties of Doped Semiconductor Nanocrystals, Angew. Chem. Int. Ed. , 56 (2017) 7038-7054.
[24] D. Rossi, D. Parobek, Y. Dong, D.H. Son, Dynamics of Exciton–Mn Energy Transfer in Mn-Doped CsPbCl3 Perovskite Nanocrystals, J. Phys. Chem. C, 121 (2017) 17143-17149.
[25] C.C. Lin, K.Y. Xu, D. Wang, A. Meijerink, Luminescent Manganese-Doped Cspbcl3 Perovskite Quantum Dots, Sci Rep, 7 (2017) 45906.

[26] D. Parobek, B.J. Roman, Y. Dong, H. Jin, E. Lee, M. Sheldon, D.H. Son, Exciton-to-Dopant Energy Transfer in Mn-Doped Cesium Lead Halide Perovskite Nanocrystals, Nano Lett., 16 (2016) 7376-7380.
[27] Z. Zeng, Y. Xu, Z. Zhang, Z. Gao, M. Luo, Z. Yin, C. Zhang, J. Xu, B. Huang, F. Luo, Y. Du, C. Yan, Rare-Earth-Containing Perovskite Nanomaterials: Design, Synthesis, Properties and Applications, Chem. Soc. Rev., 49 (2020) 1109-1143.
[28] A.J. Kenyon, Recent Developments in Rare-Earth Doped Materials for Optoelectronics, Prog. Quantum Electron., 26 (2002) 225-284.
[29] G. Pan, X. Bai, D. Yang, X. Chen, P. Jing, S. Qu, L. Zhang, D. Zhou, J. Zhu, W. Xu, B. Dong, H. Song, Doping Lanthanide into Perovskite Nanocrystals: Highly Improved and Expanded Optical Properties, Nano Lett., 17 (2017) 8005-8011.
[30] X. Zhang, Y. Zhang, X. Zhang, W. Yin, Y. Wang, H. Wang, M. Lu, Z. Li, Z. Gu, W.W. Yu, Yb3+ and Yb3+/Er3+ Doping for Near-Infrared Emission and Improved Stability of Cspbcl3 Nanocrystals, Journal of Materials Chemistry C, 6 (2018) 10101-10105.
[31] D.M. Kroupa, J.Y. Roh, T.J. Milstein, S.E. Creutz, D.R. Gamelin, Quantum-Cutting Ytterbium-Doped CsPb(Cl1–xBrx)3 Perovskite Thin Films with Photoluminescence Quantum Yields over 190%, ACS Energy Lett., 3 (2018) 2390-2395.
[32] W.J. Mir, T. Sheikh, H. Arfin, Z. Xia, A. Nag, Lanthanide Doping in Metal Halide Perovskite Nanocrystals: Spectral Shifting, Quantum Cutting and Optoelectronic Applications, NPG Asia Mater, 12 (2020) 9.
[33] J.-S. Yao, J. Ge, B.-N. Han, K.-H. Wang, H.-B. Yao, H.-L. Yu, J.-H. Li, B.-S. Zhu, J.-Z. Song, C. Chen, Q. Zhang, H.-B. Zeng, Y. Luo, S.-H. Yu, Ce3+-Doping to Modulate Photoluminescence Kinetics for Efficient CsPbBr3 Nanocrystals Based Light-Emitting Diodes, J. Am. Chem. Soc., 140 (2018) 3626-3634.
[34] J. Duan, Y. Zhao, X. Yang, Y. Wang, B. He, Q. Tang, Lanthanide Ions Doped CsPbBr3 Halides for HTM-Free 10.14%-Efficiency Inorganic Perovskite Solar Cell with an Ultrahigh Open-Circuit Voltage of 1.594 V, Adv. Energy Mater., 8 (2018) 1802346.
[35] W.J. Mir, Y. Mahor, A. Lohar, M. Jagadeeswararao, S. Das, S. Mahamuni, A. Nag, Postsynthesis Doping of Mn and Yb into CsPbX3 (X = Cl, Br, or I) Perovskite Nanocrystals for Downconversion Emission, Chem. Mater., 30 (2018) 8170-8178.
[36] X. Zhang, H. Wang, Y. Hu, Y. Pei, S. Wang, Z. Shi, V.L. Colvin, S. Wang, Y. Zhang, W.W. Yu, Strong Blue Emission from Sb3+-Doped Super Small CsPbBr3 Nanocrystals, : J. Phys. Chem. Lett., 10 (2019) 1750-1756.
[37] Y. Xie, B. Peng, I. Bravić, Y. Yu, Y. Dong, R. Liang, Q. Ou, B. Monserrat, S. Zhang, Highly Efficient Blue-Emitting CsPbBr3 Perovskite Nanocrystals through Neodymium Doping, Adv. Sci., 7 (2020) 2001698.
[38] H. Shi, X. Zhang, X. Sun, X. Zhang, Deep Blue Emission of All-Bromide-Based Cesium Lead Perovskite Nanocrystals, J. Phys. Chem. C, 124 (2020) 1617-1622.
[39] H. Gao, W. Feng, H. Liu, S. Liu, Z. Wang, D. Yao, Y. Liu, D.-K. Teng, B. Yang, H. Zhang, Cesium–Lead Bromide Perovskite Nanoribbons with Two-Unit-Cell Thickness and Large Lateral Dimension for Deep-Blue Light Emission, ACS Appl. Nano Mater., 3 (2020) 4826-4836.
[40] X. Wu, H. Li, K. Wang, X. Sun, L. Wang, CH3NH3Pb1−xEuxI3 mixed halide perovskite for hybrid solar cells: the impact of divalent europium doping on efficiency and stability, RSC Advances, 8 (2018) 11095-11101.
[41] S. Parveen, K.K. Paul, P.K. Giri, Precise Tuning of the Thickness and Optical Properties of Highly Stable 2D Organometal Halide Perovskite Nanosheets through a Solvothermal Process and Their Applications as a White LED and a Fast Photodetector, ACS Appl. Mater. Interfaces, 12 (2020) 6283-6297.
[42] W. Kohn, L.J. Sham, Self-Consistent Equations Including Exchange and Correlation Effects, Phys. Rev., 140 (1965) A1133-A1138.
[43] G. Kresse, J. Furthmüller, Efficient Iterative Schemes for Ab Initio Total-Energy Calculations Using a Plane-Wave Basis Set, Phys. Rev. B, 54 (1996) 11169-11186.
[44] P.E. Blöchl, Projector Augmented-Wave Method, Phys. Rev. B, 50 (1994) 17953-17979.

[45] J.P. Perdew, K. Burke, M. Ernzerhof, Generalized Gradient Approximation Made Simple, Phys. Rev. Lett., 77 (1996) 3865-3868.
[46] H.J. Monkhorst, J.D. Pack, Special Points for Brillouin-Zone Integrations, Phys. Rev. B, 13 (1976) 5188-5192.
[47] L. Mao, C.C. Stoumpos, M.G. Kanatzidis, Two-Dimensional Hybrid Halide Perovskites: Principles and Promises, J. Am. Chem. Soc., 141 (2019) 1171-1190.
[48] B.J. Bohn, Y. Tong, M. Gramlich, M.L. Lai, M. Döblinger, K. Wang, R.L.Z. Hoye, P. Müller-Buschbaum, S.D. Stranks, A.S. Urban, L. Polavarapu, J. Feldmann, Boosting Tunable Blue Luminescence of Halide Perovskite Nanoplatelets through Postsynthetic Surface Trap Repair, Nano Lett., 18 (2018) 5231-5238.
[49] Y. Jiang, J. Yuan, Y. Ni, J. Yang, Y. Wang, T. Jiu, M. Yuan, J. Chen, Reduced-Dimensional α-CsPbX3 Perovskites for Efficient and Stable Photovoltaics, Joule, 2 (2018) 1356-1368.
[50] L. Gan, J. Li, Z. Fang, H. He, Z. Ye, Effects of Organic Cation Length on Exciton Recombination in Two-Dimensional Layered Lead Iodide Hybrid Perovskite Crystals, J. Phys. Chem. Lett., 8 (2017) 5177-5183.
[51] L. Wang, P. Yao, F. Wang, S. Li, Y. Chen, T. Xia, E. Guo, K. Wang, B. Zou, H. Guo, Pressure-Induced Structural Evolution and Bandgap Optimization of Lead-Free Halide Double Perovskite (NH4)2SeBr6, Adv. Sci., 7 (2020) 1902900.
[52] T. Zhang, M.I. Dar, G. Li, F. Xu, N. Guo, M. Grätzel, Y. Zhao, Bication lead iodide 2D perovskite component to stabilize inorganic α-CsPbI₃ perovskite phase for high-efficiency solar cells, Sci. Adv., 3 (2017) e1700841.
[53] M. Roy, Vikram, S. Banerjee, A. Mitra, A. Alam, M. Aslam, Composition-Controlled Synthesis of Hybrid Perovskite Nanoparticles by Ionic Metathesis: Bandgap Engineering Studies from Experiments and Theoretical Calculations, Chem. Eur. J., 25 (2019) 9892.
[54] F. Yuan, Y.-K. Wang, G. Sharma, Y. Dong, X. Zheng, P. Li, A. Johnston, G. Bappi, J.Z. Fan, H. Kung, B. Chen, M.I. Saidaminov, K. Singh, O. Voznyy, O.M. Bakr, Z.-H. Lu, E.H. Sargent, Bright High-Colour-Purity Deep-Blue Carbon Dot Light-Emitting Diodes via Efficient Edge Amination, Nat. Photonics, 14 (2020) 171-176.
[55] L. Brus, Electronic Wave Functions in Semiconductor Clusters: Experiment and Theory, J. Phys. Chem., 90 (1986) 2555-2560.
[56] L. Protesescu, S. Yakunin, M.I. Bodnarchuk, F. Krieg, R. Caputo, C.H. Hendon, R.X. Yang, A. Walsh, M.V. Kovalenko, Nanocrystals of cesium lead halide perovskites (CsPbX3, X= Cl, Br, and I): novel optoelectronic materials showing bright emission with wide color gamut, Nano Lett., 15 (2015) 3692-3696.
[57] I. Levchuk, A. Osvet, X. Tang, M. Brandl, J.D. Perea, F. Hoegl, G.J. Matt, R. Hock, M. Batentschuk, C.J. Brabec, Brightly Luminescent and Color-Tunable Formamidinium Lead Halide Perovskite FAPbX3 (X = Cl, Br, I) Colloidal Nanocrystals, Nano Lett., 17 (2017) 2765-2770.
[58] J. Even, L. Pedesseau, C. Katan, Understanding Quantum Confinement of Charge Carriers in Layered 2D Hybrid Perovskites, ChemPhysChem, 15 (2014) 3733-3741.
[59] R. Prasanna, A. Gold-Parker, T. Leijtens, B. Conings, A. Babayigit, H.-G. Boyen, M.F. Toney, M.D. McGehee, Band Gap Tuning via Lattice Contraction and Octahedral Tilting in Perovskite Materials for Photovoltaics, J. Am. Chem. Soc., 139 (2017) 11117-11124.
[60] H. Mathieu, P. Lefebvre, P. Christol, Simple Analytical Method for Calculating Exciton Binding Energies in Semiconductor Quantum Wells, Phys. Rev. B, 46 (1992) 4092-4101.
[61] C.-Y. Wang, P. Liang, R.-J. Xie, Y. Yao, P. Liu, Y. Yang, J. Hu, L. Shao, X.W. Sun, F. Kang, G. Wei, Highly Efficient Lead-Free (Bi,Ce)-Codoped Cs2Ag0.4Na0.6InCl6 Double Perovskites for White Light-Emitting Diodes, Chem. Mater., 32 (2020) 7814-7821.
[62] S. Das, A. De, A. Samanta, Ambient Condition Mg2+ Doping Producing Highly Luminescent Green- and Violet-Emitting Perovskite Nanocrystals with Reduced Toxicity and Enhanced Stability, J. Phys. Chem. Lett., 11 (2020) 1178-1188.

[63] J. Li, L. Gan, Z. Fang, H. He, Z. Ye, Bright Tail States in Blue-Emitting Ultrasmall Perovskite Quantum Dots, J. Phys. Chem. Lett., 8 (2017) 6002-6008.
[64] P. Sadhukhan, A. Pradhan, S. Mukherjee, P. Sengupta, A. Roy, S. Bhunia, S. Das, Low temperature excitonic spectroscopy study of mechano-synthesized hybrid perovskite, Appl. Phys. Lett., 114 (2019) 131102.
[65] H. Ji, Z. Shi, X. Sun, Y. Li, S. Li, L. Lei, D. Wu, T. Xu, X. Li, G. Du, Vapor-Assisted Solution Approach for High-Quality Perovskite CH3NH3PbBr3 Thin Films for High-Performance Green Light-Emitting Diode Applications, ACS Appl. Mater. Interfaces, 9 (2017) 42893-42904.
[66] J. Ghosh, R. Ghosh, P.K. Giri, Strong Cathodoluminescence and Fast Photoresponse from Embedded CH3NH3PbBr3 Nanoparticles Exhibiting High Ambient Stability, ACS Appl. Mater. Interfaces, 11 (2019) 14917-14931.
[67] M.I. Dar, G. Jacopin, S. Meloni, A. Mattoni, N. Arora, A. Boziki, S.M. Zakeeruddin, U. Rothlisberger, M. Grätzel, Origin of Unusual Bandgap Shift and Dual Emission in Organic-Inorganic Lead Halide Perovskites, Sci. Adv., 2 (2016) e1601156.
[68] W. Zhai, C. Ge, X. Fang, K. Zhang, C. Tian, K. Yuan, S. Sun, Y. Li, W. Chen, G. Ran, Acetone vapour-assisted growth of 2D single-crystalline organic lead halide perovskite microplates and their temperature-enhanced photoluminescence, RSC Adv., 8 (2018) 14527-14531.
[69] S. Parveen, K.K. Paul, R. Das, P.K. Giri, Large Exciton Binding Energy, High Photoluminescence Quantum Yield and Improved Photostability of Organo-Metal Halide Hybrid Perovskite Quantum Dots Grown on a Mesoporous Titanium Dioxide Template, J. Colloid Interface Sci., 539 (2019) 619-633.
[70] K. Wang, F. You, H. Peng, S. Huang, Temperature-Dependent Photoluminescence of Ce3+ Doped CsPbCl3 Perovskite Quantum Dots, J. Nanosci. Nanotechnol. , 18 (2018) 7561-7565.
[71] F. Chen, C. Zhu, C. Xu, P. Fan, F. Qin, A. Gowri Manohari, J. Lu, Z. Shi, Q. Xu, A. Pan, Crystal Structure and Electron Transition Underlying Photoluminescence of Methylammonium Lead Bromide Perovskites, J. Mater. Chem. C, 5 (2017) 7739-7745.
[72] J. Tilchin, D.N. Dirin, G.I. Maikov, A. Sashchiuk, M.V. Kovalenko, E. Lifshitz, Hydrogen-like Wannier–Mott Excitons in Single Crystal of Methylammonium Lead Bromide Perovskite, ACS Nano, 10 (2016) 6363-6371.
[73] Z. Xiao, Y. Zhou, H. Hosono, T. Kamiya, N.P. Padture, Bandgap Optimization of Perovskite Semiconductors for Photovoltaic Applications, Chem. Eur. J., 24 (2018) 2305-2316.
[74] L. Wang, C. Lu, J. Lu, L. Liu, N. Liu, Y. Chen, Y. Zhang, E. Gu, X. Hu, Influence of Carrier Screening and Band Filling Effects on Efficiency Droop of Ingan Light Emitting Diodes, Opt. Express, 19 (2011) 14182-14187.
[75] L. Xu, S. Yuan, H. Zeng, J. Song, A Comprehensive Review of Doping in Perovskite Nanocrystals/Quantum Dots: Evolution of Structure, Electronics, Optics, and Light-Emitting Diodes, Materials Today Nano, 6 (2019) 100036.
[76] P.J.S. Rana, T. Swetha, H. Mandal, A. Saeki, P.R. Bangal, S.P. Singh, Energy Transfer Dynamics of Highly Stable Fe3+ Doped CsPbCl3 Perovskite Nanocrystals with Dual-Color Emission, J. Phys. Chem. C, 123 (2019) 17026-17034.
[77] X. Huang, T.R. Paudel, P.A. Dowben, S. Dong, E.Y. Tsymbal, Electronic Structure and Stability of The CH3NH3PbBr3 (001) Surface, Phys. Rev. B, 94 (2016) 195309.
[78] C.-Y. Chang, W.-L. Hong, P.-H. Lo, T.-H. Wen, S.-F. Horng, C.-L. Hsu, Y.-C. Chao, Perovskite White Light-Emitting Diodes with a Perovskite Emissive Layer Blended with Rhodamine 6G, J. Mater. Chem. C, 8 (2020) 12951-12958.

Chapter 6

Europium Doped Organo-Metal Halide 2D Perovskite Nanosheet Based UV Photodetector with Improved Responsivity and Fast Response

In this chapter, we have investigated the role of Eu^{3+} doping on the 2D $CH_3NH_3PbBr_3$ nanosheet (NS) based photodetector. Introduction of $EuCl_3$ in the $CH_3NH_3PbBr_3$ crystal structure enabled the tuning of lateral and vertical dimensions of the NS from large area NS to monolayer quantum dots by a solvothermal method. Characteristic 2D diffraction peaks arise in the low diffraction angle in the Eu doped NS, indicating a pure 2D structure. The bandgap of the Eu doped mixed halide perovskite systematically enlarges by ~0.599 eV with increasing doping concentration. The introduction of a small amount (10 mol%) of Eu ion in the pure $CH_3NH_3PbBr_3$ crystal enhances the absorbance resulting into high performance photodetection. Under the 405 nm laser illumination, $CH_3NH_3Pb_{0.9}Eu_{0.1}Br_{2.7}Cl_{0.3}$ photodetector exhibits self-biased behavior with On/off up to ~10^3 times, which is significant. The device achieves responsivity as high as 5.29 A/W and detectivity of 1.06×10^{12} Jones under 405 nm laser illumination of power density of 0.14 mW/cm^2 at 5 V. Very fast response time is observed in the device with rise/fall time of 17.5/38.5 µs, which is ~4 times faster than the pristine $CH_3NH_3PbBr_3$ counterpart. A linear relationship of photocurrent with light intensity in the $CH_3NH_3Pb_{0.9}Eu_{0.1}Br_{2.7}Cl_{0.3}$ photodetector signifies low recombination or charge trapping loss, and most of the photogenerated carriers are utilized for the photodetection performance without any loss due to charge trapping. High photodetection performance in the Eu doped device ascribed to the suppression of trap states and fast charge transfer process. This work paves the way for future outdoor and indoor photodetection applications using the new family of europium doped mixed halide perovskite materials.

6.1. Introduction

Recently, the metal halide perovskite nanomaterials have sprung to the forefront of optoelectronic and photovoltaic devices due to their extraordinary characteristics that permit them to use in diverse applications[1-14]. Typically, the characteristics such as large absorption coefficient, long diffusion length, high carrier mobility, etc. make them a perfect candidate for photovoltaic

application, whereas properties like high exciton binding energy, high photoluminescence (PL) quantum yield (QY), narrow full width at half maxima (FWHM), wide color gamut are very appealing for light-emitting diodes and laser applications[15-24]. Thus, based on the application, the properties of the perovskite materials can be tuned.

Despite having many appealing features, the commercialization of perovskite-based device is facing many roadblocks such as toxicity, low ambient stability, photo, and temperature stability[25]. This triggered the research for finding a suitable replacement of lead (Pb), keeping all the interesting features of pure perovskite crystal. Doping is one of the effective methods to introduce impurity in the pure perovskite crystal to tune and enhance its features. Though primarily early research mostly focused on replacing Pb with the neighboring elements in the periodic table such as Bi, Sn, Sb, etc., however, these dopant elements destabilize the perovskite structures and reduce the stability and performance compared to pure perovskite crystal[26-30]. In contrast, doping of lanthanide elements as the Pb substitution in the perovskite crystal is comparatively less explored and only in recent times, it is attracting a great deal of attention. Lanthanide materials are reported to fine-tune the electronic, optical and chemical properties of the pristine perovskite and 4f electrons of lanthanides enrich the band-edge states, which are the primary sources for the enhancement of luminescence properties of the host crystal[31, 32]. Although the emission property of lanthanide doped perovskite crystal is studied, but the effect of lanthanide ion on the photovoltaic and photodetection properties of the perovskite crystal is less explored. A few groups have reported about the impact of lanthanide elements on the photovoltaic performance of the perovskite. Lanthanide materials are reported to increases the grain size of perovskite film, thereby increasing the carrier lifetime and efficiency of solar cells[33]. In addition, the stability of the solar cell was significantly improved with the introduction of lanthanide materials[33]. Wang et al. prepared Nd^{3+} doped $CH_3NH_3PbI_3$ ($MAPbI_3$, $MA=CH_3NH_3$) planar heterojunction solar cell, which improved charge carrier mobility, reduced trap states, and prolonged carrier lifetime[34]. $Eu^{3+/2+}$ ions also were reported to eliminate Pb^0 and I^0 defects in $CsPbI_3$ perovskite devices, which in turn increased the solar cell efficiency[35]. Zhou et al. improved the power conversion efficiency of Si solar cell from 18.1 % to 21.5 % by coating the device with Yb^{3+} and Ce^{3+} codoped $CsPbCl_{1.5}Br_{1.5}$ nanocrystal (NC) layer using quantum cutting technique[36]. Wu et al. achieved a power conversion efficiency of 16.7 % by inserting a low doping ratio of 0.04 % EuI_2 as the dopant in $MAPbI_3$[37]. The power conversion efficiency of $CsPbBr_3$ solar cell was enhanced from 5.66

% to 7.28 % by optimizing the doping concentration of Eu ions[38]. $Eu(Ac)_3$ doped $CsPbI_2Br$ perovskite is reported to give a high-quality inorganic perovskite film with a low defect density, long carrier lifetime and high efficiency of 15.25 %[39]. Xiang and coworkers demonstrated a maximum power-conversion efficiency of 13.71 % for an inorganic perovskite solar cell with the $CsPb_{0.95}Eu_{0.05}I_2Br$ perovskite and a stable power output of 13.34 %[40]. Hence, europium appears to be an efficient sensitizer of photoluminescence since it decreases the non-radiative recombination, which in turn increases the open-circuit voltage. Engineering of excitonic luminescence was achieved for Eu^{3+}-doped $CsPbCl_{3-x}Br_x$ NCs for the first time by Dai et al.[41]. Eu^{2+} recently served as a suitable replacement of Pb^{2+} in all-inorganic perovskite, and $CsEuBr_3$ NCs were synthesized using a hot-injection method exhibiting a narrow PL peak at 413 nm with a PLQY of 39 %[42]. Single-crystalline $CsEuCl_3$ nanocrystals with a uniform size distribution centered around 15 nm were also synthesized, but the PL QY at room temperature was very low (~2 %)[43]. Rare-earth cation (Tb^{3+}, Eu^{3+})-doped $CsPbBr_3$ quantum dots (QDs) glass with tunable luminescence had been synthesized by conventional melt-quenching methods for the fabrication of white LED[44]. Eu^{3+}-doped lead-free $Cs_3Bi_2Br_9$ perovskite QDs were employed as a highly sensitive fluorescent probe for Cu^{2+} ion detection in water[45]. Hence, europium doping in perovskite crystal not only tunes its optical properties but also improves the photovoltaic performance. To the best of our knowledge, impact of lanthanide material on the photodetection performance of $MAPbBr_3$-based devices are not studied yet, and most of the Eu doping study was done on all-inorganic perovskite.

Here, we have studied the effect of Eu^{3+} ion on the structural and optical properties of solvothermally synthesized 2D $MAPbBr_3$ nanosheet (NS) and further fabricate Eu doped 2D mixed halide perovskite photodetector. Variation in thickness and size of the 2D perovskite NS with increasing Eu doping concentration is studied using TEM and AFM images. The bandgap is also tuned by varying the Eu concentration, which is analyzed using absorbance and PL analyses. Finally, we have performed a comparative study of the $EuCl_3$ doped $MAPbBr_3$ and pristine $MAPbBr_3$ photodetectors and show that Eu doping enables high performance photodetection in the hybrid 2D perovskites.

6.2. Experimental Procedure

6.2.1. Materials

The materials, which were used to synthesize the undoped and doped samples are methylamine solution (CH_3NH_3, 33 wt% in absolute ethanol, Sigma-Aldrich), lead(II) bromide ($PbBr_2$, 99.999 %, Sigma-Aldrich), hydrobromic acid (HBr, 48 wt% in water, Sigma-Aldrich), N, N-dimethylformamide (DMF, >99 %, Sigma-Aldrich), diethyl ether (>99 %, Merck), toluene (Merk), oleic acid ($CH_3(CH_2)_7CH=CH(CH_2)_7COOH$, Merk), oleylamine (OAm) (≥98 % (primary amine), Sigma-Aldrich), europium(III) chloride ($EuCl_3$, 99.9 %, Sigma-Aldrich). All the materials were used as received without any further purification.

6.2.2. Synthesis Procedures

6.2.2.1. Synthesis of CH_3NH_3Br

First, the organic part of the hybrid perovskite was synthesized by diluting the 8 mL of CH_3NH_3 solution with 20 mL of absolute ethanol with stirring in a round-bottom flask. Then, 3 mL HBr was slowly added to the previous solution in an ice bath with vigorous stirring at 1400 rpm for two h. The solution was then heated at 70 °C for several hours to evaporate the solvents. The remaining CH_3NH_3Br (MABr) salt was washed several times with ethanol to remove the impurities from the dry salt. Then, the powder was washed with anhydrous diethyl ether to recrystallize and finally, the powder was dried at 70 °C in a vacuum oven for 24 hours.

6.2.2.2. Synthesis of Undoped and Eu Doped 2D Perovskite NS

The undoped and doped 2D $MAPbBr_3$ NS was synthesized by solvothermal method[46]. First, equal mole of MABr and $PbBr_2$ were dry mixed, and then to make the solution, 1 ml DMF, oleic acid, and 60 µl OAm were added. Afterward the solution was transferred into a Teflon-lined autoclave without any pretreatment and solvothermally treated it at 120 °C for 30 min. Post the solvothermal process, the autoclave was allowed to cool down naturally for 30 min. Then 80 µl of the product solution was added into 10 ml toluene during vigorous stirring. To wash the as-prepared NS and separate it from the crude solution, the solution was centrifuged two times at 10000 rpm for 10 min. The supernatant was discarded each time, and the precipitate was redispersed in 6 ml toluene for further characterization. Please note that all the synthesis procedures were carried out in an ambient environment without the use of a glove box.

To synthesize the Eu doped 2D mixed halide perovskite NS, different amounts of $PbBr_2$ was replaced by $EuCl_3$ according to the desired doping concentrations. Typically, for 10 mol% doping concentration of $EuCl_3$, 0.1 mM MABr, 0.01 mM $EuCl_3$, and (0.1-0.01) = 0.09 mM $PbBr_2$ were first mixed and afterward same solvothermal procedure was followed, as discussed earlier. We varied the concentrations of $EuCl_3$ from 0 to a maximum of 60 mol%. The 0, 10, 20, 30, 40, 50 and 60 mol% $EuCl_3$ doped samples are named as Eu0, Eu10, Eu20, Eu30, Eu40, Eu60, respectively.

6.2.2.3. Fabrication of Photodetector

To fabricate the photodetector, first the Si/SiO_2 substrate was cleaned by ultra-sonication using water, acetone and 2-propanol sequentially for 15 min each. It was cleaned with water again, followed by heating at 180 °C to remove the impurities. Further, to ensure complete removal of residue, the substrate was UV-ozone treated for 20 min. We have first deposited the gold (Au) contacts on the substrate and then the perovskite solution to avoid the sample degradation while depositing the contacts. The Au contacts/electrodes were deposited on the wafers using the shadow masks using the vacuum thermal evaporation method. Then, the undoped and doped 2D NS were drop cast between the electrodes and annealed at 60 °C.

6.3. Characterization Techniques

The surface morphology of the $MAPbBr_3$ thin film was characterized using FESEM (Sigma, Zeiss). The high magnification surface morphology and thickness of the undoped and Eu doped perovskite NSs have been characterized using a field-emission TEM (JEOL-JEM 2010) operated at 200 kV and AFM (Cypher, Oxford Instruments). XRD (Rigaku RINT 2500 TRAX–III, Cu-Kα radiation) patterns were recorded to determine the crystal structure of different samples. UV−Vis absorption spectra of the $MAPbBr_3$ NSs were measured using a commercial spectrophotometer (PerkinElmer, Lamda 950). The room temperature steady-state PL spectra were recorded using 350 nm lamp excitation in a commercial fluorimeter (Fluoromax-4, Horiba Scientific). Time-resolved PL (TRPL) measurements were performed using a 375 nm pulsed laser excitation for perovskite NSs, with an instrument response time of <50 ps (LifeSpecII, Edinburgh Instruments). Photodetector measurement was taken using an in-house built set up consisting of a microprobe station (Ecopia, Korea), a 405 nm diode laser, a source meter (Keithley 2400, Germany), a pulse

generator (Agilent), and a digital oscilloscope (Agilent). The spectral response was measured using a 150 W Xe lamp (Newport, USA), a monochromator (Newport, USA), and a power meter (Newport, USA).

6.4. Results and Discussions

6.4.1. Morphology and Structural Analyses

6.4.1.1. FETEM Analysis

To understand the effect of Eu doping on the morphology of mixed halide perovskite, TEM images were recorded (see **Fig. 6.1**). Large area NS of dimension ~361 × 334 nm is observed in the undoped pristine $MAPbBr_3$ perovskite (Eu0), as shown in **Fig. 6.1(a)**. The high-resolution TEM (HRTEM) lattice fringe pattern for Eu0 is shown in **Fig. 6.1(b)** and the corresponding inverse fast Fourier transform (IFFT) image is presented in the inset. The measured interplanar spacing for

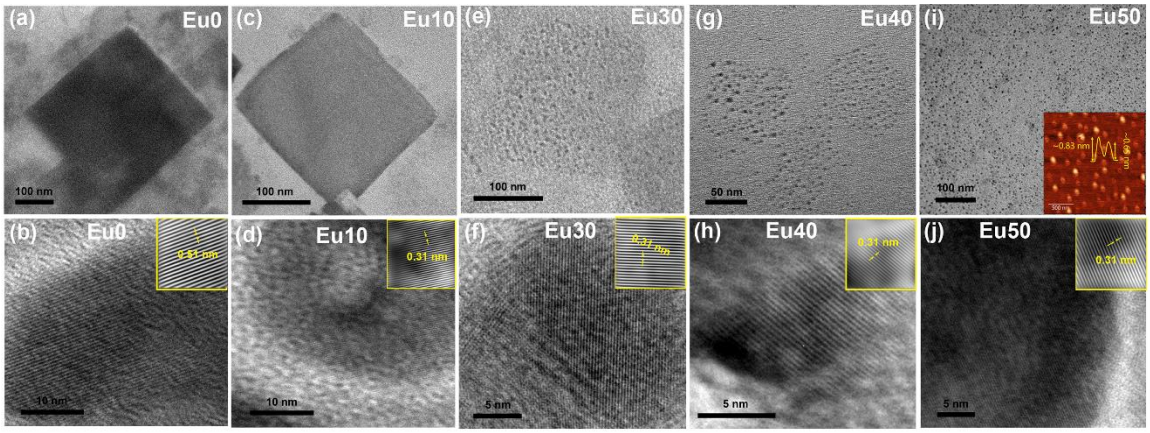

Fig. 6.1. TEM images of (a) undoped 2D perovskite, and Eu^{3+} doped perovskite NSs with various $EuCl_3$ concentrations: (c) 10 mol%, (e) 30 mol%, (g) 40 mol% and (i) 50 mol%. HRTEM images of (a, c, e, g, i) are shown in Fig. (b, d, f, h, j) and the inset of each figure shows the corresponding IFFT images.

Eu0 is found to be ~0.51 nm corresponding to (001) plane (see **Fig. 6.1(b)**). For 10 mol% Eu doping in $MAPbBr_3$ perovskite (Eu10), the lateral size of the NS decreases to ~207 nm × 218 nm, as shown in **Fig. 6.1(c)**. The interplanar spacing of Eu10 as seen in the HRTEM image is found to be ~0.31 nm and the corresponding IFFT image is shown in the inset of **Fig. 6.1(d)**. From the light contrast of the TEM image of Eu10, it can be understood that the thickness of the NS is decreased in Eu10 compared to the undoped one. The TEM image of Eu30 is shown in **Fig. 6.1(e)**, revealing

the QD decorated NS of lateral size ~189 nm × 188 nm. The HRTEM image of Eu30 with lattice spacing ~0.31 nm is shown in **Fig. 6.1(f)** and the corresponding IFFT image is shown in the inset. Further increase in Eu concentration to 40 mol% results in the complete transformation of the NS to QDs, as shown in **Fig. 6.1(g)**. **Fig. 6.1(h)** and inset of **Fig. 6.1(h)** demonstrate the HRTEM and corresponding IFFT image of Eu40, showing the lattice spacing of ~0.31 nm. The TEM image of Eu50 reveals the uniform distribution of QDs of average size ~3.1 nm over large area (see **Fig. 6.1(i)**). The inset of **Fig. 6.1(i)** shows the AFM image of QDs in Eu50, revealing the thickness of the QDs as ~0.65 nm corresponding to the monolayer thickness since the unit cell size of the $MAPbBr_3$ is ~5.93 Å. The HRTEM image of QDs in Eu50 is shown in **Fig. 6.1(j)**, and the corresponding IFFT image is shown in the inset, revealing lattice spacing of ~0.31 nm. The decrease in lattice spacing with Eu^{3+} doping in host $MAPbBr_3$ lattice is attributed to lattice contraction due to the partial replacement of Pb^{2+} (1.33 Å) and Br by smaller size Eu^{3+} (0.947 Å) and Cl ions. High doping concentration of $EuCl_3$ during the solvothermal synthesis procedure may also act as solvent and increase the reactivity of the ligands promoting the exfoliation of NS layer along the vertical direction[46]. This gives rise to thinner NS with increasing doping concentration and finally the disintegration of NS to QDs. **Fig. 6.2(a)** shows the FESEM image of Eu10 and the area on which the elemental mapping was taken is marked with square box. **Fig. 6.2(b)** shows the energy dispersive X-ray spectra (EDS) of Eu10, revealing the atomic ratio of Eu/Pb to be 0.196,

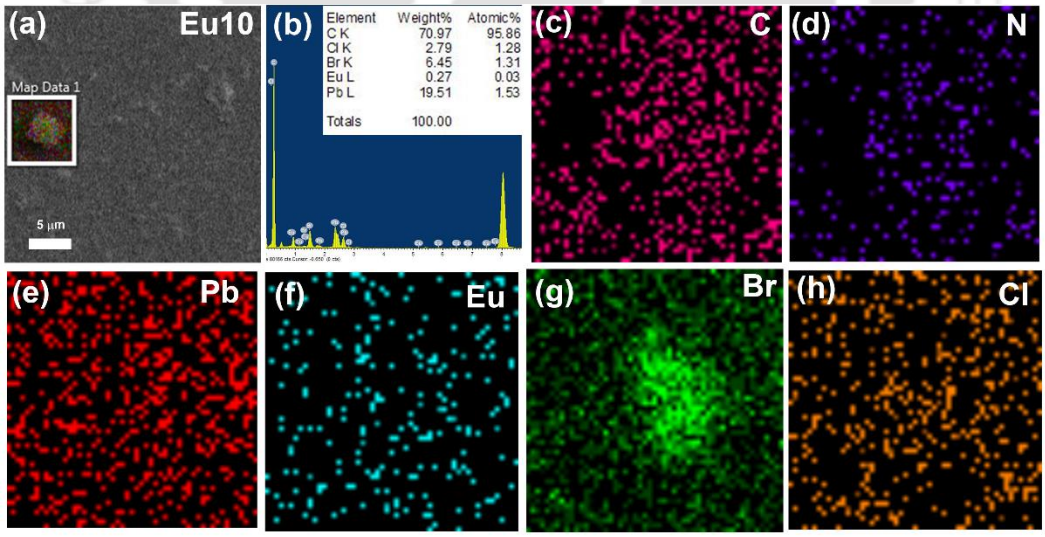

Fig. 6.2. (a) FESEM image of Eu10 and the marked square show the region on which the mapping is done. (b) Energy dispersive x-ray spectrum of Eu^{3+} doped NS with 10 mol% $EuCl_3$ concentrations. (c-h) Corresponding elemental mapping images of C, N, Pb, Eu, Br and Cl.

which confirms successful substitution of Pb^{2+} by Eu^{3+} to form mixed halide Eu doped 2D QDs. The elemental mapping of Eu10 is shown in **Fig. 6.2(c-h)**, revealing uniform distribution of all the elements including the Eu in the sample.

6.4.1.2. Structural Analysis

XRD patterns for $MAPbBr_3$ NS doped with different concentrations of $EuCl_3$ were studied to understand the doping effect in the perovskite crystal structure, as shown in **Fig. 6.3(a)**. XRD patterns of undoped NS reveals the cubic structure of the perovskite with diffraction peaks at 14.78º assigned to (001). After the incorporation of Eu^{3+} ion in $MAPbBr_3$, the characteristic diffraction peaks corresponding to 2D layered structure was observed below 14.78º. The peak at

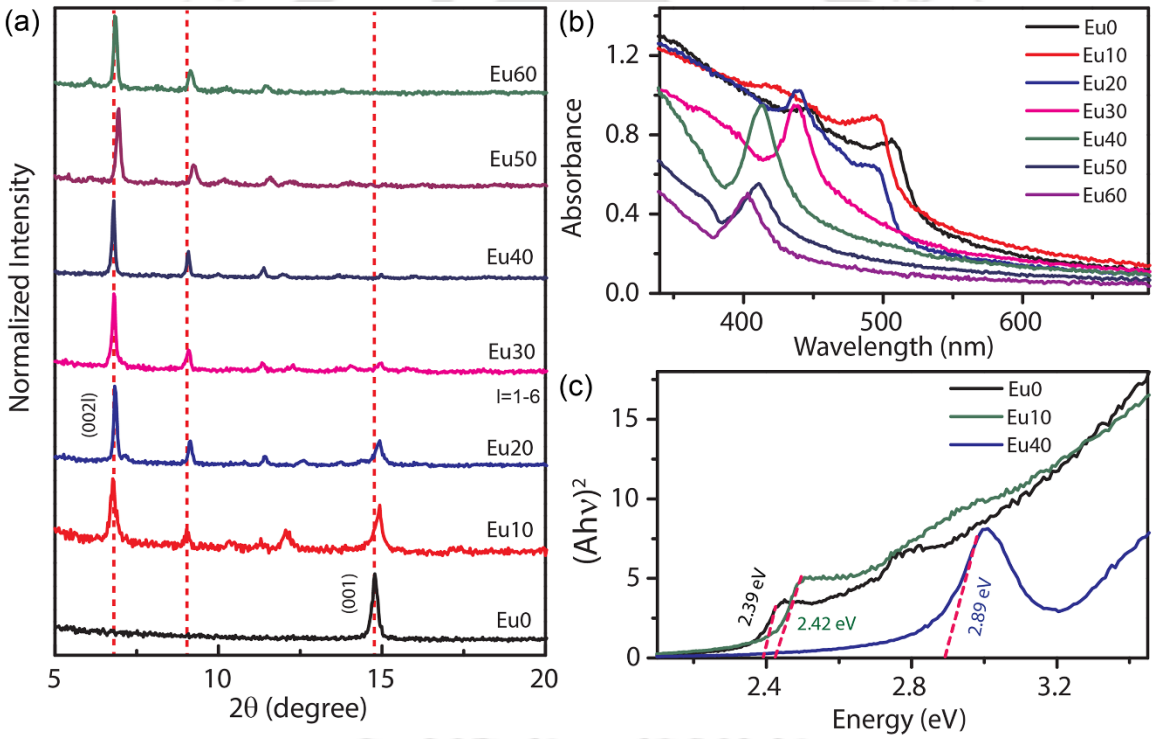

Fig. 6.3. (a) A comparison of XRD patterns of perovskite NS before and after the doping with Eu^{3+} at different molar concentrations. (b) Comparison of absorption spectra of 2D NS with increasing Eu doping concentrations. (c) Comparison of the Tauc Plots of Eu0, Eu10 and Eu40.

6.77º corresponding to (002) plane becomes prominent in Eu doped mixed halide 2D NS[47]. The peaks at 11.3º and 12.03º correspond to $PbBr_2$ and it appears due to layered structure since thin NS comprises layers of corner-sharing $PbBr_6$ octahedral. The intensity of (100) diffraction peak gradually decreases as the Eu doping concentration increases and finally disappears in Eu40,

indicating exfoliation of the sheets from the cleavage (100) plane to form the 2D structure. The diffraction peaks systematically shift towards higher angle with increasing Eu^{3+} concentration indicating a decrease in interplanar spacing due to the replacement of Pb^{2+} by smaller size Eu^{3+} and decrease in radii of halide ions from Br to Cl in doped mixed halide NS. The absence of (001) peak at higher doping concentration is ascribed to the formation of pure 2D structure.

6.4.2. Optical Analysis

To understand the effect of doping concentrations on the optical properties of the 2D perovskite NS, first the UV-vis spectroscopy was performed and the result is shown in **Fig. 6.3(b)**. With increasing $EuCl_3$ concentration, the first excitonic absorption peak is blue-shifted by 102 nm due to the thinning of the NS that causes quantum confinement effect (see **Fig. 6.3(b)**). Absorption intensity is slightly increased for 10 mol% doping concentration indicating better light-harvesting capability of doped NS, and further increment in doping concentration results in decrease in absorbance may be due to reduction in effective thickness of the NS. Enhancement in absorbance for Eu10 is ascribed to increased crystallinity and decrease in defect density. Considering this, 10 mol% doping concentration of $EuCl_3$ was selected to fabricate and study photodetection properties with respect to undoped $MAPbBr_3$ NS (discussed later). **Fig. 6.3(c)** shows the comparison of Tauc plot of Eu0, Eu10 and Eu40 revealing the respective bandgaps as 2.39 eV, 2.42 eV and 2.89 eV, respectively. Similarly, bandgap is calculated for all the samples and bandgap is found to be tuned from 2.39 eV to 2.94 eV with Eu^{3+} doping in 2D perovskite NS.

Comparison of PL spectra of various doping concentrations is shown **Fig. 6.4(a)**, revealing a systematic blue shift in excitonic PL peak from 515 nm to 412 nm with increasing $EuCl_3$ doping concentration. A large blue shift for 40 mol% $EuCl_3$ concentration is attributed to the strong quantum confinement effect due to the transformation of 2D NS to monolayer QDs. Replacement of Pb and Br by Eu and Cl, respectively, may also result in the lattice distortion, which gives rise to bandgap enlargement. Halide substitution of Br by Cl results into change in valence state from *4p* to *3p* giving rise to increase in bandgap. The absence of characteristic Eu^{3+} (*d-f*) transition peaks in this system is attributed to the fact that *Eu-5d* does not contribute to the valance band of $MAPbBr_3$ perovskite as it was observed in Eu doped all-inorganic perovskite[41]. Hence, the well-known *5d-4f* rare-earth transition is not expected from Eu^{3+} in $MAPbBr_3$ host. The intensity of excitonic PL emission first increases with increasing Eu^{3+} doping concentration then it approaches

an optimum value for Eu30 and finally decreases with increase in Eu^{3+} doping concentrations in Eu40, Eu50 and Eu60. An increase in PL intensity with increasing Eu^{3+} doping concentration is ascribed to improved crystallinity, suppression in defect states and non-radiative recombination. Further increase in $EuCl_3$ concentration leads to the substitution of the larger atomic radius Br by a smaller atomic radius Cl and Eu ions may trapped into the mixed halide perovskite lattice,

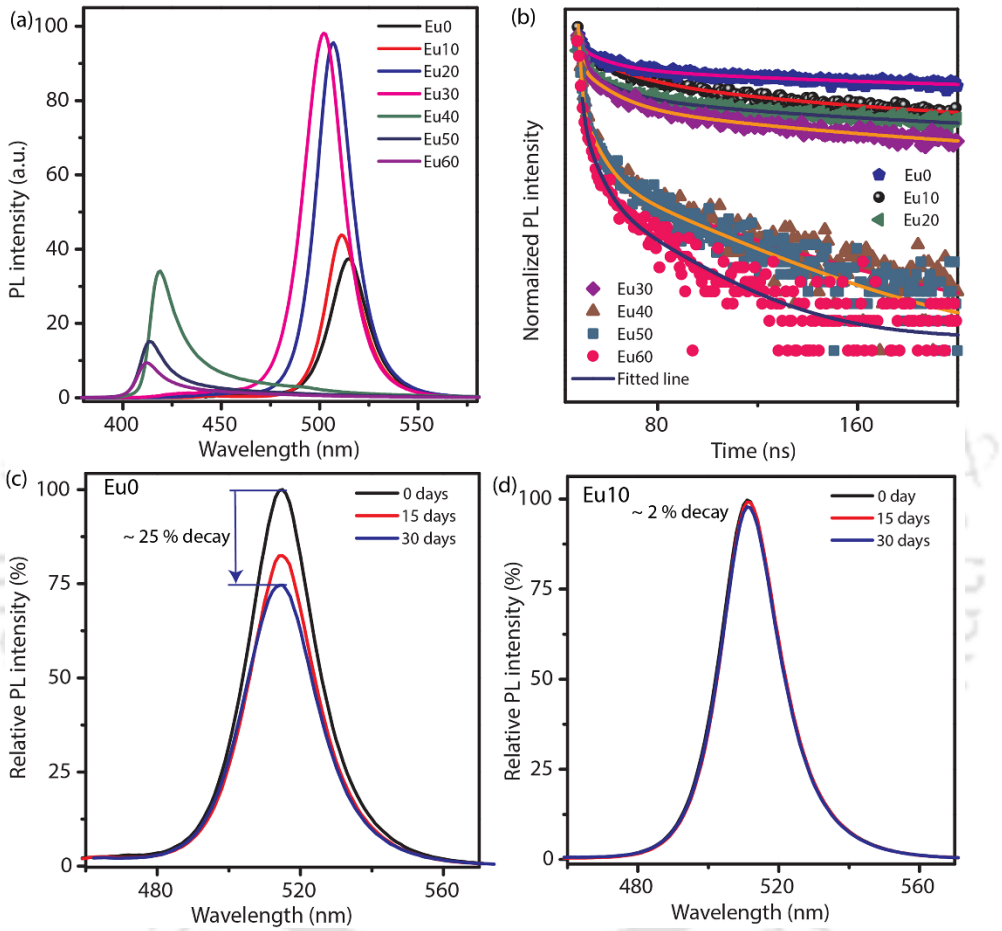

Fig. 6.4. (a) Comparison of PL spectra of various Eu doped $MAPbBr_3$ NS. (b) Comparison of TRPL spectra of undoped and Eu doped mixed halide perovskite NS. Change in PL spectra of (c) Eu0 and (d) Eu10 after storing it for one month.

inducing the decrease in Eu concentration in NCs[41]. In addition, structural distortion due to higher doping concentration may also affect the emission properties due to the formation of structural defect states. Higher doping concentration may introduce deep impurity levels which may increase the non-radiative recombination resulting into the decrease in emission intensity. This kind of behavior was reported earlier observed in Eu^{3+} doping in $CsPbBr_3$ crystal[32].

TRPL spectra were examined to study the charge recombination and extraction behavior of undoped and $EuCl_3$ doped 2D $MAPbBr_3$ NS, as shown in **Fig. 6.4(b)**. The TRPL decay profiles of the samples were recorded by monitoring them at their respective PL peak positions. The TRPL spectra were fitted with the tri-exponential decay function given by, $I(t) = \sum_{i=1}^{3} A_i \, exp(-t/\tau_i)$, where A_i is the amplitude of the PL decay component corresponding to the lifetime τ_i. The spectra were fitted with tri-exponential decay function since the PL spectra have contributions from three different states such as the QDs present along with NS, band to band transition and defect states. The average lifetimes (τ_{avg}) of the NSs are calculated using the following relation: $\tau_{avg} = \sum_{i=1}^{3} A_i \tau_i^2 / \sum_{i=1}^{3} A_i \tau_i$. The details of the decay components are presented in **Table 6.1**. The average carrier lifetime is observed to be decreased from ~124.03 ns to ~9.77 ns with increasing Eu^{3+}

Table 6.1. Details of TRPL decay components of the samples fitted with tri-exponential function.

Sample	τ_1 (ns)	A_1 %	τ_2 (ns)	A_2 %	τ_3 (ns)	A_3 %	τ_{avg} (ns)
Eu0	1	1.84	11.15	9.74	139.04	88.42	124.03
Eu10	1.01	2.52	14.440	15.04	111.44	82.445	94.08
Eu20	1.09	3.88	11.81	14.83	110.24	81.29	91.4
Eu30	1.09	4.55	11.53	17.23	105.26	78.21	84.39
Eu40	1.33	8.19	49.26	35.60	26.19	38.21	21.44
Eu50	0.78	5.65	38.43	62.24	2.38	16.43	9.61
Eu60	0.956	4.92	26.17	38.56	0.36	31.47	9.77

doping concentration primarily due to the quantum confinement effect. The contribution of faster components substantially increases with increasing doping concentration, which is attributed to increase in non-radiative recombination and defect states. Though PL emission intensity decreases in $EuCl_3$ doping concentration higher than 30 mol%, but lifetime still gets faster owing to the substitution of Br ion by Cl ion[41]. Lifetime becomes faster with increase in bandgap, which is consistent with the literature[48]. The decay time of several 94.08 ns is generally observed in $MAPbI_3$ which is considered as a good candidate for photovoltaic applications. Hence large lifetimes in Eu0 and Eu10 NS are attributed to long diffusion length[46, 48]. A slightly shorter

carrier lifetime in Eu10 compared that of the undoped $MAPbBr_3$ NS is attributed to the faster charge transfer mechanism due to the increase in carrier mobility[49, 50].

The storage stability of undoped and Eu doped NS is studied by storing the samples in ambient conditions (~65 % humidity). The PL spectra of the undoped $MAPbBr_3$ NS shows ~25 % decay in the PL intensity in one month, as shown in **Fig. 6.4(c)**. In contrast, the PL peak intensity of Eu10 is almost unchanged after storage of one month (see **Fig. 6.4(d)**). However, higher doping concentration decreases the stability of the 2D NS due to structural distortion. Therefore, the introduction of a small amount of $EuCl_3$ (10 mol%) improves the stability of 2D NS making it suitable for practical application. Higher stability in Eu10 is ascribed to an increase in tolerance factor and passivation of halide vacancy states.

6.4.3. Performance of Eu Doped Perovskite NS Based Photodetector

In order to characterize the effect of europium doping on the photophysical properties of perovskite, we have fabricated doped $MAPb_{0.9}Eu_{0.1}Cl_{0.3}Br_{2.7}$ and undoped perovskite based photodetectors. **Fig. 6.5(a)** illustrates the schematic diagram of perovskite photodetector where perovskite solution was deposited on top patterned Au contact with inter electrode spacing of 70 µm, to avoid any degradation of perovskite during contact deposition and performance of the device was studied under 405 nm laser irradiation. The inset of **Fig. 6.5(a)** shows the optical microscope image of Au patterned device. **Fig. 6.5(b)** shows the current-voltage (I−V) characteristics of pristine $MAPbBr_3$ NS photodetector under dark and 405 nm excitation with power density 4.94 mW/cm^2. Undoped $MAPbBr_3$ photodetector does not show any measurable photocurrent under zero bias condition, even at high power density. The turn-on voltage of the undoped device is found to be −0.4 V. The I−V characteristics of Eu0 photodetector exhibits nearly symmetric behavior indicating the formation of Schottky diode contact. **Fig. 6.5(c)** shows the comparison of I−V characteristics of Eu0, Eu10 and Eu40 photodetectors revealing enhanced photocurrent in Eu doped cases. Interestingly, the Eu10 photodetector shows much higher photocurrent than Eu40 due to better charge transfer/separation and fewer defects. Note that higher doping concentration results in the formation of monolayer QDs that gives rise to leakage in current due to the formation of deep trap states and structural defect-related states. It was reported that low doping concentration improves the perovskite crystal tolerance factor and reduces the electron trap density, which is consistent with our results[37, 39]. **Fig. 6.5(d)** displays the I−V

characteristics of Eu10 under dark and light conditions showing dramatic increases in photocurrent, especially under reverse bias voltage due to superior charge separation and exceptional light-matter interaction in the crystal[51]. I–V curve of Eu10 exhibits asymmetric

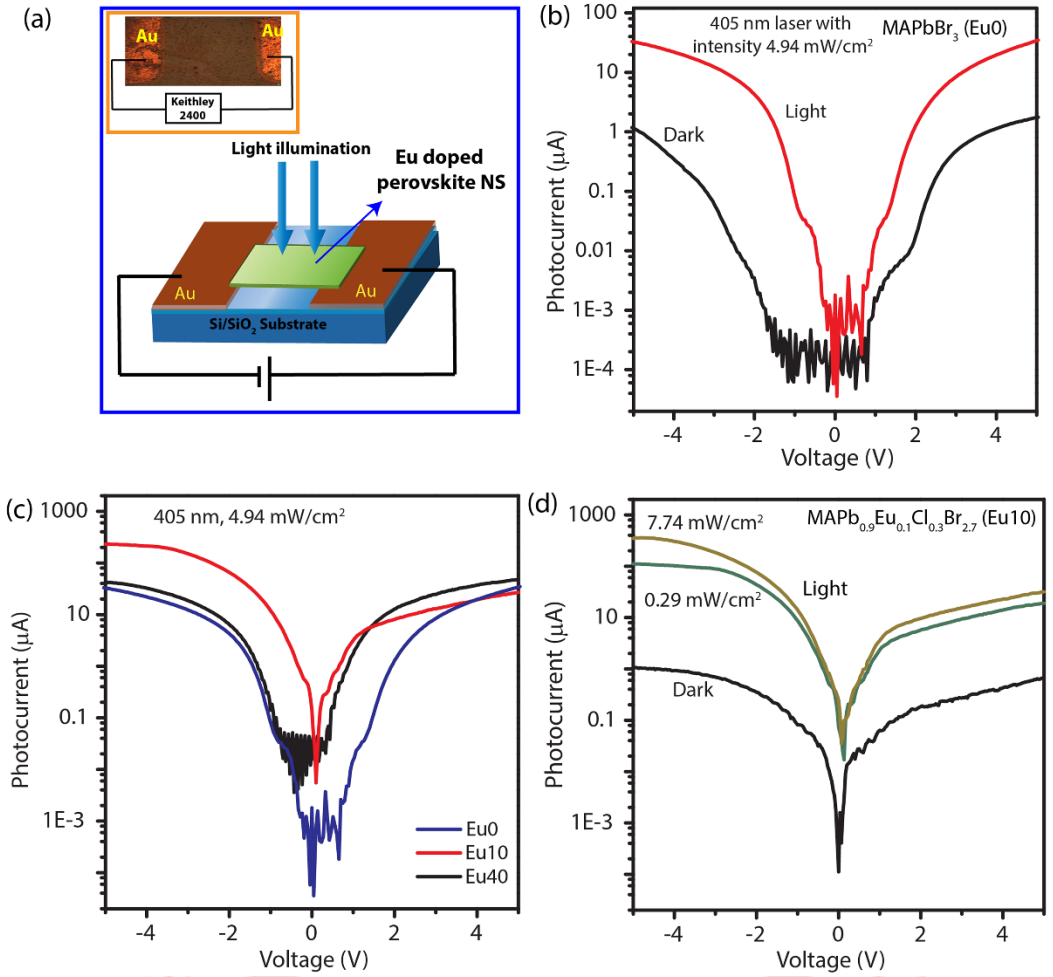

Fig. 6.5. (a) Schematic illustration of Eu doped 2D perovskite NS photodetector and inset shows optical image of Au patterned doped perovskite device. (b) Comparison of I-V characteristics curves of undoped $MAPbBr_3$ NS under dark and 405 nm laser irradiation. (c) Comparison of I-V characterization of Eu0, Eu10 and Eu40. (d) Comparison of I-V characteristics of Eu doped mixed halide NS photodetector under dark and light illumination of different intensities.

diode like rectifying behavior under illumination. Interestingly, high photocurrent at self-biased condition (zero bias) reveals self-powered characteristics of Eu10 confirming stronger intrinsic charge separation in Eu^{3+} doped mixed halide perovskite photodetector. Self-biased and asymmetric I–V behaviors, even under very low intensity are responsible for the enhanced photodetection performance in the doped photodetector device. **Fig. 6.6(a)** shows temporal photoresponse of Eu0 and Eu10 under the bias voltage of −5 V and 405 nm laser excitation

exhibiting dramatic enhancement (~7 times) in photocurrent in Eu doped device compared to that of the undoped one. The presence of small lead halide peak (~12º) in the layered $MAPb_{0.9}Eu_{0.1}Cl_{0.3}Br_{2.7}$ structure is believed to be beneficial to passivate the defects and reduce the electron-hole recombination resulting into high photocurrent[52]. Eu doped mixed halide

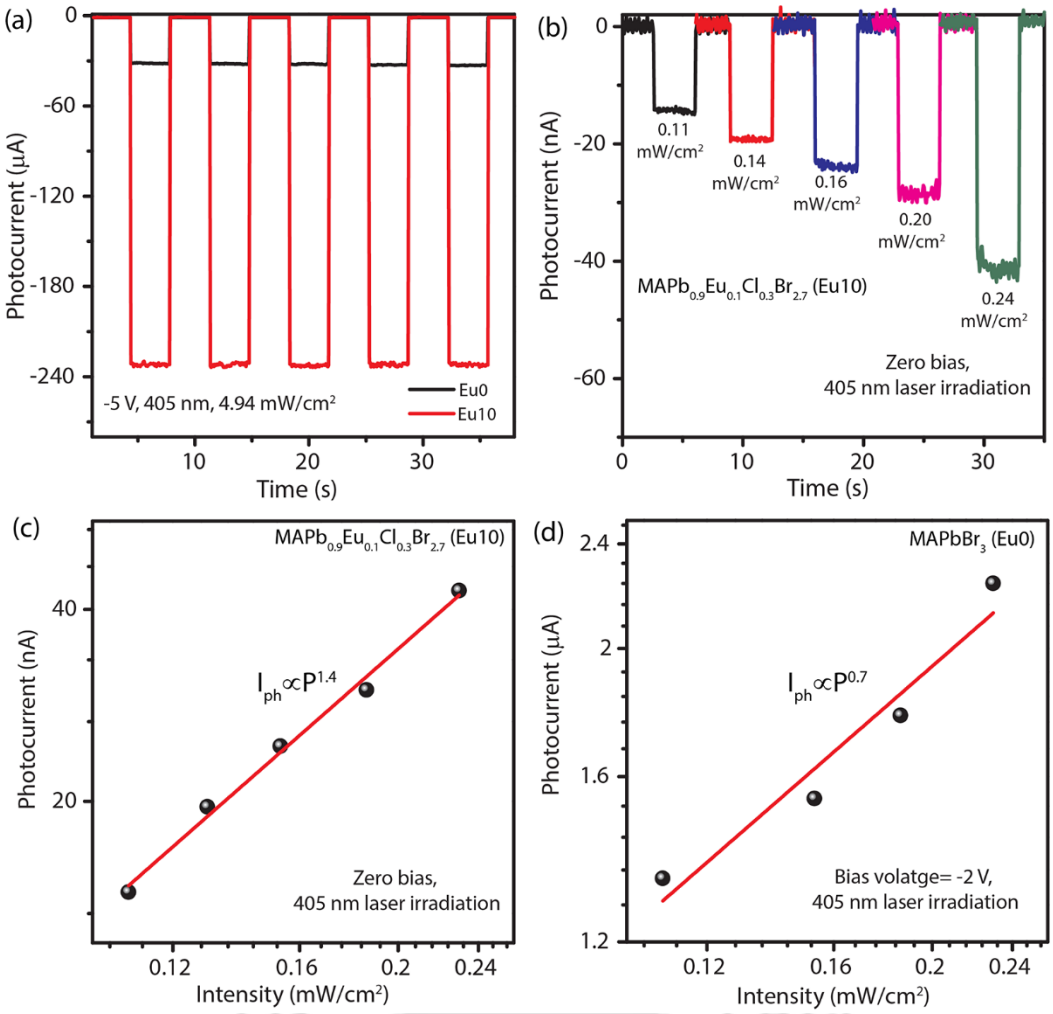

Fig. 6.6. (a) Comparison of time dependent photoresponse of undoped and doped mixed halide perovskite photodetector under 405 nm laser irradiation recorded at −5 V bias voltage. (b) Self biased temporal response of $MAPb_{0.9}Eu_{0.1}Br_{2.7}Cl_{0.3}$ photodetector under 405 nm laser irradiation of various intensities. The logarithmic plot of the photocurrent vs light intensities for (c) Eu10 and (d) Eu0 under bias voltage of 0 V and 2 V, respectively.

photodetector (Eu10) was illuminated with varying intensity of light at a fixed wavelength (405 nm) to understand the photosensitivity of the device at zero bias with the light on and off. The planar device without any heterojunction clearly shows intensity-dependent photocurrent even in self-biased condition, as shown in **Fig. 6.6(b)**, which is significant. Increased photocurrent with

increasing light intensity is produced by the amplified number of photogenerated carriers through the absorption of light. Even at a very low intensity, the Eu doped device shows excellent sensitivity to the incident light and it swiftly changes from high to low resistance condition without much delay demonstrating good photoconductive response. The photogenerated electron-hole pairs get sufficient energy under illumination to drift to the opposite contacts leading to an increase in photocurrent. The self-biased behavior of the photodetector can be extremely beneficial to use in energy-efficient signal receiving devices since it can operate without any extra power supply[53]. The dependence of photocurrent of Eu10 with the intensity of the illuminated light is plotted in a logarithmic curve as shown in **Fig. 6.6(c)** and the data are fitted with the power law[46]: $I_{ph} = AP^{\theta}$, where I_{ph} and P are the photocurrent and incident light power density. While A is the constant and θ determines the response of the photocurrent to light intensity. The fitting of the photocurrent vs intensity graph of doped $MAPb_{0.9}Eu_{0.1}Cl_{0.3}Br_{2.7}$ photodetector in the low power density region (0.11−0.24 mW/cm^2) fits with exponent, θ = 1.4 indicating a highly linear relationship of photogenerated carriers and incident flux. Hence, in the low power density regions, most of the generated carriers are separated without any recombination loss[46]. The linear fitting of the logarithmic plot of photocurrent of undoped $MAPbBr_3$ photodetector vs intensity gives the exponent value of 0.67 (<1), implying that majority of the photogenerated charge carriers are lost due to trapping and recombination (see **Fig. 6.6(d)**). Linear dynamic range (LDR) is calculated to quantitatively understand the sensitivity of the device with increasing intensity using the relation[53]: $LDR = 20log(I_{ph}/I_{dark})$. As the light intensity increases from 0 to 20.04 mW/cm^2, the current in the $MAPb_{0.9}Eu_{0.1}Cl_{0.3}Br_{2.7}$ device increases from 1.12×10^{-10} A to 2.83×10^{-7} A at self-biased condition resulting into a LDR of 68.05.

Fig. 6.7(a) shows the typical temporal response of $MAPb_{0.9}Eu_{0.1}Br_{2.7}Cl_{0.3}$ photodetector under light illumination (4.94 mW/cm^2) and low bias voltages (−0.1 to −1 V). Note that the device exhibits excellent detectivity of light even at low bias voltage due to suppression of trap states and efficient charge extraction. If a large number of trap states exist, the photogenerated electrons may get trapped in the defect states before it could reach to the Au electrodes. When the defects are filled with doped ions, the electrons in the conduction band easily move towards electrodes resulting into the enhancement of the photocurrent[51]. Inset of **Fig. 6.7(a)** shows the variation in photocurrent with bias voltage, indicating nearly exponential increase in photocurrent. The variation in the ratio of photo to dark current as a function of bias voltage is shown in **Fig. 6.7(b)**,

demonstrating a maximum value of ~1.2×10^3 at the self-biased condition, which is comparable to other transport layer free devices[54, 55]. With increasing bias voltage, initially the photocurrent/dark current ratio decreases due to an increase in dark current, however, at higher bias voltage, it again increases since the device gets sufficient energy to extract the photogenerated charge carriers giving rise to very high photocurrent (see **Fig. 6.7(b)**).

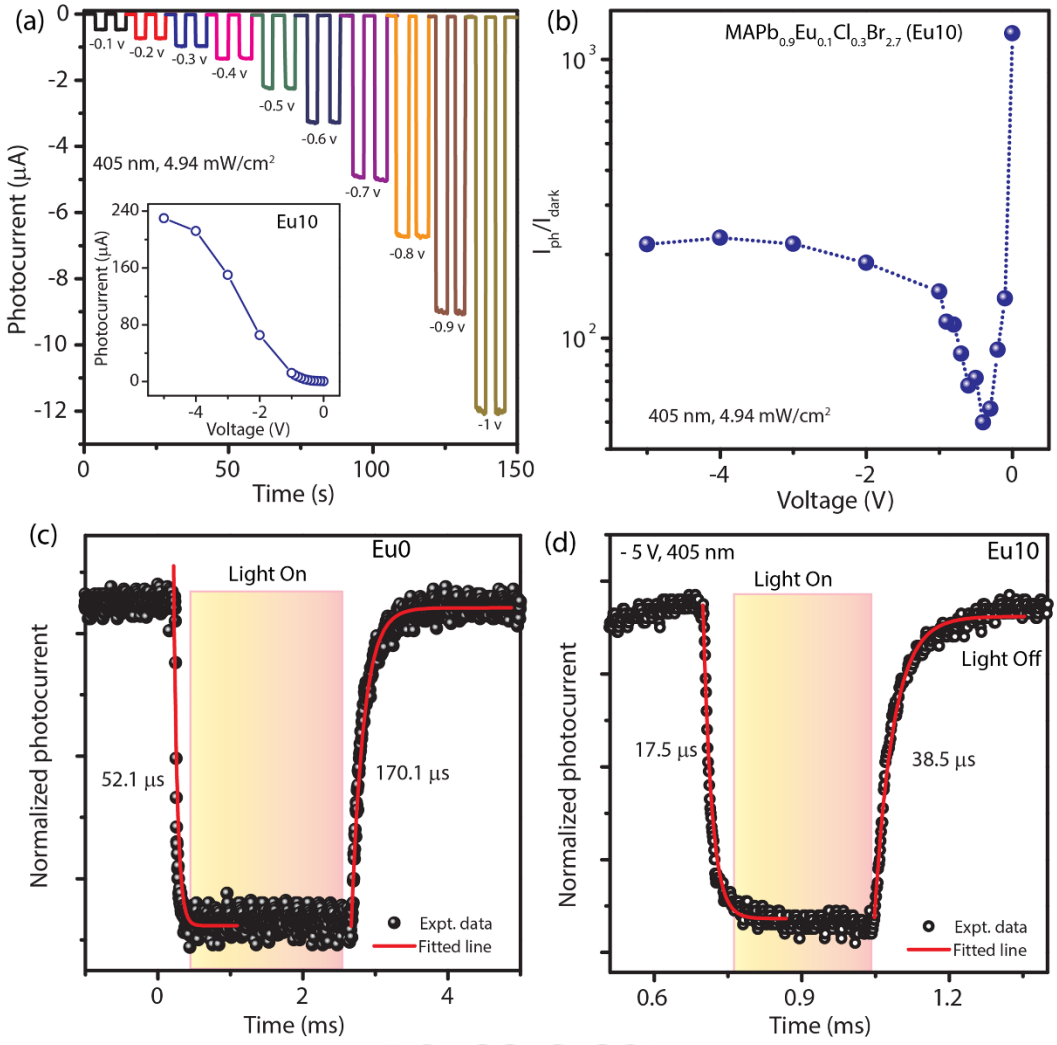

Fig. 6.7. (a) Temporal response of $MAPb_{0.9}Eu_{0.1}Br_{2.7}Cl_{0.3}$ photodetector under 405 nm laser irradiation at various intensities. The inset shows a plot of the photocurrent vs voltage for Eu10 under illumination. (b) Variation of photo/dark current with bias voltage of Eu10. Temporal photoresponses of (c) undoped $MAPbBr_3$ and (d) $EuCl_3$ doped $MAPbBr_3$ photodetectors under −5 V bias voltage with exponential fits.

Note that the temporal response of $MAPb_{0.9}Eu_{0.1}Br_{2.7}Cl_{0.3}$ photodetector demonstrates a very fast sweep under dark to a light condition indicating rapid rise and fall time. Hence, to measure the ultrafast photoresponse of the device, a digital storage oscilloscope was used and the laser source

was modulated up to 20 KHz using a function generator. High-resolution photoresponse curves of pristine $MAPbBr_3$ and $MAPb_{0.9}Eu_{0.1}Cl_{0.3}Br_{2.7}$ photodetectors are shown in **Fig. 6.7(c,d)**, respectively. To estimate the rise and fall times of the devices, the photoresponse curves are fitted with a single exponential function, given by: $I_{ph}(t) = I_0 + Aexp(-t/\tau)$, where I_{ph} is the photocurrent, I_0 and A are the constants and τ is the time constant. From the fitted data, the rise and fall times of undoped $MAPbBr_3$ device are found to be 52.1 µs and 170.1 µs, respectively, as shown in **Fig. 6.7(c)**. In contrast the rise and fall times of doped $MAPb_{0.9}Eu_{0.1}Cl_{0.3}Br_{2.7}$ photodetector are 17.5 µs and 38.5 µs, respectively, indicating good sensitivity of the device to detect high-frequency light signals (see **Fig. 6.7(d)**). Therefore, both the Eu doped and undoped devices exhibit a sharp rise in photocurrent when light is switched on due to quick generation of light-induced carriers followed by the slow decay of photocurrent. However, photocurrent decay is much faster in the doped device. The rise and fall times are observed to be ~3 times and ~4.4 times faster in the doped device than the undoped one due to efficient charge separation and passivation of trap states with the incorporation of lanthanide ion in the perovskite crystal.

It is well-known that the inclusion of moderate dopant concentration in semiconductor increases the mobility of the carriers, space charge and electric field in the Schottky junction allowing efficient transfer of the charge carriers to the opposite electrodes[37]. Here, the inclusion of 10 mol% of $EuCl_3$ in the $MAPbBr_3$ crystal increases the charge density and mobility of the carriers along with the reduction in the probability of trapping and de-trapping of photocarriers during their transfer, which is believed to be contributing to the fast photoresponse of the device. However, at high Eu^{3+} doping concentration, the structural defect-related trap states contribute to the loss of the charge carriers. Also, at higher Eu^{3+} concentration, QDs thickness was too thin to absorb sufficient photons to generate electron-hole pairs without any transport layers and most of the carriers are lost before they could reach the anodes. It is noteworthy that the present $MAPb_{0.9}Eu_{0.1}Br_{2.7}Cl_{0.3}$ photodetector exhibits superior device performance without any charge-transporting layers compared to other p-i-n type perovskite devices reported earlier[56].

The performance of the as-fabricated photodetector is analyzed by calculating the figures of merit of the device, such as responsivity and detectivity in the spectral range 300-800 nm under −5 V bias. The responsivity (R) of a device can be expressed by the following equation: $R = (I_{ph} - I_{dark})/PA$, I_{ph} and I_{dark} are photocurrent and dark current. P and A are incident power

density and the effective area of the device. Eu^{3+} doped mixed halide perovskite shows remarkable photosensitization in the wavelength range of UV to the visible region and shows relatively lower responsivity in the higher wavelength range similar to its absorption behavior, as shown in **Fig. 6.8(a)**. Although responsivity decreases in the high wavelength region, it still shows a good sensitivity in this region. Hence, our doped device shows a typical flat response in the range of 300−540 nm. The $MAPb_{0.9}Eu_{0.1}Br_{2.7}Cl_{0.3}$ photodetector shows maximum responsivity of 5.02 A/W at 480 nm, whereas the responsivity of undoped $MAPbBr_3$ photodetector is found to be 1.13 A/W at 480 nm. Hence, the responsivity of the device is found to be increased by ~4.4 times with the introduction of Eu^{3+} in the mixed halide perovskite lattice. The observed high responsivity in the UV-vis region of the Eu doped device is associated with strong absorption by the sample. The

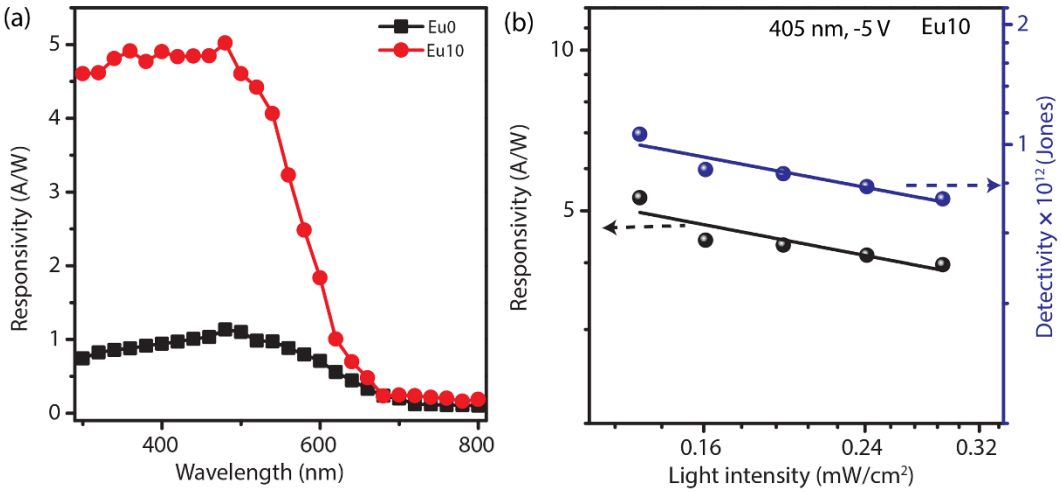

Fig. 6.8. (a) Variation in responsivity with light wavelengths of Eu0 and Eu10 photodetectors under -5 V bias voltage. (b) Variation of spectral responsivity and detectivity with light intensities of $MAPb_{0.9}Eu_{0.1}Br_{2.7}Cl_{0.3}$ photodetector.

variation of responsivity and detectivity of Eu10 with the intensity of 405 nm laser light is shown in **Fig. 6.8(b)**. Interestingly, the extremely high responsivity of 5.29 A/W and detectivity of 1.06×10^{12} Jones are observed in Eu10 under 405 nm laser irradiation, at a low power density of 0.14 mW/cm^2 and a bias voltage of −5 V. Next, the detectivity (D) of the device is calculated using the following relation: $D = R(A/2qI_{dark})^{1/2}$, where q is the electronic charge. The responsivity and detectivity of the device are almost constant over the intensity range of 0.14-0.29 mW/cm^2. A slight decrease in responsivity with increasing power density of occurs due to a higher probability of scattering and recombination of photo-excited charge carriers under the influence of strong illumination[52]. Based on the literature reports it is found that the present Eu doped mixed

Table 6.2. *Summary of the photodetction performance of some reported perovskite devices and the present work.*

Device structure	Bias voltage (V)	I_{light}/I_{dark}	Rise time/Fall time	Responsivity (A/W)	Ref
$MAPbBr_3$ nanowire/Au	1	~62	0.12 /0.086 s	-	[8]
$SiO_2/CsPbCl_3$ NS/Au	8	$\sim10^3$	70/45 ms	-	[54]
$SiO_2/MAPbI_{3-x}Br_x$ film/Au	10	~200	<20/20 µs	0.055	[57]
$SiO_2/CH_3NH_3PbI_{3-x}Cl_x$-$CsPbBr_3$/Au	1	~3	121/107 µs	0.39	[58]
Glass/TiO_2/$MAPbIBr_2$ film/Al	5	~1600	0.66/0.58 s	0.70	[59]
FTO/$CH_3NH_3PbI_3/TiO_2$	3	~70	0.02/0.02 s	0.49×10^{-6}	[60]
SiO_2/ $MAPb_{0.9}Eu_{0.1}Br_{2.7}Cl_{0.3}$/Au	0	~1200	17.5/38.5 µs	5.02	This work

halide perovskite photodetector exhibits comparable or even superior performance in comparison to other perovskite based devices of similar structure, as summarized in **Table 6.2**.

The operational stability and sustainability of the Eu doped mixed halide perovskite photodetector are also studied to assess its efficacy in practical application. The photocurrent of the device is

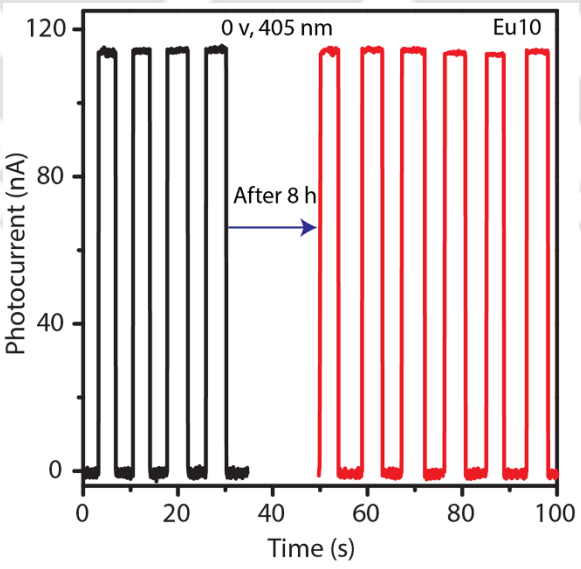

Fig. 6.9. Comparison of temporal response of Eu doped mixed halide perovskite photodetector before and after continuous operation of 8 h.

observed to be constant at zero bias condition even after continuous operation for 8h, as shown in **Fig. 6.9**, demonstrating excellent photostability and long-term operational stability with good repeatability. Further, the storage stability of the device is also studied since ambient stability is a major issue for perovskite-based devices. *I*−*V* characteristic curve of the Eu doped device was almost unchanged after storing it for one month in a desiccator without any encapsulation, which may be due to passivation of Br vacancy by Cl and improved structural stability (See **Fig. 6.10(a)**).

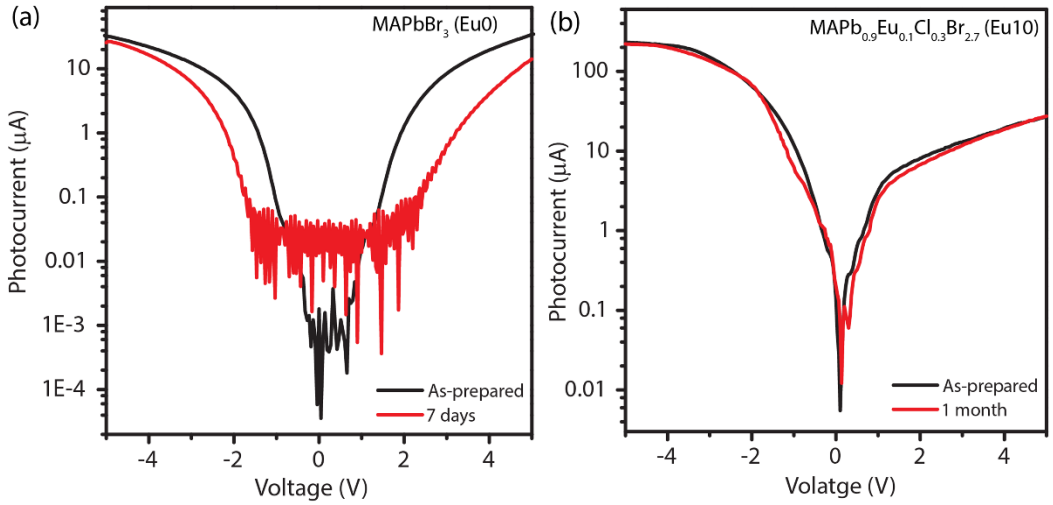

Fig. 6.10. (a) Comparison of I-V characteristics of freshly prepared Eu0 photodetector and after storing it for 7 days. (b) Comparison of I-V characteristics of freshly prepared Eu10 photodetector and after storing it for one month.

In contrast, a substantial decrease in photocurrent is observed in the *I*−*V* characteristic of the undoped $MAPbBr_3$ photodetector after 7 days (see **Fig. 6.10(b)**). In general, interface degradation occurs fast in device structure and intrinsic degradation of the active material affects the device slowly[3, 52]. Here, the enhanced structural stability by the inclusion of a small amount of Eu^{3+} in the 2D perovskite increases the overall structural stability of the doped device, which prevents the moisture ingress into the lattice. Thus, enhanced photo, operational and storage stability of the Eu doped mixed halide perovskite photodetector signify its suitability for outdoor applications such as on windows, clothes and human skin[61].

6.5. Summary and Conclusions

In this chapter, we have successfully developed Eu doped mixed halide 2D perovskite NS using a solvothermal route and expanded the family of doped perovskite for high-quality photodetection application. Further, we have fabricated a self-biased photodetector using $MAPb_{0.9}Eu_{0.1}Br_{2.7}Cl_{0.3}$

by taking advantage of high absorbance and improved charge separation in 10 mol% Eu doped 2D NS. Our findings stimulate further investigation and application of Eu^{3+} doped 2D perovskite NS in the field of optoelectronics and photovoltaics devices. The key findings of the chapter are summarized below.

1. Inclusion of Eu^{3+} ion in the $MAPbBr_3$ perovskite crystal allowed tuning of the lateral size and thickness of the NS and at 60 mol% $EuCl_3$ concentration, monolayer mixed halide perovskite QDs are obtained.
2. Characteristic 2D diffraction peaks at low angles are observed due to the formation of a uniform 2D layered structure. Lattice contraction with increasing doping concentration indicates partial substitution of Pb and Br ions by Eu and Cl ions, respectively.
3. The PL peak and excitonic absorption peak are systematically blue-shifted with increasing Eu doping concentration due to the quantum confinement effect.
4. Interestingly, Eu doped mixed halide perovskite photodetector exhibits self-biased behavior with photocurrent to dark current ratio of ~10^3, while the turn-on voltage of undoped device is −0.4 V.
5. Photo responsivity of the $MAPb_{0.9}Eu_{0.1}Br_{2.7}Cl_{0.3}$ photodetector is found to be 5.02 A/W at 480 nm light illumination, which is ~4.4 times higher than the undoped counterpart.
6. From the temporal photoresponse, the rise and fall times of the Eu doped device are calculated to be 17.5 and 38.5 µs, respectively, which puts the device among the fastest mixed halide perovskite photodetectors reported till date.
7. Enhanced performance of the Eu doped perovskite photodetector is due to the decrease in trap density and efficient transfer of photogenerated carriers.
8. The doped device shows excellent photo, operational and storage stability by keeping its photodetection ability unaltered for one month due to increased intrinsic stability with the introduction of a small amount of Eu^{3+} ion in the perovskite crystal.

References

[1] A. Kojima, K. Teshima, Y. Shirai, T. Miyasaka, Organometal halide perovskites as visible-light sensitizers for photovoltaic cells, J. Am. Chem. Soc., 131 (2009) 6050-6051.
[2] H.-S. Kim, C.-R. Lee, J.-H. Im, K.-B. Lee, T. Moehl, A. Marchioro, S.-J. Moon, R. Humphry-Baker, J.-H. Yum, J.E. Moser, Lead iodide perovskite sensitized all-solid-state submicron thin film mesoscopic solar cell with efficiency exceeding 9%, Sci. Rep., 2 (2012) 591.
[3] A. Turak, Interfacial Degradation in Organic Optoelectronics, RSC Adv., 3 (2013) 6188-6225.
[4] S.T. Ha, X. Liu, Q. Zhang, D. Giovanni, T.C. Sum, Q. Xiong, Synthesis of Organic–Inorganic Lead Halide Perovskite Nanoplatelets: Towards High-Performance Perovskite Solar Cells and Optoelectronic Devices, Adv. Opt. Mater, 2 (2014) 838-844.
[5] C.S. Ponseca Jr, T.J. Savenije, M. Abdellah, K. Zheng, A. Yartsev, T.r. Pascher, T. Harlang, P. Chabera, T. Pullerits, A. Stepanov, Organometal halide perovskite solar cell materials rationalized: ultrafast charge generation, high and microsecond-long balanced mobilities, and slow recombination, J. Am. Chem. Soc., 136 (2014) 5189-5192.
[6] Z.-K. Tan, R.S. Moghaddam, M.L. Lai, P. Docampo, R. Higler, F. Deschler, M. Price, A. Sadhanala, L.M. Pazos, D. Credgington, F. Hanusch, T. Bein, H.J. Snaith, R.H. Friend, Bright Light-Emitting Diodes Based on Organometal Halide Perovskite, Nat Nanotechnol., 9 (2014) 687.
[7] Y.H. Kim, H. Cho, J.H. Heo, T.S. Kim, N. Myoung, C.L. Lee, S.H. Im, T.W. Lee, Multicolored Organic/Inorganic Hybrid Perovskite Light-Emitting Diodes, Adv. Mater., 27 (2015) 1248-1254.
[8] S. Zhuo, J. Zhang, Y. Shi, Y. Huang, B. Zhang, Self-Template-Directed Synthesis of Porous Perovskite Nanowires at Room Temperature for High-Performance Visible-Light Photodetectors, Angew. Chem. Int. Ed., 54 (2015) 5693-5696.
[9] H. Lu, W. Tian, F. Cao, Y. Ma, B. Gu, L. Li, A Self-Powered and Stable All-Perovskite Photodetector–Solar Cell Nanosystem, Adv. Funct. Mater., 26 (2016) 1296-1302.
[10] S.I. Seok, M. Grätzel, N.-G. Park, Methodologies toward Highly Efficient Perovskite Solar Cells, Small, 14 (2018) 1704177.
[11] J.-S. Yao, J. Ge, B.-N. Han, K.-H. Wang, H.-B. Yao, H.-L. Yu, J.-H. Li, B.-S. Zhu, J.-Z. Song, C. Chen, Q. Zhang, H.-B. Zeng, Y. Luo, S.-H. Yu, Ce3+-Doping to Modulate Photoluminescence Kinetics for Efficient CsPbBr3 Nanocrystals Based Light-Emitting Diodes, J. Am. Chem. Soc., 140 (2018) 3626-3634.
[12] X. Tang, W. Chen, Z. Liu, J. Du, Z. Yao, Y. Huang, C. Chen, Z. Yang, T. Shi, W. Hu, Z. Zang, Y. Chen, Y. Leng, Ultrathin, Core–Shell Structured SiO2 Coated Mn2+-Doped Perovskite Quantum Dots for Bright White Light-Emitting Diodes, Small, 15 (2019) 1900484.
[13] W.S. Subhani, K. Wang, M. Du, X. Wang, N. Yuan, J. Ding, S. Liu, Anti-Solvent Engineering for Efficient Semitransparent CH3NH3PbBr3 Perovskite Solar Cells for Greenhouse Applications, J ENERGY CHEM, 34 (2019) 12-19.
[14] Y. Zheng, T. Niu, X. Ran, J. Qiu, B. Li, Y. Xia, Y. Chen, W. Huang, Unique Characteristics Of 2d Ruddlesden–Popper (2drp) Perovskite For Future Photovoltaic Application, J. Mater. Chem. A, 7 (2019) 13860-13872.
[15] S.D. Stranks, G.E. Eperon, G. Grancini, C. Menelaou, M.J. Alcocer, T. Leijtens, L.M. Herz, A. Petrozza, H.J. Snaith, Electron-hole diffusion lengths exceeding 1 micrometer in an organometal trihalide perovskite absorber, Science, 342 (2013) 341-344.
[16] A. Kojima, M. Ikegami, K. Teshima, T. Miyasaka, Highly Luminescent Lead Bromide Perovskite Nanoparticles Synthesized with Porous Alumina Media, Chem. Lett., 41 (2012) 397-399.
[17] G. Xing, N. Mathews, S. Sun, S.S. Lim, Y.M. Lam, M. Grätzel, S. Mhaisalkar, T.C. Sum, Long-Range Balanced Electron-and Hole-Transport Lengths in Organic-Inorganic CH3NH3PbI3, Science, 342 (2013) 344-347.

[18] C. Wehrenfennig, G.E. Eperon, M.B. Johnston, H.J. Snaith, L.M. Herz, High charge carrier mobilities and lifetimes in organolead trihalide perovskites, Adv. Mater., 26 (2014) 1584-1589.
[19] K. Wu, A. Bera, C. Ma, Y. Du, Y. Yang, L. Li, T. Wu, Temperature-dependent excitonic photoluminescence of hybrid organometal halide perovskite films, Phys. Chem. Chem. Phys., 16 (2014) 22476-22481.
[20] M. Zhang, H. Yu, M. Lyu, Q. Wang, J.-H. Yun, L. Wang, Composition-dependent photoluminescence intensity and prolonged recombination lifetime of perovskite CH3NH3PbBr3−xClx films, Chem. Commun., 50 (2014) 11727-11730.
[21] A. Miyata, A. Mitioglu, P. Plochocka, O. Portugall, J.T.-W. Wang, S.D. Stranks, H.J. Snaith, R.J. Nicholas, Direct measurement of the exciton binding energy and effective masses for charge carriers in organic–inorganic tri-halide perovskites, Nat. Phys., 11 (2015) 582.
[22] F. Zhang, H. Zhong, C. Chen, X.-g. Wu, X. Hu, H. Huang, J. Han, B. Zou, Y. Dong, Brightly Luminescent and Color-Tunable Colloidal CH3NH3PbX3 (X= Br, I, Cl) Quantum Dots: Potential Alternatives for Display Technology, ACS nano, 9 (2015) 4533-4542.
[23] H. Zhu, Y. Fu, F. Meng, X. Wu, Z. Gong, Q. Ding, M.V. Gustafsson, M.T. Trinh, S. Jin, X.Y. Zhu, Lead Halide Perovskite Nanowire Lasers with Low Lasing Thresholds and High Quality Factors, Nat. Mater, 14 (2015) 636-642.
[24] S. Parveen, K.K. Paul, R. Das, P.K. Giri, Large Exciton Binding Energy, High Photoluminescence Quantum Yield and Improved Photostability of Organo-Metal Halide Hybrid Perovskite Quantum Dots Grown on a Mesoporous Titanium Dioxide Template, J. Colloid Interface Sci., 539 (2019) 619-633.
[25] D. Aldakov, P. Reiss, Safer-by-Design Fluorescent Nanocrystals: Metal Halide Perovskites vs Semiconductor Quantum Dots, J. Phys. Chem. C, 123 (2019) 12527-12541.
[26] M. Saliba, T. Matsui, K. Domanski, J.-Y. Seo, A. Ummadisingu, S.M. Zakeeruddin, J.-P. Correa-Baena, W.R. Tress, A. Abate, A. Hagfeldt, M. Grätzel, Incorporation of Rubidium Cations into Perovskite Solar Cells Improves Photovoltaic Performance, Science, 354 (2016) 206.
[27] J. Sun, J. Yang, J.I. Lee, J.H. Cho, M.S. Kang, Lead-Free Perovskite Nanocrystals for Light-Emitting Devices, J. Phys. Chem. Lett., 9 (2018) 1573-1583.
[28] T.C. Jellicoe, J.M. Richter, H.F.J. Glass, M. Tabachnyk, R. Brady, S.E. Dutton, A. Rao, R.H. Friend, D. Credgington, N.C. Greenham, M.L. Böhm, Synthesis and Optical Properties of Lead-Free Cesium Tin Halide Perovskite Nanocrystals, J. Am. Chem. Soc., 138 (2016) 2941-2944.
[29] M. Leng, Z. Chen, Y. Yang, Z. Li, K. Zeng, K. Li, G. Niu, Y. He, Q. Zhou, J. Tang, Lead-Free, Blue Emitting Bismuth Halide Perovskite Quantum Dots, Angew. Chem. Int. Ed., 55 (2016) 15012-15016.
[30] J. Zhang, Y. Yang, H. Deng, U. Farooq, X. Yang, J. Khan, J. Tang, H. Song, High Quantum Yield Blue Emission from Lead-Free Inorganic Antimony Halide Perovskite Colloidal Quantum Dots, ACS Nano, 11 (2017) 9294-9302.
[31] W.J. Mir, T. Sheikh, H. Arfin, Z. Xia, A. Nag, Lanthanide Doping in Metal Halide Perovskite Nanocrystals: Spectral Shifting, Quantum Cutting and Optoelectronic Applications, NPG Asia Mater, 12 (2020) 9.
[32] G. Pan, X. Bai, D. Yang, X. Chen, P. Jing, S. Qu, L. Zhang, D. Zhou, J. Zhu, W. Xu, B. Dong, H. Song, Doping Lanthanide into Perovskite Nanocrystals: Highly Improved and Expanded Optical Properties, Nano Lett., 17 (2017) 8005-8011.
[33] J. Duan, Y. Zhao, X. Yang, Y. Wang, B. He, Q. Tang, Lanthanide Ions Doped CsPbBr3 Halides for HTM-Free 10.14%-Efficiency Inorganic Perovskite Solar Cell with an Ultrahigh Open-Circuit Voltage of 1.594 V, Adv. Energy Mater., 8 (2018) 1802346.
[34] K. Wang, L. Zheng, T. Zhu, X. Yao, C. Yi, X. Zhang, Y. Cao, L. Liu, W. Hu, X. Gong, Efficient Perovskite Solar Cells by Hybrid Perovskites Incorporated with Heterovalent Neodymium Cations, Nano Energy, 61 (2019) 352-360.

[35] L. Wang, H. Zhou, J. Hu, B. Huang, M. Sun, B. Dong, G. Zheng, Y. Huang, Y. Chen, L. Li, Z. Xu, N. Li, Z. Liu, Q. Chen, L.-D. Sun, C.-H. Yan, A Eu3+-Eu2+ Ion Redox Shuttle Imparts Operational Durability to Pb-I Perovskite Solar Cells, Science, 363 (2019) 265.
[36] D. Zhou, D. Liu, G. Pan, X. Chen, D. Li, W. Xu, X. Bai, H. Song, Cerium and Ytterbium Codoped Halide Perovskite Quantum Dots: A Novel and Efficient Downconverter for Improving the Performance of Silicon Solar Cells, Adv. Mater., 29 (2017) 1704149.
[37] X. Wu, H. Li, K. Wang, X. Sun, L. Wang, CH3NH3Pb1−xEuxI3 mixed halide perovskite for hybrid solar cells: the impact of divalent europium doping on efficiency and stability, RSC Advances, 8 (2018) 11095-11101.
[38] S.K. Karunakaran, G.M. Arumugam, W. Yang, S. Ge, S.N. Khan, Y. Mai, X. Lin, G. Yang, Europium (II)-Doped All-Inorganic CsPbBr3 Perovskite Solar Cells with Carbon Electrodes, Sol. RRL., n/a (2020) 2000390.
[39] S. Yang, H. Zhao, Y. Han, C. Duan, Z. Liu, S. Liu, Europium and Acetate Co-doping Strategy for Developing Stable and Efficient CsPbI2Br Perovskite Solar Cells, Small, 15 (2019) 1904387.
[40] W. Xiang, Z. Wang, D.J. Kubicki, W. Tress, J. Luo, D. Prochowicz, S. Akin, L. Emsley, J. Zhou, G. Dietler, M. Grätzel, A. Hagfeldt, Europium-Doped CsPbI2Br for Stable and Highly Efficient Inorganic Perovskite Solar Cells, Joule, 3 (2019) 205-214.
[41] Q. Li, Y. Liu, P. Chen, J. Hou, Y. Sun, G. Zhao, N. Zhang, J. Zou, J. Xu, Y. Fang, N. Dai, Excitonic Luminescence Engineering in Tervalent-Europium-Doped Cesium Lead Halide Perovskite Nanocrystals and Their Temperature-Dependent Energy Transfer Emission Properties, J. Phys. Chem. C, 122 (2018) 29044-29050.
[42] F. Alam, K.D. Wegner, S. Pouget, L. Amidani, K. Kvashnina, D. Aldakov, P. Reiss, Eu2+: A Suitable Substituent for Pb2+ in CsPbX3 Perovskite Nanocrystals?, J. Chem. Phys., 151 (2019) 231101.
[43] J. Huang, T. Lei, M. Siron, Y. Zhang, S. Yu, F. Seeler, A. Dehestani, L.N. Quan, K. Schierle-Arndt, P. Yang, Lead-free Cesium Europium Halide Perovskite Nanocrystals, Nano Lett., 20 (2020) 3734-3739.
[44] Y. Cheng, C. Shen, L. Shen, W. Xiang, X. Liang, Tb3+, Eu3+ Co-doped CsPbBr3 QDs Glass with Highly Stable and Luminous Adjustable for White LEDs, ACS Appl. Mater. Interfaces, 10 (2018) 21434-21444.
[45] N. Ding, D. Zhou, G. Pan, W. Xu, X. Chen, D. Li, X. Zhang, J. Zhu, Y. Ji, H. Song, Europium-Doped Lead-Free Cs3Bi2Br9 Perovskite Quantum Dots and Ultrasensitive Cu2+ Detection, ACS Sustainable Chem. Eng. , 7 (2019) 8397-8404.
[46] S. Parveen, K.K. Paul, P.K. Giri, Precise Tuning of the Thickness and Optical Properties of Highly Stable 2D Organometal Halide Perovskite Nanosheets through a Solvothermal Process and Their Applications as a White LED and a Fast Photodetector, ACS Appl. Mater. Interfaces, 12 (2020) 6283-6297.
[47] L. Zhang, T. Jiang, C. Yi, J. Wu, X.-K. Liu, Y. He, Y. Miao, Y. Zhang, H. Zhang, X. Xie, P. Wang, R. Li, F. Gao, W. Huang, J. Wang, Bright Free Exciton Electroluminescence from Mn-Doped Two-Dimensional Layered Perovskites, J. Phys. Chem. Lett., 10 (2019) 3171-3175.
[48] L. Protesescu, S. Yakunin, M.I. Bodnarchuk, F. Krieg, R. Caputo, C.H. Hendon, R.X. Yang, A. Walsh, M.V. Kovalenko, Nanocrystals of cesium lead halide perovskites (CsPbX3, X= Cl, Br, and I): novel optoelectronic materials showing bright emission with wide color gamut, Nano Lett., 15 (2015) 3692-3696.
[49] H. Wang, J.W. Lim, L.N. Quan, K. Chung, Y.J. Jang, Y. Ma, D.H. Kim, Perovskite–Gold Nanorod Hybrid Photodetector with High Responsivity and Low Driving Voltage, Adv. Opt. Mater., 6 (2018) 1701397.
[50] P. Chen, Z. Wang, S. Wang, M. Lyu, M. Hao, M. Ghasemi, M. Xiao, J.-H. Yun, Y. Bai, L. Wang, Luminescent Europium-Doped Titania for Efficiency and Uv-Stability Enhancement of Planar Perovskite Solar Cells, Nano Energy, 69 (2020) 104392.
[51] K. Patel, P. Chauhan, A.B. Patel, G.K. Solanki, K.D. Patel, V.M. Pathak, Orthorhombic SnSe Nanocrystals for Visible-Light Photodetectors, ACS Appl. Nano Mater. , (2020).
[52] S. Tong, C. Gong, C. Zhang, G. Liu, D. Zhang, C. Zhou, J. Sun, S. Xiao, J. He, Y. Gao, J. Yang, Fully-Printed, Flexible Cesium-Doped Triple Cation Perovskite Photodetector, Appl. Mater. Today, 15 (2019) 389-397.

[53] R. Liu, J. Zhang, H. Zhou, Z. Song, Z. Song, C.R. Grice, D. Wu, L. Shen, H. Wang, Solution-Processed High-Quality Cesium Lead Bromine Perovskite Photodetectors with High Detectivity for Application in Visible Light Communication, Adv. Optical Mater., 8 (2020) 1901735.
[54] W. Zhai, J. Lin, C. Li, S. Hu, Y. Huang, C. Yu, Z. Wen, Z. Liu, Y. Fang, C. Tang, Solvothermal Synthesis of Cesium Lead Halide Perovskite Nanowires with Ultra-High Aspect Ratios for High-Performance Photodetectors, Nanoscale, 10 (2018) 21451-21458.
[55] Y. Li, Z. Shi, L. Lei, F. Zhang, Z. Ma, D. Wu, T. Xu, Y. Tian, Y. Zhang, G. Du, C. Shan, X. Li, Highly Stable Perovskite Photodetector Based on Vapor-Processed Micrometer-Scale CsPbBr3 Microplatelets, Chem. Mater., 30 (2018) 6744-6755.
[56] J. Miao, F. Zhang, Recent Progress on Highly Sensitive Perovskite Photodetectors, J. Mater. Chem. C, 7 (2019) 1741-1791.
[57] F. Wang, J. Mei, Y. Wang, L. Zhang, H. Zhao, D. Zhao, Fast Photoconductive Responses in Organometal Halide Perovskite Photodetectors, ACS Appl. Mater. Interfaces, 8 (2016) 2840-2846.
[58] Y. Yang, H. Dai, F. Yang, Y. Zhang, D. Luo, X. Zhang, K. Wang, X.W. Sun, J. Yao, All-Perovskite Photodetector with Fast Response, Nanoscale Res Lett, 14 (2019) 291.
[59] K. Abbas Ahmad, Y. Zhinong, K. Ubaid, L. Yan, E. Deborah, Solution-processed photodetector based on Br incorporated perovskite materials, in: Proc.SPIE, 2019.
[60] H.-R. Xia, J. Li, W.-T. Sun, L.-M. Peng, Organohalide Lead Perovskite Based Photodetectors with Much Enhanced Performance, Chem. Commun., 50 (2014) 13695-13697.
[61] S.V.N. Pammi, V.-D. Tran, R. Maddaka, J.-H. Eom, J.S. Jung, H.-M. Jeong, M.-D. Kim, V. Pecunia, S.G. Yoon, Bromine Doping of MAPbI3 Films Deposited via Chemical Vapor Deposition Enables Efficient and Photo-Stable Self-Powered Photodetectors, Adv. Optical Mater., 8 (2020) 2000845.

Chapter 7

Summary and Outlook

In this chapter, an overview of the contributions of the present thesis and highlights of the important findings are presented. At the end, outlooks and future scopes are discussed.

7.1. Summary and Highlights of the Thesis Contribution

In this dissertation, at first the growth kinetics and scaling behavior of vacuum deposited $CH_3NH_3PbBr_3$ ($MAPbBr_3$) thin film on ITO coated glass and SiO_2 substrates are presented, and the scaling exponents are correlated with its microstructural and optical properties **(Chapter 2)**. Next, we have demonstrated a novel synthetic route for the template-assisted growth of size tunable perovskite quantum dots (QDs) exhibiting large exciton binding energy, high photoluminescence (PL) quantum yield (QY) and improved photostability **(Chapter 3)**. Next, a novel, highly reproducible and facile solvothermal route is implemented to synthesize and tailor the thickness and optical band gap of $MAPbBr_3$ perovskite nanosheets (NSs) and these are explored for the application as white light converter and high-speed photodetector **(Chapter 4)**. Next, the solvothermally synthesized 2D $MAPbBr_3$ NSs were doped at high concentration with Ce^{3+} and Tb^{3+} to achieve stable and deep blue emission with absolute unity PL QY and density functional theory (DFT) based calculations was used to disclose the origin of large blue shift and high PL QY in the doped NSs **(Chapter 5)**. Finally, the 2D $MAPbBr_3$ NSs are doped with europium chloride to fabricate a high performance self-biased, stable mixed halide perovskite NS photodetector **(Chapter 6)**.

The major contributions of the present thesis are summarized below.

A. Growth Kinetics of vacuum deposited $MAPbBr_3$ thin film

First, we have studied the controlled growth of vacuum deposited 3D $MAPbBr_3$ thin film and its structural evolution on SiO_2 and ITO substrates at various substrate temperatures (25–100 °C) and various thicknesses (4–120 nm). The growth kinetics of perovskite thin film is evaluated with the help of scaling parameters using atomic force microscopy (AFM), height-height correlation function (HHCF), X-ray diffraction, UV-vis absorption and photoluminescence analyses. The

perovskite films exhibit an anomalous scaling behavior for film thickness (d) less than 40 nm, and a stable growth for, d≥40 nm. Interestingly, the growth exponent (β) is distinctly different, ~0.22 and ~0.90, for the films on ITO and SiO_2 substrates, respectively. For the first time, we have investigated the substrate temperature dependent growth front scaling parameters for perovskite thin film in the temperature range 50–100 °C and activation energies are calculated to be 0.10 eV and 0.15 eV for the film on ITO and SiO_2 substrates, respectively, which implies an easier diffusion of molecules and smooth film in case of ITO substrate. The film on SiO_2 substrate deviates from the conventional scaling law and that on ITO substrate reveals higher crystallinity and high PL intensity. At lower thicknesses, we observe a thickness dependent blue shift in the absorption and emission edge, due to the lattice expansion. The low-temperature PL analysis shows high exciton binding energy supporting a strong PL. Interestingly, the vacuum deposited films exhibit high stability under prolonged laser irradiation. These findings provide new insights on the growth kinetics and optimum conditions for the vacuum deposition of hybrid perovskite thin films of ultralow thickness. This work has been published in "*Applied Surface Science 530 (2020) 147224".*

B. Mesoporous TiO_2 Template Assisted Growth of $MAPbX_3$ QDs Exhibiting High PL QY and Improved Photostability

We have developed a novel synthetic route for the template assisted growth of size tunable perovskite ($MAPbBr_3$ and $MAPbI_3$) QDs. Fluorine doped mesoporous TiO_2 template acts as a template and the nucleation site for the growth of perovskite QDs. The pore size in TiO_2 template is tuned by varying the hydrofluoric acid molar concentration during its solvothermal growth and size of the perovskite QDs embedded in TiO_2 pores is tuned in the range of 1.7-5.1 nm. $MAPbI_3$ QD with average size ~1.7 nm exhibits ~47 nm blue shift in the PL spectra, ~43 fold enhancement in PL intensity and ~25 % PL QY. On the other hand, $MAPbBr_3$ QD of similar size exhibits dramatically enhanced (~124 times) PL emission with narrow band and PL QY of ~57 %. The optical tunability of the QDs is quantitatively discussed with the help of Brus equation, confirming strong confinement effect. Interestingly, the embedded QDs exhibit very high exciton binding energy (162–272 meV) as compared to that of the bulk film (32 meV) due to high effective dielectric constant, and high electron-hole recombination probability in the QDs. The perovskite QDs embedded in porous TiO_2 template show very high photostability up to several hours (≥10 h)

under the UV laser exposure (18 mW), while that of bulk film decreases by >33 %. High photostability of perovskite QDs inferred to the partial coverage of the QDs by TiO_2 nanocrystals, which restrict complete exposure to external environment. This work has been published in "*J. Colloids & Inter. Sci. 539, 619 (2019)".*

C. Solvothermal Synthesis of Shape Tailored 2D $MAPbBr_3$ Nanostructures for White LED and Photodetector Applications

We have developed a novel, highly reproducible and facile solvothermal route to tailor the morphology, thickness and optical bandgap of 2D perovskite nanosheets. In contrast to the time consuming and tedious methods reported mostly for inorganic perovskites, we have demonstrated a precise control of the thickness of 2D $MAPbBr_3$ perovskite layer from 14 to 2 layers simply by tuning the reaction temperature of the solvothermal process. The growth mechanism of the NS is qualitatively discussed based on the classical theory of nucleation growth. The bandgap of the perovskite NS was tuned over ~200 meV from green luminescent nanorods to cyan luminescent 2D QDs owing to strong quantum confinement effect. The 2D perovskite NS and QDs exhibit high PL QYs of 77.6 % and 84.5 %, respectively. A white light converter is demonstrated by using orange luminescent $MAPbBr_1I_2$ nanostructure on a blue LED chip. Also, The 2D perovskite photodetector was fabricated exhibiting fast rise/fall time (24 μs/103 μs) along with high responsivity and detectivity of ~ 1.93 A/W and 1.04×10^{12} Jones, respectively. This method is very versatile and appealing for controlled synthesis of the large area, stable perovskite 2D layers for cutting edge optoelectronic and imaging applications. This work has been published in "*ACS Appl. Mater. Interfaces, 12, 5, 6283-6297 (2020)".*

D. Rare-Earth Ion Doped 2D $MAPbBr_3$ Perovskite Nanosheet as Bright, High Color Purity Deep Blue Emitter with Unity Quantum Yield

We have achieved rare-earth doped 2D perovskite NS through our newly developed solvothermal route to tune its optoelectronic properties. Two-dimensional layered structure of the $MAPbBr_3$ NS allows easy, effortless substitution of the rare-earth dopant ions, Ce^{3+} and Tb^{3+}. The thickness of the NS is tuned from 8.4 nm to 1.6 nm by increasing doping concentration from 0 to 70 mol%, respectively. Interestingly, pure layered structure is observed with doping as confirmed by the presence of characteristic X-ray diffraction peaks at low angles ($2\theta<14.81^{o}$). The excitonic

absorption peak of the 2D NS is tuned by 42 nm and 86 nm to the deep blue region with Ce^{3+} and Tb^{3+} doping, respectively. With Ce doping at high concentration, we achieved a deep blue emitting NSs with 100 % QY, narrow linewidth (~24 nm), and a color coordinate of (0.145, 0.054) closely matching with the standard color Rec. 2020 (0.131, 0.046) specification, making it one of the most efficient perovskite blue light emitters reported to date. Interestingly, multiple PL peaks appear at low temperature due to the coexistence of ordered and disordered orthorhombic phases, as layered structure allows easy orientation under environmental change. High PL QY and large blue shift with Ce and Tb doping in 2D perovskite was explained using DFT based calculation of its electronic structure. Finally, the Ce^{3+} doped $MAPbBr_3$ blue-emitting NSs were utilized to demonstrate an efficient white light LED with CIE coordinates (0.334, 0.326) for their practical application in solid-state lightning. This work has been published in *"J. Mater. Chem. C, 2021,9, 2437-2454"*.

E. Fabrication of Self-biased, Highly Sensitive and Fast Europium Doped $MAPbBr_3$ Photodetector

Next, we have demonstrated high performance europium chloride ($EuCl_3$) doped 2D $MAPbBr_3$ perovskite NS photodetectors. The morphology of 2D $MAPbBr_3$ perovskite is tuned from 10 layer NS to monolayer QDs with increasing Eu^{3+} doping concentration as confirmed using TEM and AFM analyses. Characteristic 2D diffraction peaks is observed in the low diffraction angle ($2\theta<14^{o}$) in the doped sample indicating the formation of pure 2D structure. Bandgap of the Eu doped mixed halide perovskite NS is tuned by 0.595 eV due to strong quantum confinement effect and replacement of Br by Cl. Finally, we have fabricated europium doped perovskite photodetector and the device performance is compared with the undoped $MAPbBr_3$ photodetector. The $MAPb_{0.9}Eu_{0.1}Cl_{0.3}Br_{2.7}$ photodetector shows a higher photodetection performance compared to the pristine $MAPbBr_3$ counterpart. $MAPb_{0.9}Eu_{0.1}Cl_{0.3}Br_{2.7}$ photodetector exhibits self-biased behavior with high switching ratio of ~10^3, whereas turn on voltage of pristine $MAPbBr_3$ photodetector is ~-0.4 V. The response rise and fall times of $MAPb_{0.9}Eu_{0.1}Cl_{0.3}Br_{2.7}$ photodetector are reduced to 17.5 µs and 38.5 µs, respectively, from 52.1 µs and 170.1 µs of the pristine $MAPbBr_3$ photodetector due to efficient charge separation and passivation of trap states with the introduction of Eu ion in the perovskite crystal. Eu doped mixed halide perovskite photodetector shows high responsivity (5.29 A/W) under 405 nm laser irradiation. Therefore, employing rare-earth ions in

the perovskite crystal structure may pave the way for a promising route for future novel high-performance optoelectronic devices.

7.2. Scope of Future Work

In this present thesis, we have demonstrated the growth study of perovskite thin film and nanostructures for its application in LEDs and photodetectors. Our study was focused on lowering the dimension and rare-earth doping to improve the photophysical properties of $MAPbBr_3$ perovskite structure. There is vast scope to extend the present work for the broad range of applications as outlined below.

1. Study the doping effect of different lanthanide materials (Er, Yb, Sr etc.) on 2D $MAPbBr_3$ NS, since there are very few reports on the doping effect on organic-inorganic halide perovskites.
2. Fabricate 2D perovskite based photodetector with other conventional 2D material (MoS_2, $MoSe_2$, WS_2, WSe_2, h-BN, Bi_2O_2Se, MXenes, etc.) heterostructure.
3. The lead free double perovskite synthesis and study the doping mechanism to reduce the lead toxicity for the fabrication of optoelectronic devices.
4. Improve the stability of blue luminescent perovskite nanomaterials with encapsulation and functionalization with stable materials.
5. Finally, fabricate high quality, stable perovskite based optoelectronic devices for the commercialization.

भारतीय प्रौद्योगिकी संस्थान गुवाहाटी
Indian Institute of Technology Guwahati